UNIVERSITY OF CALIFORNIA, SAN DIEGO

Developing a Multi-Scale Understanding of the B Cell Immune Response

A dissertation submitted in partial satisfaction of the
requirements for the degree Doctor of Philosophy

in

Bioinformatics and Systems Biology

by

Maxim Nikolaievich Shokhirev

Committee in charge:

Professor Alexander Hoffmann, Chair
Professor Andrew McCulloch, Co-Chair
Professor Robert Rickert
Professor Scott Rifkin
Professor Ruth Williams

2014

The Dissertation of Maxim Nikolaievich Shokhirev is approved, and it is acceptable in quality and form for publication on microfilm and electronically:

_____

_____

_____

_____
Co-Chair

_____
Chair

University of California, San Diego

2014

DEDICATION

To my dear parents Nikolai and Tatiana for taking me along with them to the lab and nurturing my love for science.

To my wiser older brother Kirill for paving the way and lending a knowin ear.

To my brilliant childhood friends Adiv, Boris, Jordan, and Yan for throwing gasoline on the fire of creativity.

To my outstanding group of friends in the Signaling Systems Lab for suffering along with me and making this experience an absolute pleasure.

To my mentor Professor Ann Walker, for inviting my family to the US and giving me the chance to succeed early.

To Alex, for accepting me into the lab with a smile, and giving me the opportunity and freedom to work on these fascinating biological challenges.

Most importantly, to my beautiful fiancée Ella, for loving and supporting me despite the late nights and weekends in the lab.

EPIGRAPH

"*Bottomless wonders spring from simple rules, which are repeated without end.*"

- Benoit Mandelbrot

Fractals and the Art of Roughness

TABLE OF CONTENTS

LIST OF ABBREVIATIONS

ABM	Agent based model
Bcl_{XL}	B-cell lymphoma-extra large
BCR	B cell receptor
BAFFR	B cell activating factor receptor
BAFF	B cell activating factor
CD40L	TNF superfamily member 5 ligand
CFSE	Carboxyfluorescein succimidyl ester
CpG	unmethylated C-G rich DNA
cRel	Rel reticuloendotheliosis oncogene
CyclinD	Cyclin D2 or Cyclin D3 transcription factors
EMSA	Electrophoretic mobility shift assay
FAST	Force Algorithm Semi-automated Tracker
FO	Follicular Mature
IF	Immunofluorescence
RT PCR	Real time polymerase chain reaction
TRAIL	TNF-related apoptosis-inducing ligand
NFκB	Nuclear Factor kappaB
TNF	Tumor necrosis factor
LPS	Lipopolysaccharide
Ig	Immunoglobulin
IgM	Immunoglobulin M
IκBα	Inhibitor of kappaB alpha
IκBβ	Inhibitor of kappaB beta

IκBδ	Inhibitor of kappaB delta
IκBε	Inhibitor of kappaB epsilon
IKK1	Inhibitor of kappaB kinase alpha
IKK2	Inhibitor of kappaB kinase beta
mTOR	Mammalian Target of Rapamycin
Myc	c-myc transcription factor
MZ	Marginal Zone
NLR	Nod-like receptor
ODE	Ordinary differential equation
PAMP	Pathogen Associated Molecular Pattern
PLoS	Public Library of Science
RelA	v-rel reticuloendotheliosis viral oncogene homolog A
RelB	v-rel reticuloendotheliosis viral oncogene homolog B
RLR	Rig-I-like receptor
T1	Transitional-1 B cells
T2	Transitional-2 B cells
TLR	Toll-like receptor
TLR9	DNA sensing Toll-like receptor 9
UCSD	University of California San Diego
WT	wildtype

LIST OF SUPPLEMENTAL FILES

FlowMax.zip	The FlowMax source code, executables, and tutorial
CFSEdatasets.zip	FCS3.0 flow cytometry files used in Chapter 2
CFAnalyzer.zip	Program for analyzing immunofluorescence images
IFImages.zip	PNG images quantified with CFAnalyzer
SeqAnalysis.zip	Spreadsheet containing all normalized gene counts
WT250nM.mpg	Video of tracked wildtype 250 nM CpG B cells
CKO250nM.mpg	Video of tracked NFκB cRel deficient 250 nM CpG B cells
WT10nM.mpg	Video of tracked wildtype 10 nM CpG B cells
Rap250nM.mpg	Video of tracked wildtype 250 nM CpG B cells + rapamycin
FAST.jar	Force Algorithm Semi-automated Tracker program
MultiScale.zip	Matlab files for simulating the multi-scale B cell model

LIST OF FIGURES

LIST OF TABLES

ACKNOWLEDGEMENTS

I am very fortunate to have been supported by many friends and loved ones over the years. Without their inspiration, knowledge, wisdom, and love this dissertation would not be possible.

My fiancée, Ella Trubman, provided day-to-day unwavering support, friendship, and love and made sure to keep me well-grounded and focused over the years. She was always a happy thought in the back of my mind even when I had to stay in the lab overnight, or face stubborn reviewers.

Drs. Nikolai, Tatiana, and Kirill Shokhirev have been an inspiration and role models for my aspirations. Having grown up in a household of scientists, I was fortunate to be exposed to critical thinking, scientific ideas, and a hard-working attitude, without which I would not have had a chance among my peers. They were always there to provide advice, voice their concerns, and give me pointers on chemistry, physics, computer science, mathematics, statistics …

The Signaling Systems Lab at UCSD has grown to a whole community of supportive friends over the years. I could always count on them to drop what they were doing to go grab a beer, teach me a new technique, get me a mouse from the mouse house, or explain the ins and outs of an algorithm or assay. I would like to especially acknowledge Jeremy Davis-Turak, Jon Almaden, Bryce Alves, Harry Birnbaum, Kim Ngo, and Jesse Vargas, who have provided expert training, and both experimental and computational expertise to make chapters 3, 4, and 5 of this thesis a success. In addition, I will always keep several previous lab members Paul Loriaux, Tony Yu, Jenny Huang, and Krystin Feldman close to heart for their friendship. BacT 4 life! Diana Rios, Rachel Tsui, Karen Fortman, Brooks Taylor and honorary lab member Romila Mukerjea

were always there to provide a sympathetic ear and a witty retort. I wish all the labbies all the best!

My dear and brilliant childhood friends and collaborators Adiv, Boris, Jordan, and Yan have supported me over the decades, challenged my viewpoints, and fuelled my creativity, whether we were publishing papers together, writing stories, designing card games, or creating the next big computer game.

Alexander Hoffmann, has provided invaluable training and wisdom over the years. His enthusiasm and friendly welcoming nature and expert knowledge in diverse fields cultured an easy-going and supportive environment in the lab. Furthermore, it was Alex's excellent ideas for research on the heterogeneity of the B cell response that first got me interested in his lab and led to a successful application for the NSF Graduate Research Fellowship. He supported my own ideas and gave me the latitude to work on time-lapse imaging, multi-scale modeling, and other projects, even when it wasn't clear that the problems were surmountable.

Regents Professor Emerita Ann Walker invited our family to the states and gave me my first taste of scientific research when she hired me out of high-school to work on Nitrophorin proteins in her lab alongside my parents and under the guidance of an awe-inspiring graduate student, Lillya Yatsunik (now Professor) and brilliant post-doctorate researchers Robert Berry and Igor Filippov.

Dr. Osamu Miyashita was my undergraduate thesis advisor in biochemistry and first got me interested in physics-based simulations which I have taken with me to San Diego and applied to the study of miRNA structures and B-cell tracking.

Finally, the support, helpful discussions, and time that my Ph.D. committee provided freely made this entire process as painless as possible.

Chapter 2, in full, is a reprint of the material as it appears in PLoS One 2013. Maxim N. Shokhirev and Alexander Hoffmann, A. Public Library of Science, 2013. Alexander Hoffmann is the corresponding author. The dissertation author was the primary investigator and author of this paper.

Chapter 3, in part, is currently being prepared for submission for publication of the material and may appear as Maxim N. Shokhirev, Jonathan Almaden, Jeremy Davis-Turak, Harry Birnbaum, Theresa M. Russell, Jesse A.D. Vargas, Alexander Hoffmann. "A multi-scale approach reveals that NFκB enforces a decision to divide or die in B cells." Jesse A.D. Vargas helped train me to run single-cell microscopy experiments. The dissertation author was the primary investigator and author of this paper.

Chapter 4, in part, is currently being prepared for submission for publication of the material and may appear as Maxim N. Shokhirev, Jonathan Almaden, Jeremy Davis-Turak, Harry Birnbaum, Theresa M. Russell, Jesse A.D. Vargas, Alexander Hoffmann. "A multi-scale approach reveals that NFκB enforces a decision to divide or die in B cells." Jonathan Almaden helped with B-cell purification, western blotting, and RT-PCR. Jeremy Davis-Turak and Harry Birnbaum collaborated to align and map single-cell RNAseq results. Theresa M. Russell and I collaborated to produce the single-cell RNA sequencing datasets. Jesse A.D. Vargas devised the immunofluorescence protocol and trained me to run immunofluorescence and single-cell microscopy experiments. The dissertation author was the primary investigator and author of this paper.

Chapter 5, in part, is currently being prepared for submission for publication of the material and may appear as Maxim N. Shokhirev, Jonathan Almaden, Jeremy Davis-Turak, Harry Birnbaum, Theresa M. Russell, Jesse A.D. Vargas, Alexander Hoffmann. "A multi-scale approach reveals that NFκB enforces a decision to divide or die in B

cells.” Jonathan Almaden helped with B-cell purification. The dissertation author was the primary investigator and author of this paper.

VITA

2003-2008	Undergraduate Researcher, University of Arizona
2008	Bachelor of Science, University of Arizona
2010-2011	ScienceBridge Scientist Lecturer, Correia Middle School, San Diego
2010-2013	NSF Graduate Research Fellow, University of California, San Diego
2011-2012	Independent Contractor, NanoCellect Biomedical Inc. San Diego, CA.
2014	Doctor of Philosophy, University of California, San Diego

SELECTED PUBLICATIONS

"Effect of mutation of carboxyl side-chain amino acids near the heme on the midpoint potentials and ligand binding constants of nitrophorin 2 and its NO, histamine, and imidazole complexes." *J Am Chem Soc*. 2009.

"Biased coarse-grained molecular dynamics simulation approach for flexible fitting of X-ray structure into cryo electron microscopy maps." *J Struct Biol*. 2010.

"Paternal RLIM/Rnf12 is a survival factor for milk-producing alveolar cells." *Cell*. 2012.

"FlowMax: A Computational Tool for Maximum Likelihood Deconvolution of CFSE Time Courses." *PLoS One*. 2013.

"Effects of extrinsic mortality on the evolution of aging: a stochastic modeling approach." *PLoS One*. 2014.

"IκBε Is a Key Regulator of B Cell Expansion by Providing Negative Feedback on cRel and RelA in a Stimulus-Specific Manner" *The Journal of Immunology*. 2014.

"BAFF engages distinct NFκB effectors in maturing and proliferating B cells." *In press.*

"Sequence Signatures and Polymerase Dynamics Favor Co-transcriptional Splicing Genome-wide." *In press.*

"A multi-scale approach reveals that NFκB enforces a decision to divide or die in B cells." *In preparation.*

ABSTRACT OF THE DISSERTATION

Developing a Multi-Scale Understanding of the B Cell Immune Response

by

Maxim Nikolaievich Shokhirev

Doctor of Philosophy in Bioinformatics and Systems Biology

University of California, San Diego, 2014

Professor Alexander Hoffmann, Chair
Professor Andrew McCulloch, Co-Chair

The immune system is composed of hundreds of highly-specialized cell types that collaboratively orchestrate an efficient response to pathogens and damage. Central to immune function, B lymphocytes participate in both the fast but non-specific innate, and persistent adaptive immune responses by sensing conserved pathogen-associated molecular patterns such as bacterial or viral CpG DNA as well as pathogen-specific patterns recognized by uniquely generated B-cell receptors. Upon activation, B cells

undergo rapid expansion in number, deal with the threat by carrying out specific effector functions, and eventually die by programmed cell death or become long-lived memory cells. As a result, B-cell dynamics dictate vaccine efficiency, while aberrant proliferation and/or survival is the hallmark of autoimmune disorders, immune deficiency, and cancer. Decades of Nobel-worthy studies have characterized the key molecular players, cellular behaviors, and population dynamics of B cells, but the implicit heterogeneity and multi-scale nature of the B-cell response pose fundamental challenges to meaningful interpretation in specific contexts. A multi-scale understanding has only recently become possible with the advent of single-cell assays and the advancement of computational methods. To better-understand how individual cells orchestrate the population response, we developed CFSE flow cytometry deconvolution of cell populations, time-lapse cell tracking, and agent-based multi-scale computational modeling methods which we combined with single-cell and traditional biochemical assays and literature mining to develop a mechanistic understanding of the B cell immune response from the molecular pathways governing NFκB signaling, growth, cell-cycling, and apoptosis to cellular behavior and ultimately the population dynamics. We find that 1)the population behavior is best explained by individual B cells making decisions to either grow and divide, or die 2)that NFκB signaling serves as a central enforcer of B cell decision making by promoting division and survival and 3)that a multi-scale model can accurately predict population behavior with a lower dose of the stimulus, when NFκB cRel missing, and when pretreated with the drug rapamycin. The methods and models developed as part of this dissertation serve as predictive frameworks for future hypothesis-driven discovery and model-driven analysis, enabling meaningful interpretation of patient data, and drug target prediction across biological scales.

Chapter 1

Introduction

Developing an understanding of the multi-scale B-cell immune response requires a diverse background in the underlying biological processes as well as a working knowledge of various experimental and computational techniques. In the following sections I provide an overview of B-cell biology, the stochastic multi-scale dynamics of the B-cell immune response, the role of NFκB signaling, an overview of the interplay between NFκB, Myc, and mTOR, as well as highlighting the current state of the art approaches to time-lapse microscopy, cell tracking, single-cell molecular assays, stochastic modeling of CFSE flow cytometry datasets, and multi-scale agent based modeling. My aim is to provide a general overview of these topics and to highlight the findings pertinent to these studies, while referring readers to more in-depth reviews.

1.1. Overview of B cell development and function

The immune system is a collection of diverse cells that are typically dormant but can rapidly respond to pathogens, inflammatory signals, and other stresses by upregulating metabolism, proliferating, traveling to the source of infection, producing secondary messenger molecules, differentiating into specialized cell types and ultimately dying or resuming a quiescent steady state [1,2]. First characterized in the middle 1960's and early 1970's [3-5], B cells serve important roles in both the adaptive and innate immune responses and so it is not surprising that their homeostasis is under control at multiple development and functional checkpoints [6]. B lymphocytes are continuously being produced from a stem-cell pool in the bone marrow, where they undergo a stringent vetting process that removes auto-reactive, and potentially dangerous clones. The remaining ~10% migrate to the secondary lymphoid tissues (spleen, lymph nodes), where they undergo further maturation into naïve mature B cells, and are primed to rapidly respond to pathogens and inflammatory signals [5-9]. B cells that pass the necessary checkpoints during development and differentiation receive tonic survival signals allowing them to survive for weeks and providing plenty of opportunity for them to sample the blood (spleen), gut (Payer's Patches), and periphery (lymph nodes) for potential pathogens [4,10].

Unlike most other immune cells, B cells play important roles in both the innate and adaptive immune responses [11]. Adaptive immunity is achieved through diversification followed by rapid clonal selection and the establishment of immune memory. During B cell development, B cells recombine immunoglobin (Ig) heavy and light chains via a specialized genetic editing mechanism that is able to generate incredible receptor diversity, thereby ensuring that any potential pathogen will be recognized [12,13]. Furthermore, since B-cells are clonal, rapid proliferation upon

pathogen recognition will produce a geometrically increasing population of B-cells that recognize the specific pathogen [6]. B cell receptor binding is further optimized during clonal expansion in germinal centers (GC) due to somatic hyper-mutation of the Ig genes [14]. After the threat is neutralized, most of the proliferating B cells die, leaving a population of long-lived memory B-cells that are poised to rapidly reactivate in the event of a subsequent reinfection by the same pathogen potentially decades later. This adaptability comes at the cost of speed as the response ramps up over the span of days and even weeks, requiring the presence of the right B cell that is expressing the right antigen-specific receptor, secondary signaling from other immune cells, and clonal selection prior to full activation. On the other hand, the more ancient innate immune response results in the immediate activation of B cells expressing sets of highly-conserved receptors that recognize specific pathogen-associated molecular patterns (PAMPS) [15]. There are three main classes of pattern recognition receptors (PRRs) that have evolved to recognize various pathogen-specific structures [16]. In addition to Nod-like receptors (NLRs) and RIG-I-like receptors (RLRs) which sense viruses and other pathogens in the cytosol, Toll-like receptors (TLRs) span the cell membrane or internalized endosomes and recognize structures indicative of bacteria, viruses, or fungi outside of the cell [17]. There are at least 13 different TLRs known to exist, however the specific combination of TLRs expressed differs between species (Table 1.1). Of particular interest, TLR9, which recognizes bacterial and viral unmethylated CG-rich sequences, is found in both mice an humans, and leads to T-cell independent B-cell expansion and cytokine/chemokine/growth-factor production when exposed to nM concentrations of CpG [18-20]. Furthermore, cells stimulated with CpG are not self-adherent, enabling direct imaging and tracking of stimulated B cells with a microscope [21]. Figure 1.1 shows an overview of B cell development and activation.

An efficient B-cell immune response is essential for survival while dysregulation is the hallmark of B-cell cancers, autoimmunty, and immune deficiency. B-cell lymphomas, like other types of cancers, occur due to a loss of proliferative/death checks and balances in B cells, causing uncontrolled accumulation of lymphocytes. Lymphomas are the fifth most common type of cancer in the United States and are the sixth deadliest causing an estimated 21,530 deaths in 2010 [22]. B cell lymphomas typically arise during an error in V(D)J recombination, somatic hyper mutation during the germinal center (GC) expansion, or class-switch recombination [23]. For example, the anti-apoptotic Bcl2 regulator is found to be translocated into the heavy chain Ig locus in 90% of follicular lymphomas, promoting its constitutive transcription and immortality. Other types of lymphomas arise from similar translocations of growth and cell-cycle regulators such as Myc and Cyclin D. Importantly, cancerous transformation results in considerable cell-to-cell heterogeneity within even clonal sub-sets of cells, posing significant challenges for drug-based treatment [24-30]. In addition to B cell cancers, buildup of constitutively active B cells can lead to autoimmune disorders and chronic inflammation, due to excess proliferation, cytokine production, or antigen presentation to auto-reactive T-cells [31]. Excessive B-cell activation can be caused by defects in the B-cell ablation mechanisms during Ig maturation in the bone marrow or caused by somatic hyper mutation in the GC, as well as due to aberrant signaling through pro-survival BAFF receptor and defective TLR signaling as reviewed in recent works [31-33]. Unfortunately, since B-cell activation and survival are hallmarks of cancer, autoimmune diseases often predispose individuals to B cell cancers [34]. While out of control B cell activation can lead to autoimmunity, chronic inflammation, and lymphomas, developmental blocks caused by dysfunctional Ig production and problems with activation or survival result in immune deficiency and susceptibility to diseases [35] .

Interestingly, a shift in B cell subsets caused by developmental blocks can result in autoimmunity [36] and further highlights the complexity of the immune system as well as a need for stringent regulation for proper function. Thus, the complexity, heterogeneity, and dynamic nature of B cell homeostasis and function demands stringent regulation at all points during B cell development and activation. The potential for malignancy cannot be overstated as activated B-cells essentially resemble specialized “cancer” cells due to their fast proliferation, anaerobic metabolism, and the upregulation of potentially mutagenic processes (i.e. V(D)J recombination, somatic hyper-mutation, class-switch recombination).

Table 1.1. Summary of various TLRs and their abundance in mice and humans. Compiled from various sources [16,17,37-42].

TLR	PAMPS recognized	Mouse	Human
1/2	Triacyl lipopeptides	+	+
2	Peptidoglycan, LAM, Hemagglutinin, phospholipomannan, Glycosylphosphophatidyl inositol mucin	+	+/-
3	ssRNA virus, dsRNA virus, RSV, MCMV	+/-	+/-
4	Lipopolysaccharides, Mannan, Glycoinositolphospholipids, Envelope proteins	+	-
5	Flagellin	+	+
6/2	Diacyl lipopeptides, LTA, Zymosan	+	+
7	ssRNA viruses	+	+
8	ssRNA from RNA virus	-	+
9	dsDNA viruses, CpG motifs from bacteria and viruses, Hemozoin	+*	+
10	Bacterial peptidoglycan	-	+
11	Uropathogenic bacteria, profillin-like molecule	+	-
12	Profilin	+	-
13	Bacterial RNA	+	-

*-TLR9 is expressed in B1, marginal zone, and follicular murine B-cells

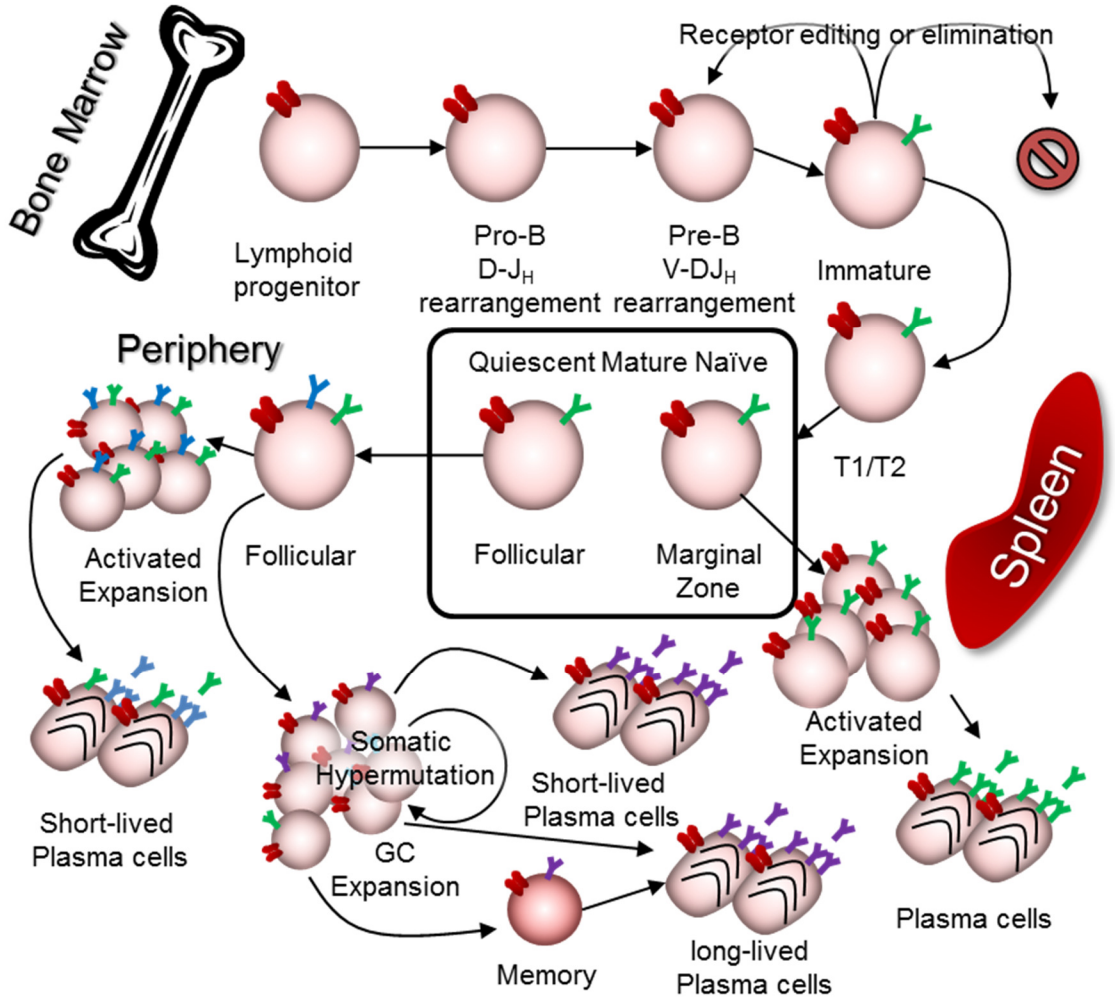

Figure 1.1. Diagram summarizing the development and activation of B cells. B cells develop from lymphoid progenitors in the bone marrow, undergo selection for self-tolerance, and finish maturation in the spleen. Quiescent mature naïve B cells undergo rapid population expansion and differentiate into long- or short-lived antibody producing plasma cells, or memory cells. Innate toll-like receptors (red), membrane-bound and excreted IgM (green), class-switched IgD (blue), and somatically hypermutated Igs (purple) are depicted on cell membranes. Recently reviewed in [4-6,9].

1.2. Stochastic cellular behavior orchestrates the response

Given the complexity of B cell signaling, presence of numerous B cell subtypes, and inherent randomization of Igs during development, it is clear that heterogeneity is a central theme of the B-cell immune response. Strikingly, the apparent stochasticity is most evident when observing individual B-cells stimulated with mitogenic signals such as unmethylated bacterial or viral CpG DNA (Figure 1.2). Individual B cells interpret these signals by undergoing 1-6 rounds of cell cycling, followed by cell cycle exit, and death by programmed cell death [21]. The population response is the sum of these single-cell decisions and characteristically lasts several days to a week by first producing a dramatic increase in the number of activated B cells for several days, followed by a return to starting cell counts [43]. While the population response is robust (i.e. reproducible total cell coun dynamics), the behavior of individual cells is seemingly stochastic since only a fraction of cells respond in each generation and because the timing of division and death is highly variable between these genetically identical synchronized cells. In fact, the timing of division and death is well-modeled by long-tailed distributions (e.g. log-normal) as a function of cell age, resulting in a distribution of cells across many generations after only a few days of stimulation [21,44]. Furthermore, progenitor cells (generation 0) typically take much longer to divide or die, while dividing cells (generation 1+) divide again within six to twelve hours [21,45]. After several days of intense proliferation, the population response returns back to basal levels which is caused primarily by cell-cycle exit followed by programmed cell death [21]. In fact, the fraction of cells that progress to the next generation (i.e. the fraction that divides) decreases approximately sigmoidally with each generation such that the final division number, or “division destiny” of a cells is approximately normally distributed as a function of generation [20,21,44].

But what gives rise to this variability in cell fate and timing? Previous studies offer evidence that the inherent variability in timing of the apoptosis is caused primarily by cell-to-cell protein abundance variability [24] and presumably variability in cell-cycle regulators generate cell-to-cell variability in cell-cycle duration, however, it is still unclear if variability in timing of competing division/death processes determine fate. There are competing theories for how fate (division/death) is determined. On one hand there is recent support for a molecular race hypothesis, which posits that cell-cycle and apoptosis processes are proceeding concurrently within cells, and that fate is determined by the faster of these mutually exclusive outcomes [44,46]. Specifically, an age-structured population model, the cyton model, which incorporates competition between division and death fates can reproduce the major population features and produces excellent fits to experimental datasets [44]. Furthermore, a recent study [46] demonstrated that a probabilistic model that assumes correlation of fate timing between siblings and mutual censorship between competing processes (e.g. division and death) can reproduce the correlations between non-concordant fates as well as the observed censored distributions for the time to divide, time to isotype switch, and time to plasmablast differentiation (although the best-fit censored model death time distributions were typically earlier than the observed death distributions). On the other hand, there is also evidence that cells decide their fate early and are protected from the alternate outcome. Single-cell time-lapse videos of stimulated B cells revealed that cells that died did not grow, while cells grew prior to dividing in all except the last and pen-ultimate generations, indicative of a lack of fate competition [21]. Furthermore, the authors found that the size of the progenitor cells was predictive of the number of divisions suggesting that fate is decided in the initial generation. As a result, we described the fcyton model, which unlike the cyton model, commits responding cells to division, and showed that cell

commitment to a specific fate nevertheless resulted in excellent model fits for all experimental datasets [47]. Further support for a molecular decision comes from a recent study, demonstrating that levels of cell cycle inhibitor p21, which directly inhibits CDK2 activity is sufficient for promoting cell-cycle reentry in cell lines and human primary cells [48]. Therefore, while extrinsic variation in initial protein levels determines timing of cell death (and presumably cell-cycle timing), cell fate may be a function of competing mutually exclusive processes or stochastic variation in the concentrations of key regulators. Knowing whether cells make decisions will determine how we model cell fate determination on the molecular level and in turn informs experimental and drug design.

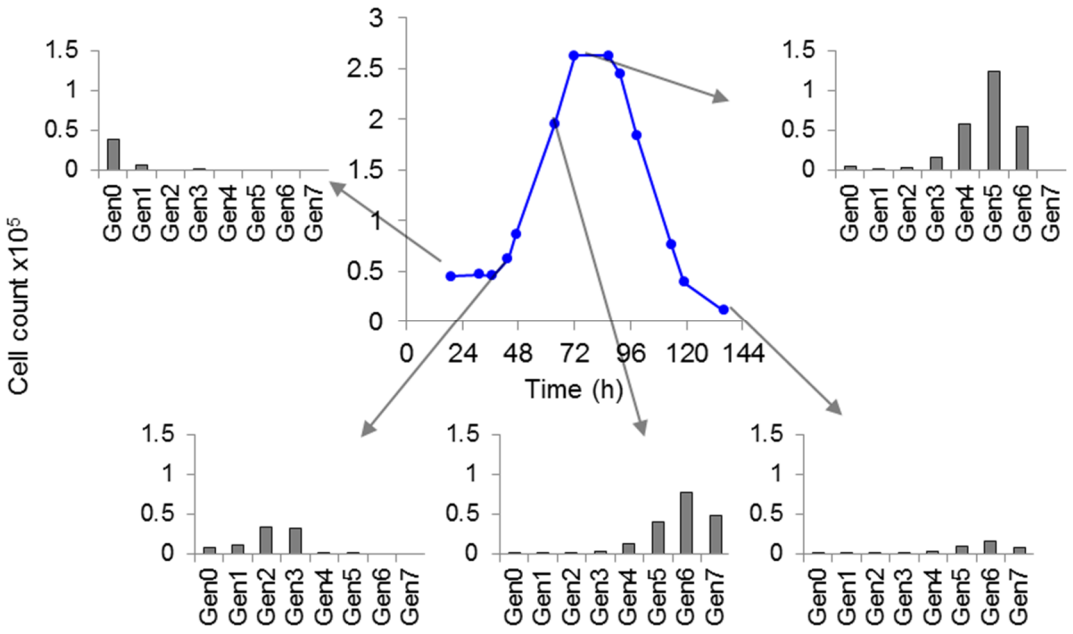

Figure 1.2. The B cell population response is composed of heterogeneous single-cell behaviors. While the population response is robust with a period of expansion followed by programmed cell death, timing and fate of individual cells is heterogeneous. Results were obtained from fitting mixed Gaussian distributions to CFSE log-fluorescence histograms measured by flow cytometry after the indicated times of 250 nM CpG stimulation.

1.3. The role of NFκB signaling in the B cell response

While it is unclear how B cell fate is ultimately determined, the underlying biochemical processes involved in transducing receptor signals, cell growth, cell cycling, and programmed cell death by apoptosis are known and well-studied (recently reviewed in [4,17], [49], [50], respectively). In B cells, which remain small and in an actively maintained quiescent state (G0 phase of the cell-cycle), activation can be achieved through TLR signaling as well as through the BCR resulting in the activation of growth, cell-cycling, and apoptosis pathways through various signaling networks. As mentioned previously, signaling through TLR9 by adding nM-uM concentrations of non-methylated CpG independently leads to dramatic non-self-adherent B cell activation, providing a convenient window into the behavior of proliferating B cells. Importantly, CpG robustly activates the canonical branch of the well-studied and essential NFκB signaling pathway (Figure 1.3) [51], resulting in the upregulation of hundreds of genes associated with survival and proliferation, providing a natural molecular connection between signaling and cell fate [52]. Specifically, activation of TLR9 by CpG results in the activation of the kinase IKK2, which rapidly phosphorylates NFκB inhibitor proteins, the IkBs, which sequester NFκB dimers in the cytoplasm. Phosphorylation of IkBs results in their ubiquitination and degradation, releasing NFκB dimers (primarily RelA:p50 and cRel:p50 in B cells [4]) and allowing them to enter the nucleus where they bind to promoters of genes containing the NFκB motif, and activate gene expression. Importantly, the genes coding for cRel [53] and p50 [54] as well as the inhibitors IkBα [55] and IkBε [56] are themselves target genes, resulting in waves of NFκB activation lasting potentially several days (Figure 1.4). Therefore, many essential molecular players involved in the B cell immune response have been identified but it remains unknown how their dynamics

lead to the observed cell fate and timing variability and in turn the B cell population response.

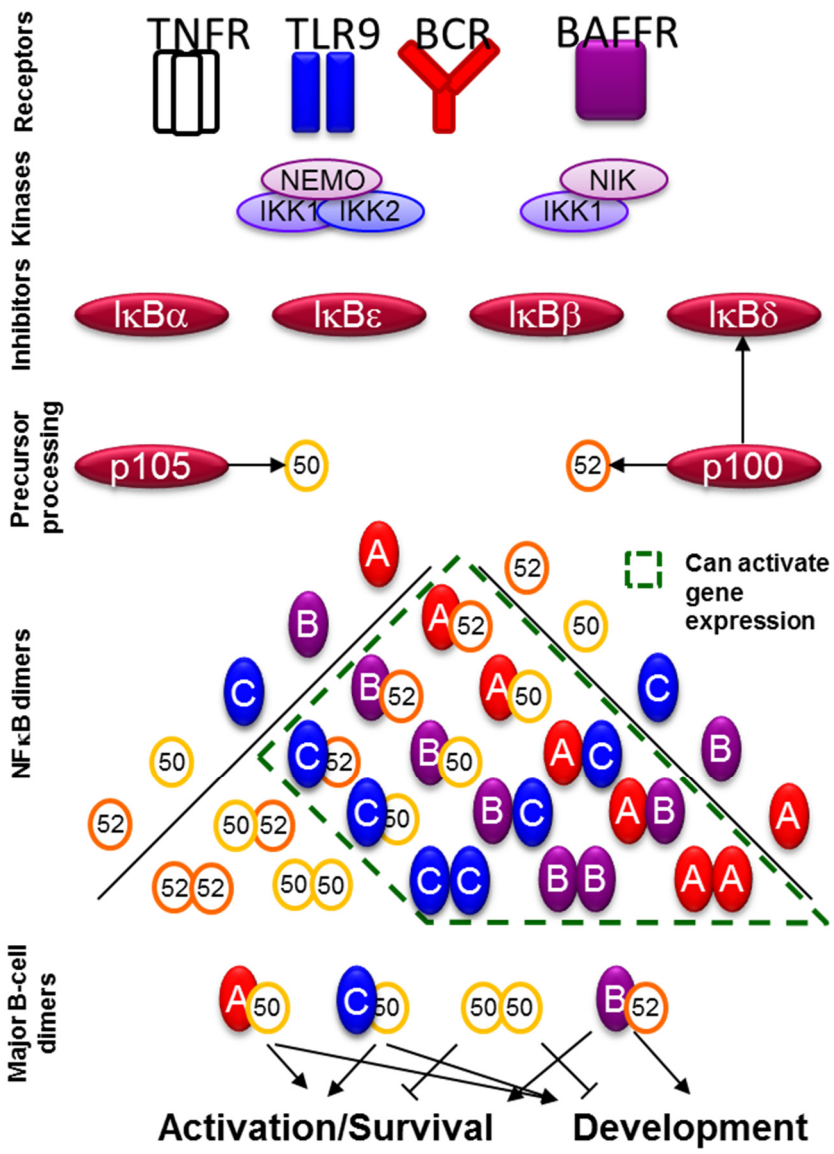

Figure 1.3. Components of the NFκB signal transduction system. Receptors lead to the downstream activation of kinases, the IKKs, which phosphorylate inhibitors of NFκB, the IkBs, targeting them for ubiquitin-mediated protease degradation. IkB degradation leads to release of NFκB dimers that are free to enter the nucleus and upregulate gene expression programs. While RelA:p50 is the canonical dimer responsible for signaling in most cells, in B-cells both RelA:p50 and cRel:p50 can activate growth, cell-cycle progression, and survival programs. Recently reviewed by [57] and [4].

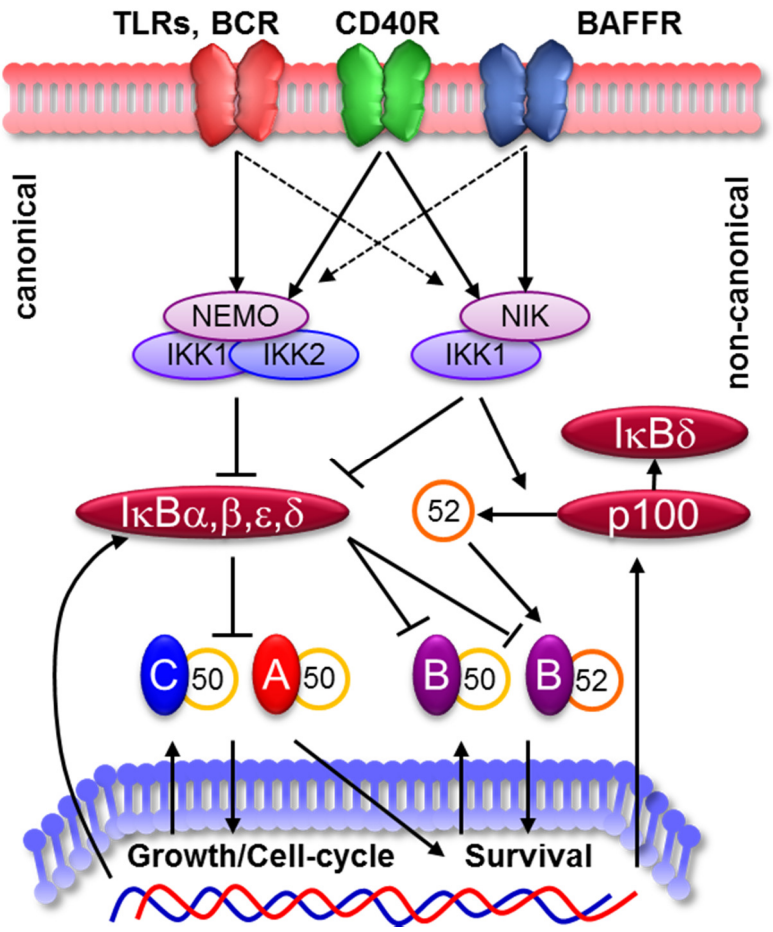

Figure 1.4. NFκB signaling pathway in B-cells. The canonical and non-canonical branches of the NFκB signaling pathway are shown. Receptors initiate downstream signaling through the canonical or non-canonical branches by activating kinases IKK1 and IKK2. Canonical signaling results in IKK2-mediated degradation of IkBs which serve to sequester NFκB dimers in the cytoplasm, whereas non-canonical activation of NIK results in processing of p100 precursor to p52. Free NFκB dimers that contain transactivation domains (A,B, or C) bind to kB elements in the promoters of genes and promote activation of growth/cell-cycle and survival genes. Importantly, NFκB can upregulate the production of IkBα and IkBε as well as p105, p100, RelB, and cRel proteins, leading to waves of NFκB activation. Recently reviewed by [57] and [4].

1.4. NFκB, Myc, and mTOR in B cell division and death

While NFκB can activate survival and proliferative genetic programs, the exact mechanisms leading to cell growth, cell-cycle progression, and survival, as well as the roles that central regulators myc and mTOR play are still not fully understood.

Like NFκB, myc is a central transcription factor that promotes growth and proliferation by promoting the production of cellular machinery (e.g. ribosomes)[4,49]. Whereas, myc has traditionally been traditionally associated with the control of growth in cells, recently, it has been shown that myc is best thought of as a global regulator of transcriptional activation in lymphocytes, a central regulator of cell activation [58]. Unsurprisingly, myc dysfunction is prevalent in cancers which exist in a perpetually active state [49]. Importantly, myc is a direct downstream target of NFκB activation, providing a direct link between NFκB signaling to cell growth and activation [59]. In addition to being NFκB target genes, genetic knockout of NFκB cRel and p105/p50 (leading to effective removal of canonical gene-inducing NFκB dimers cRel:p50 and RelA:p50) results in B cells that are unable to grow and proliferate due to a failure to upregulate myc, showing that at least in B cells, signaling through NFκB is essential for activation and function [60]. NFκB-dependent regulation of myc has also been observed in T-cells further enforcing an NFκB regulation in myc activity.

Mammalian target of rapamycin (mTOR) is another key regulator of metabolism in cells, and acts to promote growth and proliferation by inducing general cellular machinery required for metabolite uptake, protein synthesis, and DNA replication [61,62]. Importantly, mTOR is activated by the presence of metabolites as well as by general mitogenic signals, enabling it to serve as a general sensor and regulator of metabolism. As with NFκB and myc, mTOR dysfunction is a hallmark of cancer and

inhibitors of mTOR such as rapamycin, hold promise for cancer treatment [63-65]. However, the interplay between Myc or NFκB with mTOR signaling in lymphocytes remains poorly understood. Myc and mTOR signaling seem to form a mutual feedback loop, as depeletion of myc leads to lower mTOR, while inhibition of mTOR function leads to lower Myc [66]. The crosstalk between NFκB and mTOR remains uncertain. Signaling through the Akt/mTOR axis has been shown to activate NFκB via IKK in a prostate cancer cell line [67]. On the other hand, in myocytes NFκB and mTOR impose a mutual bidirectional control [68]. Finally, NFκB and mTOR may be activated in parallel through IKK signaling to mTOR and NFκB in a cancer cell line [69].

How can NFκB, Myc, and mTOR control cell growth, cell-cycle progression and survival in B cells? In addition to NFκB control of myc, the genes coding for CyclinD [70-72], E2F3 [73], and Bcl_{XL} [74], which are essential for cell-cycle progression and survival, are all known to be NFκB target genes. Cyclins D1-3, are cell-cycle regulator responsible for G1-S checkpoint progression by phosphorylating and thereby inactivating retinoblastoma protein [75], however only Cyclin D2 and D3 have been shown to be important for G1-S checkpoint progression in B cells[76-78] and reviewed in [79]. Inhibition of NFκB signaling in lymphoma cell lines resulted in cell-cycle arrest in the G1 phase due to downregulation of Cyclin D1 expression, further supporting a direct link between NFκB signaling and cyclin D1 driven cell-cycle progression in B cells [80]. Furthermore, NFκB promotes the activation of transcription factor E2F3 which helps drive cell-cycle progression in the G1 phase of the cell cycle. E2F3 is a transcription factor that is typically bound to the retinoblastoma protein (Rb) in quiescent cells, and upon Rb hyperphosphorylation can activate the transcription of other cyclins [81,82]. In addition to its role in growth and cell-cycle progression, there is a direct link between

NFκB signaling and survival in B cells. NFκB is known to promote the expression of anti-apoptotic BCL family members Bcl_{XL} [73] as well as A1[83]. A1 is thought to serve an early survival function, while Bcl_{XL} builds up to provide prolonged survival [73,83]. Furthermore, NFκB signaling contributes to the ERK-dependent degradation of the pro-apoptotic BH3-only protein Bim, via the IKK/p105/Tpl2 axis[84-87]. Both myc and mTOR are important for turning on general machinery and show bi-directional regulation. In addition, myc and mTOR play indirect roles in survival as gene expression and protein synthesis are required for programmed cell death. As such, quiescent cells are protected from death as compared to actively growing and metabolically active cells. Whereas NFκB can control myc expression directly, its role in mTOR signaling is currently poorly understood. These interdependencies are summarized in Figure 1.5.

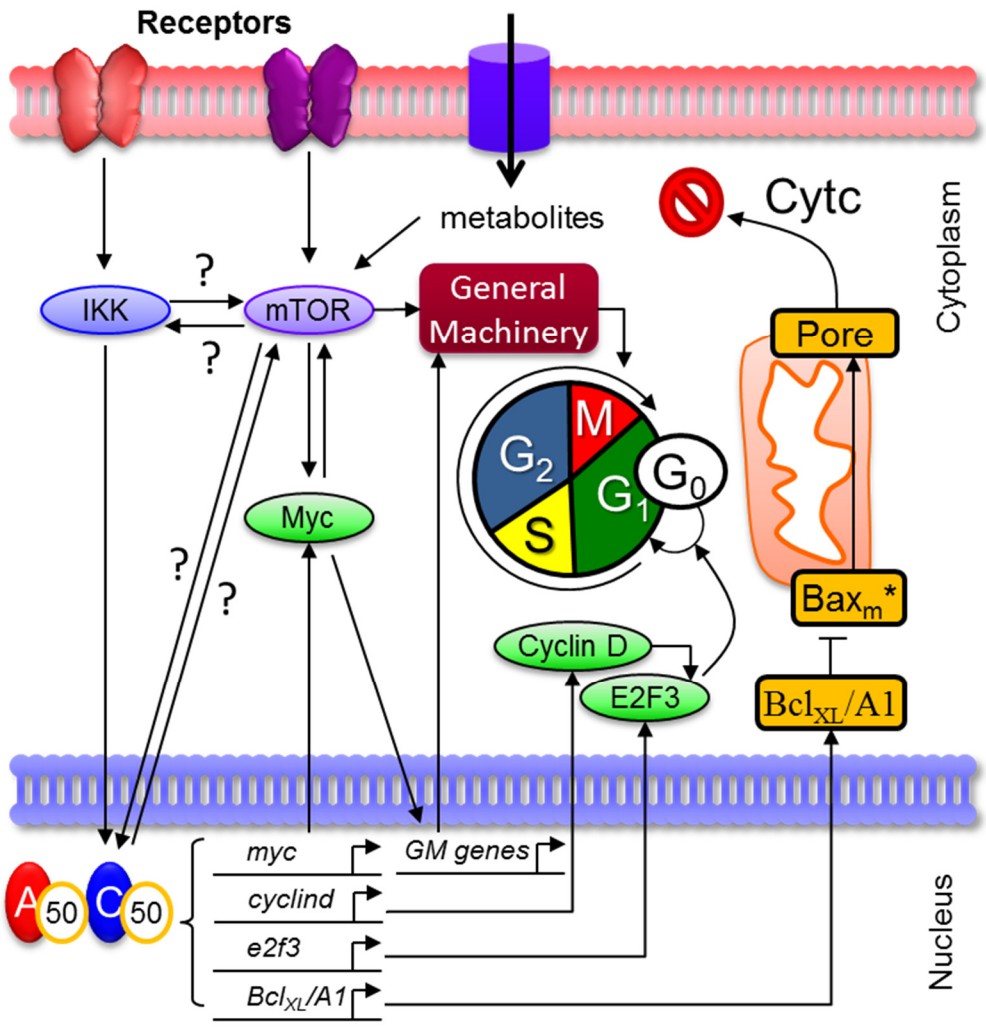

Figure 1.5. The NFκB, Myc, mTOR interplay in B cell division and death. NFκB signaling promotes the expression of Myc, cell-cycle progression genes, and anti-apoptotic Bcl proteins. Myc serves to upregulate global gene expression programs as well as general machinery proteins which are required for cell growth and subsequently for B cell progression through the cell-cycle. In addition, mTOR is important for ribosome activation and protein synthesis. Cell death is caused by the oligomerization of Bax protein on the mitochondria leading to pore formation, release of cytochrome c and subsequent apoptosome-mediated executioner caspase activation and death. Interplay between NFκB, Myc, and mTOR is poorly understood with possible cross-talk between NFκB and mTOR as well as Myc.

1.5. Interpreting B cell CFSE population dynamics

A current experimental approach for tracking lymphocyte population dynamics involves flow cytometry of carboxyfluorescein succimidyl ester (CFSE)-stained cells. First introduced in 1990 [88], CFSE tracking relies on the fact that CFSE is irreversibly bound to proteins in cells, resulting in progressive halving of cellular fluorescence with each cell division. By measuring the fluorescence of thousands of cells at various points in time after stimulation, fluorescence histograms with peaks representing divisions are obtained. However, interpreting CFSE data confronts two challenges. In addition to intrinsic biological complexity arising from generation- and cell age-dependent variability in cellular processes, fluorescence signals for a specific generation are not truly uniform due to heterogeneity in (i) staining of the founder population, (ii) partitioning of the dye during division, and (iii) dye clearance from cells over time. Thus, while high-throughput experimental approaches enable population-level measurements, deconvolution of CFSE time courses into biologically-intuitive cellular parameters objectively remains a major challenge and is susceptible to misinterpretation [89].

To address the experimental and biological variability associated with CFSE time courses, a number of theoretical models have been developed (see [90,91] for recent reviews) and some of the most recent are summarized in Table 1. Early models adopted the ordinary differential equation (ODE) approach, modeling division [92-99] and death [92-95,97-105] as first-order processes. As experimental information about cellular processes became available, models were updated to account for the non-exponential nature of division, imposing a delay, or skewed distribution for the interdivision time [44,92,100-109]. While both the time to divide and time to die are well-modeled by skewed distributions, only several models allow arbitrary distributions for cell death times [44,107-111].To account for the large difference in the division and death times between

undivided and dividing cells, most recent models have explicit generation structure or heterogeneity [44,100-102,104-109,111,112]. Also, some models explicitly incorporate mechanisms that can account for the decrease in cell numbers after an initial period of population expansion [44,93,95,101,104,105,107-109,111]. In addition, a few models incorporate fractional progression of cells to the next division [44,101,104-106,109,111]. Finally, more recent models are formulated to account for both sources of variability, modeling population dynamics and fluorescence effects in an integrated manner [98,99,107,108], while others account for cell fluorescence with a time-independent mixture of Gaussians models [107,111,112]. Modeling the population fluorescence dynamics is advantageous as models can be compared to the experimental data directly during fitting, but this approach typically suffers from computational intractability. While the computational complexity has been shown to be greatly reduced by decoupling dye intrinsic effects from population dynamics and employing approximations [107], potentially important biological features such as cell age-dependent rates for division and death and late-phase population contraction (in the form of decreasing fractions of responding cells) must be taken into account. Several extensions of the DLSP model [107] incorporating age-structure and fractional responses of cell populations have recently been proposed which incorporate cell age structure [108], or fractional response to stimulus [109], however there is no label-structured model available that incorporates all of the important biological features. Of note, the Hyrien-Chen-Zand general branching process model [111] can be adopted to include all desired biological features, however, efficient computation is not straightforward, and a late-phase contraction mechanism is not explicitly shown. Upon comparing recent models (Table 1.2), only the generalized cyton model explicitly accounts for all of the essential biological features: age- and generation-structured division and death, fractional response to stimulus, and late-phase

contraction of the population [44]. A competition between independent division and death pathways in responding cells is at the heart of the cyton model. Responding cells have a non-zero probability of dying before division. However, more recent single-cell microscopy studies have shown that growing cells are protected from death [21]. Therefore, the cyton model was recently reformulated to include an explicit decoupling of the division and death pathways [113]. In the reformulated fcyton model responding cells are committed to age-dependent division, while non-responding cells are committed to age-dependent death. This model is covered in depth in chapter 2.

The biggest challenge for interpreting heterogeneous CFSE datasets is the availability of validated computational tools for deriving biological insights. To date, only two freely available user-friendly computational tools for interpreting CFSE datasets are available. The Cellular Calculator (Cyton Calculator) is a free polished computational tool that relies on user-provided generational cell counts and manual estimates of cyton model parameters to find the a local optimum set of cyton model parameters [44,45]. The problem with this approach is that it confidence in the solution was not known. First, any computational tool requires a characterization of its performance to establish how the solution accuracy, sensitivity, and redundancy will depend on the underlying data. Second, solutions were provided as is, leaving the user without a measure of solution confidence. Third, the tool found a local optimum, precluding multiple solutions. Finally, the source code for the tool was not provided, severely limiting its expandability. Our approach was to create, validate, and use a user-friendly open-source computational tool for fitting population model parameters to CFSE datasets with measures of confidence [47]. This tool is the subject of chapter 2 of this thesis.

Table 1.2 Summary of recent cell population models for interpreting CFSE datasets.

Reference	Cell Cycle	Cell Death	Late-phase contraction	Fractional activation	Fl. Dyn.
Gett *et al* (2000) [100]	Tdiv0 ~normal. Tdiv1 const.	Exponential decay. Generation-invariant.	N/A	N/A	N/A
De Boer *et al* (2001) [93]	Piece-wise constant division rate of activated cells	Piece-wise constant generation-invariant rate.	Fate = f(t)	N/A	N/A
Revy *et al* (2001)	Constant division rate.	Exponential decay. Generation-invariant.	N/A	N/A	N/A
De Boer *et al* (2003) [95]	Constant division rate for activated cells	Constant death rate. Differs between active/resting cells	Cells inactivate at constant rate	N/A	N/A
Deenick *et al* (2003) [106]	Age-dependent division rate for responding undivided cells. Constant division time for dividing cells	Constant death rate for undivided cells, constant fractional survival of divided cells.	N/A	Undivided cells only	N/A
Pilyugin *et al* (2003) [96]	Average cell cycle time and variance of generation times can be calculated	Prob. dying during each division can be calculated. Death is generation- and time-invariant.	N/A	N/A	N/A
Leon *et al* (2004) R. G-H [101]	Gamma-distributed division rates. Dif. parameters for gen 0 and gen 1+ cells.	Exponential decay. Generation-invariant.	N/A	N/A	N/A
Leon *et al* (2004) E Nordon [101]	Delayed exponential division for undivided cells. Gen 1+ have constant division times.	Exponential decay of resting cells. Generation-invariant.	Active cells inactivate with constant prob.	Prob. to continue cycling	N/A
Ganusov *et al* (2005) [103]	Delayed exponential Tdiv0. Rate is generation-invariant	Exponential decay with different rates: resting/cycling	N/A	N/A	N/A
De Boer *et al* (2005) [102]	Delayed exponential division that differs for dividing cells.	Constant death rates specific to resting and cycling cells.	N/A	N/A	N/A
De Boer *et al* (2006) [104]	Tdiv0 ~ delayed log-normal. Tdiv1 ~ const.	Exponential decay with death rate dependent on generation	Gen. dependent exponential decay	Undivided cells only	N/A
Luzyanina *et al* (2007a) [97]	Constant generation-dependent rates for div.	Constant generation-dependent rates for death.	N/A	N/A	N/A
Luzyanina *et al* (2007b) [98]	Constant generation-independent rates for division.	Constant generation-independent rates for death.	N/A	N/A	Dye decay, and dilution.
Hawkins *et al* (2007) [44]	Age- and generation-dependent Tdiv. Tdiv0 different from Tdiv1+	Age- and generation-dependent Tdie. Tdie0 different from Tdiv1+. Responders can die.	Number of divisions ~ normal.	Gen 0 const. Gen 1+ decays.	N/A
Lee *et al* (2008) [105]	Tdiv0 follows delayed Gamma distribution, then generation-dependent constant Tdiv.	Exponential decay with different rates for dividing vs undivided cells.	Linearly-increasing Tdivs.	Undivided cells only.	N/A
Banks *et al* (2011) [99]	Constant generation-independent rates for division.	Constant generation-independent rates for death.	N/A	N/A	Gompertz decay, auto-fluroescence
Hasenauer *et al* (2012) [110]	Age- and generation-specific rates for division*.	Age- and generation-specific rates for death*.	Not explicitly but framework general	N/A	Dye decay, auto fl, and dilution.
Shokhirev and Hoffmann (2013) [113]	Age- and generation-dependent Tdiv. Tdiv0 different from Tdiv1+. Non-responders do not divide.	Age- and generation-dependent Tdie. Tdie0 different from Tdiv1+. Responders do not die.	Number of divisions ~ normal.	Gen 0 const. Gen 1+ decays	Manual input and auto fl.

***-** optimized computation method for age-independent division and death only [110].

1.6. Time-lapse imaging and cell tracking approaches

The dynamics of individual cells are lost when using traditional bulk biochemical assays (e.g. western blot, real-time PCR, gel-electrophoresis, and etc.). Flow cytometry and classical microscopy experiments provide snapshots of cell populations. Unfortunately the assayed cells are typically fixed or lost after measurement, making it impossible to analyze single-cell behavior across time. An alternative approach is to culture cells on an incubated microscope and take periodic images, making it possible to track single-cell behavior over long periods. This was recently performed using primary B cells stimulated with the TLR9 agonist CpG [21]. To avoid issues with cell motility and to simplify cell tracking, microfluidic devices that confine cells to small compartments have also been used with success [46,114,115], although paracrine signaling maybe disrupted if cells are forced to grow in micro-wells. After cell growth on microscopes has been optimized, the challenge of digitizing cell behavior (tracking) remains. Tracking B cells is especially challenging because B cells are non-adherent, motile, and divide or die. This problem is further compounded by the fact that primary B cells are difficult to manipulate *ex vivo*, as they readily die and are resistant to viral transduction.

Approaches to tracking cells in images are diverse but can be placed into three main categories (recently reviewed in [116,117]: fully automated, semi-automated, and manual. Each approach has associated benefits and drawbacks. Automated approaches maximize throughput while minimizing human labor at the cost of accuracy. Numerous algorithms for automated cell tracking have been described, but are not implemented or readily available to the public [118-124]. Other tools are freely available for automated tracking [125-127] but typically do not allow for track curation in real-time and/or do not handle cell division/death events, making them ill-suited for accurate tracking of dividing and dying B-cell contours over time. Furthermore, the accuracy of extant automated

tracking tools is typically low (especially if only phase-contrast images are available)[120], necessitating track curation. On the other hand, manual approaches provide the best tracking accuracy at the high cost of human labor and therefore throughput/statistical power [21,46,128,129]. Semi-automated approaches, which strive to automate as much as possible, while relying on human input for error-prone tasks (i.e. track curation), represent a compromise between throughput and accuracy. Since curation of cell-tracks is essential to avoid runaway error propagation [124], tools that enable the identification and correction of errors are a pre-requisite for accurate lineage tracking. An automated error identification and correction methodology was recently developed, however it does not handle apoptosis events and has not been integrated into freely available tools [124]. Specialized tools for tracking embryogenesis and which allow track curation have been developed, but are not applicable to studies where cells are motile and dying [130,131]. Of particular note, the recently-developed tracking tool: TrackAssist [116] allows for semi-automated tracking of B-cells by providing automated cell detection and tracking in addition to manual track curation tools. A pre-requisite of the tool is that cells must be easily discernable in all images, which requires the use of transgenic mice expressing fluorescently-labeled cells, or manually identification of all cells in all images (i.e. manual tracking). Nevertheless, this tool highlights the importance of semi-automated approaches for deriving meaningful information from B-cell time lapse microscopy datasets.

In summary, automated tracking remains inaccurate (as even a miniscule error rate rapidly propagates), while manual tracking is intractable for more than a few dozen cells [116]. Semi-automated methods promise a viable alternative as long as tracks can be easily curated, however most tools do not offer real-time track curation. Time-lapse

microscopy imaging of B cells and the semi-automated tracking tool, FAST, are the topic of the third chapter of this thesis.

1.7. Single-cell RNA sequencing and immunofluorescence

Single-cell molecular assays are useful for correlating cellular features (e.g. size) to molecular pathways. Specifically, immunofluorescence (IF) allows for quantitative measurement of fluorescently-labeled proteins in hundreds of individual cells [132,133]. This is accomplished by fixing cell samples with formaldehyde or other fixatives, followed by permeabilization of the cell membrane, and "staining" via introduction of antibodies raised against the protein of interest. Typically, this is followed by secondary staining with an antibody raised against the particular species that produced the first antibody. The secondary "detector" antibody is conjugated to a fluorescent marker which enables visualization of the proteins of interest by flow cytometry or microscopy. Alternatively, a fluorescently-labeled primary antibody specific for the protein of interest may be used bypassing the secondary staining step. Unfortunately, antibody specificity is often an issue, resulting in non-specific binding. Therefore, each experiment must include control experiments which show that the antibody is binding only to the protein of interest. Furthermore, staining/measurement conditions may change from sample to sample, requiring that all samples are measured simultaneously and compared to baseline controls (e.g. a 0 h control measured at the same time). Finally, IF requires chemical crosslinking, resulting in cell death and making single-cell tracking impossible. The upside is that IF provides high-throughput measurements of individual cells in a population, enabling the simultaneous measurement of several proteins as well as the cell size.

On the other hand, single-cell RNA sequencing can be used to quantify whole transcriptomes of individual cells [134-138]. A relatively new technology, single cell RNAseq uses microfluidic devices to trap individual cells and perform the necessary chemistry to lyse cells, and reverse transcribe transcripts into cDNA for library preparation (purification, segmentation, barcoding, normalization, and etc.) and sequencing. Furthermore, captured cells can be stained and measured under the microscope prior to lysis, allowing for filtering of transcriptomes by cell size, surface markers, and viability. This allows for the unbiased whole-genome testing of differential gene expression between individual cells. There are several considerations associated with single-cell RNA sequencing. First, since the amount of RNA fluctuates between individual cells due to differences in cell-cycle phase, activation, as well as extrinsic cell state, RNA spike-in controls are required to provide an accurate normalization of transcript counts, this is achieved by addition of RNA spike-ins directly into microfluidics chip prior to lysis, ensuring that each cell receives approximately equal amounts of the spike-in RNA[138]. Furthermore, since cell size is typically used to isolate cells in the microfluidics chambers, cells with particular sizes and geometries may be captured with different efficiencies. Finally, since there is considerable cell-to-cell biological variability, the number of cells analyzed should be significantly high to avoid artifacts and sample bias (typically dozens of cells in each tested category).

Analysis of IF and single-cell RNAseq datasets requires software tools. Fluorescence can be measured by flow cytometry, or by taking fluorescence microscopy images. Flow cytometry datasets are then typically analyzed with commercial third-party software such as FlowJo (TreeStar Inc.), or FCS Express (De Novo Software), however, fluorescence localization within cells cannot be accurately measured by flow cytometry, and fixing cells often diminishes the forward scatter characteristics of cells [139], making

cell size quantification potentially problematic. Alternatively, fixed and stained cells may be quantified by fluorescence microscopy. On the other hand, fluorescence microscopy provides direct measurements of cell size and protein localization, but requires image processing techniques for identifying cells in images (segmentation), and as such is more labor intensive. Single-cell RNA sequencing results in the quantification of global gene expression for individual cells. Typically, bar-coded libraries are pooled and sequenced in parallel, with outputs comprising several hundred million read-barcode pairs. Software for aligning the reads to a reference genome, and associating the read with a genomic feature (e.g. gene) is freely available (recently reviewed in [140]). Of particular interest, the STAR algorithm was implemented and characterized recently which shows advances in both alignment sensitivity and speed as it aligns reads directly to the genome [141]. After reads are aligned and associated with genomic features (i.e. genes), read counts are normalized using counts from artificial spike-in sequences and counts from different conditions are evaluated for differential expression using statistical software such as Homer [142] or WebGestalt [143] among others (reviewed in [134,144]). Immunofluorescence and single-cell RNA sequencing are used to interrogate individual B cells in chapter 4 of the thesis.

1.8. Computational modeling across scales

Systems biology offers an understanding of how simple rules lead to the emergent complexity as one zooms out from macromolecules to biochemical pathways to cells to organs and indeed to entire organisms [145,146]. Typically, computational models connect two scales. For example, biochemical interactions can be modeled to produce cellular outcomes such as NFκB activation [147-150], cell-cycle progression [151-154], and apoptosis [24,155,156]. This is typically done using the law of mass action, which assumes under the limiting conditions of perfectly mixed infinite systems, biochemical reactions are proportional to the product of the reaction concentrations [157], while rule-based models naturally abstract reactions between related reactants[158], and stochastic Gillespie-type models [159] enable modeling of low copy number species (e.g. individual allele activities, chromatin rearrangements, or the dynamics of relatively scarce proteins in non-mammalian cells). Alternatively, cell populations have been modeled as stochastic processes incorporating cellular parameters (such as the distribution of division and death times) to predict population dynamics [44,93,95-106,110,113]. However, since the cellular decisions are themselves the product of the underlying biochemical connections, predicting the effects of drug targets require an ability to directly model the molecular interactions occurring inside heterogeneous cells [160].

Bridging the scale gap requires alternate modeling strategies. Kinetic models consisting of multiple compartments or multiple models operating on multiple scales provide link scales with logical/event-driven rules [153,161,162]. For example, the Basic Immune Simulator models tissues comprised of autonomous agents existing in a two dimensional plane, enabling rule-based modeling of cells and tissues during an infection [163]. In a more recent example, angiogenesis was modeled using a combination of

agent-based cellular agents, algebraic equations, and partial differential equations for oxygen diffusion and blood flow [164]. Finally, agent-based models have been used to simulate the evolution of murine populations under specific selective genetic pressures [165,166].

As the B-cell immune response is comprised of a heterogeneous population of individual B-cells making seemingly-stochastic decisions to divide and die, multi-scale agent-based models, consisting of cellular agents simulating the biochemical processes driving signaling, growth, cell-cycle progression, and death are required to bridge the gap. A mechanistic framework for exploring the effects of molecular perturbations on the population response enables *in silico* hypothesis testing and clinical trials, facilitating an era of personalized medicine [167,168].

1.9. Motivation

The B-cell immune response is a multi-scale process with key molecular plays controlling heterogeneous cellular processes which interleave from generation to generation to produce a robust population response to pathogens. While B-cell immune response is essential for vaccine design whereas dysregulation leads to autoimmune disorders, immune deficiencies, and cancers, a multi-scale mechanistic understanding of this essential process is still an outstanding problem. To date, the B-cell immune response has been studied using traditional bulk biochemical assays, flow cytometric assays that quantify snapshots of populations, time-lapse microscopy studies, as well as ordinary differential equation and stochastic process models. These studies have amassed a wealth of observations about the biochemical, cellular, and population level characteristics of the response, but the complexity and heterogeneity of B cells make meaningful interpretation in specific contexts challenging. Therefore, we developed experimental and computational pipelines and tools for deriving mechanistic insights which we used to construct, calibrate, and validate a multi-scale agent-based predictive model, utilizing established ODE-based models of NFκB signaling, growth, cell-cycle progression, and apoptosis (Figure 1.6). The methods and tools developed as part of these studies were designed to enable model-driven derivation of meaningful biological insights in the lab and clinic and are provided free-of charge in the supplementary files.

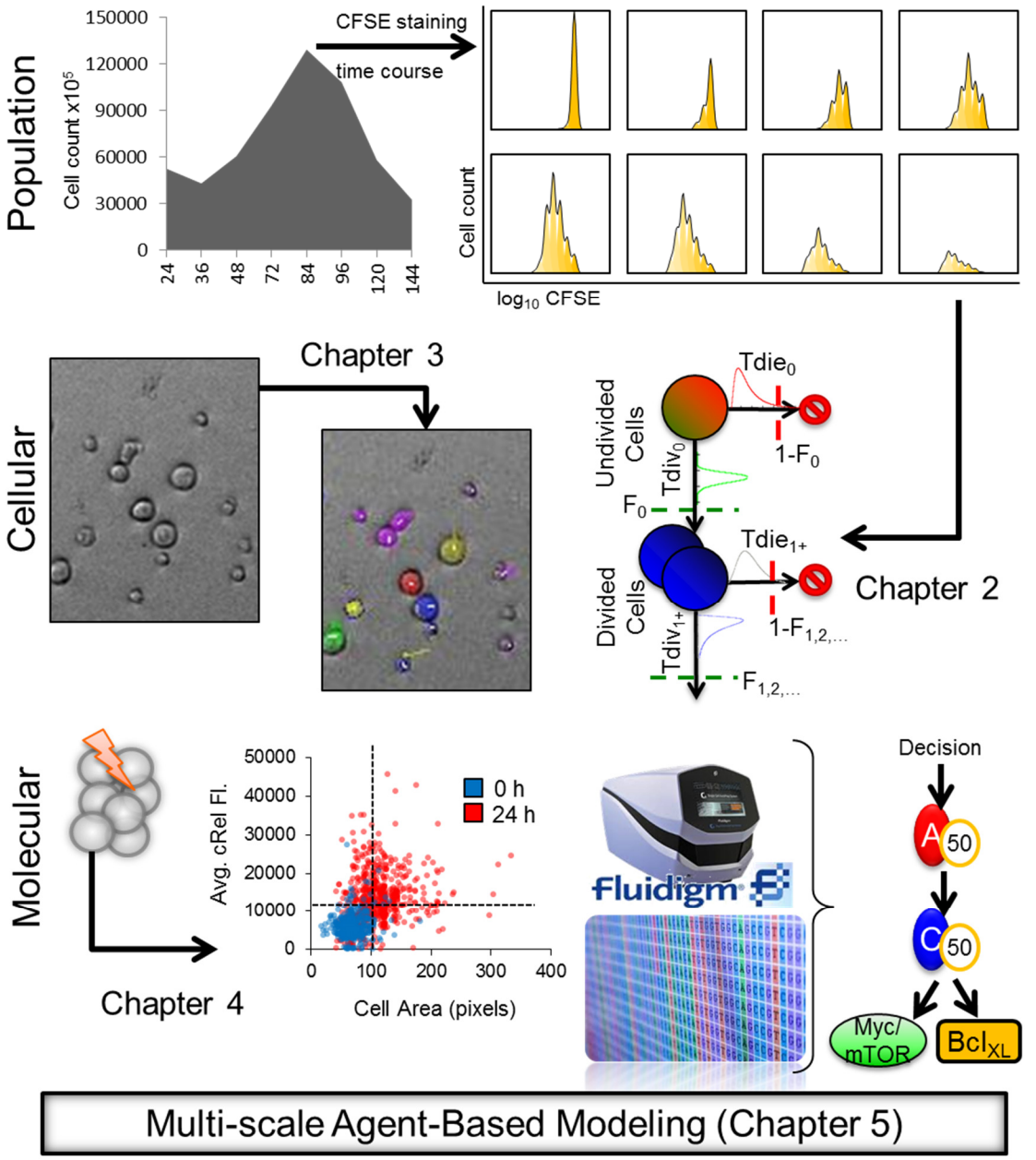

Figure 1.6. Summary of the approach. The first task is to develop, characterize, and validate a methodology and tool for deconvoluting CFSE histograms into cellular parameters. Next, an experimental and computational pipeline must be designed for extracting single-cell B-cell behavior directly. Next, single-cell molecular assays are used to test key molecular plays associated with B-cell decision enforcement. Finally, the multi-scale observations are combined into a multi-scale agent based model which is used to predict molecular perturbations.

Chapter 2

FlowMax: a computational tool for maximum likelihood deconvolution of CFSE time courses

The immune response is a concerted dynamic multi-cellular process. Upon infection, the dynamics of lymphocyte populations are an aggregate of molecular processes that determine the activation, division, and longevity of individual cells. The timing of these single-cell processes is remarkably widely distributed with some cells undergoing their third division while others undergo their first. High cell-to-cell variability and technical noise pose challenges for interpreting popular dye-dilution experiments objectively. It remains an unresolved challenge to avoid under- or over-interpretation of such data when phenotyping gene-targeted mouse models or patient samples. Here we develop and characterize a computational methodology to parameterize a cell population model in the context of noisy dye-dilution data. To enable objective interpretation of model fits, our method estimates fit sensitivity and redundancy by stochastically sampling the solution landscape, calculating parameter sensitivities, and clustering to determine the maximum-likelihood solution ranges. Our methodology accounts for both technical and biological variability by using a cell fluorescence model as an adaptor during population model fitting, resulting in improved fit accuracy without the need for *ad hoc* objective functions. We have incorporated our methodology into an integrated

phenotyping tool, FlowMax, and used it to analyze B cells from two NFκB knockout mice with distinct phenotypes; we not only confirm previously published findings at a fraction of the expended effort and cost, but reveal a novel phenotype of NFκB1/p105/50 in limiting the proliferative capacity of B cells following B-cell receptor stimulation. In addition to complementing experimental work, FlowMax is suitable for high throughput analysis of dye dilution studies within clinical and pharmacological screens with objective and quantitative conclusions.

2.1. Introduction

Lymphocyte population dynamics within the mammalian immune response have been extensively studied, as they are a predictor of vaccine efficacy, while their misregulation may lead to cancers or autoimmunity [1]. Lymphocyte population dynamics involve seemingly stochastic cellular parameters describing the decision to respond to the stimulus, the time spent progressing through the cell cycle, the time until programmed cell death, and the number of divisions progenitor cells undergo [44]. Specifically, experimental observations show that population dynamics are well modeled at the cellular level by skewed distributions for the time to divide and die, that these distributions are different for undivided and dividing cells, and that the proliferative capacity is limited [21]. Recently, Hawkins *et al* showed that cells, that exhibit growth in size invariably divide (though at highly variable times), while cells that do not are committed to cell death, albeit at highly variable times [21]. A high degree of biological variability may ensure that population-level immune responses are robust [44,169], but renders the deconvolution of experimental data and their subsequent interpretation challenging.

A current experimental approach for tracking lymphocyte population dynamics involves flow cytometry of carboxyfluorescein succimidyl ester (CFSE)-stained cells. First introduced in 1990 [88], CFSE tracking relies on the fact that CFSE is irreversibly bound to proteins in cells, resulting in progressive halving of cellular fluorescence with each cell division. By measuring the fluorescence of thousands of cells at various points in time after stimulation, fluorescence histograms with peaks representing generations of divided cells are obtained. However, interpreting CFSE data confronts two challenges. In addition to intrinsic biological complexity arising from generation- and cell age-dependent variability in cellular processes, fluorescence signals for a specific generation are not truly uniform due to heterogeneity in (i) staining of the founder population, (ii) partitioning of the dye during division, and (iii) dye clearance from cells over time. Thus, while high-throughput experimental approaches enable population-level measurements, deconvolution of CFSE time courses into biologically-intuitive cellular parameters is susceptible to misinterpretation [170].

To recapitulate lymphocyte population dynamics a number of theoretical models have been developed (see [90,91] for recent reviews). However, the available computational methodologies to utilize them for analyzing CFSE time series data remain cumbersome, and these are prone to under- or over- interpretation. First, commercial software such as FlowJo (Tree Star Inc.) and FCExpress (De Novo Software) is typically used to fit Gaussian distributions to log-fluorescence data on a histogram-by-histogram basis to determine cell counts at each generation, but these do not provide an objective measure of fit quality. Then mathematical models of population dynamics must be employed to fit cell cycle and cell death parameters to the fitted generational cell counts [45,104]; however, they also do not provide a measure of fit quality, and they are affected by errors in cell-counts determined by aforementioned software tools. Without

an estimate of solution sensitivity and redundancy in the quantitative conclusions, computational tools do not give a sense of whether the information contained in CFSE data is used appropriately (or whether it is under- or over-interpreted). This may be the underlying reason for why population dynamic models have not yet impacted experimental or clinical research for the interpretation of ubiquitous CFSE data.

Here, we introduce an integrated computational methodology for phenotyping lymphocyte expansion in terms of single-cell parameters. We first evaluate the theoretical accuracy of each module in the phenotyping process by fitting generated data. We then show that implementing them in an integrated, rather than sequential, workflow reduces expected parameter error. Next, we describe our approach to estimating the quality of the fit and demonstrate the advantages of using our integrated methodology compared to phenotyping with the current state-of-the-art approach, the Cyton Calculator [45]. We then evaluate how different types of imperfections in data quality affect performance. Finally, we demonstrate the method's utility in phenotyping B cells from *NFκB1*$^{-/-}$ and *rel*$^{-/-}$ mice stimulated with anti-IgM and LPS, extending the conclusions of previously published studies [60,171] and disaggregating the role of distinct cellular parameters by using the model simulation capabilities. FlowMax, a Java tool implementation of our methodology as well as the experimental datasets are available for download from http://signalingsystems.ucsd.edu/models-and-code/. The FlowMax code and program is provided as FlowMax.zip in the supplementary materials, while the FCS 3.0 flow cytometry datasets are available as CFSEdatasets.zip.

2.2. Results

To enable objective interpretation of dye dilution lymphocyte proliferation studies, we constructed a suite of integrated computational modules (Figure 2.1). Given a CFSE

dye-dilution time course, the first step involves fitting the cell fluorescence model to CFSE fluorescence histograms recorded at various times, accounting for dye dilution from cell division and intrinsic variability from biological and technical sources. In a second step, a cell population model, describing the fraction of responding cells in each generation and times to cell division or death, is fit to the CFSE time series data directly, using the best-fit cell fluorescence parameters as adaptors during fitting. Repeating the second fitting step numerous times allows for a critical third step: estimating the sensitivity and degeneracy of the best fit parameter set, providing the maximum likelihood non-redundant solutions ranges.

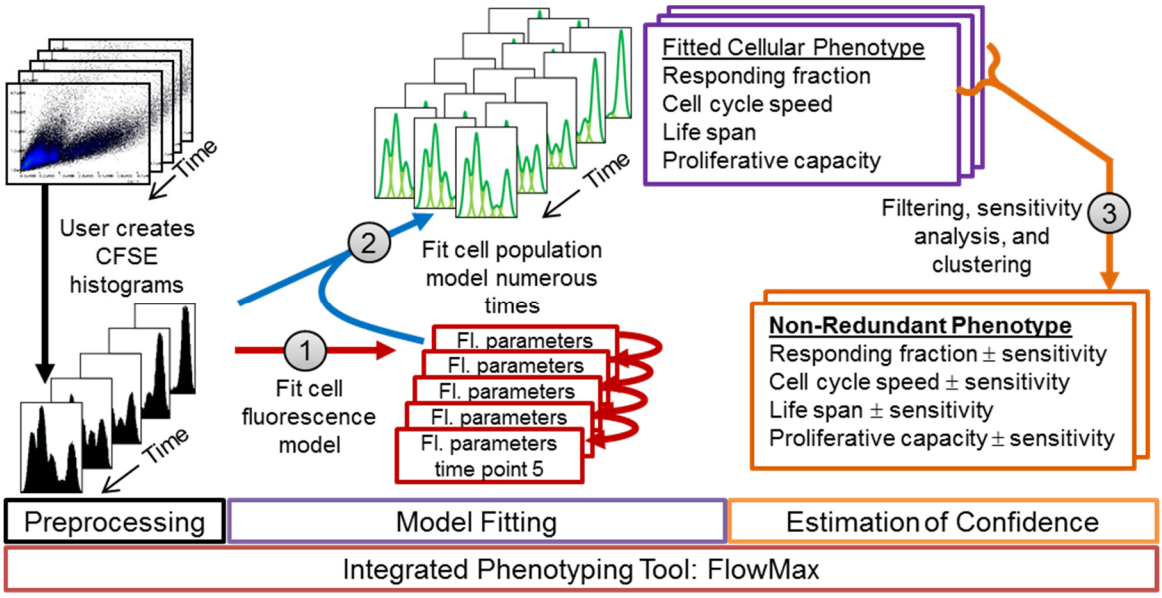

Figure 2.1. Proposed integrated phenotyping approach (FlowMax). CFSE flow-cytometry time series are preprocessed to create one-dimensional fluorescence histograms that are used to determine the cell proliferation parameters for each time point, using the parameters of the previous time points as added constraints (step 1). Fluorescence parameters are then used to extend a cell population model and allow for direct training of the cell population parameters on the fluorescence histograms (step 2). To estimate solution sensitivity and redundancy, step 2 is repeated many times, solutions are filtered by score, parameter sensitivities are determined for each solution, non-redundant maximum-likelihood parameter ranges are found after clustering, and a final filtering step eliminates clusters representing poor solutions (step 3).

2.2.1. Evaluating the accuracy of cell fluorescence model fitting

The first computational module addresses the challenge of converting fluorescence histograms of CFSE data into generation-specific cell counts and experimental dye parameters. We selected a simple time-independent cell fluorescence model (Figure 2.2A) similar to the models used in current flow cytometry analysis tools (TreeStar Inc., De Novo Software) and recent studies [107,111,112]. We assume that the log-transformed fluorescence of populations of cells is well-modeled by a mixture of Gaussians, as observed previously [45]. We selected this simple model because recent models [98,99,107,108], which incorporate both cell dynamics and dye dynamics, do not naturally account for both cell age-dependent death and division rates, as well as for the observation that only a fraction of lymphocytes choose to respond to the stimulus. While the cell fluorescence model does not explicitly account for time-dependent dye catabolism, the model allows for the fluorescence of the initial population, μ_0, to be manually specified for each time point when log-fluorescence histograms are constructed.

In order to quantify the cell fluorescence model fitting accuracy, we tested it with a panel of generated realistic CFSE time courses. Specifically, the cell fluorescence model was fitted to the generated histograms and the average normalized % error between generated and fitted peak counts as a function of time point (Figure 2.2B). As expected, the average error in generation counts was highest for early time points due to absence of a second peak, which may help constrain parameter fitting. However, the % error between generated and fitted peak counts (Figure 2.2B) suggested that the fluorescence model fitting was on average quite successful as the maximum average normalized error was 7.1%. Finally, direct comparison of cell fluorescence model fits to

experimental data showed good agreement throughout the entire time course, even when late generation peaks are poorly resolved (Figure 2.2C).

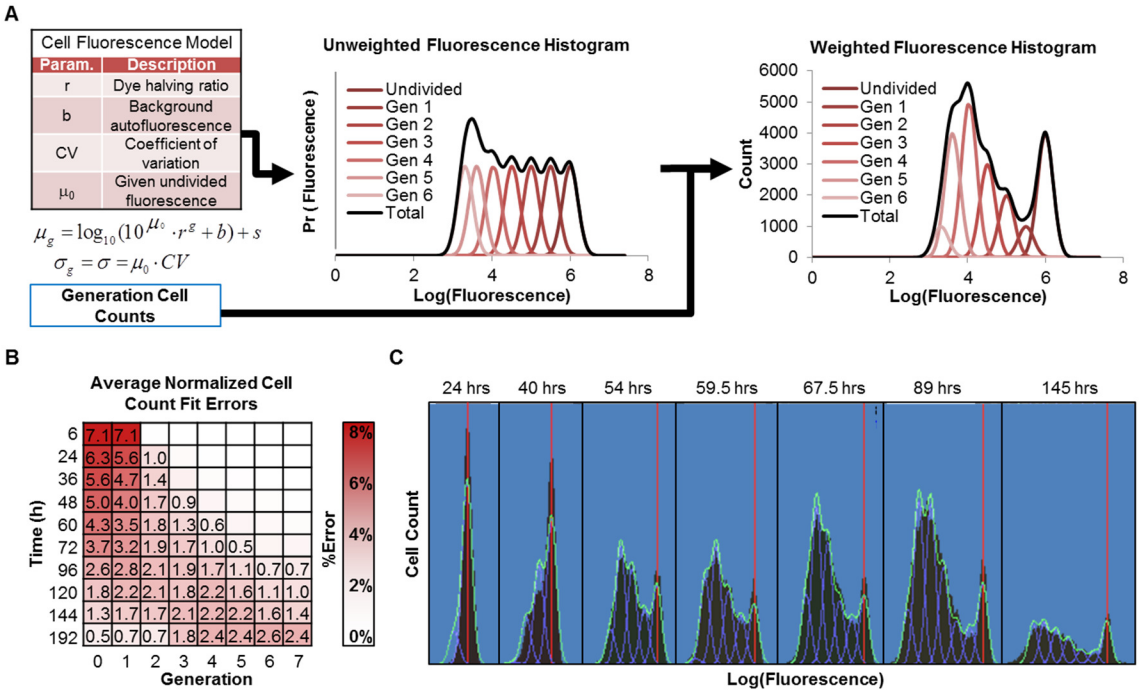

Figure 2.2. The cell fluorescence model. (A) Noisy log-transformed cell fluorescence is modeled by a weighted mixture of Gaussian distributions for each cell division: $\sum_g w_g N(\mu_g, \sigma)$, parameterized according to equations describing variability in staining (CV), background fluorescence (b), dye dilution (r), and a small correction for the fluorescence of the initial population of cells (s). Weights for each Gaussian correspond to cell counts in each generation. (B) Analysis of the cell fluorescence model fitting accuracy for 1,000 generated CFSE fluorescence time courses (see also Tables 2.3 and 2.4). Average percent error in generational cell counts normalized to the maximum generational cell count for each time course. Numbers indicate an error ≥ 0.5%. (C) Representative cell fluorescence model fitting to experimental data from wildtype B cells at indicated time points after start of lipopolysaccharides (LPS) stimulation (red lines indicate undivided population).

2.2.2. Evaluating the accuracy of cell population model fitting

Employing the fcyton model described above (Figure 2.3A), we examined the accuracy associated with fitting the fcyton population model with the generated panel of datasets directly to the known generational cell counts, and calculated both the average normalized cell count error (Figure 2.3B) as well as the error distributions associated with fitting particular fcyton parameters (Figure 2.3C). Fitting the fcyton model to given counts resulted in very low generational cell count errors : the maximum average normalized error was 3.5%, while the maximum average normalized error for all time points ≤ 120 h was always less than 2%. The median errors in the key parameters N, F_0, $E[Tdiv_0]$, $E[Tdie_0]$, $E[Tdiv_{1+}]$) were small: 1.2%, 0.02, 5.8%,4.0%, and 2.6%, respectively. However, interestingly, even with perfect knowledge of generational cell counts and a large number of time points, not all cellular parameters were accurately determined. This is illustrated by a median % error value of about 18% for $E[Tdie_{1+}]$ and a median error of about 1 generation for Dμ, the average number of divisions a divided cell will undergo, and suggests that these parameters do not contribute substantially to the cell count data within the physiologically relevant parameter regime.

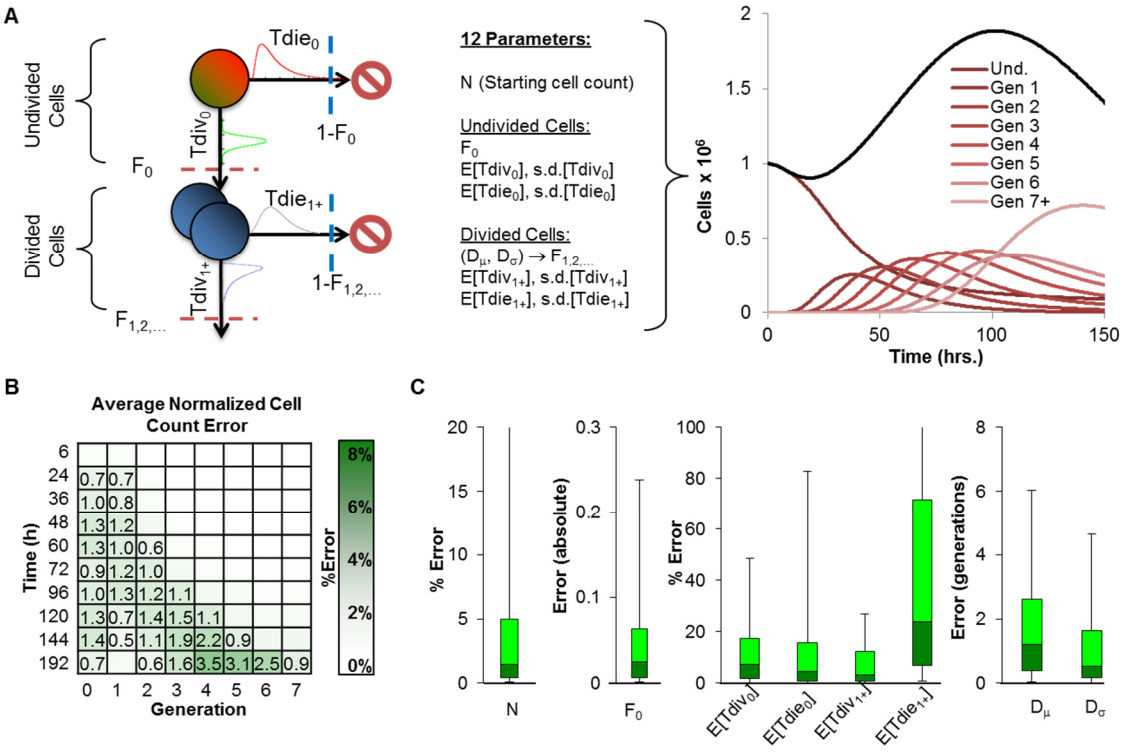

Figure 2.3. **The fcyton cell proliferation model.** (A) A graphical representation summarizing the model parameters required to calculate the total number of cells in each generation as a function of time. Division and death times are assumed to be log-normally distributed and different between undivided and dividing cells. Progressor fractions (Fs) determine the fraction of responding cells in each generation committed to division and protected from death. (B,C) Analysis of the accuracy associated with fitting fcyton parameters for a set of 1,000 generated realistic datasets of generational cell counts assuming perfect cell counts and an optimized *ad hoc* objective function (see Text 2.1 and Tables 2.3 and 2.4). (B) Average percent error in generational cell counts normalized to the maximum generational cell count for each time course. Numbers indicate an error ≥ 0.5%. (C) Analysis of the error associated with determining key fcyton parameters. Box plots represent 5, 25, 50, 75, and 95 percentile values. Outliers are not shown. For analysis of all fcyton parameter errors see also Figure 2.9 (green).

2.2.3. Evaluating the accuracy when both model fitting steps are incorporated

Interpreting the population dynamics provided by dye dilution data in terms of cellular parameters requires both computational modules: the cell fluorescence model describes variability in experimental staining, while cell proliferation modeling explains evolution of the population through time. We first assessed their performance when linked sequentially, fitting the population model to best-fit cell counts, using the above-described generated dataset. Since the objective function that determines the fit of model output to experimental cell counts is a key determinant of the performance, we compared a simple squared deviation scoring function (SD) with a more complex, manually-optimized objective function which takes into account multiple measures of similarity (Equations 46 and 47). The results showed that a complex *ad hoc* optimized scoring function drastically outperformed the simpler SD-based scoring function with all fcyton parameter error distributions significantly (each p-value < 1E-12; Mann-Whitney U test) shifted toward zero (Figure 2.4).

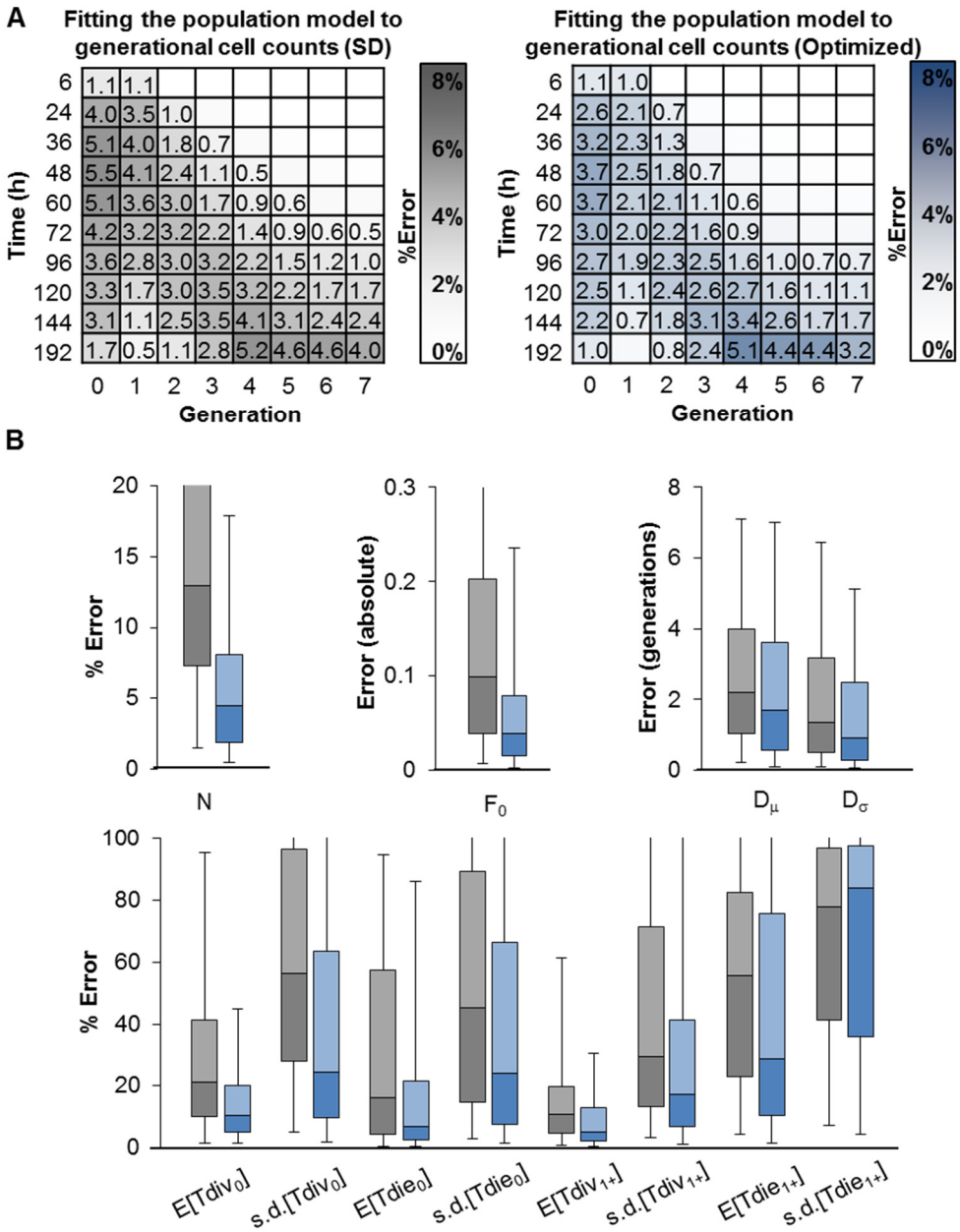

Figure 2.4. Accuracy of fitting the population model to generated fitted generational cell counts. The simple squared deviation (grey) and *ad hoc* optimized (blue) scoring functions were used to fit the fcyton model to fitted generational cell counts for 1,000 sets of randomly generated CFSE time courses with parameters sampled uniformly from ranges in Table 2.3, and evaluated at times described in Table 2.4. (A) Average percent error in fitted generational cell counts normalized to the maximum generational cell count for each generated time course. Numbers indicate an error ≥ 0.5%. (B) Analysis of the error associated with determining all fcyton cellular parameters. Box plots represent 5, 25, 50, 75, and 95 percentile values. Outliers are not shown.

Next, we integrated the two modules (Figure 2.1) and characterized the resulting performance. This integrated approach uses the best-fit cell fluorescence parameters to represent the cell population solutions as fluorescence histograms, enabling direct comparison to the experimental data, and obviating the need for an *ad hoc* objective function during population model fitting (compare Equations 47 and 48). After applying each approach to the panel of generated datasets, we calculated the generational average normalized percent count errors (Figure 2.5A), as well as parameter error distributions (Figure 2.5B). Both the sequential and integrated approaches resulted in relatively low generational cell count errors on average, however, the integrated approach outperformed sequential model fitting for predicting the generational cell counts at late time points (Figure 2.5A). The improvement was more readily apparent in the distribution of parameter fit errors: all parameter error distributions were shifted toward zero when the integrated rather than the sequential model fitting approach was used (p-values for each parameter distribution ≤ 1E-5, Mann-Whitney U test). In fact, all but the $Tdie_{1+}$ parameter errors showed a very dramatic improvement (p-value ≤ 1E-10, Mann-Whitney U test). To determine if the improvement was due to a propagation of fit errors caused by sequential fitting steps, we compared both the sequential and integrated method when the population model was fitted to perfect counts or when perfect fluorescence parameters were used, respectively. (Figure 2.6) When comparing both approaches under ideal conditions, integrated fitting resulted in overall better cell count errors at later time points (Figure 2.6A.), and improved error distributions for fcyton parameters F_0 and N (p-value ≤ 0.05, Mann-Whitney U test). Next, by comparing the integrated approach to individual computational modules, we found that the accuracy of the integrated approach was comparable to the accuracy associated with fitting the fcyton model cell counts to known counts using the *ad hoc* optimized objective function,

as well as when the integrated method was used with known cell fluorescence parameters (Figure 2.6). This suggests that the integrated method minimizes the propagation of errors, as it is comparable to fitting to the original generated cell counts using a complex optimized objective function, and because eliminating the fluorescence model fitting error did not significantly improve the fit.

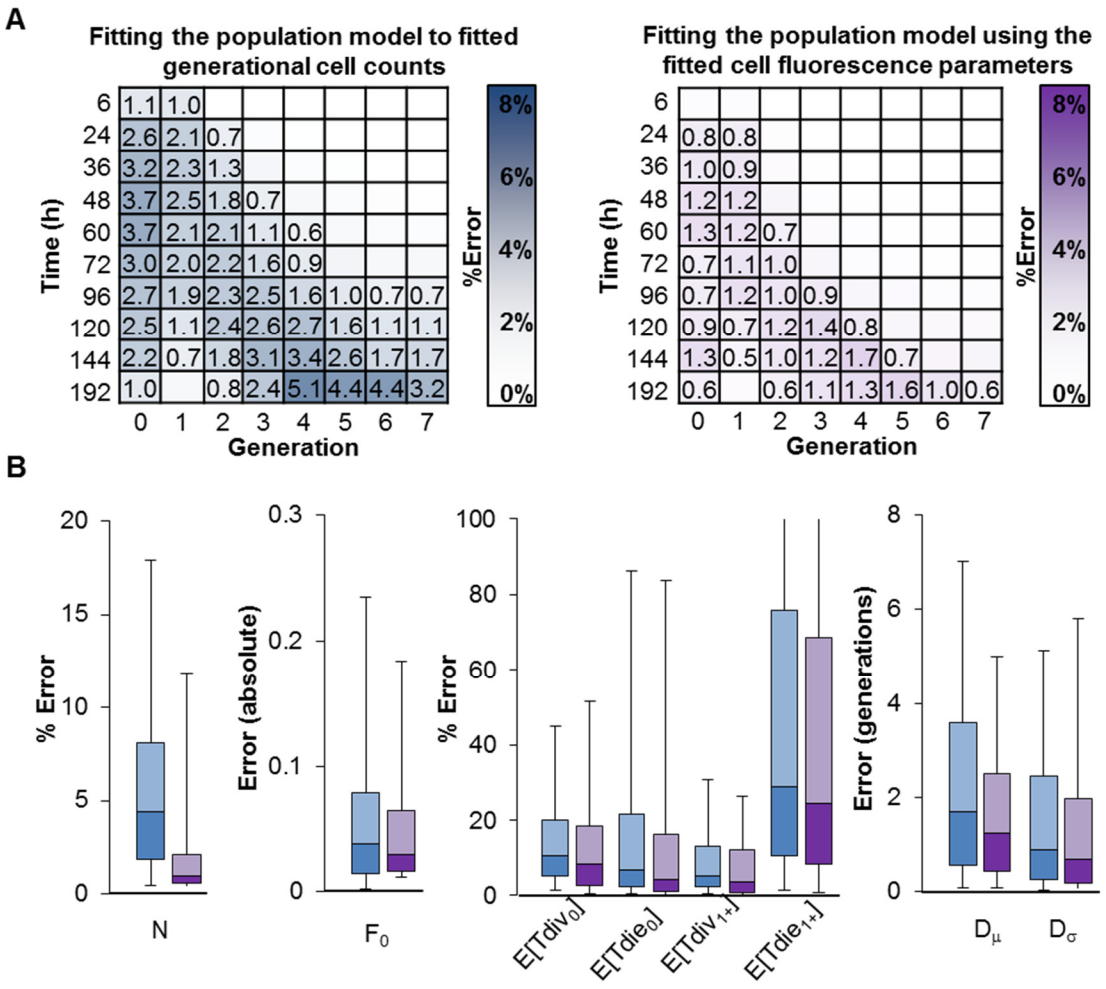

Figure 2.5. **Accuracy of phenotyping generated datasets in a sequential or integrated manner.** The accuracy associated with sequential fitting Gaussians to fluorescence data to obtain cell counts for each generation (blue) and integrated fitting of the fcyton model to fluorescence data directly using fitted fluorescence parameters as adaptors (purple) was determined for 1,000 sets of randomly generated realistic CFSE time courses (see also Tables 2.3 and 2.4). (A) Average percent error in generational cell counts normalized to the maximum generational cell count for each time course. Numbers indicate an error ≥ 0.5%. (B) Analysis of the error associated with determining key fcyton cellular parameters. Box plots represent 5,25,50,75, and 95 percentile values. Outliers are not shown. For a comparison of all 12 parameters see Figure 2.4 (blue) and Figure 2.6 (purple).

Figure 2.6. Comparison of the integrated model fitting approach to training each model independently. A collection of 1,000 randomly generated sets of CFSE time courses was used to analyze the errors associated with training the cell fluorescence model only (red), training the fcyton model on known cell counts (green), training the fcyton model using the known (orange) or fitted (purple) cell fluorescence parameters as adaptors during fcyton population model fitting. See also Tables 2.3, and 2.4. (A) Average percent error in fitted generational cell counts normalized to the maximum generational cell count for each generated time course. Numbers indicate an error ≥ 0.5%. (B) Analysis of the error associated with determining all fcyton cellular parameters. Box plots represent 5, 25, 50, 75, and 95 percentile values. Outliers are not shown.

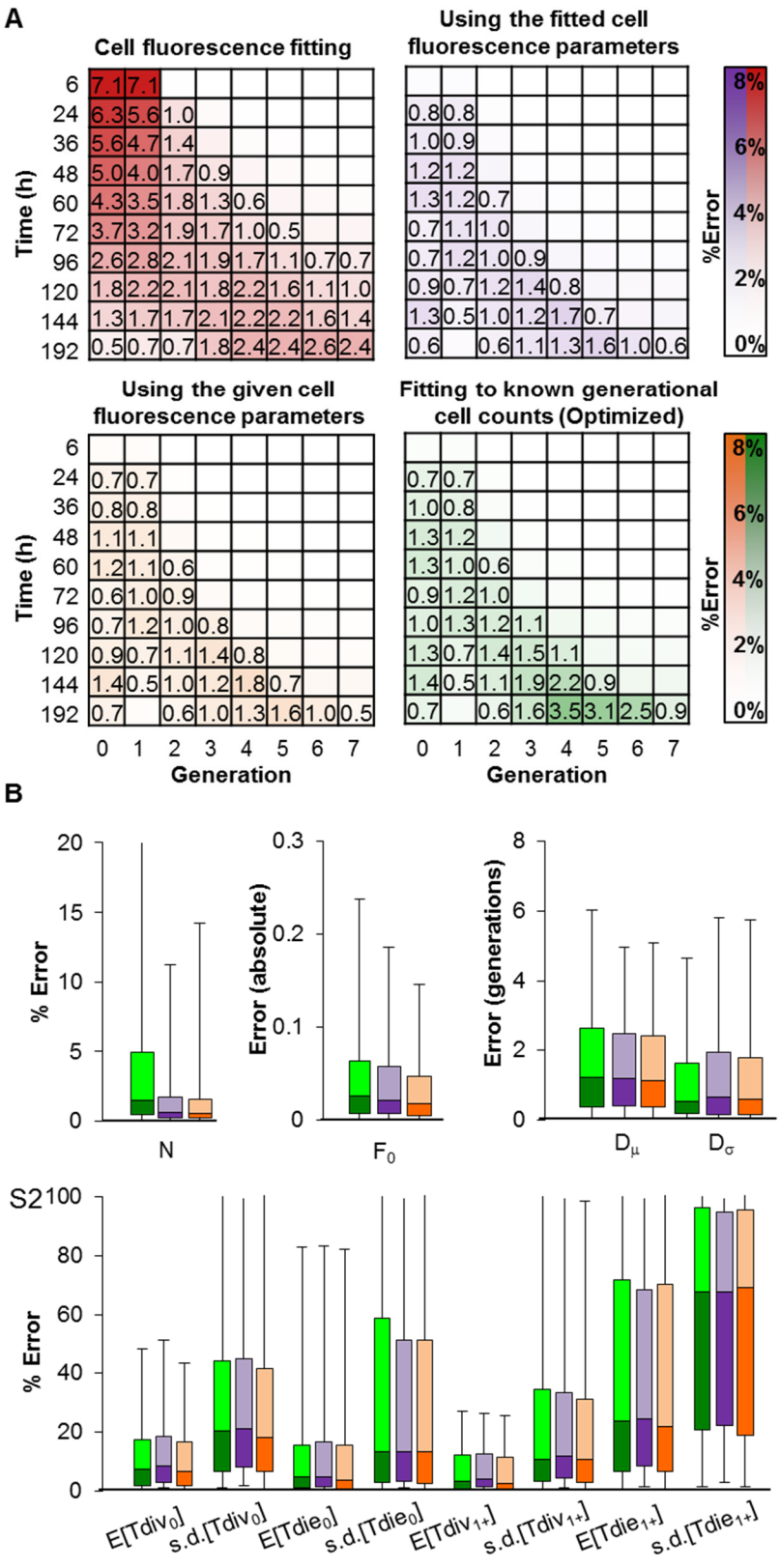
A
Cell fluorescence fitting
Using the fitted cell fluorescence parameters
Using the given cell fluorescence parameters
Fitting to known generational cell counts (Optimized)
Time (h)
Generation
%Error
8%
6%
4%
2%
0%
B
% Error
Error (absolute)
Error (generations)
N
F0
Dμ
Dσ
S2
E[Tdiv0]
s.d.[Tdiv0]
E[Tdie0]
s.d.[Tdie0]
E[Tdiv1+]
s.d.[Tdiv1+]
E[Tdie1+]
s.d.[Tdie1+]

To develop best practices for employing integrated fitting, we examined how the number of experimental time points, the number of computational fit attempts, and selection of the objective function would affect fitting accuracy. We found that using the best of eight, three or one computational fit attempts decreased the average normalized generational cell count errors and asymptotically improved the distributions of parameter errors (Figure 2.7). Since choice of time points can also affect solution quality, we repeated our error analysis with fewer time points. While more frequent sampling improved the median and variance of the error distributions, key time points turned out to be those close to the start of the experiment, just when the first cell divisions have occurred, and when the founding generation has all but disappeared, affecting fcyton parameters F_0, N, and $Tdie_0$ to a higher degree (Figure 2.8). To test which objective function to use for integrated model fitting, we tested three objective functions of increasing complexity: simple mean sum of absolution deviations (MAD), mean root sum of squared deviations (MRSD), and mean root sum of squared deviations with Pearson correlation (MRSD+). We fitted sets of 1,000 generated time courses (see Methods) with each of the three objective functions (Figure 2.9B) and we calculated the generational average normalized percent count errors (Figure 2.9A), as well as parameter error distributions (Figure 2.9C). The results showed that using the MRSD+ objective function resulted in the lowest average normalized generation percent count errors, however all three objective functions resulted in comparable fcyton parameter error distributions (p-value>0.05, Mann-Whitney U test), except error in N for MAD was significantly higher compared to MRSD/MRSD+ (p-value < 1E-10, Mann-Whitney U test).

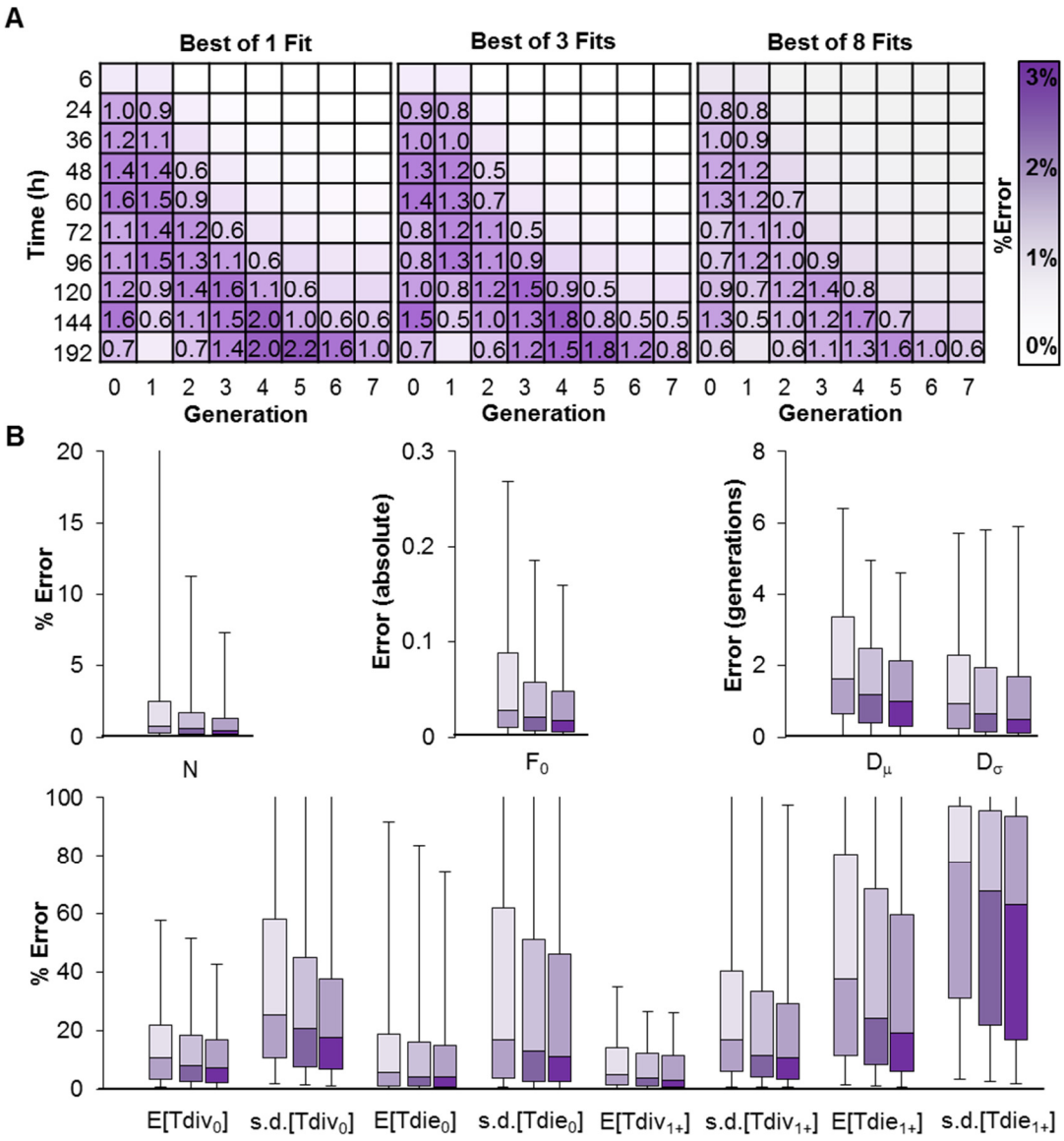

Figure 2.7. Analysis of the phenotyping accuracy as a function of the number of fit attempts (trials). For each experiment, 1,000 CFSE time courses were generated with model parameters within ranges described in Table 2.3 and times described in Table 2.4. Generated time courses were used to fit the fcyton population model using the fitted cell fluorescence parameters as adaptors, using the best of one (light), three (medium), or eight (dark) fit trials. (A) Average percent error in fitted generational cell counts normalized to the maximum generational cell count for each generated time course. Numbers indicate an error ≥ 0.5%. (B) Analysis of the error associated with determining all fcyton cellular parameters. Box plots represent 5, 25, 50, 75, and 95 percentile values. Outliers are not shown.

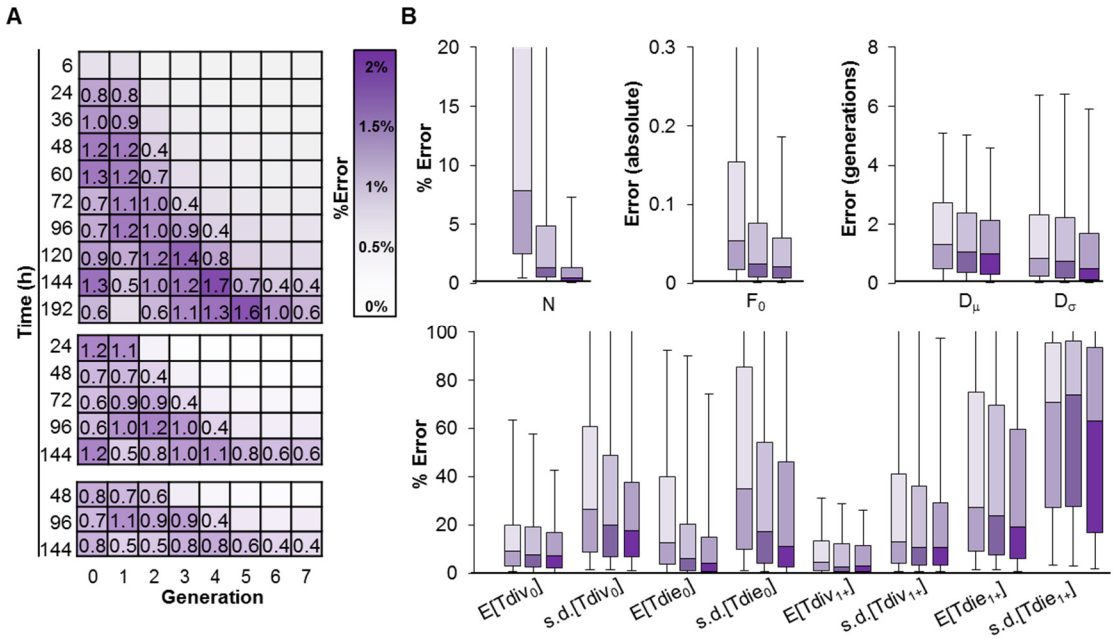

Figure 2.8. **Analysis of the fitting accuracy when using fewer experimental time points**. For each experiment, three (light), five (medium), or ten (dark) time points were considered from a collection of 1,000 generated CFSE time courses with parameters sampled uniformly from ranges in Table 2.3, and evaluated at times described in Table 2.4. Generated time courses were then phenotyped using the integrated computational method (cell fluorescence parameters used as adaptors during fcyton fitting). (A) Average percent error in fitted generational cell counts normalized to the maximum generational cell count for each generated time course. Numbers indicate an error ≥ 0.3%. (B) Box plots represent 5, 25, 50, 75, and 95 percentile error values. Outliers are not shown.

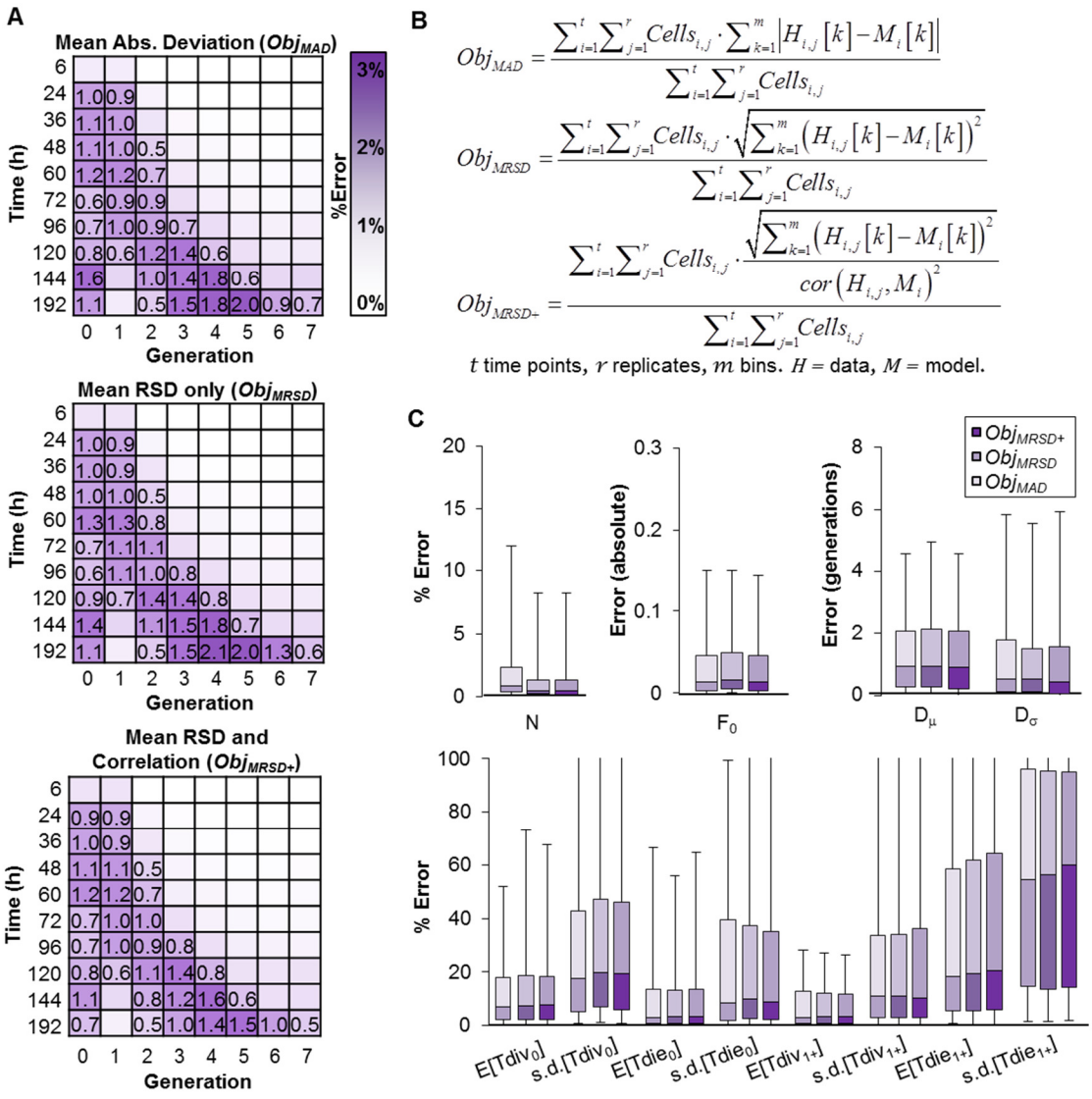

Figure 2.9. Analysis of the fitting accuracy as a function of objective function choice. For each experiment, a mean absolute deviation (Obj_{MAD}, light), a mean root square deviation (Obj_{MRSD}, medium), and a mean root square deviation with correlation (Obj_{MRSD+}, dark) were used to phenotype a collection of 1,000 generated CFSE time courses with parameter sampled uniformly from ranges in Table 2.3, and evaluated at times described in Table 2.4, using the integrated computational method (cell fluorescence parameters used as adaptors during fcyton fitting). (A) Average percent error in fitted generational cell counts normalized to the maximum generational cell count for each generated time course. Numbers indicate an error ≥ 0.5%. (B) Mathematical description of the objective functions used. (C) Analysis of the error associated with determining all fcyton cellular parameters. Box plots represent 5, 25, 50, 75, and 95 percentile values. Outliers are not shown.

Finally, we tested how the length of time needed to fit both of the models depends on the number of time points and cell generations used. As expected, the running time increased approximately linearly with the number of time points fitted and number of generations modeled, with typical time courses (9 generations, 7 time points) taking on average 2.11 minutes to fit (Table 2.1).

Table 2.1. **Analysis of fit running time dependence on the number of time points and generations.** The average running time for fitting the cell fluorescence followed by fitting the fcyton cell population model using the best-fit cell fluorescence parameters to 300 generated time courses with four, seven, and ten time points is shown. Fitting was carried out using an assumed 6, 9, or 12 generations during fitting. Times are in minutes and errors are SEM. See also Table 2.3 and 2.4

Generations	Four Time Points	Seven Time Points	Ten Time Points
6	0.86±0.01	1.37±0.01	1.62±0.01
9	1.43±0.01	2.11±0.02	2.54±0.02
12	1.84±0.01	2.82±0.02	3.52±0.02

2.2.4. Developing solution confidence and comparison to the most recent tool

As part of a crucial third step, we developed a computational pipeline for estimating both the sensitivity and redundancy of solutions. At the end of population model fitting, multiple candidate best-fit parameter sets are found (Figure 2.1, step 2). To enable objective evaluation of solutions, we estimate parameter sensitivities for candidate fits with particularly low ending objective function values and use an agglomerative clustering approach to combine pairs of candidate solutions until only disjoint clusters remain, representing non-redundant maximum-likelihood parameter ranges (Figure 2.10A and see Methods). To demonstrate the benefit of using our solution sensitivity and redundancy estimation procedure, we compared our approach to the most recent phenotyping tool, the Cyton Calculator [45]. The Cyton Calculator was designed for fitting the cyton model [44] to generational cell counts determined using

flow cytometry analysis tools. The cyton model incorporates most of the key biological features of proliferating lymphocytes, with the exception that responding cells are subject to competing death and division processes. We demonstrated the utility of our method, by phenotyping a CFSE time course of wildtype B cells stimulated with bacterial lipopolysaccharides (LPS) with both the Cyton Calculator as well as FlowMax, a tool implementing our methodology. While several qualitatively good solutions were found using the Cyton Calculator for four different starting combinations of parameters (Table 2.2), we could not objectively determine if the best-fit solutions were representative of one solution with relatively insensitive parameters, or four unique solutions (Figure 2.10B blue dots). As a comparison, we repeated the fitting using FlowMax under identical fitting conditions (Figure 2.10B, red individual solutions and clustered averages in green). Best-fit clustered FlowMax cyton parameters yielded one unique quantitatively excellent average fit (3.01% difference in normalized percent histogram areas). The best-fit parameter ranges showed that the division times and the propensity to enter the first round of division are important for obtaining a good solution, while predicted death times can be more variable without introducing too much fit error (Figure 2.10C). Plotting cell count trajectories using parameters sampled uniformly from maximum-likelihood parameter sensitivity ranges revealed that while the early B cell response is constrained, the peak and late response is more difficult to determine accurately (Figure 2.10D).

Table 2.2. Starting and fitted cyton model parameters for four successful Cyton Calculator fitting trials. Starting cyton model parameter values that resulted in successful fits of our CFSE LPS-stimulated wildype B cell time course (columns 2-5) were chosen manually within ranges specified in Table 2.3. Corresponding Cyton Calculator [45] best-fit parameters are shown in columns 6-9. The data for experimental replicates is shown in Figure 2.13 (WT LPS).

Parameter	Starting Value 1	Starting Value 2	Starting Value 3	Starting Value 4	Fitted Value 1	Fitted Value 2	Fitted Value 3	Fitted Value 4
F_0	0.001	1	0.57	0.72	0.41	0.67	0.47	0.37
$E[Tdiv_0]$	30.6	80.8	41.2	33.8	39.3	45.1	43	38.6
$s.d.[Tdiv_0]$	0.21	0.33	0.68	0.22	7.58	19.9	14.1	8.54
$E[Tdiv_{1+}]$	17.6	49	20.7	14.5	14	17.7	9.43	8.96
$s.d.[Tdiv_{1+}]$	0.18	0.35	0.36	0.35	13.3	11.6	0.48	2.2
$E[Tdie_0]$	110	94.7	200	130	130	275	137	119
$s.d.[Tdie_0]$	0.57	0.42	0.8	0.6	123	260	129	113
$E[Tdie_{1+}]$	32.9	52.3	66.3	51.6	45.2	18.7	49.5	69.6
$s.d.[Tdie_{1+}]$	0.8	0.5	0.17	0.8	42.7	0.95	46.8	47.2
$D\ \mu$	1.04	1.16	2.37	4.7	3.16	1.37	1.57	1.23
$D\ \sigma$	1.28	0.53	4.91	5.7	1.53	5.9	1.95	1.95

Table 2.3. **Cell fluorescence and population parameter ranges used to generate realistic CFSE time courses**. Selected ranges were chosen to exclude biologically implausible scenarios. Parameters were sampled evenly from the specified ranges whenever generating 1,000 time courses. The standard deviation parameters for the log-normal distributions: $Tdiv_0$, $Tdiv_{1+}$, $Tdie_0$, $Tdie_{1+}$ were further restricted to be less than or equal to their corresponding log-normal expected value parameters (e.g. $s.d[Tdiv_0] \leq E[Tdiv_0]$). Model fitting was restricted within these parameter ranges. Refer to Table 2.4 for the specific time points used.

Cell Fluorescence Parameter	**Minimum**	**Maximum**
Peak width(CV)	0.015	0.021
Dye Dilution Ratio	0.45	0.5
Background Fluorescence	0	1000
Fluorescence Shift	-0.001	0.001
Population Parameter	**Minimum**	**Maximum**
$E[Tdiv_0]$	6 h	72 h
$E[Tdie_0]$	6 h	192 h
$E[Tdiv_{1+}]$	6 h	48 h
$E[Tdie_{1+}]$	6 h	96 h
$s.d.[Tdiv_0]$	0.001 h	72 h
$s.d.[Tdie_0]$	0.001 h	192 h
$s.d.[Tdiv_{1+}]$	0.001 h	48 h
$s.d.[Tdie_{1+}]$	0.001 h	96 h
$D\ \mu$	-3 generations	8 generations
$D\ \sigma$	0.001 generations	10 generations
F_0	0.001	1
Start Cells (N)	10,000 cells	200,000 cells
K mech death	0	0
Fraction mech death	0	0

Table 2.4. **Time points considered for analysis of generated time courses.** For generated time courses, model solutions were sampled according to these time course schedules. Three, five, and ten time points were used in Figure 2.8. Four, four early, and eight time points were used in Figure 2.11. Four, seven, and ten time points were used when generating Table 2.1. Otherwise 10 time points were sampled from generated datasets. See also Table 2.3.

Time Point	3 Time points	4 Time points	4 early time points	5 Time Points	7 Time Points	8 Time Points	10 Time Points
1	48 h	24 h	12 h	24 h	24 h	24 h	6 h
2	96 h	60 h	24 h	48 h	48 h	32 h	24 h
3	144 h	96 h	36 h	72 h	60 h	48 h	36 h
4		144 h	48 h	96 h	72 h	60 h	48 h
5				144 h	96 h	80 h	60 h
6					144 h	100 h	72 h
7					180 h	144 h	96 h
8						192 h	120 h
9							144 h
10							192 h

Figure 2.10. Comparison of FlowMax to the Cyton Calculator. The Cyton Calculator [45] and a computational tool implementing our methodology, "FlowMax," were used to train the cyton model with log-normally distributed division and death times on a CFSE time course of wildtype B cells stimulated with lipopolysaccharides (LPS). The best-fit generational cell counts were input to the Cyton Calculator. (A) Visual summary of solution quality estimation pipeline implemented as part of FlowMax. Candidate parameter sets are filtered by the normalized % area difference score, parameter sensitivity ranges are calculated, parameter sensitivity ranges are clustered to reveal non-redundant maximum-likelihood parameter ranges (red ranges). Jagged lines represent the sum of uniform parameter distributions in each cluster. (B) Best fit cyton model parameters determined using the Cyton Calculator (blue dots) and our phenotyping tool, FlowMax (square red individual fits with sensitivity ranges represented by error bars and square green weighted cluster averages with error bars representing the intersection of parameter sensitivity ranges for 41 solutions in the only identified cluster). (C) Plots of Fs (the fraction of cells dividing to the next generation), and log-normal distributions for the time to divide and die of undivided and dividing cells sampled uniformly from best-fit cluster ranges in (B). (D) Generational (colors) and total cell counts (black) are plotted as a function of time for 250 cyton parameter sets sampled uniformly from the intersection of best-fit cluster parameter ranges. Red dots show average experimental cell counts for each time point. Error bars show standard deviation for duplicate runs.

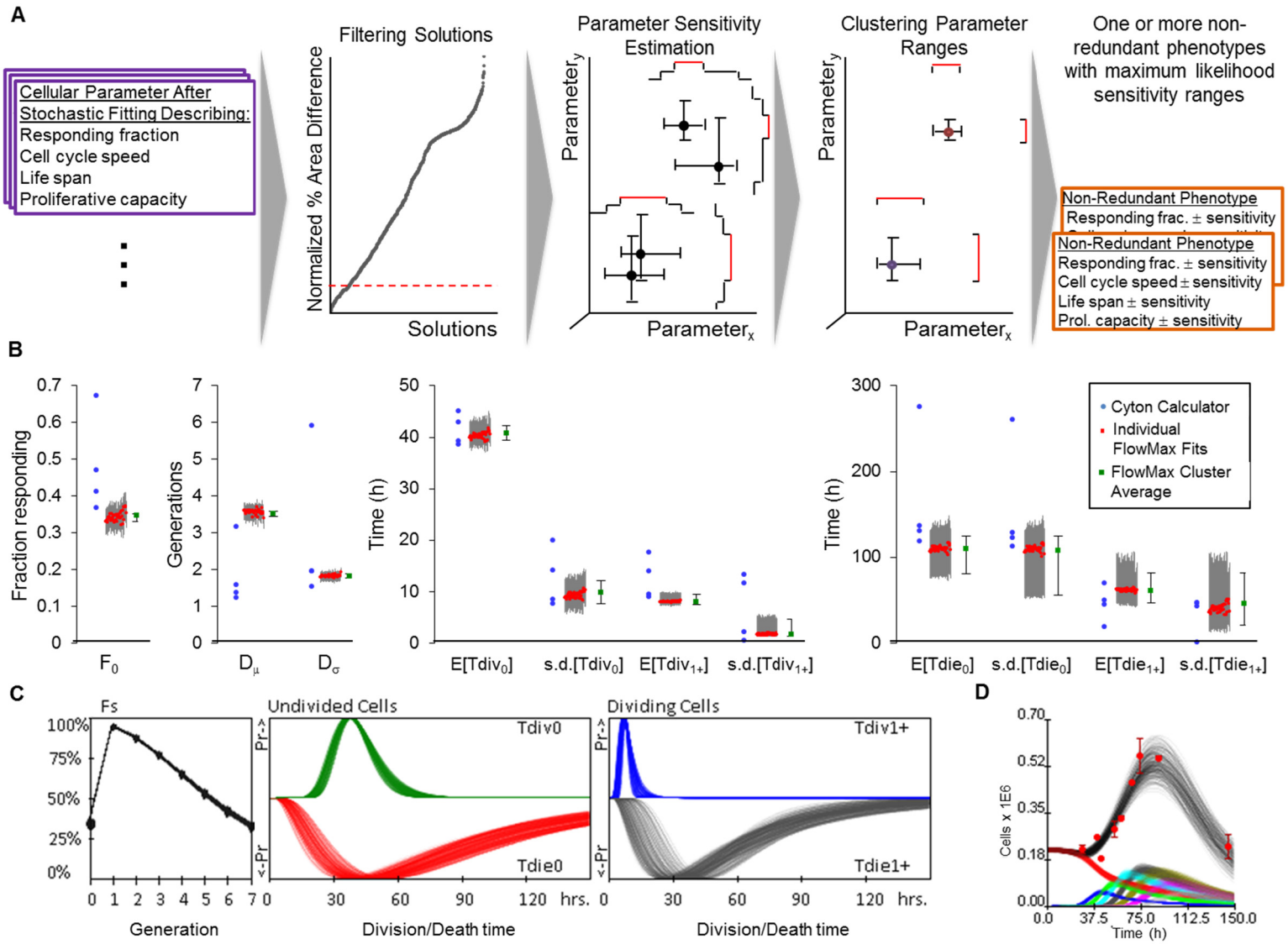
A
Cellular Parameter After Stochastic Fitting Describing:
Responding fraction
Cell cycle speed
Life span
Proliferative capacity
Filtering Solutions
Normalized % Area Difference
Solutions
Parameter Sensitivity Estimation
Parameter_y
Parameter_x
Clustering Parameter Ranges
One or more non-redundant phenotypes with maximum likelihood sensitivity ranges
Non-Redundant Phenotype
Responding frac. ± sensitivity
Non-Redundant Phenotype
Responding frac. ± sensitivity
Cell cycle speed ± sensitivity
Life span ± sensitivity
Prol. capacity ± sensitivity
B
Fraction responding
F0
Generations
Dμ
Dσ
Time (h)
E[Tdiv0]
s.d.[Tdiv0]
E[Tdiv1+]
s.d.[Tdiv1+]
Cyton Calculator
Individual FlowMax Fits
FlowMax Cluster Average
E[Tdie0]
s.d.[Tdie0]
E[Tdie1+]
s.d.[Tdie1+]
C
Fs
Generation
Undivided Cells
Tdiv0
Tdie0
Division/Death time
Dividing Cells
Tdiv1+
Tdie1+
Division/Death time
D
Cells x 1E6
Time (h)

2.2.5. Investigating how data quality affects solution sensitivity and redundancy

We tested how sources of imperfections in typical experimental CFSE data affected the outcome of our integrated fitting procedure. Starting with the best fit average wildtype B cell time course stimulated with bacterial lipopolysaccharides (LPS), we generated *in silico* CFSE datasets. Specifically, we wanted to test the effect of time point frequency, increased fluorescence CV (e.g. due to poor CFSE staining), increased Gaussian noise in generational counts (e.g. mixed populations), and increased Gaussian noise in the total number of cells collected during each time point (e.g. mixing/preparation noise) (Figure 2.11). For each generated dataset, we fitted cell fluorescence parameters, used the best-fit fluorescence parameters as adaptors during a subsequent 100 rounds of population model fitting, filtered poor solutions, calculated parameter sensitivities, and clustered the solution ranges to obtain maximum-likelihood non-redundant solution ranges (Figure 2.1).

Results show that increasing CV or using only four, albeit well positioned time points, does not significantly impact the quality of the fit, with all parameters still accurately recovered (blue triangles, pink crosses). On the other hand, adding random noise in the number of cells per peak or per time point results in increased error in fcyton parameters F_0, $Tdie_0$ and to a lesser degree s.d.[$Tdiv_0$] and s.d.[$Tdiv_{1+}$] (Figure 2.11 green circles and purple bars). However, only using early time points resulted in egregious errors with most parameters displaying diminished sensitivity and higher deviation from the actual parameter value. Indeed, our method identified four non-redundant solutions when fitting the early time point only time course (Figure 2.11, orange).

Figure 2.11. Testing the accuracy of the proposed approach as a function of data quality. Six typical CFSE time courses of varying quality were generated and fitted using our methodology (Figure 2.1). (A-F) The best-fit cluster solutions are shown as overlays on top of black histograms for indicated time points. Conditions tested were (A) low CV, (B) high CV (e.g. poor staining), (C) 10% Gaussian count noise (e.g. mixed populations), (D) 10% Gaussian scale noise (poor mixing of cells), (E) four distributed time points (e.g. infrequent time points), (F) four early time points from the first 48 hours (see Methods for full description). (G) Parameter sensitivity ranges for each solution in each non-redundant cluster next to the maximum likelihood parameter ranges are shown for fcyton fitting. The actual parameter value is shown first (black dot).

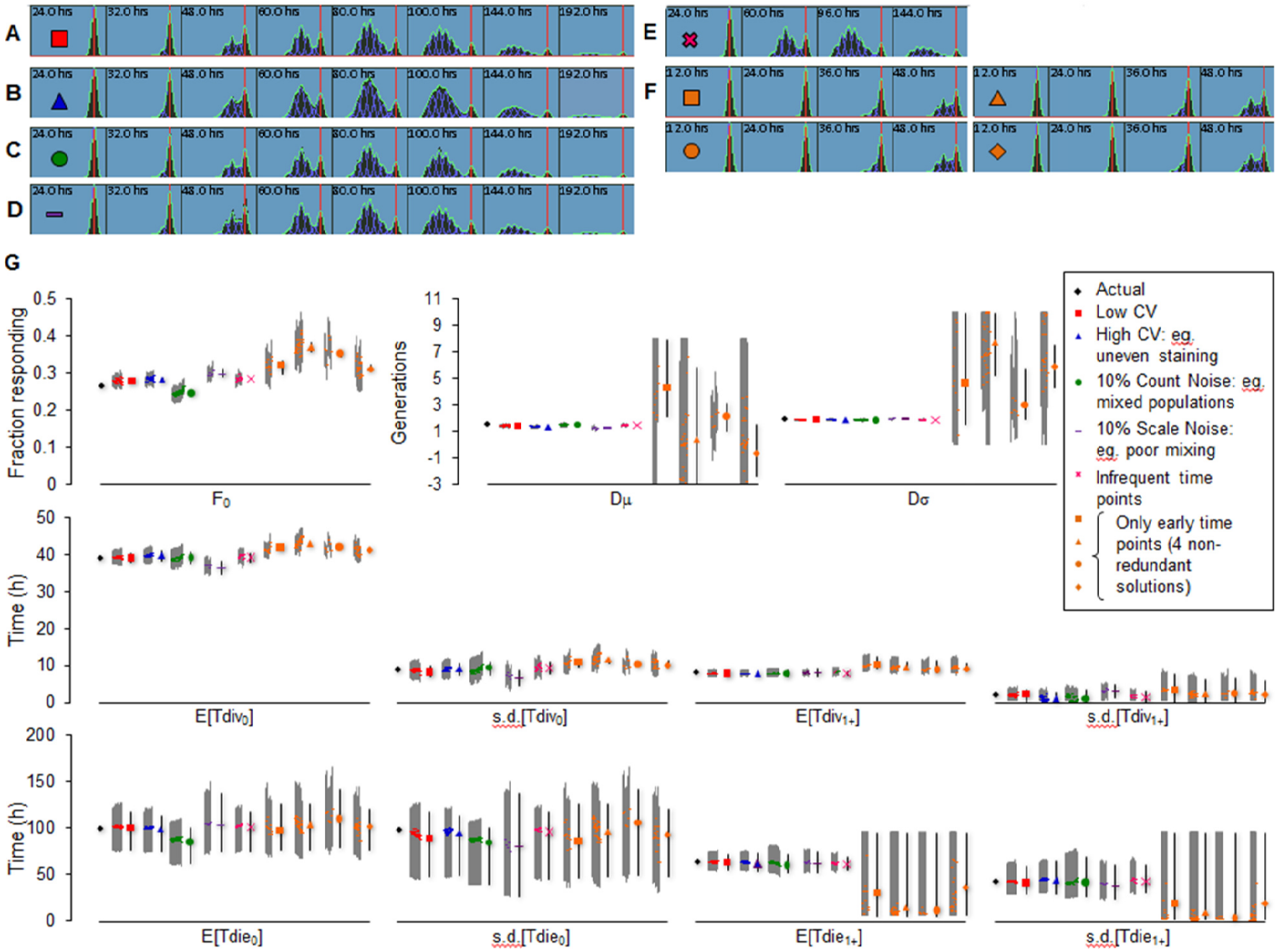
A
B
C
D
E
F
G
24.0 hrs
32.0 hrs
48.0 hrs
60.0 hrs
80.0 hrs
100.0 hrs
144.0 hrs
192.0 hrs
96.0 hrs
12.0 hrs
36.0 hrs
Fraction responding
Generations
Time (h)
F0
Dμ
Dσ
E[Tdiv0]
s.d.[Tdiv0]
E[Tdiv1+]
s.d.[Tdiv1+]
E[Tdie0]
s.d.[Tdie0]
E[Tdie1+]
s.d.[Tdie1+]
Actual
Low CV
High CV: eg. uneven staining
10% Count Noise: eg. mixed populations
10% Scale Noise: eg. poor mixing
Infrequent time points
Only early time points (4 non-redundant solutions)

2.2.6. Pheotyping B lymphocytes lacking NFκB family members

We next applied the integrated phenotyping tool, FlowMax, to a well-studied experimental system: the dynamics of B cell populations triggered by *ex vivo* stimulation with pathogen-associated molecular patterns (PAMPs) or antigen-receptor agonists. B cell expansion is regulated by the transcription factor NFκB, which may control cell division and/or survival. Indeed, mice lacking different NFκB family members have been shown to have distinct B cell expansion phenotypes in response to different mitogenic stimuli [33].

Using published studies as a benchmark, we tested the utility of FlowMax. Using purified naïve B lymphocytes from WT, *nfkb1*$^{-/-}$, and *rel*$^{-/-}$ mice, stained with CFSE, we obtained flow-cytometry data following LPS and anti-IgM stimulation over a six day time course. We then used FlowMax to arrive at the best-fit single-cell representation of the CFSE population data for each experimental condition tested (Figure 2.12A and Figure 2.13) and tabulated the cellular parameter values from the best family of clustered solutions for all conditions tested alongside our summary of the previously-published results (Figure 2.12B). The best-fit solution clusters fit the time courses well (11.95% median normalized percent area error), with the larger errors naturally biased toward weekly proliferating populations (Figure 2.13). Our analysis revealed that in response to anti-IgM cRel-deficient B cells are unable to enter the cell division program, as evidenced by a low F_0 value. However, in response to LPS, *rel*$^{-/-}$ and *nfkb1*$^{-/-}$ B-cells show both cell survival and activation phenotypes, suggesting the involvement of other *nfkb1* functions downstream of the receptor TLR4 (Figure 2.14). These computational phenotyping results are in agreement with the conclusions reached in prior studies using traditional methods such as tritiated thymidine incorporation, as well as staining for DNA content or membrane integrity (propidium iodide) to measure cell population growth as

well as the fractions of cycling and dying cells, respectively [171]. In particular, in response to LPS, the *nfkb1* gene product p105 (rather than p50) was shown to mediate B-cell survival via the Tpl2/ERK axis [60]. However, our results extend the published analysis by quantifying the contributions of the cell survival and decision making functions of these genes to B lymphocyte expansion. For example, whereas *NFκB1* and *rel* appear to equally contribute to cell cycle and survival, *rel* has a more critical role in the cellular decision to enter the cell division program (Figure 2.12 and Figure 2.14).

Interestingly, in response to anti-IgM, our analysis reveals a previously unknown suppressive role for *nfkb1* of limiting the number of divisions that cells undergo (Figure 2.12, compare D_μ and D_σ). In response to LPS, Fs are reduced in *nfkb1*$^{-/-}$ B cells, but they are higher in response to anti-IgM. This affects mostly the later progressor fractions, e.g. F_1, F_2. To examine the contribution of each parameter type (decision making, cell cycle times, death times) we developed a solution analysis tool, which allows for model simulations with mixed knockout- and wildtype-specific parameters to illustrate which parameter or combination of cellular processes substantially contribute to the knockout phenotype. In the case of IgM-stimulated *nfkb1*$^{-/-}$, this analysis reveals that the later cell decision parameters (e.g. $F_{1,2,...}$) are necessary and largely sufficient to produce the observed phenotype (Figure 2.12C, Figure 2.14).

Figure 2.12. Phenotyping WT, *nfkb1*$^{-/-}$, and *rel*$^{-/-}$ B cells stimulated with anti-IgM and LPS. (A) Visual summaries of best-fit phenotype clusters for WT (top), *nfkb1*$^{-/-}$ (middle), and *rel*$^{-/-}$ (bottom) genotypes stimulated with anti-IgM (left), and LPS (right). To visualize cellular parameter sensitivity, 250 sets of parameters were selected randomly from within parameter sensitivity ranges and used to depict individual curves for the fraction of responding cells in each generation (Fs) and lognormal distributions for time-dependent probabilities to divide (Tdiv) and die (Tdie) for undivided and divided cells. (B) Tables summarizing the best fit cellular parameters determined using the integrated computational tool, FlowMax, as well as the relative amount of cell cycling and survival reported in previous studies [60]. Values in parentheses represent the lognormal standard deviation parameters. (C) Total cell counts simulated with the fcyton model when indicated combinations of *nfkb1*$^{-/-}$-specific parameters were substituted by WT-specific parameters during anti-IgM stimulation ("chimeric" solutions). Dots show WT (red) and *nfkb1*$^{-/-}$ (blue) experimental counts. Error bars show cell count standard deviation for duplicate runs.

A

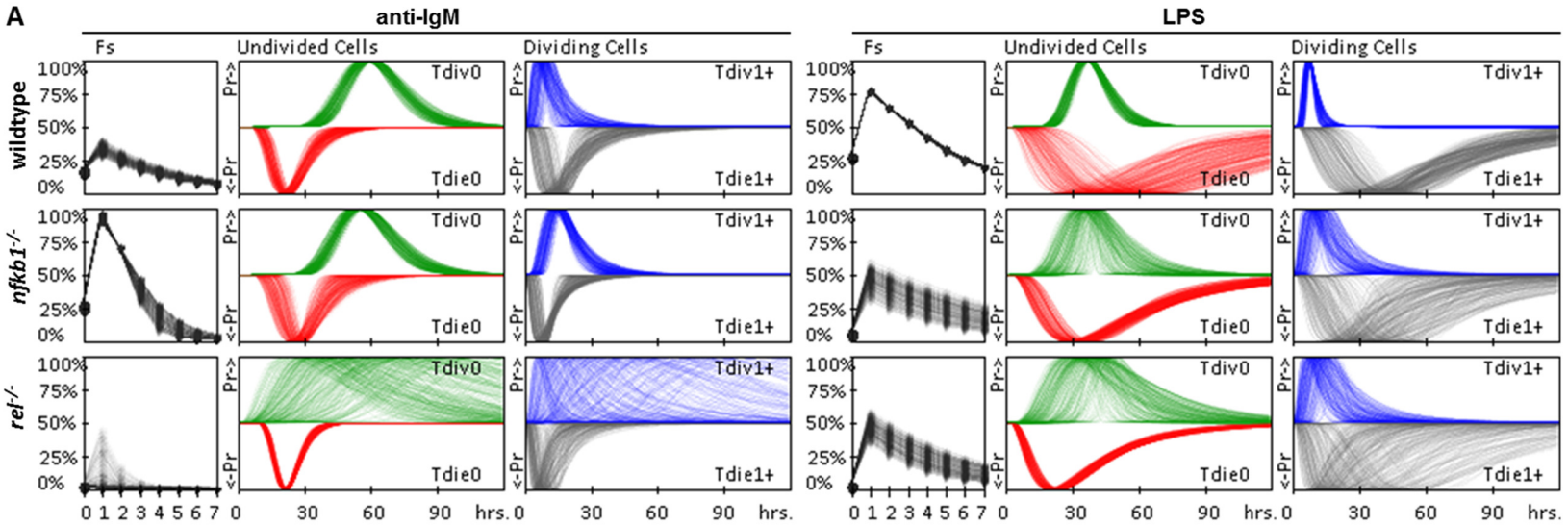

B

anti-IgM	WT	*nfkb1*$^{-/-}$	*rel*$^{-/-}$
Cell Cycle	$+++^{10}$	$+++^{10}$	$-^{10}$
F_0	15%	25%	1%
$E[Tdiv_0]$ (s.d.$[Tdiv_0]$)	62.9 h (13.5 h)	59.3 h (13.1 h)	und.
$E[Tdiv_{1+}]$ (s.d.$[Tdiv_{1+}]$)	10.5 h (3.6 h)	18.7 h (8.8 h)	und.
D_μ (D_σ)	-2.6 (1.9) gens	2.3 (1.0) gens	und.
Cell Survival	$+++^{10}$	$+++^{10}$	$+^{10}$
$E[Tdie_0]$ (s.d.$[Tdie_0]$)	25.3 h (8.7 h)	30.0 h (9.3 h)	23.0 h (5.9 h)
$E[Tdie_{1+}]$ (s.d.$[Tdie_{1+}]$)	17.5 h (4.6 h)	11.8 h (3.1 h)	7.5 h (4.9 h)

LPS	WT	*nfkb1*$^{-/-}$	*rel*$^{-/-}$
Cell Cycle	$+++^{10}$	$++^{10}$	$+^{10}$
F_0	27%	5%	1%
$E[Tdiv_0]$ (s.d.$[Tdiv_0]$)	38.9 h (8.7 h)	39.7 h (5.1 h)	41.1 h (2.4 h)
$E[Tdiv_{1+}]$ (s.d.$[Tdiv_{1+}]$)	8.0 h (2.1 h)	18.5 h (16.3 h)	18.8 h (16.7 h)
D_μ (D_σ)	1.5 (1.8) gens	-2.6(2.5) gens	-1.2 (1.9) gens
Cell Survival	$+++^{10}$	$++^{10}$	$+^{10}$
$E[Tdie_0]$ (s.d.$[Tdie_0]$)	98.8 h (97.5 h)	54.7 h (34.2 h)	41.5 h (30.4 h)
$E[Tdie_{1+}]$ (s.d.$[Tdie_{1+}]$)	62.6 h (41.7 h)	47.6 h (18.5 h)	38.5 h (25.7 h)

C

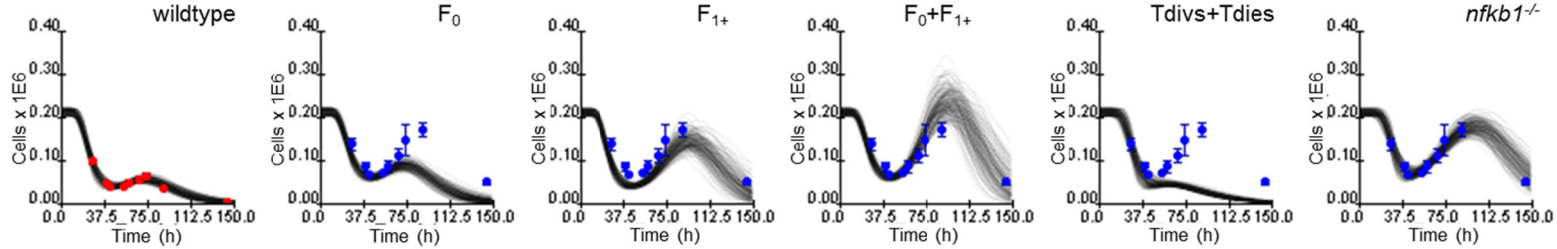

Figure 2.13. Best-fit fcyton solution overlays for stimulated wildtype, *nfkb1*$^{-/-}$, and *rel*$^{-/-}$ B cell CFSE time courses. CFSE fluorescence data was collected and phenotyped using FlowMax, a computational tool that implements our integrated methodology. Green overlays show the weighted average best-fit model solutions for six duplicate log-fluorescence CFSE time courses (filled histograms). Columns represent individual time points. Histograms are normalized to the highest count for each time course across experimental duplicates. X-axes are in log-fluorescence units and automatically chosen to encompass all fluorescence values across all time-points and experimental runs. Red line shows manually selected position of the undivided population. Times of collection are indicated next to each histogram. Background indicates stimulus (blue = LPS, purple = anti-IgM). See also Figure 2.12.

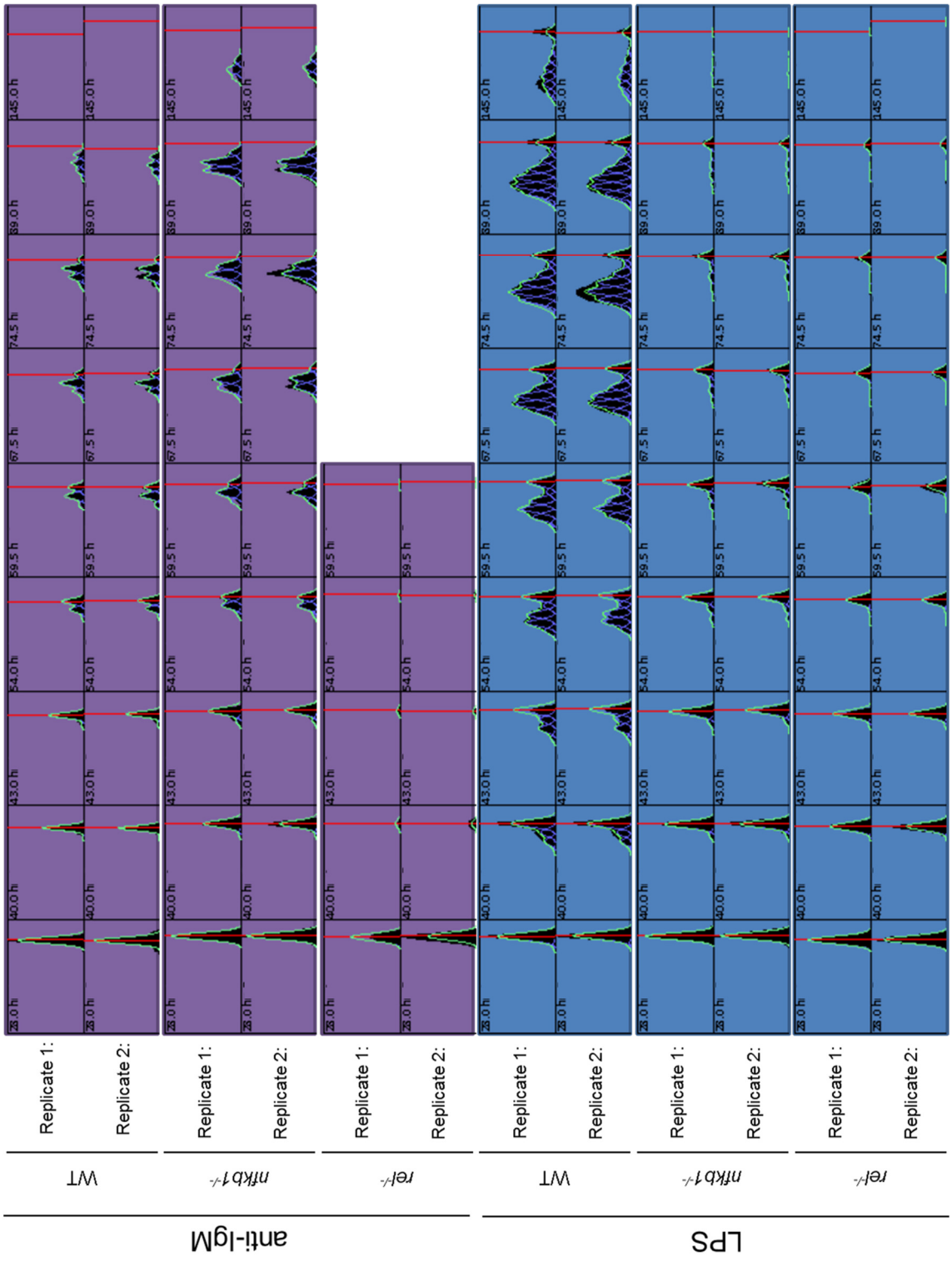
anti-IgM
LPS
WT
nfkb1-/-
rel-/-
WT
nfkb1-/-
rel-/-
Replicate 1:
Replicate 2:
Replicate 1:
Replicate 2:
Replicate 1:
Replicate 2:
Replicate 1:
Replicate 2:
Replicate 1:
Replicate 2:
Replicate 1:
Replicate 2:
28.0 h
40.0 h
43.0 h
54.0 h
59.5 h
67.5 h
74.5 h
89.0 h
145.0 h

Figure 2.14. Using chimeric model solutions to identify key fcyton parameters. Total model cell counts determined when combinations of best-fit wildtype parameters were replaced by *nfkb1*$^{-/-}$ -specific (rows 1 and 3) and *rel*$^{-/-}$-specific (rows 2 and 4) best-fit maximum-likelihood parameter ranges for anti-IgM (rows 1 and 2) and LPS (rows 3 and 4) stimulation. Dots show wildtype (red) and knockout (blue) experimental counts. Error bars show standard deviation of cell counts from duplicate runs. Poor fitting indicates that the indicated parameters do not sufficiently describe the mutant phenotype.

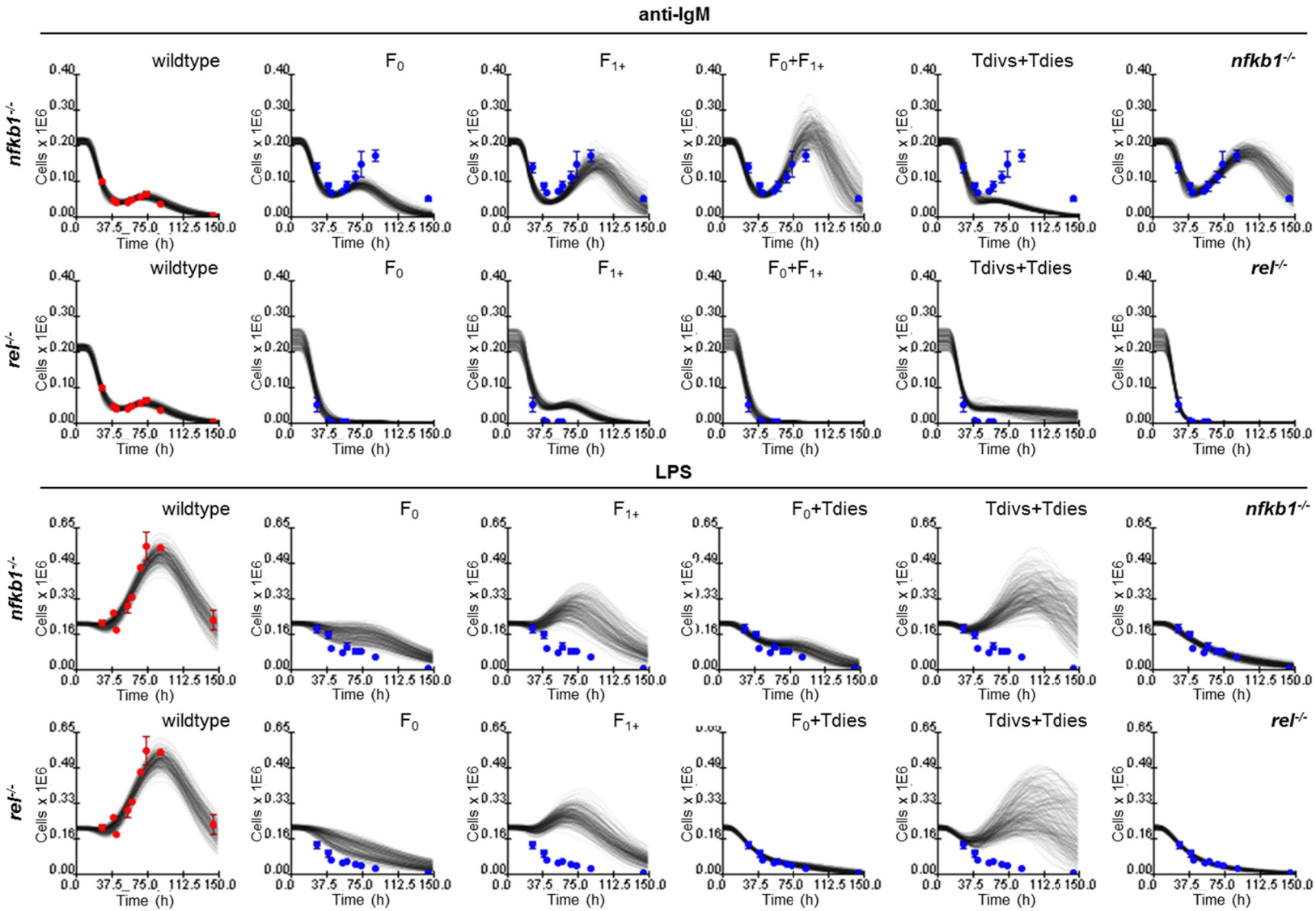
anti-IgM
LPS
wildtype
F0
F1+
F0+F1+
F0+Tdies
Tdivs+Tdies
nfkb1-/-
rel-/-
Cells x 1E6
Time (h)
0.0
37.5
75.0
112.5
150.0

2.3. Discussion

Recent advances in flow cytometry and mathematical modeling have made it possible to study cell population dynamics in terms of stochastic cellular processes that describe cell response, cell cycle, and life span. Interpreting CFSE dye dilution population experiments in terms of biologically intuitive cellular parameters remains a difficult problem due to experimental and biological heterogeneity on the cellular level. While available population models may be fitted to generational cell counts, a remaining challenge lies in determining the redundancy and size of the solution space, a requirement for developing confidence in the quantitative deconvolution of CFSE data. Developing a methodology for objective interpretation of CFSE data may lead to quantitative mechanism-oriented insights about cellular decision-making, and allow for improved and automated diagnosis of such data in the clinic.

In this study we present an integrated phenotyping methodology, exemplified by the computational tool FlowMax, which addresses these challenges. FlowMax comprises the tools needed to construct CFSE histograms from flow cytometry data, fit a fluorescence model to each histogram, determine sets of best fit cellular parameters that best describe the CFSE fluorescence time series, and estimate the sensitivity and redundancy of the best fit parameters (Figure 2.1). By using the cell fluorescence model to translate between generation-specific cell counts of the cell population model and the CFSE fluorescence profiles, the method ensures that the population dynamics model is trained directly on the experimental fluorescence data, without relying on *ad hoc* scoring functions. While our general methodology can be relatively easily adopted for use with any population dynamics and cell fluorescence models (including population models that incorporate both CFSE label and population dynamics [98,99,107,108]), we adopted a version of the cyton model because it explicitly incorporates most features of

proliferating lymphocytes in an intuitive manner, forms the basis of the Cyton Calculator tool, and could be easily adapted to include new observations from single-cell studies. While, the cyton model is over-determined and it is possible that minimal alternative models may describe the noisy CFSE data equally-well [90]. For example, it is possible that models with exponential distributions for the time to divide and die, or models which do not include generational dependence for division/death may be able to describe the data. However, independent studies have shown that lymphocyte cycling and programmed cell death show delay times and conform to log-normal distributions, and that the fraction of lymphocytes exiting the cell cycle as well as the timing for division and death of lymphocytes are generation-dependent [21,44,46]. Our attempts at fitting a typical experimental dataset using minimal models confirmed that to model B cell dynamics both a delay in division/death timing (e.g. using log-normal distributions) as well as distinguishing between generations (e.g. undivided/divided) is essential (unpublished data). Within FlowMax we chose to decouple treatment of cell fluorescence from population dynamics and allow for manual compensation for general fluorescence changes such as dye catabolism (supplementary file FlowMax.zip). Treating such experimental heterogeneity separately from biological variability was essential for computational tractability of solution finding via repeated fitting.

Fitting generated datasets allowed us to evaluate individual fitting steps, and when these were combined in an integrated or sequential manner. While, the cell fluorescence model is readily trained on the generated data, especially if multiple peaks are present (Figure 2.2B-C), not all fcyton model parameters are equally determinable, as parameters for $Tdie_{1+}$ and $D\mu$ were associated with significant median errors (Figure 2.3C and Figure 2.6). When both models were fitted, doing so in an integrated manner (using the fitted cell fluorescence parameters as adaptors during population model

optimization) outperformed doing so sequentially in terms of both solution statistical significance (Figure 2.5A) and fcyton parameter error distributions (Figure 2.5B and Figure 2.4). This is not surprising as the integrated method avoids errors introduced during fluorescence model fitting, by optimizing the cell population model on the fluorescence histograms directly (Figure 2.6). Furthermore, by using the fluorescence model as an adaptor, contributions from each fluorescence intensity bin are automatically given appropriate weight during population model fitting, while the sequential approach must rely on *ad hoc* scoring functions to achieve reasonable, albeit worse, fits. The accuracy of the integrated fitting approach improves asymptotically with the number of fit points used (Figure 2.7), and is dependent on the choice of time points used, with errors in key fcyton model early F_0, N, and late $Tdie_0$ parameters especially sensitive to sufficiently early and late time points, respectively (Figure 2.8). Testing potential scoring functions demonstrated that while the methodology is relatively robust to specific objective function selection, an objective function including both a mean root sum of squared deviations as well as a correlation term resulted in lower errors in average fitted generational counts (Figure 2.9). Finally, fitting both the cell fluorescence and fcyton model typically requires only a few minutes on a modern computer (Table 2.1), suggesting that our methodology and tool can be used to process a long duplicate time course in about a day.

The analysis of our fitting methodology revealed a limit on the accuracy of fitted model parameters, even under idealized conditions of perfect knowledge of experimental heterogeneity and assuming the fcyton model is a perfect description of B cell dynamics (Figure 2.3), suggesting that objective interpretation requires solution sensitivity and redundancy estimation. We compared several qualitatively good model fits obtained with the Cyton Calculator [45] to our phenotyping tool FlowMax (Table 2.2 and Figure 2.10).

Using the Cyton Calculator, best-fit parameter sets (Figure 2.10B blue dots) are subject to choice of initial parameters (Table 2.2). Repeated fitting with different fitting conditions yielded qualitatively good solutions with different parameter values. Conversely, the solution quality estimation integrated into our methodology (Figure 2.10A) revealed that only one set of parameters best describes the dataset, and that only a relatively small range of maximum-likelihood parameter values was common to good fits (Figure 2.10B green dots and ranges). Interestingly, most of the fitted parameters are in approximate quantitative agreement between the two methods, however, the maximum-likelihood parameter ranges determined by our methodology usually showed agreement with outlying parameter values determined by the Cyton Calculator, suggesting that picking a specific or average solution may be inappropriate (Figure 2.10B).

Testing how data quality affects solution redundancy and sensitivity reveals that the methodology is relatively robust to poor CFSE staining (high CV) as well as the frequency of time points used for fitting, assuming they are spaced throughout the time course (Figure 2.11). However, this is only true if time points are selected such that they capture the population behavior throughout the response, as picking only early time points resulted in global parameter insensitivity, degeneracy, and large parameter errors. Furthermore, poor mixing/preparation of cells (scale noise) or the presence of other cell populations (count noise) resulted in qualitatively good fits at the cost of some errors in perceived population parameters, highlighting the importance of fitting to two or more replicate time courses and working with a single cell type.

Finally, to demonstrate that our computational tool can provide valuable insights into the cellular processes underlying lymphocyte dynamics, we used FlowMax to phenotype B cells from NFκB-deficient mice, which show strong proliferative and

survival phenotypes when stimulated with anti-IgM and LPS mitogenic signals (Figure 2.13). Our analysis of these cells confirmed the previously published data [60,171] and extended the analysis to specific cellular processes in a quantitative manner. We found for example that the phenotype of *NFκB1*$^{-/-}$ and *rel*$^{-/-}$ is similar in the proliferation and survival of B-cells, except in the ability of resting B cells to exit the G_0 stage, which is more critically controlled by *rel* gene product cRel (Figure 2.12A). This may reflect that while cRel is activated early and required for all aspects of B-cell proliferation, the *NFκB1* gene product p105 is thought to provide for lasting ERK1 activity [86] that may facilitate primarily later stages of B-cell proliferation. Furthermore, our analysis revealed a previously unappreciated anti-proliferative role for NFκB gene *NFκB1* during anti-IgM stimulation (Figure 2.12B). Although more subtle, this phenotype was revealed because we were able to distinguish between early pro-proliferative cellular processes (F_0, $Tdiv_0$, $Tdie_0$) and later ones (F_{1+}, $Tdiv_{1+}$, $Tdie_{1+}$), which may otherwise be overshadowed by early parameters that more prominently determine bulk population dynamics, but importantly determine the proliferative capacity of B cells. We confirmed the importance of the later parameters by modeling population dynamics with “chimeric” parameter sets derived from wildtype and knockout model fits (Figure 2.12C and Figure 2.14). How *NFκB1* may dampen late proliferative functions in response to anti-IgM but not LPS remains to be investigated. Preliminary results indicate that the *NFκB1* gene product p50, which may have repressive effects as homodimers, is actually less abundant following anti-IgM than LPS stimulation. Conversely the *NFκB1* gene product p105 is more abundant following anti-IgM than LPS stimulation and could inhibit signaling in two ways. Induced expression of p105 may block MEK1/ERK activation by Tpl2 [85], or it may function to provide negative feedback on NFκB activity, as a component of the

inhibitory IκBsome complex [148,172]. Future studies may distinguish between these mechanisms and examine the role of the IκBsome in limiting the proliferative capacity of antigen-stimulated B cells.

2.4. Models and Methods

FlowMax source code, executable, and a short tutorial can be found in supplementary file FlowMax.zip. CFSE datasets used are provided as CFSEdatasets.zip supplementary file.

2.4.1. Ethics Statement

Wildtype and gene-deficient *rel* and *NFκB1* mice were maintained in ventilated cages. Animal studies were approved by the Institutional Animal Care and Use Committee of the University of California, San Diego.

2.4.2. Modeling experimental fluorescence variability

For the cell fluorescence model, we adopted a mixture of Gaussians model for representing log-fluorescence CFSE histograms. The mean, μ, and standard deviation, σ, for a Gaussian distribution of cellular fluorescence in a specific generation, g, is calculated as

$$\mu_g = \log_{10}(10^{\mu_0} \cdot r^g + b) + s \ , \quad (1)$$

$$\sigma_g = \sigma = \mu_0 \cdot CV \ , \quad (2)$$

where *r* represents the halving ratio (~0.5), *b* the background (autofluorescence) [173], *s* is a shift parameter used to adjust the fluorescence of the whole distribution during fitting, and *CV* is the generation-invariant Gaussian coefficient of variation. While the CV is generation-invariant, fluorescence parameters are allowed to vary from time point to time point during fitting. These fluorescence parameters must be combined with generation-specific cell counts to describe a weighted fluorescence histogram that resembles typical CFSE data. Recent studies have shown that a mixture of Gaussians closely approximates experimental CFSE log-fluorescence histograms [45,111,112]. Our model is based on those suggested by Hodgkin et al [45]. In addition, Hasenauer *et al* suggest a mixture of log-normal distributions to approximate the combined heterogeneity in CFSE staining and autofluorescence [107]. A description of our model fitting strategy can be found below.

2.4.3. Modeling Population Dynamics

For modeling population dynamics, we started with the generalized cyton model, which straightforwardly incorporates most biological features of lymphocyte proliferation [44], and forms the basis of the Cyton Calculator [45], the current state-of-the-art computational tool for interpreting CFSE-derived generational cell count data. To reflect the recent experimental finding that growing (i.e. responding) cells are resistant to death [21] we logically decoupled the division and death processes by explicitly removing the cell fate competition. In the so called, fcyton model, the fraction of responding cells in each generation (the Fs) control cell fate by ensuring that responding cells are protected from death, however the timing to the chosen fate (division or death) is still stochastically distributed. Specifically, the number of cells that divide and die for each cell generation, g, as a function of time, *t*, is found using

$$n_{g=0}^{div}(t) = F_0 \cdot N \cdot \phi_0(t) \ , \tag{3}$$

$$n_{g=0}^{die}(t) = (1-F_0) \cdot N \cdot \psi_0(t) \, , \tag{4}$$

$$n_{g>0}^{div}(t) = 2 \cdot F_g \cdot \int_0^t n_{g-1}^{div}(t') \phi_{1+}(t-t') dt' \, , \tag{5}$$

$$n_{g>0}^{die}(t) = 2 \cdot (1-F_g) \cdot \int_0^t n_{g-1}^{div}(t') \cdot \psi_{1+}(t-t') dt' \, . \tag{6}$$

In equations (3-6) $\phi_0(t)$, $\phi_{1+}(t)$, $\psi_0(t)$, and $\psi_{1+}(t)$ represent the cell age-dependent probability density functions that undivided cells will divide, divided cells will divide, undivided cells will die, and divided cells will die, respectively. The parameters *N* and F_i, represent the starting cell count, and fraction of cells responding in generation i, respectively. The total number of cells, $N_g(t)$ at time t and generation g is given by

$$N_{g=0}(t) = N - \int_0^t \left(n_0^{div}(t') + n_0^{die}(t') \right) dt' \, , \tag{7}$$

$$N_{g>0}(t) = \int_0^t \left(2n_{g-1}^{div}(t') - n_g^{div}(t') - n_g^{die}(t') \right) dt' \, . \tag{8}$$

The progressor fractions, $F_{i\geq 1}$, are calculated using a truncated Gaussian distribution similar to the “division destiny” curve suggested by Hawkins *et al* in the cyton model [44]:

$$F_{i\geq 1} = \begin{cases} \dfrac{1-cdf(i)}{1-cdf(i-1)}, & cdf(i-1)<1 \\ 0, & cdf(i-1)=1 \end{cases}, \quad (9)$$

where $cdf(i)$ is the cumulative normal distribution with mean D_μ and standard deviation D_σ. Since lymphocyte inter-division and death times are well-approximated by log-normal distributions [44], a total of 12 parameters are required to determine the cell count at any point in time in each generation: *N*, F_0, D_μ, D_σ, and eight parameters specifying the log-normal division and death distributions. For a full list of parameters and the ranges used during fitting, refer to Table 2.3.

2.4.4. Testing model accuracy with generated CFSE fluorescence time courses

A total of 1,000 sets of randomized fcyton and fluorescence parameters within realistic ranges [21,44,45,174], were generated (Table 2.3). The randomized fcyton parameters were applied to construct cell counts for eight generations ten time points up to192 hours (Table 2.4). The randomly chosen fluorescence parameters were then applied to construct weighted fluorescence histograms (Figure 2.2A). To test the accuracy of cell fluorescence model fitting, we trained the fluorescence model on the generated histogram time courses one histogram at a time. During fitting, peak weights were calculated analytically using a non-linear regression approach (see below). Resulting best-fit model histogram areas under each peak were compared to their generated counterparts and the average percent errors of the counts normalized to the maximum generational count for each parameter set were plotted (Figure 2.2B, 2.3B, 2.4A, 2.5A, 2.6A, 2.7A, 2.8A, and 2.9A). To test the fcyton cell population model, we

trained the model on known generational cell counts from the generated datasets. Resulting best-fit model generational counts and fcyton parameters were compared to their generated counterparts (Figure 2.2). To evaluate the accuracy of sequential model fitting, the generated datasets were used to first train the cell fluorescence model followed by a round of fcyton model fitting on the resulting best-fit generational cell counts using a simple squared deviation and a more complex *ad hoc* objective function (Figure 2.5 (blue) and Figure 2.4). Next, the generated datasets were used to first train the cell fluorescence model followed by a round of fcyton model fitting to the fluorescence histograms using the best-fit cell fluorescence parameters to generate log-fluorescence histograms with peak weights determined by the population model, which were compared to generated histograms directly (proposed integrated fitting methodology). Different time point schedules were used when testing three or five time point time courses (see Table 2.4). For demonstrating how data quality affects fitting of typical time courses, we used the fitted experimental wildtype LPS cluster solutions to generate six separate *in silico* time courses: a low CV time course (8 time points, CV=0.18, ratio=0.5, background=100,shift=0), a high CV time course (8 time points, CV=0.23, ratio=0.5, background = 100, shift = 0), a generation count noise time course (8 time points, CV=0.18, ratio=0.5, background = 100, shift = 0, each peak count scaled randomly by $1+N(\mu=0,\sigma=0.1)$), a scaled noise time course (8 time points, CV=0.18, ratio=0.5, background=100, shift=0, number of cells in histogram scaled randomly by $1+N(\mu=0,\sigma=0.1)$), an infrequent time point time course (4 time points from 24-144 h, CV=0.18, ratio=0.5, background=100, shift=0), and an early time point time course (4 time points from 12-48 h, CV=0.18, ratio=0.5, background=100, shift=0). Each time course was fitted 100 times using our full methodology (Figure 2.1), and parameter

solution clusters were plotted (Figure 2.11). Refer to Table 2.4 for specific time point schedules used.

2.4.5. Developing measures of confidence for parameter fits

We implemented a computational pipeline for estimating the redundancy and sensitivity of model solutions (Figure 2.1 step 3). A stochastic simulated annealing fitting procedure [175] was used to determine multiple best-fit solutions with random initial parameters (see below). Next, we used a normalized percent area error (NPAE) metric for solution quality estimation which ranges between 0% and 100% difference in histogram areas:

$$NPAE = 50 \cdot \frac{\sum_{i=1}^{t}\sum_{j=1}^{r} Cells_i^j \cdot \sum_{k=1}^{m}\left|H_i^j[k] - M_i[k]\right|}{\sum_{i=1}^{t}\sum_{j=1}^{r} Cells_i^j}, \quad (10)$$

where i and j represent time point i, and experimental run j, and *Cells*, *H,* and *M* represent total cell counts, experimental discrete histogram density, and model discrete histogram density with m total bins, respectively. Solution candidates with NPAE within 0.1 of the top were kept for quality estimation:

$$Candidates = \{S_1, S_2, \ldots, S_n\}, \quad (11)$$

where S_x represents the x[th] set of best-fit parameters. These fits were subjected to one-dimensional parameter sensitivity estimation, which establishes an upper and lower bound on each parameter value that would result in the weighted percent histogram area error (NPAE) to, increase by 1 (1% normalized area difference increase), yielding two sets of sensitivity values for each parameter:

$$Sensitivities = \{<L_1, H_1>, <L_2, H_2>, \ldots, <L_n, H_n>\}, \quad (12)$$

where $< L_x, H_x >$ represents a 2-tuple consisting of sets of lower and upper parameter sets for S_x, respectively. Since more than one non-redundant set of parameters may exist, we developed an agglomerative clustering algorithm which is designed to combine clusters with the highest parameter sensitivity overlap, arriving at sets of non-redundant maximum likelihood parameter ranges. Briefly, the solutions are clustered by continually agglomerating pairs of clusters C_x, C_y with highest total normalized overlap $D_{x,y}$ between parameters:

$$D_{x,y} = \sum_{i}^{params} d_i, d_i = \begin{cases} \frac{\left[\left(A_y[i] + H_y[i]\right) - (A_x[i] - L_x[i])\right]}{|A_x[i] + H_x[i]| + |A_y[i] + H_y[i]|}, if\ A_x > A_y \\ \frac{\left[\left(A_x[i] + H_x[i]\right) - (A_y[i] - L_y[i])\right]}{|A_x[i] + H_x[i]| + |A_y[i] + H_y[i]|}, if\ A_x \le A_y \end{cases}, \quad (13)$$

where A_x and A_y are weighted parameter averages for clusters C_x and C_y, respectively. The agglomerated parameter sensitivity ranges are defined to be the intersection of ranges supported by all candidate solutions in the cluster, resulting in increasingly tighter estimates of the maximum likelihood parameter sensitivity ranges as more solutions are incorporated into the cluster. Clustering is terminated when cluster pairs for which parameter ranges are overlapping for all parameters no longer exist. When clustering parameter ranges, we keep track of a weighted average value that is guaranteed to be within the overlap between ranges being clustered, however its position is weighted according to the relative maximum distance from the average of each of the starting cluster averages:

$$
\begin{aligned}
d_a &= H_c - A_a, \\
d_b &= A_b - L_c, \\
A_c &= \frac{d_b}{d_a + d_b}\left[H_c - L_c\right] + L_c = H_c - \frac{d_a}{d_a + d_b}\left[H_c - L_c\right],
\end{aligned}
\tag{14}
$$

where the distance (d), high(H), average (A), and low (L) values are used to agglomerate clusters a and b into cluster c and letting $A_a < A_b$. Finally, since solution clusters represent linear independent combinations of parameters, solution clusters are sampled uniformly (n=1,000) within the clustered maximum- likelihood parameter ranges for all parameters simultaneously and clusters with median NPAE within 1% of the top cluster's NPAE are kept to ensure that unrealistic parameter combinations were removed.

A simple divide-and-conquer algorithm was chosen for calculating the parameter sensitivity ranges which operates on the best-fit fcyton model parameters, X = { N , F_0 , $D\mu$, $D\sigma$, $Tdiv_0\mu$, $Tdiv_0\sigma$, $Tdie_0\mu$, $Tdie_0\sigma$, $Tdiv_{1+}\mu$, $Tdiv_{1+}\sigma$, $Tdie_{1+}\mu$, $Tdie_{1+}\sigma$ }, and a constant values for the fit tolerance, ε :

ALGORITHM CalParamSensitivities (*X*, ε)

$MinScore \leftarrow AreaDiff(X)$

Define array Upper of size |X|

Define array Lower of size |X|

FOREACH parameter $x_i \in X$:

$Original = x_i$

$StepSize \leftarrow \frac{|x_i - \max(x_i)|}{1000}$

WHILE $StepSize > \frac{|x_i - \max(x_i)|}{10000}$

$x_i \leftarrow x_i + StepSize$

$CurrScore \leftarrow AreaDiff(X)$

IF $CurrScore < MinScore \cdot (1+\varepsilon)$

$x_i \leftarrow x_i - StepSize$

$StepSize \leftarrow \frac{StepSize}{2}$

ELSE

$StepSize \leftarrow \min(StepSize \cdot 2, \max(x_i) - x_i)$

ENDIF

ENDWHILE

$Upper_i \leftarrow x_i$

$x_i = Original$

ENDFOREACH

FOR EACH parameter $x_i \in X$:

$Original = x_i$

$StepSize \leftarrow \frac{|\min(x_i) - x_i|}{1000}$

WHILE $StepSize > \frac{|\min(x_i) - x_i|}{10000}$

$x_i \leftarrow x_i - StepSize$

$CurrScore \leftarrow AreaDiff(X)$

IF $CurrScore < MinScore \cdot (1+\varepsilon)$

$x_i \leftarrow x_i + StepSize$

$$StepSize \leftarrow \frac{StepSize}{2}$$

ELSE

$$StepSize \leftarrow \min(StepSize \cdot 2, x_i - \min(x_i))$$

ENDIF

ENDWHILE

$$Lower_i \leftarrow x_i$$

$$x_i = Original$$

ENDFOREACH

RETURN Upper and Lower

Since the value of the tolerance parameter ε, or the maximum percent increase in the overall normalized percent area error (NPAE), is an important implicit parameter for sensitivity analysis, an appropriate value must be used. In our experience, a value that is too small resulted in small sensitivity ranges for each parameter tested and a large number of non-overlapping solutions. Conversely, high tolerance resulted in large acceptable parameter sensitivity ranges, increasing the chance that linear sampling of parameters introduced errors into sensitivity estimation and underestimating the sensitivity of the solution to model parameters. The parameter ε was set to 1% normalized percent area error (NPAE) empirically because this resulted in parameter sensitivities of approximately ±10% of the best-fit parameter value for the determinable parameters such as F_0, $Tdiv_0$, and $Tdiv_{1+}$. In addition, this resulted in fewer than three solution clusters for experimental datasets. Conversely, values of ε smaller than 1% resulted in more than five solution clusters for the experimental datasets.

The main motivation for clustering parameters is to identify solution uniqueness since more than one set of model parameters can sufficiently describe the data. To determine if more than one solution space can fit the data, we perform a parameter sensitivity analysis for each best-fit solution then successively combine solutions with the largest overlap in the solution space until only non-disjoint solutions remain. By doing this we guarantee that the clustered solution space(s) are non-redundant.

Since parameter fits are obtained using a non-deterministic fitting procedure, the best-fit parameter solution is only an estimate of the true solution. Furthermore, we established that parameters exhibit widely varying degrees of sensitivity that is heavily determined by the underlying dataset. Therefore, we first estimate the sensitivity of each best-fit parameter in a solution, obtaining a set of independent lower and higher parameter values for each parameter, p. Repeating the fitting n times we get the set of best-fit parameter ranges for parameter p:

$$. \; S_p = \left\{ [L_{p,1}, H_{p,1}], [L_{p,2}, H_{p,2}], \ldots, [L_{p,n}, H_{p,n}] \right\}.$$

We assume that each distribution of p found is equally likely and therefore the probability of p is modeled as:

$$\phi_p = f(p = x \mid S_p) = \frac{1}{n} \sum_{i=1}^{n} \frac{I_x(L_{p,i} \le x \le H_{p,i})}{H_{p,i} - L_{p,i}},$$

Where $I(L_{p,i} \le x \le H_{p,i})$ is the indicator function and returns 1 if p is within the ith range. In other words, ϕ_p assumes a linear combination of uniform distributions for p, which comes about if one marginalizes the distribution on all other model parameters. Since ϕ_p represents the probability distribution model of the parameter p given the observed best-fit ranges, the region of maximum likelihood is the range of parameter values such that the overlap count is maximized. Furthermore, by ensuring that only overlapping

parameter ranges are clustered together, we guarantee that only one such maximum region exists for each cluster:

$$
\begin{aligned}
& f(p = x \mid S_p) = \phi_{p,\max} \forall x \in [\hat{L}_p, \hat{H}_p], \\
& \hat{L}_p = \max\left\{L_{p,1}, L_{p,2}, \ldots, L_{p,n}\right\} \\
& \hat{H}_p = \min\left\{H_{p,1}, H_{p,2}, \ldots, H_{p,n}\right\}
\end{aligned}
\tag{15}
$$

The maximum likelihood estimator for p are all values of p within the range $[\hat{L}_p, \hat{H}_p]$ or the intersection of all of the parameter ranges in S_p. In other words, $\hat{L}_p$ and $\hat{H}_p$ are the maximum likelihood estimators of the lower and upper value of p, due to the resolution of the data and methodology (i.e. the probability of p is uniform for any ith best-fit sensitivity range $[L_{p,i}, H_{p,i}]$). We report the region of p defined by $\hat{L}_p$ and $\hat{H}_p$ for which ϕ_p is maximized, or the mode of ϕ_p.

An added potential benefit of clustering is to minimize bias in how we calculate the sensitivity of each solution. Since solution spaces are created by varying parameters around the best-fit value, an implicit parameter is the amount by which a solution can worsen as we vary each parameter independently. If the allowed error is inappropriate, the clustering will either return too many similar solutions (error tolerance too low) or both clusters with poor and good fits (tolerance is too high). The later happens because only the intersection of parameter spaces is kept during the agglomeration process, which means that an overestimate of the parameter range for solutions about a region containing a local minimum will still only contain good fits, while an over estimate of the parameter range for solutions about a region containing poor fits will contain poor solutions. A subsequent filtering of the solution clusters can be used to remove these

“artifact” clusters containing poor solutions and we can alleviate the bias in selecting the error tolerance parameter.

Choosing the representative parameter value (the cluster “average”) for a specific cluster is somewhat arbitrary as the probability of the parameter within a range was assumed to be uniform during clustering. In reality, the probability of any parameter p is likely to decrease with the distance from a best-fit value. Therefore when clustering parameter ranges, we keep track of a weighted average value of p that is guaranteed to be within the overlap between ranges being clustered, but its position is weighted according to the relative maximum distance from the average of each of the starting cluster averages:

$$\begin{aligned} d_a &= H_c - A_a, \\ d_b &= A_b - L_c, \\ A_c &= \frac{d_b}{d_a + d_b}\left[H_c - L_c\right] + L_c = H_c - \frac{d_a}{d_a + d_b}\left[H_c - L_c\right], \end{aligned} \tag{16}$$

where the distance (d), high(H), average (A), and low (L) values are used to agglomerate clusters a and b into cluster c and letting $A_a < A_b$.

The pseudo code for clustering the candidates by maximizing the parameter sensitivity overlap given the set of candidate best-fit fcyton parameter values and their corresponding lower and upper bound sensitivity ranges is shown below:

ALGORITHM: *ClusterBySensitivityAgglomeration (Candidates, Sensitivities)*

Define $Clusters = \{C_1 = \{S_1\}, C_2 = \{S_2\}, \ldots, C_n = \{S_n\}\}$

Define $Averages = \{A_1 = S_1, A_2 = S_2, \ldots, A_n = S_n\}$

Define $Lows = \{D_1 = L_1, D_2 = L_2, \ldots, D_n = L_n\}$

Define $Highs = \{U_1 = H_1, U_2 = H_2, \ldots, U_n = H_n\}$

Define *best_c1* = *best_c2* = -1

Define *largestOverlap* =0

Define *clustering* = true

WHILE *clustering* = true

FOR $A_a \in Averages, A_b \in Averages, a \neq b$

Define *dist* = 0

FOREACH parameter, *i*

Define $d_i = \begin{cases} \dfrac{\left[\left(A_b[i]+U_b[i]\right)-(A_a[i]-D_a[i])\right]}{|A_a[i]+U_a[i]|+|A_b[i]+U_b[i]|}, if\ A_a > A_b \\ \dfrac{\left[\left(A_a[i]+U_a[i]\right)-(A_b[i]-D_b[i])\right]}{|A_a[i]+U_a[i]|+|A_b[i]+U_b[i]|}, if\ A_a \leq A_b \end{cases}$

d*ist* = *dist*+d_i

ENDFOREACH

IF *dist* > 0 and *dist* > *largestOverlap*

largestOverlap =*dist*

best_c1 = *a*

best_c2 = b

ENDIF

ENDFOR

IF *best_c1* ≠ -1 and *best_c2* ≠ -1

Define $newA, newD, newU$

FOREACH parameter, *i*

Define x = y=z=0

IF $A_{best\_c1}[i] < A_{best\_c2}[i]$

$x = D_{best\_c2}[i]$

$y = U_{best\_c1}[i]$

$z = A_{best\_c2}[i] - A_{best\_c1}[i]$

ELSE

$x = D_{best\_c1}[i]$

$y = U_{best\_c2}[i]$

$z = A_{best\_c1}[i] - A_{best\_c2}[i]$

ENDIF

Define $x_{\text{int}} = \dfrac{z \cdot y}{y + x}$

$newA[i] = A_{best\_c1}[i] + x_{\text{int}}$

$newD[i] =$

$newA[i] - \max(A_{best\_c1}[i] - L_{best\_c1}[i], A_{best\_c2}[i] - L_{best\_c2}[i])$

$newU[i] = \min(A_{best\_c1}[i] + U_{best\_c1}[i], A_{best\_c2}[i] + U_{best\_c2}[i]) - newA[i]$

ENDFOREACH

$Averages = (Averages / \{A_{\text{best}_{c1}}, A_{best_{c2}}\}) \cup newA$

$Lows = (Lows / \{D_{best\_c1}, D_{best\_c2}\}) \cup newD$

$Highs = (Highs / \{U_{best\_c1}, U_{best\_c2}\}) \cup newU$

$Clusters = (Clusters / \{C_{best\_c1}, C_{best\_c2}\}) \cup (C_{best\_c1} C_{best\_c2})$

ELSE

clustering = false

ENDIF

ENDWHILE

RETURN < $Averages, Lows, Highs, Clusters$ >

END

2.4.6. Comparing FlowMax to the Cyton Calculator

We used counts derived after fitting the cellular fluorescence model to the experimental wildtype B cell proliferation time courses stimulated with LPS (Figure 2.13), to repeatedly fit the cyton model using the Cyton Calculator [45] and compared to results from fitting the cyton model using FlowMax, a tool that implements our methodology and solution quality estimation procedure (Figure 2.10A). For the Cyton Calculator we used counts derived from fitting the cellular fluorescence model as input, while for FlowMax, we used the fluorescence data directly. To find Cyton Calculator solutions, we carried out Cyton Calculator fitting multiple times using varied starting parameters values sampled from ranges in Table 2.3, as suggested. Most-parameter combinations yielded qualitatively poor fits (determined visually by comparing total and generation cell counts to experimental data), and were discarded. Four qualitatively good solutions, determined visually by comparing total and generational cell counts to experimental data, were found using starting parameters listed in Table 2.2 (Figure 2.10B, blue dots). Using FlowMax involved 1,000 fits, automated solution filtering, parameter sensitivity estimation, and solution clustering. This allowed visualization of a family of solutions sampled from the maximum-likelihood sensitivity ranges for the only solution cluster identified.

2.4.7. Testing how our methodology is affected by the choice of objective function

To analyze how our methodology is affected by choice of objective function during fitting, we used 1,000 generated time courses to fit the fcyton model using best-fit cell fluorescence parameters as adaptors (our proposed integrated methodology). We tested three objective functions for comparing the model histograms to generated histograms: a simple mean sum of absolute deviations (MAD):

$$Obj_{MAD} = \frac{\sum_{i=1}^{t}\sum_{j=1}^{r} Cells_{i,j} \cdot \sum_{k=1}^{m} \left| H_{i,j}[k] - M_i[k] \right|}{\sum_{i=1}^{t}\sum_{j=1}^{r} Cells_{i,j}}, \quad (17)$$

a mean root sum of squared deviations (MRSD) objective function:

$$Obj_{MRSD} = \frac{\sum_{i=1}^{t}\sum_{j=1}^{r} Cells_{i,j} \cdot \sqrt{\sum_{k=1}^{m} \left(H_{i,j}[k] - M_i[k] \right)^2}}{\sum_{i=1}^{t}\sum_{j=1}^{r} Cells_{i,j}}, \quad (18)$$

and a mean root sum of squared deviations with Pearson correlation (MRSD+) objective function:

$$Obj_{MRSD+} = \frac{\sum_{i=1}^{t}\sum_{j=1}^{r} Cells_{i,j} \cdot \frac{\sqrt{\sum_{k=1}^{m} \left(H_{i,j}[k] - M_i[k] \right)^2}}{cor\left(H_{i,j}, M_i \right)^2}}{\sum_{i=1}^{t}\sum_{j=1}^{r} Cells_{i,j}}. \quad (19)$$

In the above equations, $Cells_i^j$ is the total cell count in run j for time point i, and cor(x,y) represents the Pearson correlation coefficient between the experimental histogram, H_i^j, and modeled histogram, M_i. See also Figure 2.10.

2.4.8. Generating chimeric solutions from two phenotypes

To dissect the contributions of several components of complex phenotypes, we used two sets of parameters (i.e. wildtype and mutant) and generated a "chimeric" set of parameters with combinations of F_0, F_{1+} ($D\mu$, $D\sigma$), Tdivs ($E[Tdiv_0]$, $s.d.[Tdiv_0]$,$E[Tdiv_{1+}]$, $s.d.[Tdiv_{1+}]$), and Tdies ($E[Tdie_0]$, $s.d.[Tdie_0]$,$E[Tdie_{1+}]$, $s.d.[Tdie_{1+}]$), copied from either set. The generated "chimeric" phenotypes were visualized (see below) and qualitatively compared to visualizations from the two originating phenotypes. In the case of *NFκB1*$^{-/-}$ anti-IgM stimulated B cells, this analysis confirmed that misregulation of the late progressor fractions (F_{1+}) constituted the primary phenotype (Figure 2.12C).

2.4.9. Visualizing solution clusters

Solution clusters were defined as sets of maximum-likelihood parameter sensitivity ranges that are overlapping between all solutions in a cluster. To visualize these solutions, parameter sets were sampled uniformly from within the clustered maximum-likelihood parameter sensitivity ranges independently for each parameter. For parameter visualization, the sampled parameters were used to plot the four lognormal distribution probability density functions ($Tdiv_0$, $Tdie_0$, $Tdiv_{1+}$, $Tdie_{1+}$), normalizing by the maximum probability per distribution. The fraction of responding cells in each generation (Fs) are plotted using connected dots on a scale between 0 and 1 for each generation (x axis), with the larger dot representing the independent F_0 parameter (Figure 2.12). For population count visualization, the sampled parameter values were used to calculate cell count time series data by solving the fcyton model with the sampled parameters (Figure 2.12C and Figure 2.14). FlowMax provides options for plotting either the sampled solutions or the best-fit solutions found during model fitting. The best-fit cluster average solution is shown as an overlay for each experimental dataset (Figure 2.13).

2.4.10. Using FlowMax to phenotype CFSE time courses

We used a computational tool, which implements all of the steps for fitting experimental CFSE B cell datasets. A succinct tutorial is included in the supplementary text (Supplementary File 2.3). In brief, we used our computational tool to construct log-fluorescence CFSE histograms of viable B cells from raw CFSE data (see experimental methods below). For each log fluorescence histogram, the average fluorescence of undivided cells was selected manually based on previous time points. Then the cell fluorescence parameters were automatically determined for each time course subject to user constraints for the coefficient of variation, background autofluorescence, and die halving ratio, and shift of the undivided peak as well as an estimate of the maximum number of generations to be fitted to each time course (The default is set to eight [45]).The fitted cell fluorescence parameters were then used during the population dynamics fitting step to represent generational cell counts derived from the fcyton model. The population dynamics fitting step was repeated 1,000 times, poor results were removed from consideration, parameter sensitivity ranges were calculated and solutions were clustered to estimate solution redundancy. The resulting best-fit families of solutions (determined by average error in histogram area sampled from parameter sensitivity ranges) for each experimental condition were compared.

2.4.11. Experimental Methods

Primary splenocytes were isolated from 6-8 week old mice, naïve B cells purified using magnetic bead separation (Miltenyi Biotec), labeled with 4 μM 5(6)-Carboxyfluorescein diacetate, N-succinimidyl ester (CFSE) dye (Axxora) for 5 minutes at room temperature, and stimulated with 10 μg/mL LPS (Sigma) or 10 μg/mL goat anti-mouse IgM (Jackson Immunoresearch Inc.) B cells were grown in fresh media with 1%

penicillin streptomycin solution (Mediatech Inc.), 5 mM L-glutamine (Mediatech Inc.), 25 mM HEPES buffer (Mediatech Inc.), 10% FCS and 2 μL/500 mL BME (Fisher Scientific) at a concentration of $2.5x10^5$ cells/mL in 48 well plates at 37°C for a period of 6 days.Cells were removed from media, stained with 10 ng/mL propidium iodide, and measured using an Accuri C6 Flow Cytometer (Accuri Inc.) at 28, 40, 43, 54, 59.5, 67.5, 74.5, 89, and 145 hours post stimulation. CFSE histograms were constructed after software compensation for fluorescence spillover and manual gating on viable (PI-negative) B cells using the FlowMax software. All measurements were performed in duplicate (B cells from the same spleen were cultured in separate wells, two wells per time point to ensure that each time course represented a single population of cells subject to only experimental variability).

2.4.12. Description of CFSE time courses

A typical CFSE time course consists of a set of time points. Each time point consists of one or more experimental bulk CFSE fluorescence measurements (experimental runs/replicates). Each experimental run consists of a set of CFSE fluorescence measurements which are typically represented by 2D log-transformed (or log-fluorescence) histograms. We assume that the total number of cells per run is also known.

2.4.13. Fitting the cell fluorescence model

The simulated annealing approach [176] was used to arrive at the set of cell fluorescence parameters (CV, Ratio, Background, and Shift) that best describe a log-fluorescence histogram. Each simulated annealing optimization routine was initialized such that for time $t \in \{1, 2, \ldots, n\}$:

$$CV_t = \begin{cases} CV_{min} \; if \; t = 1 \\ CV_{t-1} \end{cases}, \tag{20}$$

$$Ratio_t = Ratio_{max}, \tag{21}$$

$$Background_t = Background_{max}, \tag{22}$$

$$Shift_t = 0, \tag{23}$$

$$CV_{min} = \begin{cases} CV_{min} \; if \; t = 1 \\ CV_{t-1} * (1 - 0.5^{t-1}) \end{cases}, \tag{24}$$

$$CV_{max} = \begin{cases} CV_{max} \; if \; t = 1 \\ CV_{t-1} * (1 + 0.5^{t-1}) \end{cases}. \tag{25}$$

where the subscripts “min” and “max” signify the given lower and upper limit for a parameter, respectively. We used the best-fit CV parameters from each time point to constrain the CV parameter range for the subsequent time point. This was useful for fitting later time points for which individual peaks were harder to discern without some prior knowledge of the approximate CV from previous time points.

In summary, if both early and late time points are available, FlowMax uses information from fitting the early time points to constrain the cell fluorescence parameters for later time points (described in the supplementary section “Fitting the cell fluorescence model”). In this way, if the CV or dye halving ratio “drifts” between time points, the early time points can be used to guide the fitting of these parameters for later time points. However, the position of the undivided population is one of the parameters supplied by the user for each histogram as it depends on the experimental conditions (cell staining conditions, cell type, dye catabolism, cytometer setup, etc.). Instead of trying to model how these factors affect the position of the undivided peak across time/generations (which is computationally intractable [98,99] and outside of the scope

of this study), we rely on the user to specify the approximate position of the undivided peak based on the location from previous time points. To help with this, we include a fourth “shift” term in the model to find the optimal peak placement.

A score-based annealing schedule was used during simulated annealing. Initial temperature was set to half of the fit score of the initial random parameter set. The minimum temperature was set to 1/1,000 of that value. Temperature was multiplied by 0.99 at the end of each iteration. In addition, if a better solution was found, the temperature was set to the minimum of the initial temperature or the current temperature multiplied by 1.1. This “heating” was used to discourage local trapping of the solution. In practice, this artificial heating helped in cases where solutions were stuck for many iterations in a high score parameter space but proceeded toward a better solution toward the end of the optimization, in which case, the sudden frequent improvement in the solution “reheated” the system and allowed for optimization to finish. While this approach resulted in satisfactory optimization, other optimization schemes of equal or better efficiency may be possible.

A scoring function which penalized both the squared distance as well as the difference in correlation between the fluorescence histograms for a particular time point, t, and experimental run, r

$$Score_{t,r} = \sqrt{\frac{\sum_{i=1}^{m}\left(n\cdot\left(H_{normal}[i]-M[i]\right)\right)^2}{m}} + n\cdot(1-cor\left(H_{normal},M\right)) \quad (26)$$

was used where H_{normal} is the histogram of d observed fluorescence values, M is the model histogram of fluorescence values, n is the number of cells measured experimentally, and cor(x,y) represents the Pearson correlation coefficient between the histograms of x and y. The average run score was used as the time point score, and the

average time point score was used as the overall objective function during fitting. The scoring function was manually optimized for experimental data fitting: correlation was included to help guide initial optimization toward a suitable histogram shape.

While the choice of algorithm for fitting the cell-fluorescence model did not qualitatively affect the conclusions, we desired a fitting algorithm which would allow us to quickly find appropriate cell fluorescence model parameters (i.e. peak CV, ratio between peaks, autofluorescence, and offset from user-specified μ_0), while taking into account solutions from previous time points. We also wanted to exclude solutions that were outside of user-specified ranges. In addition, we wanted a fitting approach which dealt with solution trapping in local minima, as is often the case with noisy experimental data. We are not aware of a conventional method for achieving this efficiently. Therefore, we selected the stochastic simulated annealing approach for fitting the model parameters, while explicitly solving for peak weights during each step (using a conventional non-linear regression approach described above), and allowing for information from earlier time points to contribute to the fit. Our evaluation of the fitting methodology suggests good agreement between fitted and generated data (see Figure 2.2); however other methods for fitting may also be appropriate. In addition, our methodology can be adapted to incorporate other models for cell fluorescence and/or fitting approaches if desired by changing the cell fluorescence computational module.

2.4.14. Peak weight calculations during cell fluorescence model fitting

The problem of solving for the optimal model weights given the cell fluorescence parameters can be formulated as a nonlinear least squares regression problem. Given a log-fluorescence histogram with fluorescence, x, and bin size Δx:

$$H(x) = \Pr(x < X_i \le x + \Delta x \mid X_i \in Data) \tag{27}$$

Defining the cellular fluorescence model solution, $F(x)$, as a weighted sum of Gaussian distributions, $G_g(x)$:

$$F(x) = \sum_{g=1}^{G} w_g G_g(x) \ , \tag{28}$$

where w represents a weight multiplier and $G_g = G(\mu_g, \sigma_g)$. Then the sum of squared errors is:

$$E = \sum_{i=1}^{I} \left(H(i) - \int_{i-\Delta x}^{i} F(x)\,dx \right)^2 . \tag{29}$$

To solve for the optimal set of weights, minimize E. Rewriting E:

$$E = \sum_{i=1}^{I} \left(H(i) - \int_{i-\Delta x}^{i} \sum_{g=1}^{G} w_g G_g(x)\ dx \right)^2 \tag{30}$$

$$= \sum_{i=1}^{I} \left(\sum_{g=1}^{G} w_g \int_{i-\Delta x}^{i} G_g(x)\,dx - H(i) \right)^2 \tag{31}$$

$$= \sum_{i=1}^{I} \left(\sum_{g=1}^{G} w_g J_{ig} - H(i) \right)^2 . \tag{32}$$

To solve the minimization problem, solve:

$$0 = \frac{\partial E}{\partial w_b} \tag{33}$$

where:

$$\frac{\partial w_g}{\partial w_b} = \delta_{gb}, \delta_{gb} = \begin{cases} 1, g = b \\ 0, g \neq b \end{cases}, \tag{34}$$

$$0 = \sum_{i=1}^{I} 2\left(\sum_{g=1}^{G} w_g J_{ig} - H(i) \right)\left(\sum_{g=1}^{G} \delta_{gb} J_{ig} \right), \tag{35}$$

$$0 = 2\sum_{i=1}^{I} \left(\sum_{g=1}^{G} w_g J_{ig} - H(i) \right)\left(J_{ib} \right), \tag{36}$$

$$0 = \sum_{g=1}^{G} w_g \left(\sum_{i=1}^{I} J_{ig} J_{ib} \right) - \sum_{i=1}^{I} H(i) J_{ib}, \tag{37}$$

$$\sum_{g=1}^{G} \left(\sum_{i=1}^{I} J_{ig} J_{ib} \right) w_g = \sum_{i=1}^{I} H(i) J_{ib}, \tag{38}$$

$$M\vec{w} = \vec{c}. \tag{39}$$

M is a *G x G* matrix and both $\vec{c}$ and $\vec{w}$ are vectors of size G, where G is the number of generations being modeled. To calculate each element of M, and $\vec{c}$:

$$M_{ba} = \sum_{i=1}^{I} \int_{i-\Delta x}^{i} G_a(x)\,dx \int_{i-\Delta x}^{i} G_b(x)\,dx, \tag{40}$$

$$c_j = \sum_{i=1}^{I} H(i) * \int_{i-\Delta x}^{i} G_j(x)\,dx, \tag{41}$$

where G_x is the Gaussian distribution $G_x(_x,_x)$ representing fluorescence distributions for cells in division class x from equations (1) and (2). Solving for the optimal weights, $\vec{w}$, associated with each Gaussian distribution:

$$\vec{w} = M^{-1}\vec{c}, \tag{42}$$

we further ensure that the weights are non-negative and sum to 1:

$$w_g > 0 \forall\, w_g \in \vec{w}, \tag{43}$$

$$\sum_{g=1}^{G} w_g = 1. \tag{44}$$

By solving for the weights at the end of each iteration of fluorescence model optimization (see above), excellent fluorescence model parameters were found relatively quickly. Furthermore, solving explicitly for the peak weights subjected only the cell fluorescence model parameters to optimization, minimizing fitting bias that could arise due to errors in weight optimization.

2.4.15. Fitting the fcyton model to cell counts derived from fluorescence histograms

In order to fit the fcyton cell population model parameters (N, F_0, $D\mu$, $D\sigma$, $Tdiv_0\mu$, $Tdiv_0\sigma$, $Tdie_0\mu$, $Tdie_0\sigma$, $Tdiv_{1+}\mu$, $Tdiv_{1+}\sigma$, $Tdie_{1+}\mu$, $Tdie_{1+}\sigma$) to sets of division specific cell counts, a simulated annealing [176] approach was used. Specifically, fitting started with 4,000 iterations of randomized guess and check trials to establish a coarse approximation of the parameters. Then the best parameter set out of the 4,000 randomly selected parameter sets was used as the starting point for simulated annealing. Prior to the first round of optimization by simulated annealing, the temperature, T, was set to the current best-fit score, and T_{min}, or the stopping temperature, was initialized to 1/100,000 of T. Each simulated annealing iteration consisted of three steps: the current parameters were modified slightly (Gaussian sampling with sigma = 1% of the current value), the fit score was calculated for the new parameter set, and the new parameter set was adopted with probability p such that:

$$p = \begin{cases} 1, if\ the\ new\ score\ was\ lower \\ e^{-\frac{diff \cdot k}{T}}, otherwise \end{cases}. \quad (45)$$

where *diff* is the new score minus the previous score and k is a score scaling factor.

Similarly to the optimization process used to fit the fluorescence model, if the new score was an improvement over the current global best fit score, the temperature

was set to the minimum of the current temperature*1.1 or the initial temperature. This artificial “heating” was implemented to ensure that all improving parameter sets find a local minimum after leaving a parameter space of relatively poor fit scores. The annealing factor was 0.9995.

Two objective functions were used during this optimization process: a simple objective function consisting of the square deviation between the model and generated counts, and a more complex optimized objective function that takes into account multiple difference measures:

$$Obj_{SD} = \sum_{t=1}^{n}\sum_{i=1}^{G}\left(Count_{data}[t] * Prop_{data}[i,t] - Count_{model}[t] * Prop_{model}[i,t]\right)^2 \quad (46)$$

$$Obj_{OPT} = \left\{ \sum_{t=1}^{n} \left[\begin{array}{l} 2 * \dfrac{cor\left(Prop_{data}[t], Prop_{model}[t]\right)}{n} + \\ \left(\dfrac{Count_{data}[t]}{Count_{data}[t] + Count_{model}[t]} - \dfrac{Count_{model}[t]}{Count_{data}[t] + Count_{model}[t]} \right)^2 + \\ 5 * \sum_{i=1}^{G} \dfrac{\left(Prop_{data}[i,t] - Prop_{model}[i,t]\right)^2}{n} \end{array} \right] + \right. \quad (47)$$
$$\left. 2 * cor(Count_{data}, Count_{model}) \right\}$$

where *Count*[t] represents the total cell count at time point t, and *Prop*[i,t] is the proportion of cells at time point t in generation i. The cor(x,y) function represents the Pearson correlation coefficient between the functions x and y. In the optimized scoring function, G is defined as the maximum number of division classes at time point t such that $Count_{data}[G+1] = 0$ and G > 6. Therefore, all cells in division classes > 6 are treated as one population in order to reduce the penalty for cells assigned to division classes 7 and higher. This was implemented due to an increased difficulty in discriminating CFSE peaks after 6 divisions experimentally. This complex objective function was developed in a step-by-step manner, starting with a basic sum of squared differences objective

function (46), followed by the addition of correlations, and the use of *ad* hoc weights for each part of the scoring function. The annealing schedule was optimized to allow for efficient optimization of both fit scores.

After an initial round of simulated annealing, a subsequent fast round of localized simulated annealing centered on the optimal solution was carried out. Analogously to the first round, the temperature was set equal to the fit score for the current optimal solution and annealing continued until the temperature dropped below 1/1,000 of this temperature. At the beginning of each iteration a new set of parameters was generated randomly by modifying the best parameter set (Gaussian sampling with sigma = 0.1% of the current value). This limited the search to the local parameter space around the best-fit solution. In practice this often only yielded minor improvements to the fit, but on rare occasions, allowed a very poor solution to be improved significantly before it was used in the post-processing steps following model parameterization.

2.4.16. Fitting the fcyton models to fluorescence histograms directly

Analogously to the fitting approach used to fit the fcyton models to generational cell counts, a stochastic method was used to fit the models to experimental fluorescence histograms directly. The fluorescence model was used to adapt the derived model cell counts to log-fluorescence histograms. Specifically, for each set of predicted division-specific cell counts a fluorescence histogram was generated using the previously fitted cell fluorescence parameters and generational cell counts as weights (see Figure 2.2A). This facilitated the use of a relatively simple objective function for calculating the difference between the model fluorescence histograms and the experimental fluorescence histograms. A manually optimized objective function which accounted for the difference between the fluorescence histograms, the correlation

between the fluorescence histograms, and the proportion of the total cells represented in each histogram was used:

$$Obj_{MRSD+} = \frac{\sum_{i=1}^{t}\sum_{j=1}^{r} Cells_{i,j} \cdot \frac{\sqrt{\sum_{k=1}^{m}\left(H_{i,j}[k]-M_i[k]\right)^2}}{cor\left(H_{i,j},M_i\right)^2}}{\sum_{i=1}^{t}\sum_{j=1}^{r} Cells_{i,j}}. \quad (48)$$

where $Cells_i^j$ is the total cell count in run j for time point i, and cor(x,y) represents the Pearson correlation coefficient between the experimental histogram, H_i^j, and modeled histogram, M_i. We also tested if simpler scoring functions were sufficient for fitting generated datasets. Specifically we tried a simple mean absolute deviation objective function (MAD):

$$Obj_{MAD} = \frac{\sum_{i=1}^{t}\sum_{j=1}^{r} Cells_{i,j} \cdot \sum_{k=1}^{m}\left|H_{i,j}[k]-M_i[k]\right|}{\sum_{i=1}^{t}\sum_{j=1}^{r} Cells_{i,j}}, \quad (49)$$

as well as a mean root square deviation objective function:

$$Obj_{MRSD} = \frac{\sum_{i=1}^{t}\sum_{j=1}^{r} Cells_{i,j} \cdot \sqrt{\sum_{k=1}^{m}\left(H_{i,j}[k]-M_i[k]\right)^2}}{\sum_{i=1}^{t}\sum_{j=1}^{r} Cells_{i,j}}, \quad (50)$$

While even the simplest scoring function we tried produced similar results, the more complex objective function produced lower average errors in generational counts and outperformed the simplest (MAD) objective function when fitting the fcyton N parameter (see Figure 2.9). Therefore, we decided that the more complex objective function (MRSD+) was justified.

2.5. Acknowledgements

We thank N. V. Shokhirev, M. Behar, P. Loriaux, and J. Davis-Turak, for insightful discussions and critical reading of the manuscript. J. Almaden and B. Alves provided experimental training.

Chapter 2, in full, is a reprint of the material as it appears in PLoS One 2013. Maxim N. Shokhirev and Alexander Hoffmann. Public Library of Science, 2013. Alexander Hoffmann is the corresponding author. The dissertation author was the primary investigator and author of this paper.

Chapter 3

Observing cell-to-cell variability in fate decisions and timing

B lymphocyte population dynamics dictate the veracity of the immune response and vaccine effectiveness. Yet individual cells appear to undergo division or death stochastically possibly as a result of a race of the two processes running in parallel. To characterize the behaviors of hundreds of cells under various conditions, we developed a time-lapse microscopy experimental and semi-automated tracking pipeline which enabled the accurate measurement of cell size trajectories and lineages across six days and eight generations. Strikingly, we found that cells decide early whether to enter a rapid growth phase during which they are protected from death. This was verified using three different approaches: direct measurement of cell death in growing cells within a 24 h period, using the observed time to growth, time to division, and time to death distributions to predict the expect fraction of dying cells that grow, and by using two different population models (one assuming a race, and another that assumes commitment to decision) to fit CFSE time courses. All three approaches showed that a decision is more congruent with the observed behavior, while a molecular race between division and death is not.

3.1. Introduction

B cells are immune cells that are central to both the innate and adaptive immune response. When B cells encounter pathogens, a specific class of TOL-like receptors (TLRs) recognizes specific pathogen associated molecular patterns (PAMPS) such as unmethylated bacterial DNA (CpG), and initiates a dynamic cellular response [1]. Individual B cells interpret these signals by undergoing 1-6 rounds of cell cycling, followed by cell cycle exit, and death by programmed cell death [21]. Individual cells make up the populations response, which characteristically lasts several days to a week and produces a dramatic increase in the number of activated B cells for several days, followed by a return to starting cell counts [43]. Importantly, while the population response is robust, the behavior of individual cells is seemingly stochastic since only a fraction of cells respond in each generation and because the timing of division and death is highly variable between these genetically identical synchronized cells. In fact, the timing of division and death is well-modeled by long-tailed distributions (e.g. log-normal) as a function of cell age, resulting in a distribution of cells across many generations after only a few days of stimulation [21,44]. Furthermore, progenitor cells (generation 0) typically take much longer to divide or die, while dividing cells (generation 1+) divide again within six to twelve hours [21,45]. Understanding this stochastic multi-scale process is of paramount importance as it is essential for vaccine design and dysregulated in B cell lymphomas and can lead to autoimmune diseases, and immune deficiency.

Previous studies offer evidence that the inherent variability in timing of the apoptosis is caused primarily by cell-to-cell protein abundance [24] and presumably variability in cell-cycle regulators generate cell-to-cell variability in cell-cycle duration, however, it is still unclear if variability in timing of competing division/death processes

determine fate. There are competing theories for how fate (i.e. whether the cell divides or dies) is determined. Recent studies support a molecular race hypothesis, which posits that cell-cycle and apoptosis processes are proceeding concurrently within cells, and that fate is determined by the faster of these mutually exclusive outcomes. Specifically, an age-structured population model, the cyton model, which incorporates competition between division and death fates can reproduce the major population features and produces excellent fits to experimental datasets[44]. Furthermore, a recent study [46] demonstrated that a probabilistic model that assumes correlation of fate timing between siblings and mutual censorship between competing processes (e.g. division and death) can reproduce the correlations between non-concordant fates as well as the observed censored distributions for the time to divide, time to isotype switch, and time to plasmablast differentiation (although the best-fit censored model death time distributions were typically earlier than the observed death distributions). On the other hand, there is also evidence that cells decide their fate early and are protected from the alternate outcome. Single-cell time-lapse videos of stimulated B cells revealed that cells that died did not grow, while cells grew prior to dividing in all except the last and pen-ultimate generations, indicative of a lack of fate competition [21]. Furthermore, the authors found that the size of the progenitor cells was predictive of the number of divisions suggesting that fate is decided in the initial generation. As a result, we described the fcyton model, which unlike the cyton model, commits responding cells to division, and showed that cell commitment to a specific fate nevertheless resulted in excellent model fits for all experimental datasets [47]. Providing further support for a molecular decision, levels of cell cycle inhibitor p21, which directly inhibits CDK2 activity was recently shown to be sufficient for promoting cell-cycle reentry in cell lines and human primary cells[48].

Knowing whether cells make decisions will determine how we model cell fate determination on the molecular level and in turn informs experimental and drug design.

3.2. Results

3.2.1. Time-lapse microscopy reveals generation specific single-cell behavior

First, in order to determine the key cellular behaviors of the response, we tracked 1,295 live primary B cells using a time-lapse microscopy pipeline (Figure 3.1A). Since manually tracking hundreds of individual cells is impractical, while automated tracking suffers from rapid error accumulation, we developed a semi-automated computational tool which leverages human input to minimize errors, while ensuring tractability. Analysis of wildtype B cells growing under high CpG stimulation, confirmed the expected population expansion followed by a contraction period during which most cells died by programmed cell death (Figure 3.1B). After cells that died from mechanical death were filtered out (Figure 3.2), we see that approximately 38% of the progenitor cells divided while subsequent generations showed a steady decrease in the fraction of cells dividing in each generation with approximately 85% cells dividing in generation 1 but just 9% of cells dividing in generation 6 (Figure 3.1C). To quantify cell response, we classified cell size trajectories into two categories: a) cells that grew by at least 350 μM^3 or reached a final size of at least 800 μM^3 by the time of their division or death, dubbed “growers” and b) cells that did not which we labeled as “non-growers” (Figure 3.1D). Averaging the growth trajectories of “growers” (Figure 3.1E) and “non-growers” (Figure 3.1F) in each generation normalized by percent cell lifespan revealed that progenitors (generation 0) that grew exhibited a growth delay followed by rapid growth to ~ 5 fold their starting size, while “non-growers” by did not exhibit the delay phase, and started growing immediately

after mitosis. Furthermore, “grower” cells grew to the same size on average in all but perhaps the last generation. While “non-growers” by definition did not exhibit significant growth, they nevertheless typically exhibited some growth on average, especially in generation 1.

Figure 3.1. Time-lapse microscopy reveals two distinct generation-dependent growth patterns for B cells. A) Overview of the time-lapse microscopy experimental and analysis pipeline. B cells were purified from mouse spleen, stimulated with TLR9 agonist CpG, imaged on an environmentally controlled microscope for six days and tracked using a semi-automated tracking tool to quantify generation-dependent cell statistics. **B)** Generational cell counts relative to initial count. **C)** The observed fraction of cells dividing or dying in each generation. Error bars = 1/n **D)** Growth trajectories of generation 0 cells that grew by more than 350 μM^3 or ended with a volume of at least 800 μM^3 (blue) and trajectories of generation 0 cells that did not end with a large volume (black). **E)** Cell size trajectories as a function of % lifetime for growers in each generation (colors as in B). **F)** Cell size trajectories as a function of % lifetime for non-growers in each generation (colors as in B).

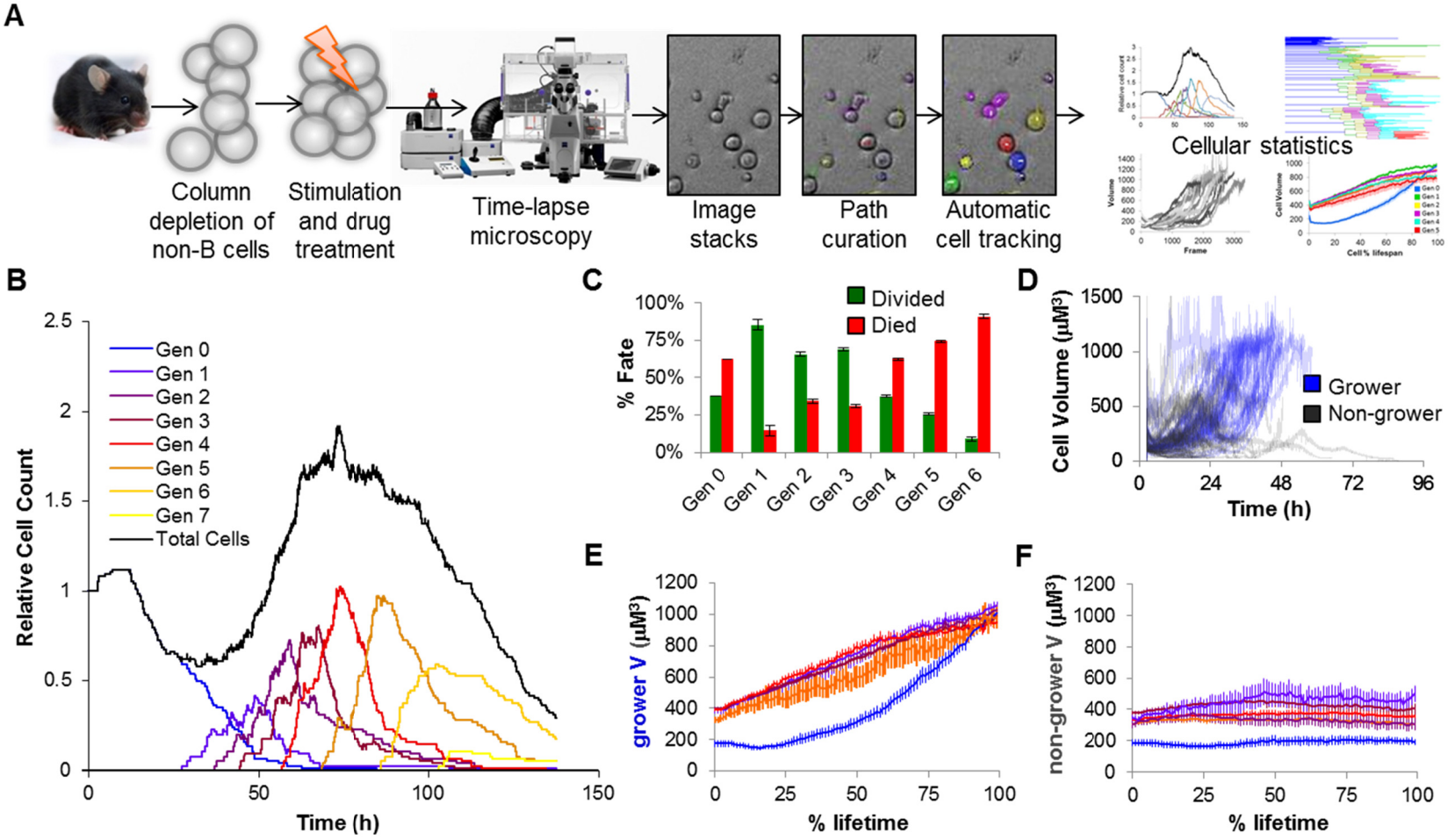
A
Column depletion of non-B cells
Stimulation and drug treatment
Time-lapse microscopy
Image stacks
Path curation
Automatic cell tracking
Cellular statistics
B
Relative Cell Count
Time (h)
Gen 0
Gen 1
Gen 2
Gen 3
Gen 4
Gen 5
Gen 6
Gen 7
Total Cells
C
% Fate
Divided
Died
D
Cell Volume (µM³)
Grower
Non-grower
Time (h)
E
grower V (µM³)
% lifetime
F
non-grower V (µM³)
% lifetime

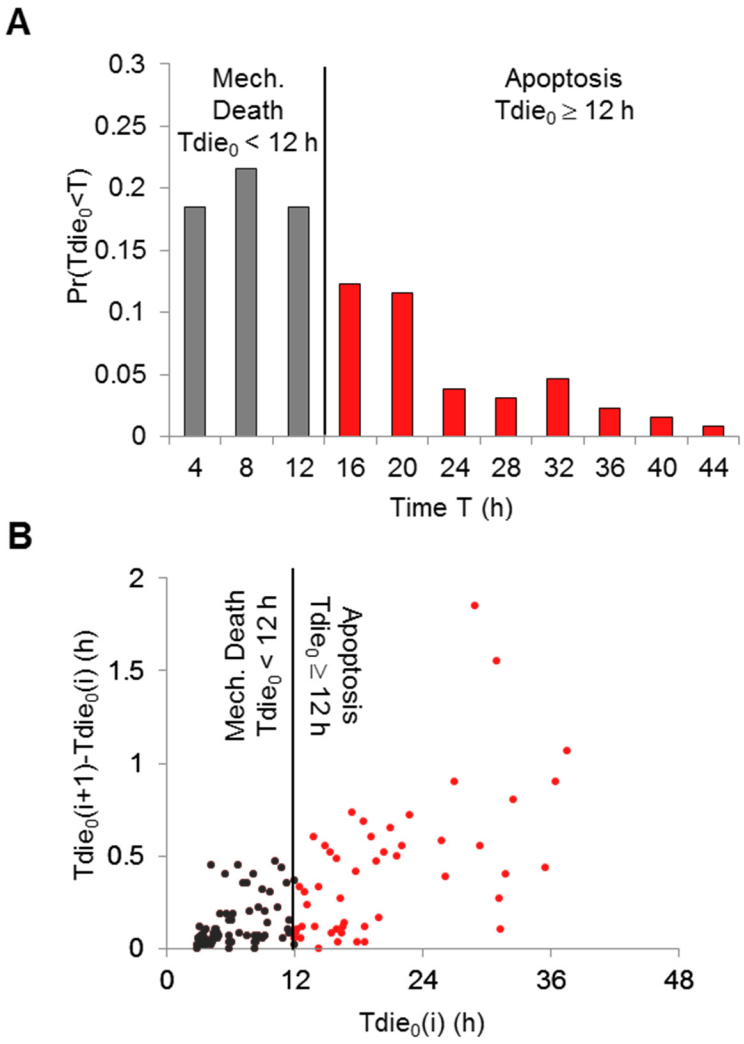

Figure 3.2. The minimum biologically-relevant death time in progenitor cells is distinct. To filter out cells that died due to artificial manipulation during preparation (mechanical death), dying generation 0 cells were binned according to their death time and biologically-relevant apoptosis was defined as death that occurred after the first wave of early death (**A**). Similarly, when ordered by death time, cells with death times higher than 12 h typically show increased separation from the previous death time (**B**). Cells that were dead at the start of time-lapse imaging were not included in this analysis.

3.2.2. B cell fate is decided: growing B cells are protected from death

To further establish the fundamental cellular mechanisms, we next tested if the cell-cycle and apoptosis were indeed parallel racing processes (Figure 3.3A), or if growth was predictive of fate (Figure 3.3B). Intuitively, if cells “decide” their fate early, one would expect most growing cells to divide, and vise-versa. We tallied the fraction of “growers” that divided and died within the first 36 (generation 0) or 24 hours (generations 1+) for each generation (Figure 3.3C) as well as the fraction of “non-growers” that divided and died within the same periods for each generation (Figure 3.3D). Our results indicate that almost all “growers” divided in the first four generations, followed by loss of decision robustness in the last two generations, indicative of an early decision that predisposed B cells to a particular fate (Figure 3.3B). Interestingly, except in the first generation, there was a significant fraction of “non-growers” that divided, due to primarily poor growth prior to the last division (Figure 3.4). To further test this important distinction, we used the observed time to decide (start of growth), time to division, and time to death of progenitor cells, and calculated the expected lower bound probability that a dying cell would have grown, given the molecular race (Figure 3.3A), and decision (Figure 3.3B) models (Figure 3.3E-F). Our analysis revealed that even under relatively relaxed assumptions, the data are inconsistent with both processes occurring simultaneously in cells (i.e. race). On the other hand, a decision which commits cells to either fate is more appropriate as grown dead cells are rare. In other words, because time to death is typically earlier than time to division, and because time to decision (i.e. growth start) is typically much earlier than division or death our analysis predicts most cells to start growing prior to death if the two processes were indeed running in parallel within B cells.

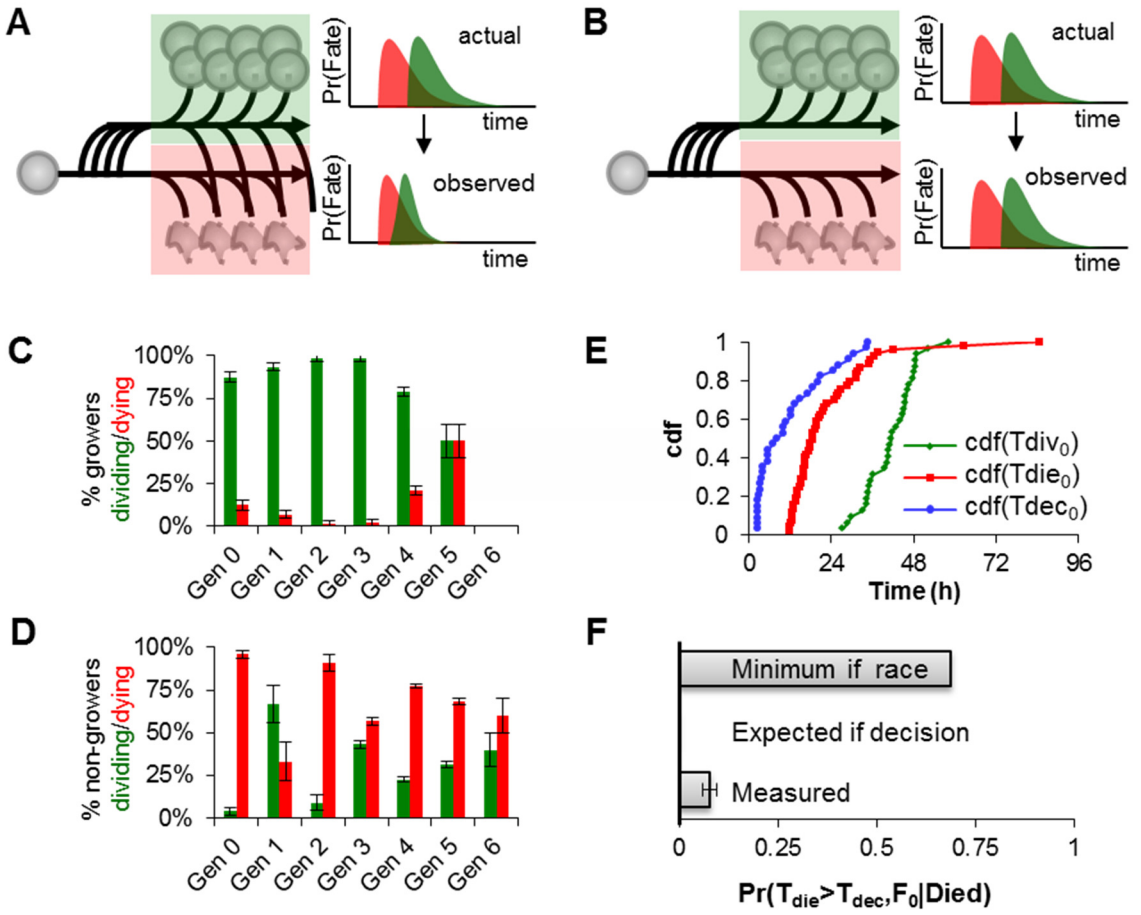

Figure 3.3. B cells decide to divide or die and are protected from the alternate fate **A)** Flowchart depicting activated cell fate determined by a race between division (green) and death (red) as well as hypothetical division and death time distributions before and after mutual censorship **B)** Flowchart showing an early commitment to one fate, and the independent division (green) and death (red) time distributions. **C-F)** Analysis of response (growth), division, and death statistics for WT B cells. Error bars = 1/n. **C)** Measured generational probabilities that a growing (**C**) or non-growing (**D**) cell divided (green) or died (red) within a 24 hour period (12-36 h for gen 0). **E)** Measured cumulative distributions for the time to start growing (blue), time to divide (green), and time to die (red) of generation 0 cells. Distributions were used to calculate the lower bound expected probability that a dying cell had started to grow **(F)** assuming a molecular race between fates or an early commitment to one fate, as compared to the measured probability. For further details please see supplementary materials.

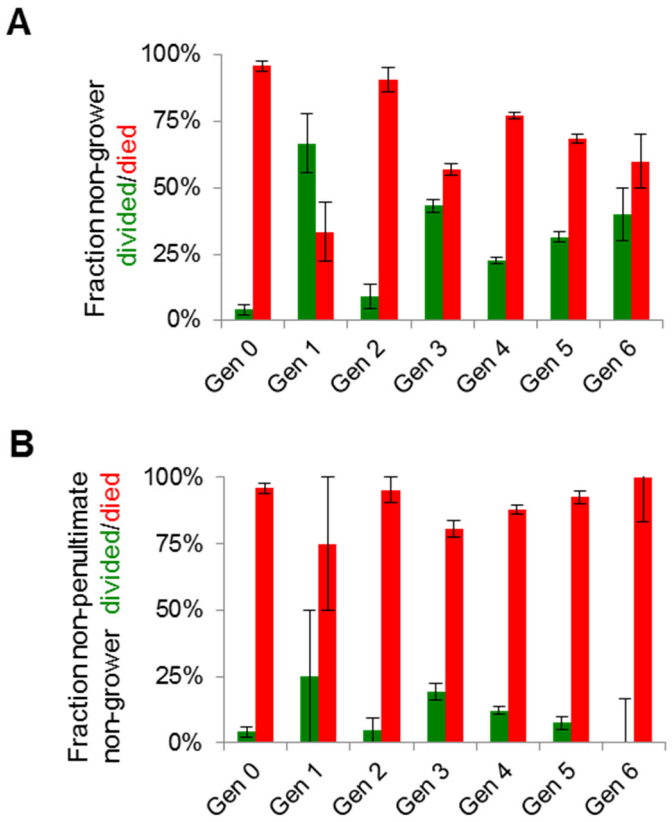

Figure 3.4. Cells typically grow less prior to the last division. Wildtype purified naïve B cells were stimulated with 250 nM CpG and tracked by time lapse microscopy. The fraction of "non-growing" cells that divided (**A green**) or died (**A red**) are shown for each generation. Error bars = 1/n. The quantification was repeated with penultimate dividing cells removed from consideration (**B**).

3.2.3. A molecular race cannot recapitulate progenitor death timing

Alternatively, if the CFSE deconvolution methodology developed in chapter 2 (Figure 3.5A) can be used to test the decision and molecular race hypothesis. To do this, we obtained CFSE fluorescence histograms for populations of B cells from the same mouse by flow cytometry. FlowMax deconvolution of the datasets into the maximum-likelihood cyton (Figure 3.5B) model and fcyton model (Figure 3.5C) parameters allowed us to test which hypothesis best agrees with the cellular parameters observed by time-lapse microscopy (Figure 3.5D), as the cyton model assumes that responding cells may die, while the fcyton model does not. While both models accurately fit the CFSE time course (Figure 3.5E), the molecular race model requires a much later $Tdie_0$ (Figure 3.5F), while the fcyton model, which assumes independence between fates, allows for a much earlier $Tdie_0$ concordant with the experimental microscopy dataset. Interestingly, both models were able to capture the experimentally observed fraction of dividing cells in each generation (Fs), but largely failed to predict the relatively late division time experienced by generation 0, and 1+ cells (Figure 3.5D green and blue distributions).

Figure 3.5. **FlowMax deconvolution of WT 250 nM CpG stimulated CFSE time series.** CFSE-stained purified murine B cells were stimulated with 250 nM CpG, assayed by flow cytometry and a computational tool, FlowMax, was applied to determine non-redundant sets of maximum-likelihood population model parameters (**A**).To test if a molecular race or a decision are more appropriate, the cyton model, which assumes a race between division and death, (**B**) and fcyton decision-based model (**C**) were used as part of the FlowMax phenotyping. Maximum-likelihood parameter sets obtained from fitting each model to the experimental CFSE time courses were sampled using a Monte-Carlo approach to expose the fraction of responding cells in each generation (Fs), as well as division and death time distributions for undivided ($Tdiv_0$,$Tdie_0$) and dividing cells ($Tdiv_{1+}$,$Tdie_{1+}$) expected to be observed after any potential censorship and compared to the actual cellular distributions measured by time-lapse microscopy (**D**). The best-fit modeled CFSE histograms from the best-fit cluster of cyton (**E purple**) or fcyton (**E blue**) model parameters overlaid on experimental CFSE histograms collected in duplicate across six days at the indicated time points.

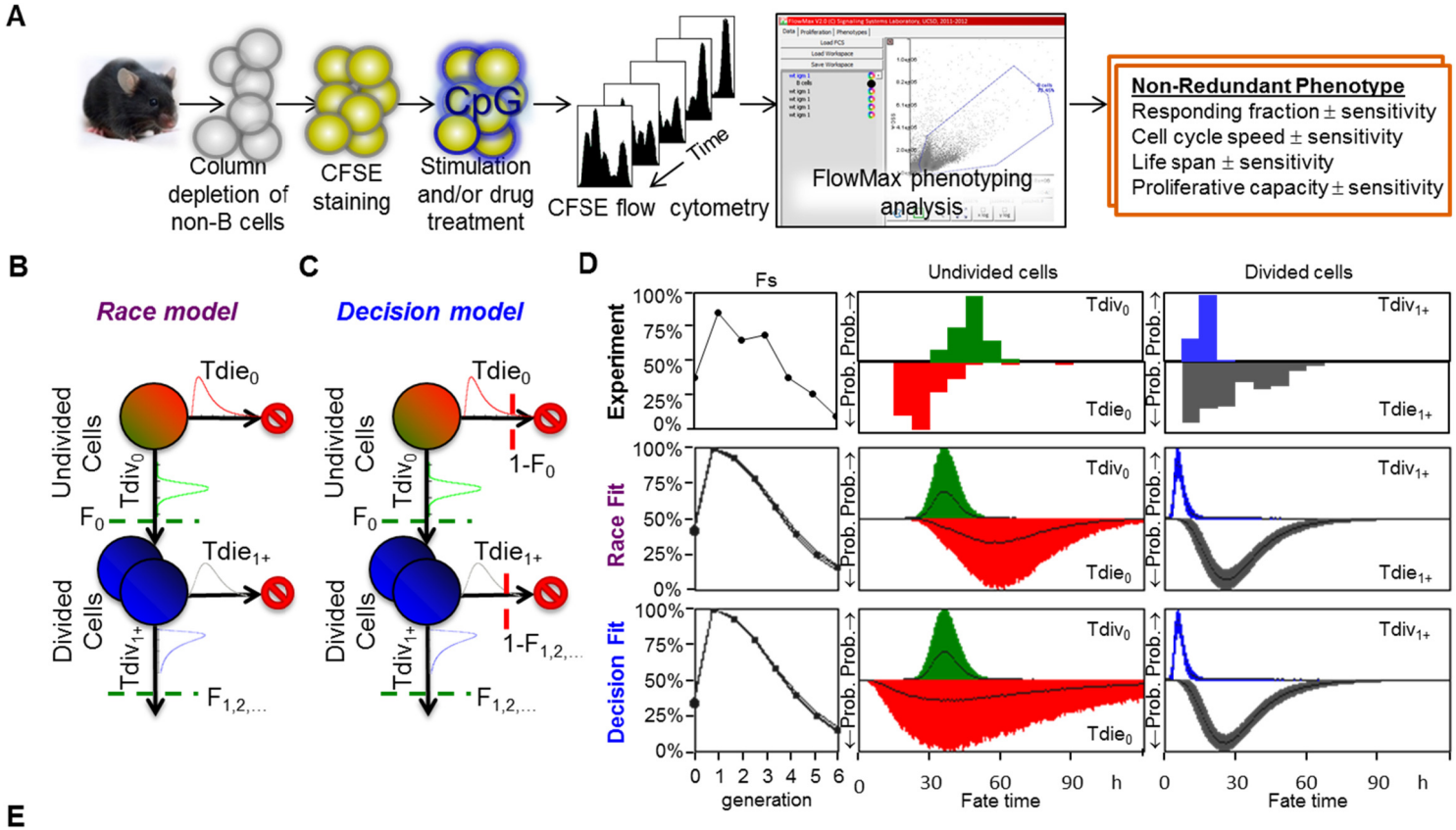
A
Column depletion of non-B cells
CFSE staining
CpG
Stimulation and/or drug treatment
Time
CFSE flow cytometry
FlowMax phenotyping analysis
Non-Redundant Phenotype
Responding fraction ± sensitivity
Cell cycle speed ± sensitivity
Life span ± sensitivity
Proliferative capacity ± sensitivity
B
Race model
Undivided Cells
Tdie0
Tdiv0
F0
Tdie1+
Divided Cells
Tdiv1+
F1,2,...
C
Decision model
1-F0
1-F1,2,...
D
Fs
Undivided cells
Divided cells
Experiment
Race Fit
Decision Fit
Prob.→
100%
75%
50%
25%
0%
0 1 2 3 4 5 6
generation
0 30 60 90 h
Fate time
E
Race Fit
Decision Fit

While our results suggest that cell fate is determined early, variability in the decision and fate timing is consistent with extrinsic cell-to-cell protein heterogeneity. To check this, we measured the correlation in the timing of the decision process (i.e. time to growth), the time to division, and the time to death in between sister and cousin cells (Figure 3.6). The timing of the decision process, interdivision time, and to a smaller extent lifespan were significantly correlated between sister cells: Pr(ΔTdecide≤ 4 h)=0.90, R^2=0.74, and R^2=0.39, respectively. Furthermore, the correlations decreased with a subsequent division (i.e. between cousins): Pr(ΔTdecide≤ 4 h)=0.77, R^2=0.44, and R^2=0.38, respectively, consistent with mixing times on the order of hours to days, ruling out genetic and epigenetic sources of cell-to-cell variability [Sorger 2011, 2009].

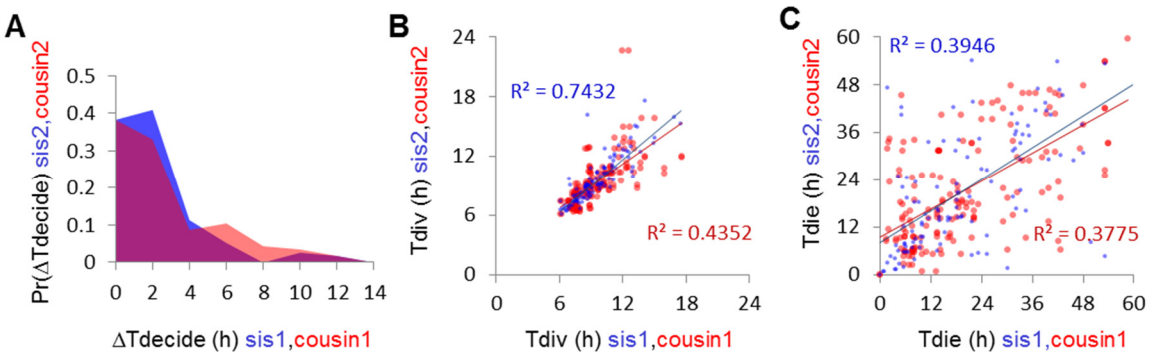

Figure 3.6. **The decision, division, and death times are correlated between siblings and cousins.** B cell lineages from WT 250 nM CpG time-lapse microscopy video were determined by semi-automated tracking. Correlations in timing to the start of growth, division, or death of sister cells (blue) and cousins (red) were calculated. Histogram of the differences between the times to decide to start growing (**A**) is shown. Division (**B**) and death (**C**) times are plotted between sister and cousin cells across all generations. Colored lines represent the linear fit through the origin with r-squared values for sisters (top) and cousins (bottom) as indicated.

3.3. Discussion

Key to parameterizing a multi-scale response was the development of a B cell live cell microscopy experimental and computational tracking pipeline, which we used to obtain accurate cell-size trajectories and lineages for hundreds of cells across a six day

period (Figure 3.1). Tracking wildtype B cells revealed several key properties of the response. B cells undergo 1-7 divisions, increasing total cell counts several fold and then most cells die by apoptosis (Figure 3.1B-C).There is a noticeable but variable delay in growth initiation prior to the first division, while generation 1+ cells start growing immediately (Figure 3.1D). This is consistent with a model in which activated generation 0 cells must prepare for several rounds of rapid divisions by simultaneously deactivating quiescence [21,177] and activating the appropriate growth pathways such as Myc and mTOR [66,178]. Tracking cell size trajectories and their eventual fate allowed us to confirm that B cells that grow are protected from death, suggesting that B cells have underlying molecular mechanisms for upregulating both survival and the cell-cycle (Figure 3.3). Furthermore, even in the absence of cell growth trajectories, a mathematical model which assumed a race between division and death [44] could not account for the typically early death we see with microscopy experiments (Figure 3.5), especially considering that we filter out death that occurs within the first 12 h caused by the experimental process (Figure 3.2) We were also able to confirm that both division and death are correlated between sibling cells (Figure 3.6), which is consistent with differences in protein turnover processes [24,25] resulting in distributions of single-cell proteomes within a population. Taken together, these data suggest an upstream decision to divide or die, while the variability in timing is caused by cell-to-cell variability in protein turnover (protein remixing).

3.4. Methods

A video showing the tracking of wildtype B cells, WT250nM.mpg can be found in the supplementary files along with FAST.jar, the tracker code and executable used to perform semi-automated tracking.

3.4.1. B cell purification and incubation

Primary splenocytes were isolated from 6-8 week old mice, naïve B cells purified using magnetic bead separation (Miltenyi Biotec), and stimulated with 250 ng/mL, or 10 ng/mL CpG ODN 1668 (Invivogen). mTORc1 inhibition was achieved by 1 hr pretreatment of 1 ng/mL Rapamycin (Sigma) prior to addition of stimulus. B cells were grown in fresh media with 1% penicillin streptomycin solution (Mediatech Inc.), 5 mM L-glutamine (Mediatech Inc.), 25 mM HEPES buffer (Mediatech Inc.), 10% FCS and 55 uM 2-ME (Fisher Scientific) at a concentration of $5x10^4$ cells/mL in 48 well plates, or 1536 flat-bottom tissue-culture plates at 37^{o}C for a period of 1-6 days.

3.4.2. CFSE flow cytometry and FlowMax analysis

Cells were removed from media, stained with 10 ng/mL propidium iodide, and measured using an Accuri C6 Flow Cytometer (Accuri Inc.) over a six day time course. CFSE histograms were constructed after software compensation for fluorescence spillover and manual gating on viable (PI-negative) B cells using FlowMax software. All measurements were performed in duplicate (B cells from the same spleen were cultured in separate wells, two wells per time point to ensure that each time course represented a single population of cells subject to only experimental variability). The FlowMax computational tool [47] was used to construct 1D log-transformed CFSE histograms of viable cells. After specifying the fluorescence of the undivided peak manually for each

time point, maximum-likelihood fcyton model parameter ranges were determined by filtering, and clustering 1000 best-fit solutions and their corresponding sensitivity ranges. The top solution cluster was plotted by randomly sampling parameters from within the maximum-likelihood parameter ranges. To account for potential censorship of the fraction of dividing cells or division and death time distributions when both division and death processes were active simultaneously (i.e. cyton model), Monte-Carlo sampling of cell populations was used to approximate population model parameters directly.

3.4.3. Time-lapse microscopy

Purified naïve B cells were grown in 1536 flat-bottom tissue-culture treated microwells (Greiner Bio-One). Images were acquired on an Axio Observer Z1 inverted microscope (Carl Zeiss Microscopy GmbH, Germany) with a 10x, 0.3 NA air immersion objective to a Coolsnap HQ2 CCDcamera (Photometrics, Canada) using ZEN imaging software (Carl Zeiss Microscopy GmbH, Germany). Environmental conditions were maintained at 37º C, 10% CO2 with a heated enclosure and CO2 controller (Pecon, Germany). Phase contrast images were taken every minute for six days.

3.4.4. Cell tracking

A semi-automated computational approach was used to track B cells in phase-contrast images. First, image intensities were normalized to maximize contrast. Next, edges were identified using a Sobel transformation and global thresholding. Cells were identified using a customized Hough transformation assuming cells were approximately circular. Next, approximate linear paths were manually drawn for each cell until the cell was observed to divide, die, or leave the field of view. Cells entering the field of view after 24 hours (i.e. potentially after the first division), and debris were tracked but

removed from the subsequent analysis. After all paths were drawn, all cell boundaries were optimized simultaneously from frame to frame. During automatic optimization, cells were modeled as deformable two-dimensional polygons with forces acting upon each vertex that ensured the polygons did not grow/shrink too quickly, did not overlap other polygons, were attracted to edges in the image, and were attracted to their respective manually-curated path. The relative magnitudes of the forces were manually calibrated to ensure appropriate behavior. Cell size trajectories were fitted using a piece-wise function consisting of a linear no-growth period, followed by exponential growth:

$$V(t) = \begin{cases} V_0 & t \le t_{decide} \\ V_0 e^{k(t-t_{decide})} & t > t_{decide} \end{cases}$$

The quality of individual cell tracks were assessed by calculating RMSD from $V(t)$, and the t_{decide} value was assumed to be the fitted inflection point in this function (i.e. when cells were predicted to start exponential growth). Growing cells were defined as having an average ending volume at least 350 μM^3 above the average starting volume, or if the final volume was at least 800 μM^3. Cells that grew but then decreased in size, or that didn't meet any of these conditions were labeled as non-growing. For implementation details please see Supplementary File CellTracker.zip. A video showing the output of tracking for the WT 250 nM CpG condition is provided as Supplementary File WT250nM.mpg.

3.4.5. Calculating the expected probability that a dying cell would have started growing

In order to test if the molecular race (Figure 3.3A) and/or the molecular decision (Figure 3.3B) hypotheses are consistent with our datasets, we used the observed

$T^0_{grow0}(t)$, $T^0_{div0}(t)$, and $T^0_{die0}(t)$ distributions (Figure 3.3E), designed with a superscript "o", to determine a lower bound on the fraction of dying cells that are expected to grow under the race or decision hypothesis. While under the decision hypothesis we would expect that all responding cells are subject only to eventual division, while non-responders will not grow or divided, the fraction of growing cells that will die, or vise-versa are not readily apparent. Therefore, we derived a lower limit on the expected probability that a dying ($fate = death$) cell will grow under the race hypothesis in terms of observed distributions, and show that the observed probability of this happening is inconsistent. We are interested in the probability that progenitors (generation 0) cells started growing and died:

$$\Pr(T_{grow0} < T_{die0}, F_0 \mid fate = death), \tag{51}$$

where T_{die0} and T_{grow0} are the true probability distributions for the time to die or start growing, and F_0 is the true fraction of cells that respond to the stimulus and start growing (still subject to death) in the race model. We define the probability censoring of some probability distribution $f(t)$ by a competing probability distribution $g(t)$ as:

$$f(t \mid g(t)) = \frac{f(t)\left(1-\int_{-\infty}^{t} g(t')dt'\right)}{\int_{-\infty}^{\infty} f(t)\left(1-\int_{-\infty}^{t} g(t')dt'\right)dt} = f(t)\left(1-\int_{-\infty}^{t} g(t')dt'\right)w_{f|g}, \tag{52}$$

where $f(t \mid g(t))$ represents $f(t)$ given that a competing mutually explosive event has probability distribution $g(t)$, and $w_{f|g}$ is a rescaling constant. From this definition it follows that

$$\int_{-\infty}^{t} f(t \mid g(t))dt \geq \int_{-\infty}^{t} f(t)dt, \forall t, \forall g(t). \tag{53}$$

Furthermore, since under the race hypothesis, all cells are subject to age-dependent death, $T_{die0}(t)$, and since $T_{die0}(t)$ is typically earlier than $T_{div0}(t)$, then for each cell that divided, there must have been at least another cell that would have divided but died, or in terms of the fraction of observed generation 0 responders:

$$2F_0^o \le F_0 . \tag{54}$$

Using (53) the observed $T_{grow0}(t)$, $T_{div0}(t)$, and $T_{die0}(t)$ distributions are biased toward earlier values, since death will censor decision and division fates, while division will censor late death fates:

$$\int_{-\infty}^{t} T_{grow0}^{o}(t)dt \ge \int_{-\infty}^{t} T_{grow0}(t)dt, \forall t , \tag{55}$$

$$\int_{-\infty}^{t} T_{die0}^{o}(t)dt \ge \int_{-\infty}^{t} T_{die0}(t)dt, \forall t .$$

However, of the cells for which both division and death are running in parallel (at least twice as many as had been observed to divide from equation (54)) a fraction would not have started measurably growing prior to dying (i.e. died before growth decision was reached and observed). Therefore, to calculate the true fraction of dying cells that are expected to start growing we first calculated the probability that a cell will start measurably growing prior to dying:

$$\Pr(T_{grow0} < T_{die0}) = \int_{-\infty}^{\infty} T_{grow0}(t)\left(1 - \int_{-\infty}^{t} T_{die0}(t')dt'\right)dt . \tag{56}$$

To do this, we used (55) to show that

$$\Pr(T_{grow0} < T_{die0}) \ge \Pr(T_{grow0} < T_{die0}^{o}) . \tag{57}$$

Furthermore, we can define a new function $T_{grow0}^{*}(t)$ in terms of observed distributions:

$$T_{grow0}^{o}(t) = T_{grow0}^{*}(t \mid T_{die0}^{o}(t)) . \tag{58}$$

Since by definition of function censorship:

$$T^{o}_{grow0}(t) = T_{grow0}(t \mid T_{die0}(t)) . \tag{59}$$

and since from (55) the $T^{o}_{die0}(t)$ distribution is shifted toward lower values compare to $T_{die0}(t)$, it follows that $T^{*}_{grow0}(t)$ is typically shifted toward later values when compared to the true $T_{grow0}(t)$:

$$\int_{-\infty}^{t} T^{*}_{grow0}(t)dt \leq \int_{-\infty}^{t} T_{grow0}(t)dt, \forall t . \tag{60}$$

Therefore, from eq. (57) and (60) we can establish a lower bound on $\Pr(T_{grow0} < T_{die0})$:

$$\Pr(T_{grow0} < T_{die0}) \geq \Pr(T_{grow0} < T^{o}_{die0}) \geq \Pr(T^{*}_{grow0} < T^{o}_{die0}) . \tag{61}$$

Since both $T^{*}_{grow0}(t)$, and $T^{o}_{die0}(t)$ are defined in terms of observed continuous probability functions, we next developed an expression for calculating $\Pr(T^{*}_{grow0} < T^{o}_{die0})$ using a collection of discrete observations. Specifically, to calculate $cdf^{*}_{grow0}(t)$ from $cdf^{o}_{grow0}(t)$ we reweighed the contribution of each, ith, observed T_{grow0} value according to the observed cdf^{o}_{die0}:

$$cdf^{*}_{grow0}(T_{grow0,i}) = \frac{cdf^{o}_{grow0}(T_{grow0,i}) \cdot w_i}{\sum_{i}^{m} w_i} , \tag{62}$$

$$w_i = \frac{1}{1 - cdf^{o}_{die0}(T_{grow0,i})} .$$

Finally, we used (62) with (54) to obtain an expression on the lower bound for (51) given m observed T_{grow0} values, and n observed T_{die0} values:

$$\Pr(T_{grow0} < T_{die0}, F_0 \mid fate = death) \geq 2F_0^o \Pr(T^*_{grow0} < T^0_{die0}) = \quad (63)$$
$$2F_0^o \sum_i^m \left[\frac{\sum_j^n \mathrm{I}\left(T_{grow,i} < T_{die,j}\right) k_i}{\mathrm{Z}} \right], Z = \sum_i^m k_i \quad .$$

In essence, we used the observed T_{die0} distribution to obtain a T_{grow0} distribution that is guaranteed to be equal to or more biased toward later values than the true T_{grow0} distribution. Combined with the fact that under the race hypothesis, the observed fraction of dividing cells is at least twice as small as the true fraction of responders, this allowed us to calculate a lower bound on the probability that a dying cell would start growing prior to actually dying (Figure 3.3F). Under the molecular decision model, cells commit to either division or death early, and are therefore protected from the alternative (growth and division for cells committed to death, and death for cells committed to growth and division). The fraction of dying cells that are expected to be also growing under the molecular decision hypothesis is zero. To test which hypothesis is best supported, we measured the fraction of dying generation 0 cells that were growing at the time of death defined as:

$$Growing_i = \begin{cases} true, & V(i,t_{\max}) > V_0(i) + 350\mu m \mid V(i,t_{\max}) > 800\mu m \\ false, & otherwise \end{cases}, \quad (64)$$

where $V(i,t_{\max})$ and $V_0(i)$ are the average final 30 volumes and the average first 30 volume measurements for cell i, respectively.

3.5. Acknowledgements

Chapter 3, in part, is currently being prepared for submission for publication of the material and may appear as Maxim N. Shokhirev, Jonathan Almaden , Jeremy

Davis-Turak, Harry Birnbaum, Theresa M. Russell, Jesse A.D. Vargas, Alexander Hoffmann. “A multi-scale approach reveals that NFκB enforces a decision to divide or die in B cells.” Jesse A.D. Vargas helped train me to run single-cell microscopy experiments. The dissertation author was the primary investigator and author of this paper.

Chapter 4

Molecular Determinants of Fate Decision and Timing

In Chapter 3, we established that B cells indeed make decisions, as growing B cells are protected from death. However, it remains unclear how fate is determined and enforced on the molecular level. Therefore, we performed a single-cell transcriptome analysis revealing an NFκB signature in growing cells. This is concordant with decades of studies establishing NFκB signaling as essential for B-cell proliferation and survival; however it remained unclear whether NFκB signaling played a direct role in the decision enforcement. Therefore, we applied an immunofluorescence and traditional biochemical assays to characterize the abundance of key molecular players in individual cells after 24 h of stimulation. We found that both NFκB RelA and cRel are upregulated at 24 h. Furthermore, mammalian target of rapamycin (mTORc1) abundance was upregulated approximately 4.5-fold in wildtype and only approximately 1.5 fold in cells deficient in NFκB cRel 24 h post stimulation. Rapamycin pretreatment resulted in reduced cell size while the abundance of cRel remained high; suggesting that cell growth is mediated by NFκB cRel activity. In addition to cell growth, NFκB is essential for the upregulation of the anti-apoptotic regulator Bcl_{XL} at 24 h as NFκB cRel deficient cells have dramatically reduced Bcl_{XL} mRNA and protein levels. These findings suggest that NFκB cRel serves

to enforce the B-cell decision to grow and survive by simultaneously upregulating growth and survival programs.

4.1. Introduction

TLR9 robustly activates the well-studied and essential NFκB signaling pathway [51], resulting in the upregulation of hundreds of genes associated with survival and proliferation, providing a natural molecular connection between signaling and cell fate [52]. Specifically, activation of TLR9 by CpG results in the activation of the kinase IKKb, which rapidly phosphorylates NFκB inhibitor proteins, the IkBs, which sequester NFκB dimers in the cytoplasm. Phosphorylation of IkBs results in their ubiquitination and degradation, releasing NFκB dimers (primarily RelA:p50 and cRel:p50 in B cells [4]) and allowing them to enter the nucleus where they bind to promoters of genes containing the NFκB motif, and activate gene expression. Importantly, the genes coding for cRel[53] and p50[54] as well as the inhibitors IkBα[55] and IkBε[56] are themselves target genes, resulting in waves of NFκB activation lasting potentially several days. Furthermore the genes coding for CyclinD [70-72], Myc [59], and Bcl_{XL} [74], which are essential for cell-cycle progression, growth, and survival, respectively, are all known to be NFκB target genes. Therefore, many essential molecular players involved in the B cell immune response have been identified but it remains unknown how their dynamics lead to the observed cell fate and timing variability and in turn the B cell population response.

Finally, single-cell molecular assays are useful for correlating cellular features (e.g. size) to molecular pathways. Specifically, immunofluorescence (IF) allows for quantitative measurement of fluorescently-labeled proteins in hundreds of individual cells. On the other hand, IF requires chemical crosslinking, which makes single-cell

tracking impossible. While IF can provide high-throughput single-cell results for specific proteins of interest, single-cell RNA sequencing can be used to quantify whole transcriptomes of individual cells [134]. A relatively new technology, single cell RNAseq uses microfluidic devices to trap individual cells and perform the necessary chemistry. Furthermore, captured cells can be stained and measured under the microscope prior to lysis, allowing for filtering of transcriptomes by the cell size and viability. This allows for the unbiased whole-genome testing of differential gene expression between individual cells.

4.2. Results

4.2.1. Single-cell transcriptome sequencing reveals NFκB signatures in big cells

We next turned to single-cell molecular assays to test the importance of key molecular players in determining fate and timing. Specifically, we stimulated purified primary naïve murine B cells, stimulated with a high dose of CpG for 24 hours and performed both single-cell RNA sequencing, as well as multi-channel immunofluorescence experiments (Figure 4.1A). We sequenced the transcriptomes of five large and small cells using the single-cell autoprep system, which allowed us to image and measure the size of individual B cells trapped inside of a microfluidics chip (Figure 4.1B). After preparing and sequencing oligomer cDNA libraries, we normalized transcript counts to RNA spikein controls, and identified 369 and 121 genes upregulated or downregulated in large cell, respectively (Figure 4.1C). We next identified and summarized the pathways that were significantly upregulated in large or small cells (Figure 4.1D). Next, since the NFκB signal transduction systems is known to be essential for the B cell immune response and because NFκB signaling was one of the

upregulated pathways in B cells, we checked if big cells had an NFκB gene expression signature compared to small cells. To do this, we performed a transcription factor enrichment analysis on the upregulated and downregulated gene sets, and tallied the transcription factors that are themselves known to be NFκB targets (Figure 4.1E). Our analysis revealed the signature of nine transcription factors that are known NFκB target genes, as well as NFκB itself among the genes upregulated in big cells (Figure 4.1E red), while we only identified p53 as a known NFκB target gene transcription factor in the set of genes downregulated in big cells, suggesting that large B cells tended to upregulate NFκB activity.

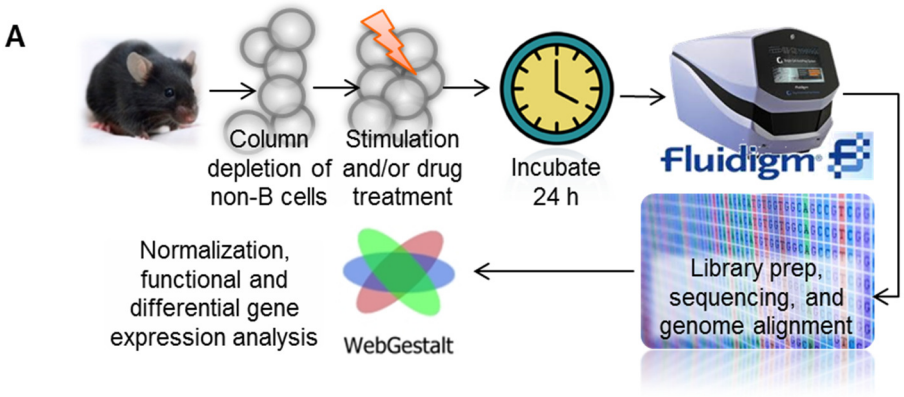

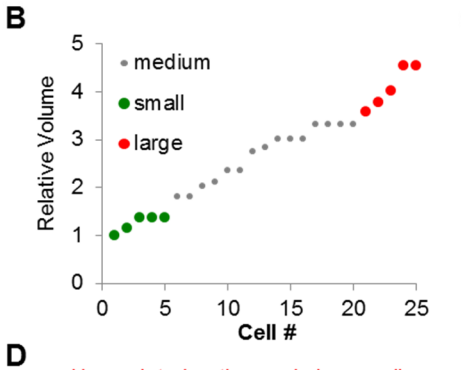

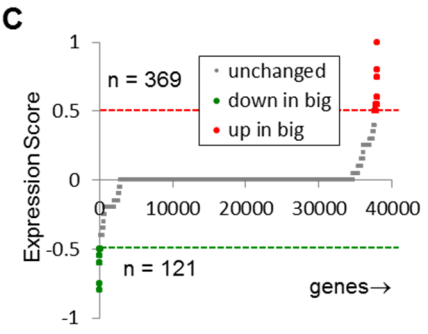

D

Upregulated pathways in large cells

Pathway	Enrich Ratio	adj. p-value	Database
Metabolic	2.19	0.0008	KEGG
B cell R. sig	7.17	0.0014	KEGG
TNFα NFκB S.	3.65	0.0046	Wikipathways
G1 to S control	5.99	0.0083	Wikipathways
Apoptosis	5.49	0.0083	KEGG
TLR Signaling	4.62	0.0124	KEGG
Cell cycle	3.68	0.0256	KEGG

Downregulated pathways in large cells

Pathway	Enrich Ratio	adj. p-value	Database
T Cell R. Sig.	8.37	0.0054	Wikipathways
Myometrial	6.06	0.0264	Wikipathways
Ca Regulation	6.3	0.0264	Wikipathways
Chemokine	5.2	0.031	Wikipathways
Integ. cell adhesion	7.18	0.031	Wikipathways
Senescence/ Autophagy	6.59	0.0324	Wikipathways

E

NFkB-related TF signatures in large cells

NFκB TF	adj. p-value	Enrich Ratio
NFKB_C	*0.0263*	*2.89*
MYC	1.08E-06	2.96
CMYB	0.000005	5.49
YY1	0.0007	3.38
E2F3	0.0046	3.72
LEF1	0.0072	1.72
STAT5A	0.0096	4.5
SOX9	0.0162	3.24
CREB	0.02	3.1
EGR1	0.0309	2.79

NFkB-related TF signatures in small cells

NFκB TF	adj. p-value	Enrich Ratio
p53	0.022	6.11

Figure. 4.1. Molecular assays suggest that NFκB enforces an upstream fate decision. Naïve purified B cells were stimulated with 250 nM CpG for 24 h, and analyzed using single-cell RNA sequencing (**A top**). Five small and five large B cells were captured in a microfluidics chip (**B**) and their transcriptomes were sequenced to reveal sets of genes typically upregulated in big cells (**C, red**) or small cells (**C, green**). Pathway analysis on genes upregulated in large B cells (**D, top**) and small cells **(D, bottom**) was performed. **E**) Transcription factor motif enrichment analysis on the genes upregulated in large cells (**E, top**) and small cells (**E, bottom**) was performed and filtered to show only significantly upregulated (p-value < 0.05) and known NFκB target genes or NFκB itself.

4.2.2. NFκB cRel mediates growth and survival in B cells

Next, we stained fixed B cells which were stimulated for 24 hours (Figure 4.2A), and measured average NFκB cRel fluorescence as a function of cell area by microscopy (Figure 4.2B). We found that compared to a 0 h control, B cells were larger (63% of cells) and had higher cRel fluorescence (63% of cells) after 24 h of stimulation. Furthermore, 68% of large cells had upregulated cRel at 24 h. To test the specificity of our immunofluorescence methodology, we showed that NFκB cRel deficient B cells had no detectable cRel fluorescence at 24 h (Figure 4.3A). Similarly to NFκB cRel, 50% of cells showed significantly increased levels of NFκB RelA after 24 h, with 70% of large cells showing increased NFκB RelA abundance after 24 h of stimulation (Figure 4.3B). In addition, we tested the role of NFκB cRel in cell growth by repeating the immunofluorescence analysis in the presence of 1 ng/mL rapamycin, the mTORc1 inhibitor (Figure 4.3C). We found that while the same fraction of cells had upregulated cRel abundance after 24 h of stimulation, the fraction of large cells was reduced, suggesting that cRel is independent of mTORc1. Furthermore, we tested the role of NFκB cRel on regulating mTORc1 directly, by measuring the abundance of p-S6, an indicator of mTORc1 activity, by western blot in wildtype and NFκB cRel deficient mice (Figure 4.2C). The data suggest that in the absence of NFκB cRel the signal is reduced by approximately a factor of 2. We also, checked the dependence of BcL_{XL} a known NFκB cRel target gene and anti-apoptotic regulator by measuring average BcL_{XL} abundance (Figure 4.2D) as well as by measuring BcL_{XL} mRNA levels by qPCR at several time points in wildtype and NFκB cRel deficient B cells (Figure 4.3E). The results show that 84% of all cells upregulated BcL_{XL} and that NFκB cRel deficient results in three-fold decrease in BcL_{XL} expression at 20 h suggesting that NFκB cRel contributes

to roughly 2/3 of the BcL_{XL} expression at 20 h. Concurrently, immunofluorescence analysis reveals that only 8% of cells upregulate BcL_{XL} in the absence of NFκB cRel and that only 8% of large cells have an upregulated BcL_{XL} abundance (Figure 4.3D).

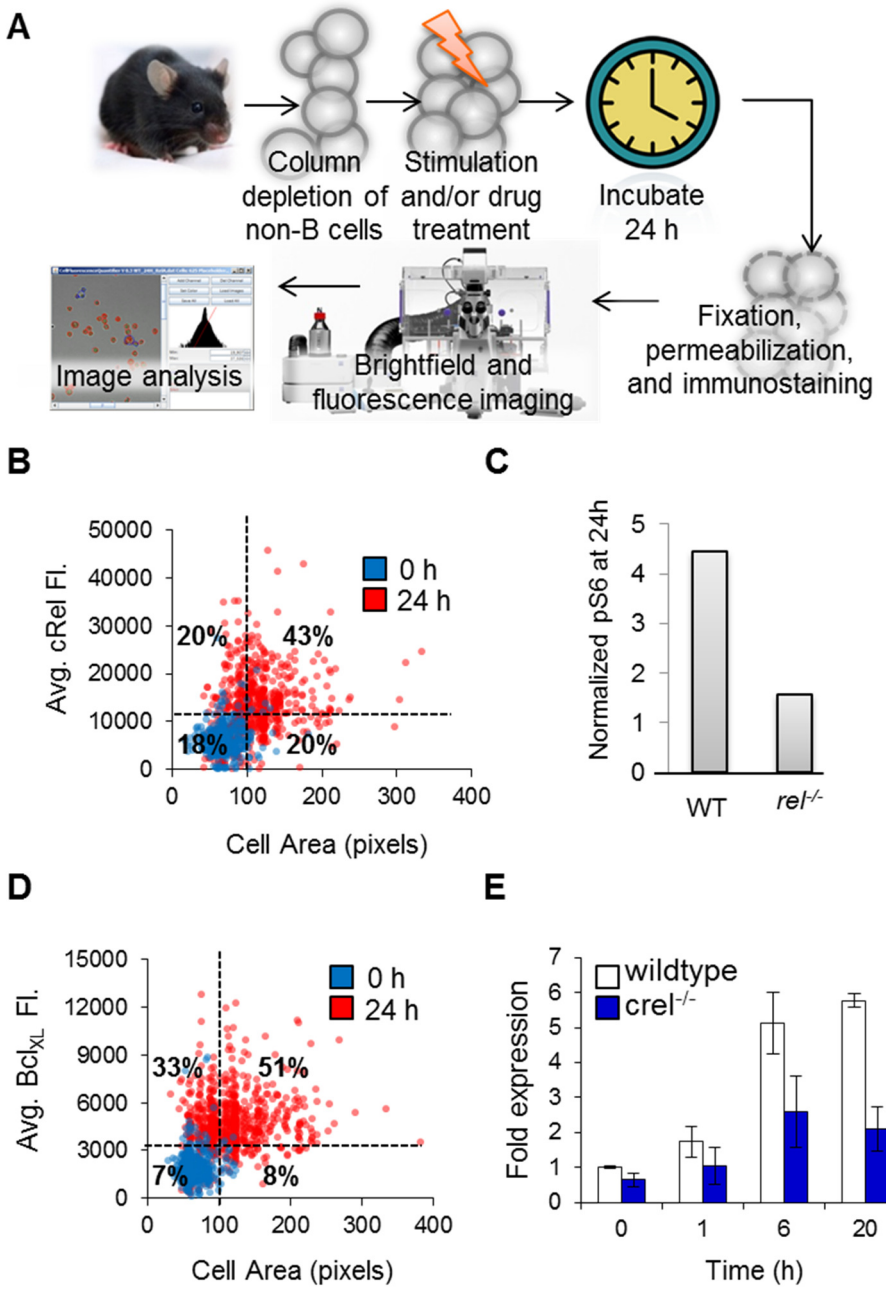

Figure 4.2. NFκB mediates growth and survival. NFκB cRel abundances of purified naïve B cells stimulated with 250 nM CpG for 24 h were obtained by quantifying average fluorescence in fixed B cells in the presence of fluorescently-labeled antibodies (**A**). NFκB cRel fluorescence as a function of cell area at 0 h and 24 h (**B**). Quantification of pS6, a downstream target of mTORc1 after 24 h by western blot normalized to tubulin control in WT and cRel deficient B cells (**C**). Anti-apoptotic Bcl_{XL} fluorescence as a function of cell size at 0 h and 24 h (**D**). Bcl_{XL} mRNA levels were measured by quantitative PCR at 0, 1, 6, and 20 h in wildtype and NFκB cRel deficient B cells (**E**). Significant fluorescence in (**B**) and (**D**) determined using 0 h fluorescence distribution. Large cells empirically defined as > 100 pixels. Error bars=s.d.

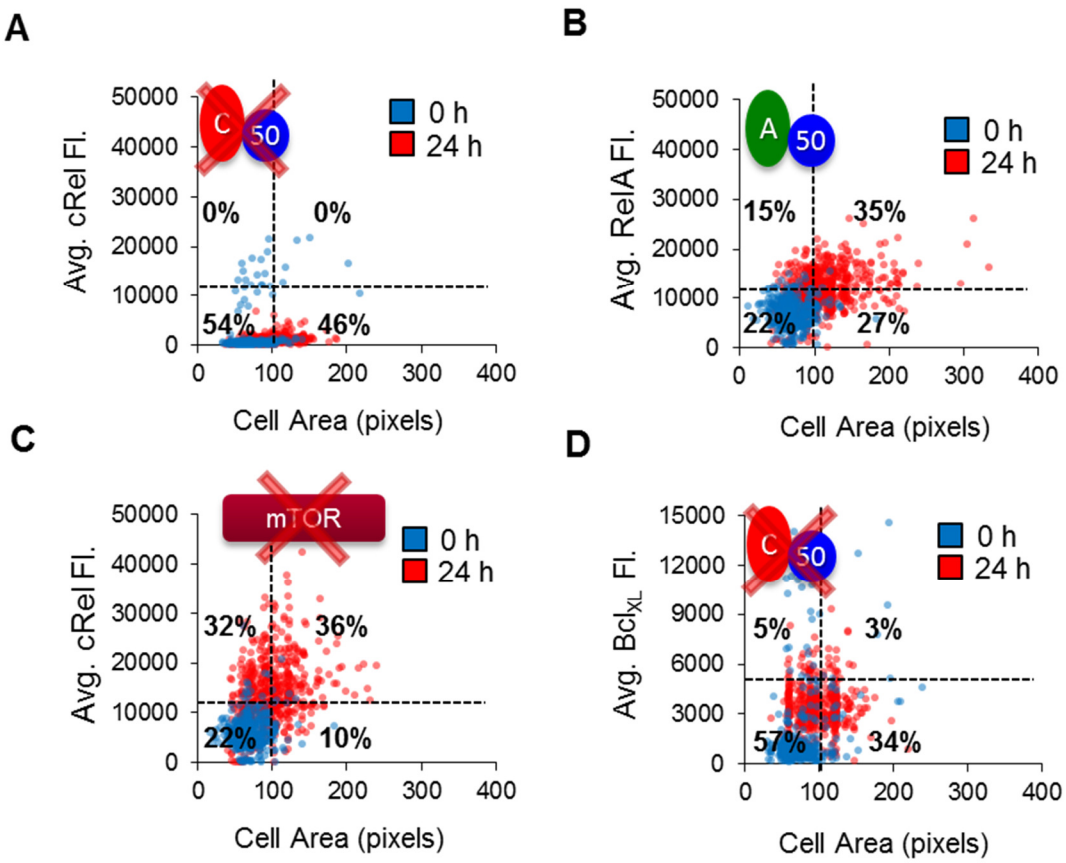

Figure. 4.3. Immunofluorescence control experiments. Immunofluorescence control experiments were performed in wildtype and cRel deficient B cells stimulated with 250 nM CpG. Average NFκB cRel fluorescence at 0 h and 24 h in NFκB cRel deficient cells (**A**). Analogously to NFκB cRel, NFκB RelA average fluorescence was quantified at 0 h and 24 h post stimulation (**B**). Average cRel fluorescence at 0 h and 24 h and 1 h pretreatment with 1 ng/mL rapamycin (**C**). Average BcL_{XL} fluorescence at 0 h and 24 h in NFκB cRel deficient B cells (**D**). Quadrants delineate significance at 24 h compared to 0 h.

4.2.3. Time-lapse microscopy confirms NFκB cRel as a decision enforcer

Since our data implicated NFκB cRel as an essential driver of the decision in B cells, we tracked NFκB cRel deficient B cells and compared the dataset against the wildtype dataset (Figure 4.4). We find that the population result is noticeably decreased in the cRel deficient dataset (Figure 4.4A) with most cell only undergoing two or three divisions compared to at least seven observed generations in wildtype cells (Figure 4.4B). Nevertheless, the growth trajectories of responding and non-responding cells remained nearly-identical with responding cells growing to approximately 1000 μM^3 before division on average (Figure 4.4C), while "non-growing" cells remained largely the same size on average (Figure 4.4D). Concomitant with the molecular observations that NFκB cRel is important for enforcing the decision, we see an elevated fraction of growing cells dying in cRel deficient cells (Figure 4.4E). In fact, we observe 40% of growing cells dying in generation 0 when NFκB cRel is knocked out, while just 12.5% of growing cells were observed to die under wildtype conditions. On the other hand, we see that non-growing cells almost never divided in the cRel knockout condition, while this was relatively common for wildtype B cells (Figure 4.4F) due to poor growth prior to the last division (Figure 3.4). Furthermore, while there wasn't a significant fate timing phenotype in NFκB cRel deficient cells (Figure 4.4G), the fraction of dying cells which grew was elevated (31%±1% compare to 8%±2% for wildtype) under knockout conditions (Figure 4.4H).

Therefore, NFκB seems to play a role in enforcing the decision to survive and progress through the cell cycle, while the timing of the cell-cycle and apoptosis remains largely independent.

Figure 4.4. Time-lapse microscopy confirms NFκB cRel as an enforcer of cell decision making. Time-lapse microscopy experiments were performed on wildtype and cRel deficient B cells stimulated with 250 nM CpG and cell size trajectories and lineages were tracked using a semi-automated approach. Cellular statistics are shown for wildtype (left column) and cRel deficient cells (right column). Generation cell counts normalized to starting cell count (**A**). Fractional division and death probabilities are shown for each generation (**B**). Error bars are 1/n. Cell size trajectories as a function of percent lifetime for growing (**C**) and non-growing (**D**) cells are plotted for each generation (blue to orange curves). Error bars show SEM. Fraction of growing (**E**) and non-growing (**D**) cells that divided or died within a 24 h period (12-36 h after stimulation) in each generation. Error bars show 1/n. Cumulative density functions for the observed progenitor time to decide to grow (blue), time to die (red), and time to divide (green) are shown (**G**). The observed cumulative distributions and fraction of dividing cells in generation 0 were used to calculate the minimum probability that dying cells were also grower cells under the molecular race or decision scenarios and compared to the fraction measured from time-lapse cell tracking.

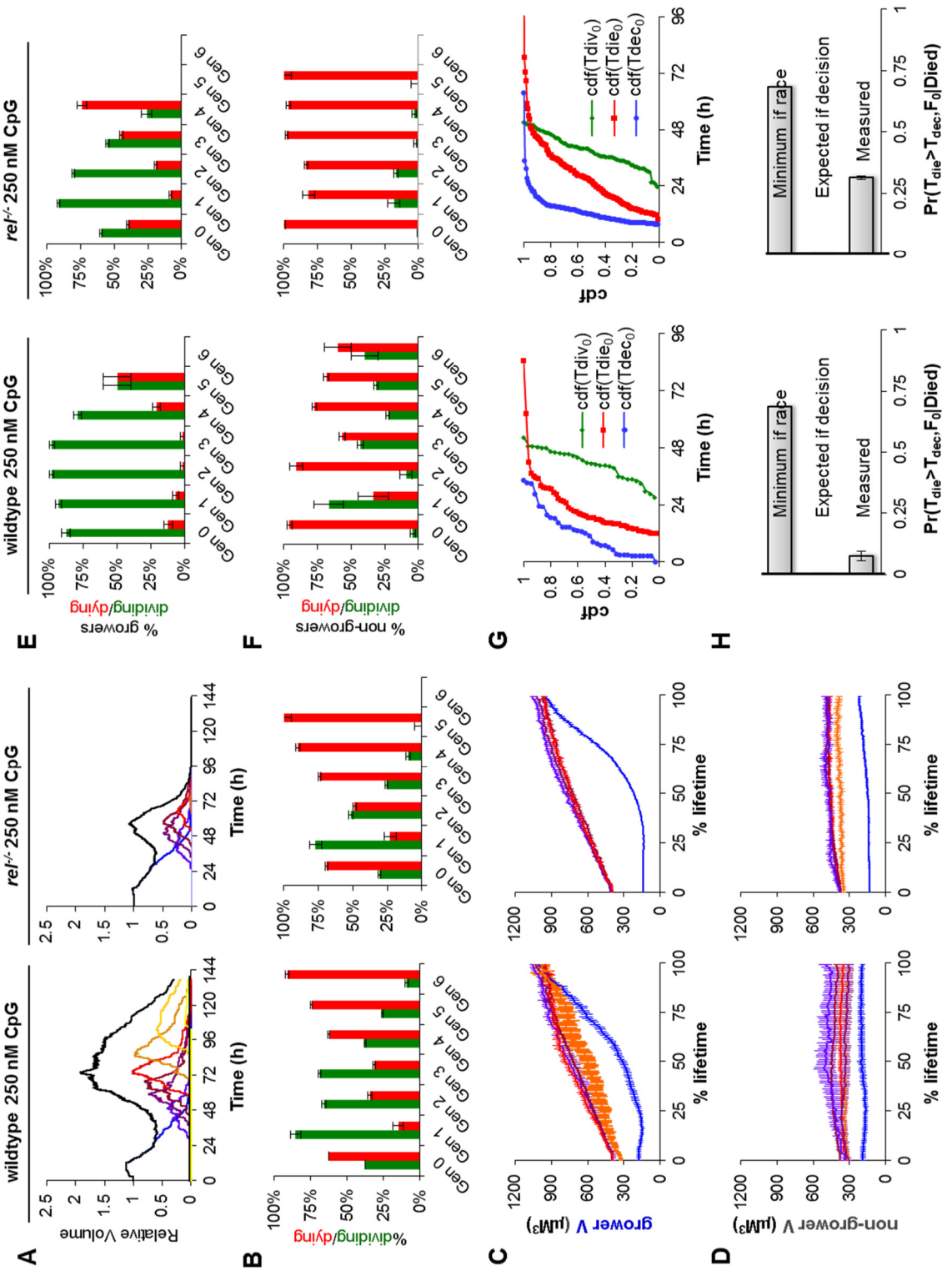
A
wildtype 250 nM CpG
rel-/- 250 nM CpG
Relative Volume
Time (h)
B
%dividing/dying
C
grower V (μM)3
% lifetime
D
non-grower V (μM)3
E
% growers
dividing/dying
F
% non-growers
G
cdf
cdf(Tdiv0)
cdf(Tdie0)
cdf(Tdec0)
H
Minimum if rape
Expected if decision
Measured
Pr(Tdie>Tdec,F0|Died)
Gen 0
Gen 1
Gen 2
Gen 3
Gen 4
Gen 5
Gen 6

4.3. Discussion

So what enforces the decision to divide and survive? Previous studies have shown that in B cells, the NFκB signaling system plays a central role in the determining fate of stimulated B cells for a wide assortment of mitogenic signals [60], therefore, we characterized key molecular players in individual cells by IF and by sequencing the transcriptomes of small and large cells after the cells have had a chance to grow, but have not yet divided. While, there was significant cell-to-cell transcriptome variability (Table 4.1), there was nevertheless an NFκB signaling signature readily apparent in large cells (Figure 4.1). Taking advantage of other molecular assays, we showed that NFκB cRel, and RelA are upregualted after 24 h of stimulation and large cells show increased NFκB abundance as compared to 0 h (Figure 4.2B and Figure 4.3B). Furthermore, inhibition of mTORc1 by rapamycin resulted in an appreciable growth defect at 24 h, while maintaining nearly identical proportions of NFκB cRel positive cells (Figure 4.3C), confirming that mTORc1 is downstream or independent of NFκB signaling. We confirmed that mTORc1 is downstream of cRel by western blot and showed that in the absence of NFκB cRel, mTORc1 activity is roughly halved (Figure 4.2C). Analogously, the anti-apoptotic regulator Bcl_{XL} was dramatically upregulated after 24 h and correlated with cell size (Figure 4.2D). Furthermore, Bcl_{XL} levels were dramatically reduced in the NFκB cRel knockout, suggesting that NFκB cRel is required for roughly 2/3 of the Bcl_{XL} transcripts at 24 h (Figure 4.2E). Therefore, molecular assays suggest that NFκB acts as an enforcer of an upstream decision by simultaneously upregulating cell growth (via mTOR), as well as survival in B cells (via Bcl_{XL}). However, it remained unclear how cRel deficiency is manifested on the population scale.

To test this, we repeated the time-lapse microscopy experiments with B cells missing NFκB cRel, and quantified the degree to which cRel is important for promoting an efficient response. Cell growth trajectories and fate time distributions were similar to wildtype, but we saw a dramatic decrease in the population response caused primarily by a failure to commit to more than a few rounds of division (Figure 4.4B). Critically, we see that NFκB cRel deficient cells were having trouble enforcing their fate, with the fraction of grown dying cells increasing four-fold (Figure 4.4H). Thus, time-lapse microscopy confirms that NFκB cRel enforces decisions during the B cell immune response.

Taken together, these results suggest that the early commitment to one fate in B cells is driven by NFκB-mediated activation of survival and cell-cycle activation.

4.4. Methods

The single-cell RNA sequencing analysis (CSV format), pertinent immunofluorescence images, and CFAnalyzer, the tool we developed for quickly quantifying fluorescence in IF images are part of the supplementary materials as IFAnalysis.csv, IFImages.zip, and CFAnalyzer.zip, respectively.

4.4.1. Single-Cell RNAseq

Stimulated wildtype B cells were collected at 24 h post stimulation and concentrated to $5x10^5$ cells per mL. Cells were loaded onto a 10-17 uM primed C_1 single-cell auto prep array IFC (Fluidigm), and phase contrast images were taken of all viable cells as determined by the Live/Dead® Viability/Cytotoxicity Kit (Invitrogen). ERCC RNA spikein controls (LifeTechnologies) were added to the lysis mix at a 1:200 dilution. Tube controls (bulk cell positive control, and no cell negative control) were also

prepared according to the Fluidigm protocol. Lysis, reverse transcription, and PCR were performed using the SMARTer Ultra Low RNA Kit (CloneTech) and Advantage® 2 PCR Kit (CloneTech) on individual cells using the C_1 Single-Cell Auto Prep System (Fluidigm). Cell size was manually determined from images using ImageJ software. Sample libraries for the five smallest and five largest cells along with the controls were prepared using the Nextera XT DNA Sample Preparation (Illumina), and library quality was assayed using the Quant-iT PicoGreen dye (Life Technologies) quantification on a Qubit® 2.0 Fluorometer (LifeTechnologies) and by gel electrophoresis. Libraries were sequenced by the UCLA Broad Stem Cell Research Center High Throughput Sequencing Core on Illumina HiSeq 2000 sequencers according to manufacturer recommendations. Reads were aligned to the ENSEMBL NCBI m37 genome [179] using rna-STAR [141]. To compute spikein concentrations for normalization purposes, the 23 most abundant RNA spikein concentrations (at least one read in all samples) were compared to the expected concenrations in log-log space, and the y-intercept in log-space was used to compute a normalized spike in concentrations for each sample, $[Spikein_j^*]$. The normalized expression of gene i, in sample j was then computed as:

$$Gene_{i,j} = \frac{Gene_{i,j}}{[Spikein_j^*]} + 100,$$

where $[Spikein_j^*]$ is the normalized spikein concentration that is ≥ 1. A constant count of 100 was added because Spikeins with counts with counts < 100 were variable across samples. To assess the overall quality of each cell, we correlated their transcriptomes to the average across all cells as well as to the positive tube control. We found that one large cell had significantly lower correlation, so we omitted it from further analysis (Table

4.1). To determine if a particular gene was upregulated in big cells, we computed an expression score:

$$Escore_i = \frac{\sum_{big} I(gene_i > 300)}{\#cells_{big}} - \frac{\sum_{small} I(gene_i > 300)}{\#cells_{small}},$$

where $I(gene_i > 300)$ is 1 if gene i has above 300 read count in a particular sample. A gene with an expression score ≥ 0.5 was considered upregulated in big cells, while a gene with an expression score ≤ -0.5 was considered downregulated in big cells. These sets of upregulated and downregulated genes were analyzed for pathway enrichment and transcription factor motif enrichment using WebGestalt [143]. Significant transcription factors were further filtered to remove non-NFκB downstream targets as defined in Table 4.2.

Table 4.1: Correlations between cell transcriptomes. Transcriptomes of five large and five small cells were sequenced and aligned to the mouse genome. Gene counts were normalized to RNA spike in pseudo-counts and a constant positive count of 100 was added to all genes to represent experimental sensitivity as seen in the variability in spikein counts between samples (see methods). Colors represent degree of correlation (Pearson's r). The second large cell was removed from further analysis due to poor correlation with all other cells (similar to negative).

	Small 1	Small 2	Small 3	Small 4	Small 5	Large 1	Large 2	Large 3	Large 4	Large 5	Neg.	bulk +
Small 1	1.00	0.77	0.58	0.63	0.63	0.65	0.40	0.65	0.67	0.59	0.27	0.61
Small 2	0.77	1.00	0.70	0.64	0.65	0.65	0.45	0.71	0.70	0.66	0.33	0.65
Small 3	0.58	0.70	1.00	0.59	0.73	0.67	0.49	0.63	0.72	0.74	0.34	0.62
Small 4	0.63	0.64	0.59	1.00	0.73	0.83	0.45	0.81	0.79	0.61	0.41	0.82
Small 5	0.63	0.65	0.73	0.73	1.00	0.82	0.49	0.76	0.87	0.77	0.39	0.73
Large 1	0.65	0.65	0.67	0.83	0.82	1.00	0.46	0.82	0.84	0.66	0.37	0.81
Large 2	0.40	0.45	0.49	0.45	0.49	0.46	1.00	0.44	0.51	0.51	0.30	0.44
Large 3	0.65	0.71	0.63	0.81	0.76	0.82	0.44	1.00	0.83	0.62	0.40	0.80
Large 4	0.67	0.70	0.72	0.79	0.87	0.84	0.51	0.83	1.00	0.71	0.43	0.75
Large 5	0.59	0.66	0.74	0.61	0.77	0.66	0.51	0.62	0.71	1.00	0.35	0.64
Negative	0.27	0.33	0.34	0.41	0.39	0.37	0.30	0.40	0.43	0.35	1.00	0.37
bulk +	0.61	0.65	0.62	0.82	0.73	0.81	0.44	0.80	0.75	0.64	0.37	1.00

Table 4.2: **NFκB target genes that are transcriptional regulators.** This list was adapted from [180]. Transcription factors with motifs upregulated in large (red) or small (green) cells have been highlighted.

Name	Description	Name	Description
Androgen receptor	Hormone receptor	IRF-2	Interferon regulatory factor-2
Bcl-3	Coactivator for NF-kB p50 and p52	IRF-4	Interferon regulatory factor-4
BMI-1	Polycomb chromatin modifier	IRF-7	Interferon regulatory factor -7
CDX1	Homeobox protein	junB	Proto-oncogene
c-fos	Proto-oncogene	Lef1	Transcription factor in Wnt/b-catenin pathway
c-myb	Proto-oncogene	LZIP	Leukocyte cell mobility
c-myc	Proto-oncogene	NLRP2	NF-kB pathway inhibitor
c-rel	Proto-oncogene	NURR1	Nuclear orphan receptor
C/EBPdelta	Transcription factor	Osterix	Bone transcription factor
DC-SCRIPT	Dendritic cell zinc finger protein	p53	TF, Tumor suppressor
Dmp1	Myb-like transcription factor	Progesterone receptor	Transcription factor
E2F3a	Cell cycle regulator	PU.1	Transcription factor
Elf3	Ets family transcription factor	relb	Transcription factor
ELYS	Embryonic large molecule derived from yolk sac	Snail	Transcription factor
Egr-1	Mitogen-induced early response gene; zinc finger	Sox9	Transcription factor
ETR101	TPA-inducible, Jun-like transcription factor	Stat5a	Transcription factor
Gata-3	T-cell differentiation Factor	Tfec	Transcription factor
Glucocorticoid receptor	Promoter 1B of the GR	Twist	Transcription repressor
HIF-1alpha	Hypoxia-inducible factor	WT1	Zinc finger transcription factor
HOXA9	Homeobox protein	YY1	Transcription factor
IRF-1	Interferon regulatory factor-1		

4.4.2. Western blot analysis

Whole cell lysates were prepared using RIPA buffer lysis of B cells. The resulting lysates were resolved on a 10% SDS-PAGE, proteins detected using the Bio-Rad ChemiDoc XRS System and SuperSignal west femto substrate (Thermo Scientific). Antibodies used to identify the protein of interest: S6 Ribosomal Protein (Cell signaling #2217) and αtubulin (Santa Cruz sc-5286).

4.4.3. RT PCR

RNA extraction was performed using RNAeasy Mini Kit (Qiagen). cDNA synthesis of purified RNA was done with iScript cDNA Synthesis kit (Bio-Rad). Quantitative RT-PCR was performed with SYBR Green PCR Master Mix reagent (Stratagene) and Eppendorf Mastercycler realplex system using the Δ(ΔCt) method with β-actin as normalization control.

4.5. Acknowledgements

Reagents, training, and expertise for single-cell RNA sequencing was provided by Fluidigm Corp. and Theresa Russell. The anti-cRel antibody conjugated to PE used in IF studies was a generous gift from Ananda Goldrath. Andrew Doedens provided training on its use.

Chapter 4, in part, is currently being prepared for submission for publication of the material and may appear as Maxim N. Shokhirev, Jonathan Almaden , Jeremy Davis-Turak, Harry Birnbaum, Theresa M. Russell, Jesse A.D. Vargas, Alexander Hoffmann. “A multi-scale approach reveals that NFκB enforces a decision to divide or die in B cells.” Jonathan Almaden helped with B-cell purification, western blotting, and RT-PCR. Jeremy Davis-Turak and Harry Birnbaum collaborated to align and map single-cell RNAseq results. Theresa M. Russell and I collaborated to produce the single-cell RNA sequencing datasets. Jesse A.D. Vargas devised the immunofluorescence protocol and trained me to run immunofluorescence and single-cell microscopy experiments. The dissertation author was the primary investigator and author of this paper.

Chapter 5

Multi-scale agent-based modeling of B-cell population dynamics

In chapters 3 and 4 we determined that B cells make decisions to survive and divide or remain quiescent and die by programmed cell death and that NFκB cRel enforces this decision by promoting the production of growth and survival processes. In fact, deficiency in NFκB cRel results in premature contraction, with cells exiting the cell cycle and dying after just a few divisions (Figure 4.4). Presumably, variability in the extrinsic state of a cell at the time of stimulation determines if a cell will respond to the stimulus as well as the observed variability in the timing until division or death. Given the complexity and non-linearity of the biochemical pathways leading to decision making, division, and apoptosis it is not apparent how the interplay between these pathways leads to the observed variability in cell fate, fate timing, and ultimately the population response. Therefore, we constructed an agent-based multi-modular computational model to simulate lymphocyte population dynamics in terms of the molecular networks that control NFκB signaling, apoptosis, and cell-cycle. Testing genetic perturbations by modeling and subsequent experimentation, we found that NFκB cRel enhancement of survival and cell-cycle progression allows it to play an essential role in enforcing the execution of the cellular decision of mutually exclusive fates. Our work demonstrates how a multi-scale modeling approach allows the harnessing of molecular mechanistic knowledge to an understanding of dynamic organ level physiology.

5.1. Introduction

At first glance, the complexity of biological systems is daunting (Figure 5.1). Coupled with the fact that hundreds of different cell types exist, and that even clonal cells of one type can have discordant fates (e.g. division vs. death in B cells) in response to the same stimuli, it is unclear how multi-cellular organisms can function. Nonetheless, multi-cellular heterogeneity and population robustness are hallmarks of the immune response and are essential for proper function [44]. Fortunately, there are fundamental rules governing biological function, making a bottom-up systems biology an attractive avenue. The central tenant of bottom up systems biology is the mechanistic description of the complex behavior of organisms, organs, and tissues in terms of underlying basic rules enabling targeted disease intervention [168,181]. Scaling from biochemical networks up to cells and ultimately organs, requires a method for connecting the output of biochemical reactions to cellular outcomes as well as a way to predict population behavior given the cellular parameters. Computational modeling provides a mathematically rigorous and powerful methodology for testing multi-scale hypothesis, enabling meaningful interpretation and iterative rounds of hypothesis generation.

Fortunately we can stand on the shoulders of giants that have successfully pioneered models connecting the interactions of macromolecules to cellular outcomes in mammalian cells. Specifically, kinetic models for NFκB signaling are well established[149,150,182-187] and recently reviewed in [188] and a recent iteration has been specifically trained on experimental data from stimulated B cells [150], which unlike most cells has mostly cRel-containg NFκB dimers [4]. Also, ODE models of the cell-cycle are abundant [152,153] and recently reviewed by [189]. Computational models of apoptosis are also available and experimentally validated in single-cells [24,155]. Of note, Loriaux and coworkers have recently published an updated version of these well-

established models that incorporates protein turnover dynamics and can allow for cell survival given extrinsic protein turnover variability [156]. Therefore, the filed is set for an integrated modeling approach, combining extant models of NFκB signaling, cell-cycle progression, and apoptosis.

What is required to bridge the cell-population divide? Since population models have already been established that map cellular parameters to population dynamics (e.g. cyton-like models that are the topic of chapter 2), one approach is to reduce the complex dynamics of the biochemical networks to a probabilistic mapping from a set to features to the parameters dictating distributions of the population network (Figure 5.2A). However, this results in essentially a parameterized black box which cannot be used to predict output under novel (i.e. unseen) conditions as the underlying mechanisms mapping inputs to output are *ad hoc*. On the other hand, physicochemical models which assume mass-action kinetics [157] and concentration-proportional rates for biochemical interactions between reactants and products can be used to test specific biologically-meaningful hypothesis *a priori* (Figure 5.2B).

Unfortunately, there is no elegant and efficient strategy for employing physicochemical models to model entire populations of cells. Each reaction in each cell must be modeled explicitly since a minimum of approximately 100 reactants must be simulated with slightly different starting conditions/reactions rates within each of at least several hundred *in silico* cells, with each generation depending on the behavior of previous generations. Typically, this is done by encapsulating each *in silico* cell into an autonomously-operating computational agent, which is responsible for the accurate bookkeeping and model iteration. Agent-based models have enjoyed popularity as hypothesis testing tools in the recent past [163-166,190,191], with the added benefit of

allowing one to test biological systems across scales even when much of the biological details are poorly understood.

In this chapter we used extant ODE models describing NFκB signaling, apoptosis, and cell-cycling to construct a multi-scale agent-based model of the population response. We parameterize the connections between these modules using results from time-lapse microscopy and molecular assays described in chapters 3 and 4. We show that the model can predict the observed behavior of cell stimulated with a lower dose of the stimulus, cells deficient in NFκB cRel, and cells pre-treated with rapamycin. Furthermore, we use the model to explore the propagation of extrinsic variability across scales.

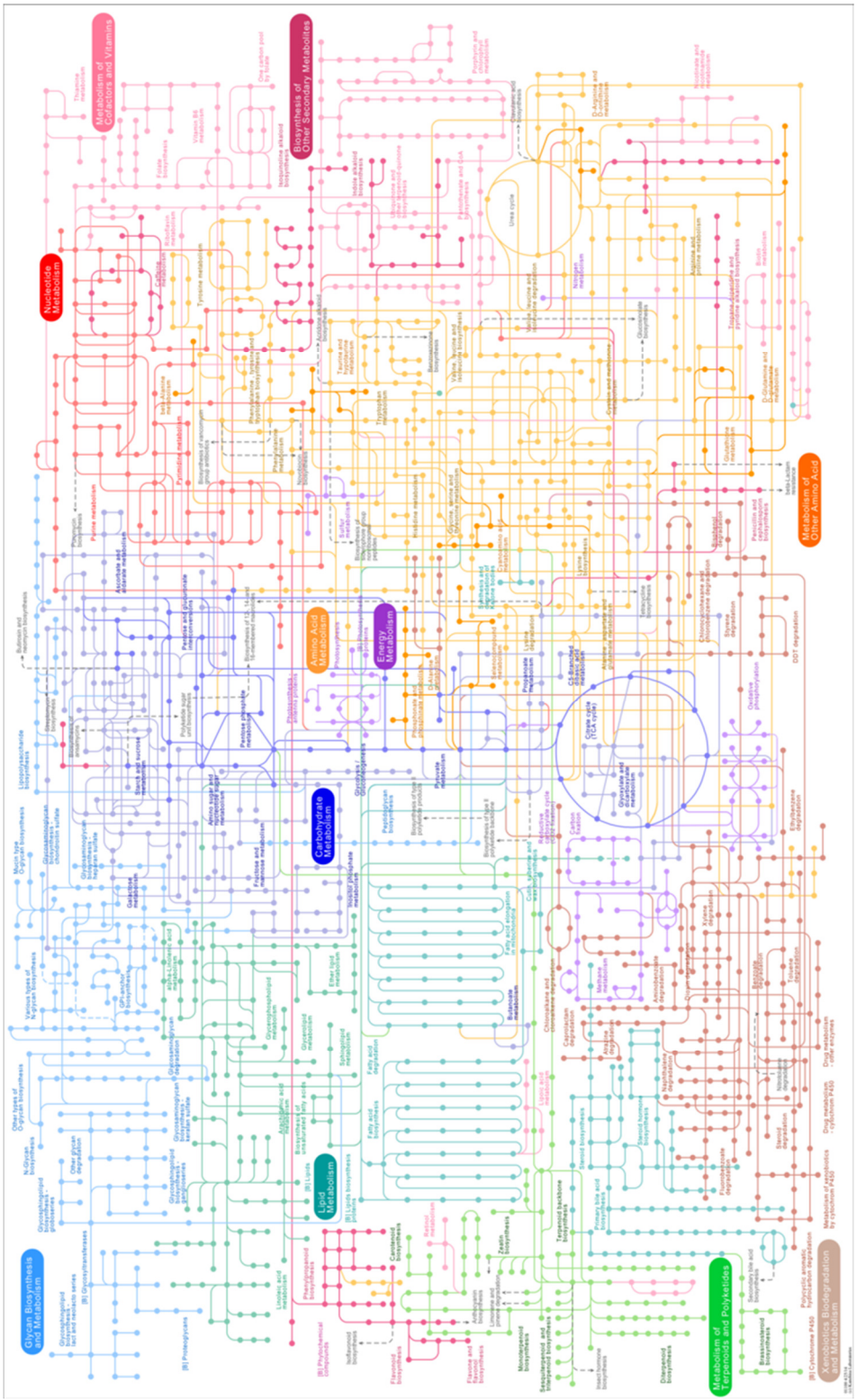

Figure 5.1 Biological processes are complex non-linear processes. The current metabolic pathway map in the Kyoto Encyclopedia of Genes and Genomes [192].

A

Observation	NFkB	Size	Age	Time	Behavior
1	Low	Small	0 h	36 h	Quiescent
2	Low	Medium	12 h	48 h	Growing
3	High	Large	24 h	60 h	Dividing
⋮	⋮	⋮	⋮	⋮	⋮

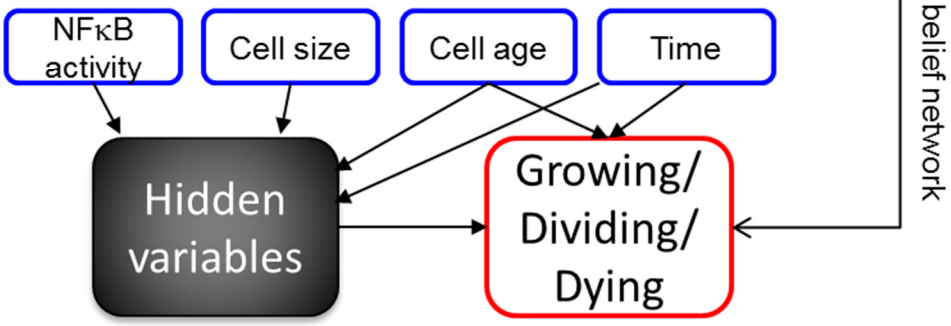

B

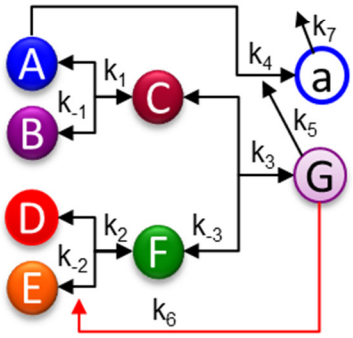

$d[A]/dt = k_{-1}[C]-k_1[A][B]-k_4[A]k_5f([G])$
$d[B]/dt = k_{-1}[C]-k_1[A][B]$
$d[C]/dt = k_1[A][B]-k_3[C][F]+k_{-3}[G]-k_{-1}[C]$
$d[D]/dt = k_{-2}[F]-k_2[D][E]$
$d[E]/dt = k_{-2}[F]k_6f([G])-k_2[D][E]$
$d[F]/dt = k_2[D][E]-k_3[C][F]+k_{-3}[G]-k_{-2}[F]k_6f([G])$
$d[a]/dt = k_4[A]k_5f([G])-k_7[a]$

"Event" triggered when $[a] > k_8$

Figure 5.2. Data-driven probabilistic vs physicokinetic modeling. An example of a probabilistic model that assumes *ad hoc* dependence of variables comprising a belief network. Data is used to parameterize the probabilities associated with the connections as well as the state of unobserved variables (**A**). If information about the components are known (e.g. the interactions and reaction rates), pharmacokinetic models can be used to mechanistically describe the abundances of all species as a function of time. An example biochemical model is shown under the assumption of mass-action kinetics and a condition governing the occurrence of some "event" (**B**).

5.2. Results

5.2.1. Multi-scale models integrate observations and predict population dynamics

Results from CFSE time courses, time-lapse microscopy, and molecular studies demonstrated the intricate behavior of B cells across biological scales, however, the mechanics of how biochemical variability leads to the observed single-cell behavior and ultimately the robust population response remained untested. Our strategy for doing this was to first implement established ordinary differential equation kinetic models of the NFκB signaling system, apoptosis, and the cell-cycle (Figure 5.3A), and introduce sources of extrinsic variability to determine if these models were sufficient for generating the variability in decision and timing we observed in our microscopy datasets. We found that, variability in protein levels alone was sufficient for producing cell-to-cell variability in nuclear NFκB concentration, cell-cycle duration, and lifetime typically observed (Figure 5.3B). Importantly, the cell-cycle model with added sources of extrinsic noise produces relatively short cell-cycle durations of ~ 10-20 h, similar to generation1+ cells, but cannot readily account for the increased delay and the six-fold increase in size (Figure 2.2). Furthermore, we found that introducing extrinsic protein variability resulted in significant cell death timing variability, with a significant fraction of cells surviving after 144 h of death stimulation as expected in heterogeneous populations of cells.

Figure. 5.3. Extrinsic noise results in cell-to-cell NFκB, division, and death variability. Models for NFκB signaling, cell-cycling, and apoptosis are summarized (**A**). Bolded species represent the input (active IKK), and output event nodes (cleaved PARP signals death, cdh1 accumulation signals cytokinesis). Extrinsic noise in the form of protein synthesis and degradation rate variability (~normal(rate,rate*0.1)), total protein abundance (~log-normal([protein], [protein]*0.25)), and initial cell size (~normal(1,0.07)) was introduced to each module and 100 simulations were carried out. Active IKK (**B**), nuclear RelA:p50 and nuclear cRel:p50 (**C**), cyclin and cdh1 (**F**), cell mass (**G**), Bcl_{XL} (**H**) and cleaved PARP (**I**) are shown. The published cell-cycle model [152] which does not include cell growth control (**D**) and the results for solving 100 independently-distributed simulations (**E**) are shown for reference. Overlapping histograms indicate division (green) and death (red) events. Error bars in (**B,C**) represent s.d.

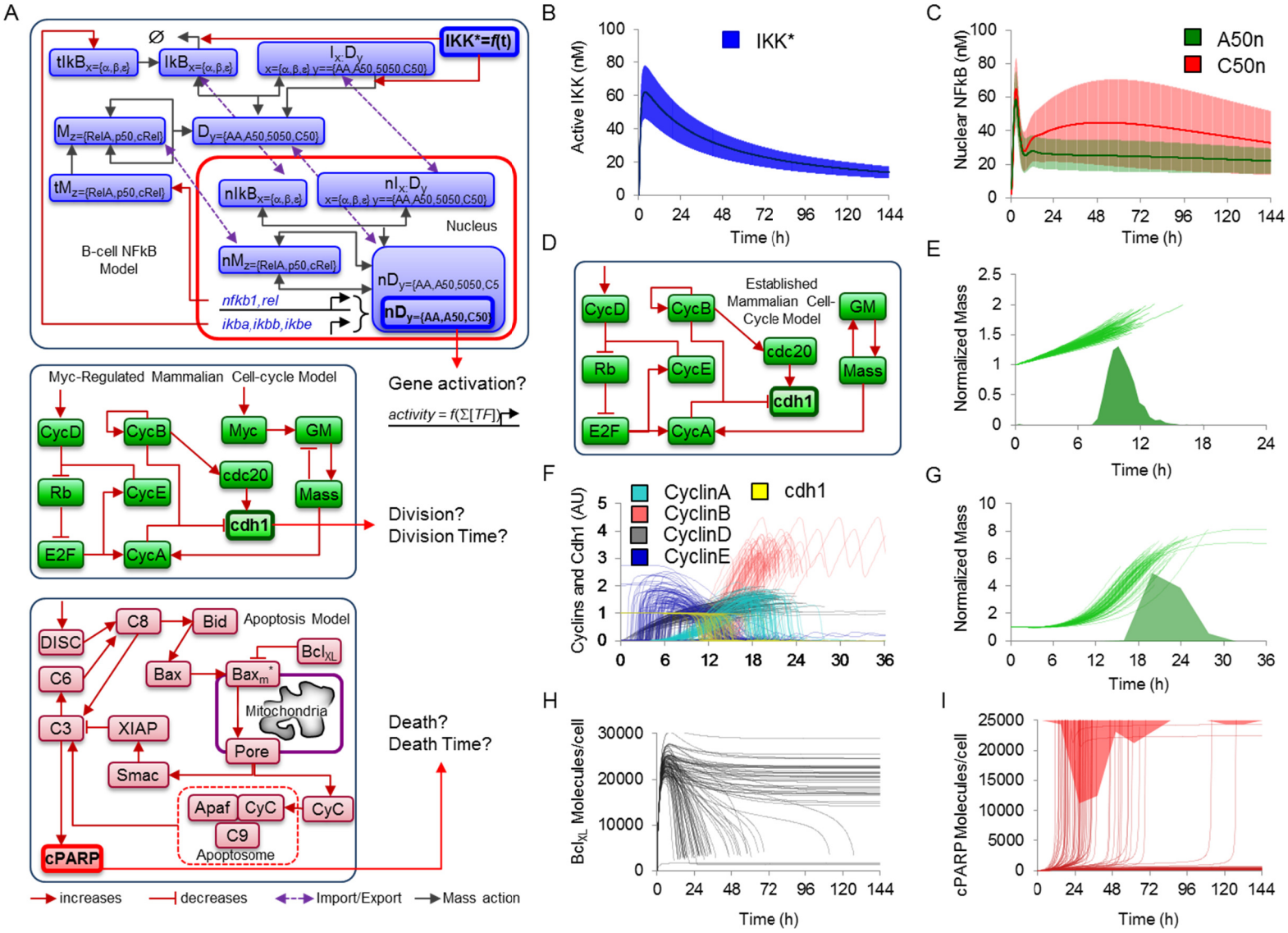
A
B
C
D
E
F
G
H
I
B-cell NFkB Model
Nucleus
Gene activation?
activity = f(Σ[TF])
Myc-Regulated Mammalian Cell-cycle Model
Division?
Division Time?
Apoptosis Model
Death?
Death Time?
Mitochondria
Apoptosome
increases
decreases
Import/Export
Mass action
Established Mammalian Cell-Cycle Model
Active IKK (nM)
IKK*
Time (h)
Nuclear NFkB (nM)
A50n
C50n
Normalized Mass
Cyclins and Cdh1 (AU)
CyclinA
CyclinB
CyclinD
CyclinE
cdh1
BclXL Molecules/cell
cPARP Molecules/cell

Confident that these models could be combined to model NFκB driven B cell division and death, we constructed an integrated ODE model (Figure 5.4A) with NFκB-controlled synthesis of anti-apoptotic Bcl_{XL}, a key protein in the apoptosis model, as well as NFκB-controlled synthesis of CycD, which is explicitly modeled in the cell-cycle model. Furthermore, in the cell-cycle model, growth is controlled by general machinery, GM, which represents the ribosomes and all other cellular components that promote the accumulation of cell mass. Mass in turn promotes the growth of general machinery, creating a positive feedback loop that results in exponential growth and cellular progression through the cell cycle. However, since we observed B cells to delay growth prior to the first division (Figure 2.2), we needed to model the control of general cell machinery in more detail. To do this, we incorporated NFκB-controlled synthesis of c-Myc, a transcription factor that promotes cell growth, which is typically low in quiescent cells prior to activation, and which is a known NFκB target gene. To obtain population dynamics, the integrated ODE model was incorporated into cellular agents (Figure 5.4B), which kept track of their generation, age, and independent set of starting synthesis/degradation or total protein concentrations, which were draw from normal or log-normal distributions, respectively. The models were solved until the agent died (defined as [cPARP]>25,000 molecules/cell) or finished mitosis ([cdh6]>0.2), at which point it was either removed or two new daughter agents were created, respectively. Daughter agents we subject to extrinsic re-mixing noise to account for loss of correlation with successive generations. When training the model on our results from the wildtype condition, we left all NFκB, cell-cycle, and apoptosis parameters largely intact leaving a set of free parameters involving the control of Bcl_{XL}, CycD, and Myc transcript synthesis and degradation, as well as parameters controlling the growth of cells (Appendix). Importantly, we were able to recapitulate the population dynamics (Figure 5.4C), the

fraction of cells dividing or dying in each generation (Figure 5.4D), as well as the growth curves of growing and non-growing cells in each generation.

Figure 5.4. Multi-scale agent-based modeling of the B cell response. Established ordinary differential equation models for NFκB signaling (Almaden, *in press*), apoptosis [193], and the cell cycle [152] were implemented and combined into one integrated model (**A**). Blue, green, and red colors represent NFκB, apoptosis, and cell-cycle modules, respectively, while bolded species represent active IKK (input), cleaved PARP (death readout), and cdh1 abundance (mitosis readout). Instances of the integrated model were incorporated into cellular agents, extrinsic noise was introduced to mimic cell-to-cell variability, and the agent-based model was solved one generation at a time, with division resulting in the creation of two new agents, and death resulting in the removal of the agent from the population (**B**). A comparison of agent-based modeling solutions to the time-lapse microscopy dataset is shown (**C-F**). Cell counts normalized to start count (**C**), fraction of cells dividing or dying in each generation (**D**), average size of growers in each generation as a function of % lifetime (**E**), and average size of non-growers in each generation as a function of % lifetime (**F**) are compared. Error bars represent SEM or 1/n.

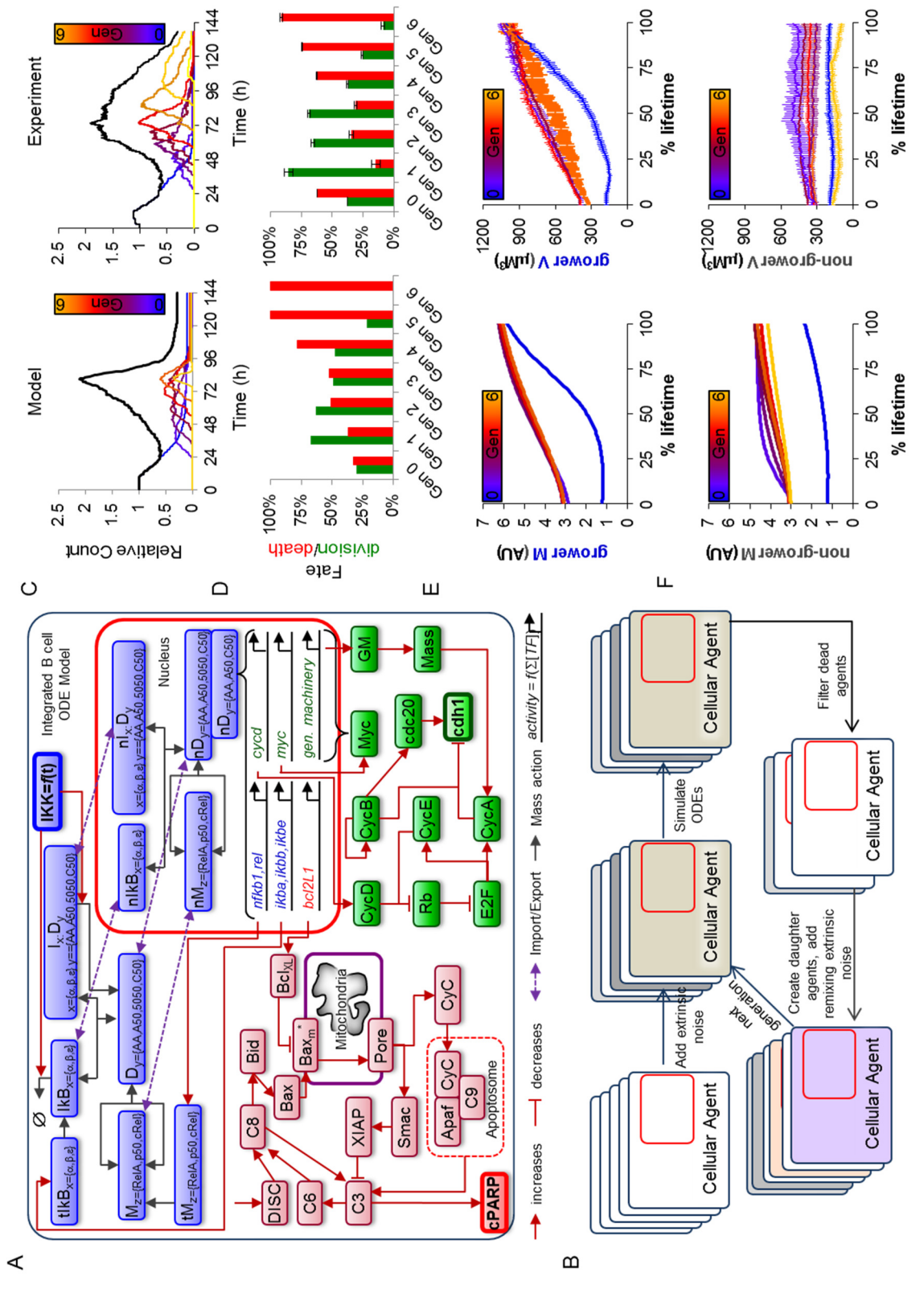
A
B
C
D
E
F
Integrated B cell ODE Model
Nucleus
IKK=f(t)
Ø
DISC
C8
C6
C3
Bid
Bax
Bax*
Bcl-XL
Mitochondria
Pore
XIAP
Smac
Apaf
CyC
C9
Apoptosome
cPARP
nfkb1,rel
ikba,ikbb,ikbe
bcl2L1
cycd
myc
gen. machinery
CycD
Rb
E2F
CycB
CycE
CycA
Myc
cdc20
cdh1
GM
Mass
increases
decreases
Import/Export
Mass action
activity = f(Σ[TF])
Cellular Agent
Add extrinsic noise
Simulate ODEs
Filter dead agents
next generation
Create daughter agents, add remixing extrinsic noise
Model
Experiment
Relative Count
Time (h)
Gen 0
Gen 1
Gen 2
Gen 3
Gen 4
Gen 5
Gen 6
Fate
division/death
grower M (AU)
grower V (μM³)
non-grower M (AU)
non-grower V (μM³)
% lifetime

5.2.2. Predicting population behavior

Next we used the model to predict the population behavior in B cells missing NFκB cRel, in cells exposed to lower concentrations of the stimulus, and in cells treated with rapamycin. This was achieved by increasing the IKK activity decay, removal of cRel monomer production, and a 30% decrease in translation rates, respectively. Time lapse imaging showed that NFκB cRel deficient cells had reduced cell counts caused by premature cell-cycle exit (Figure 4.4A-B) as well as a commitment defect (Figure 4.4E,H), while cell growth remained largely the same (Figure 4.4C). Importantly, the multi-scale model predicts exactly this behavior (Figure 5.5 B-F; red vs blue), although the decrease in cell-cycle commitment is not predicted to be as pronounced (Figure 5.5C). Importantly, the model also predicts an increased tendency for progenitor cells to start growing and then die, demonstrating a decision enforcement phenotype for NFκB cRel (Figure 5.5D). Furthermore, the model readily predicted the population response for cells stimulated with a lower dose of CpG (Figure 5.5, green), as well as the effects of rapamycin pre-treatment (Figure 5.5, purple). Specifically, the model predicts that a lower concentration of the mitogen should decrease the fraction of cells that divide in generations 3+ (Figure 5.5C, green), which adds up to a dramatic decrease in the total B cell population (Figure 5.5B, green). Rapamycin pre-treatment, which results in defective cell growth and ribosome biosynthesis, as well as a dramatic decrease in cells that divide more than once, can be recapitulated accurately by simply decreasing the protein translation rate by 30% (Figure 5.5, purple). Importantly, this also results in longer delays prior to death in both simulations and time-lapse microscopy datasets (Figure 5.5D, purple lines). Cell growth remained constant with respect to % cell lifetime under all conditions in both experiment and model simulations (Figure 5.5 F,G), suggesting that cell size is correlated with cell-cycle progression.

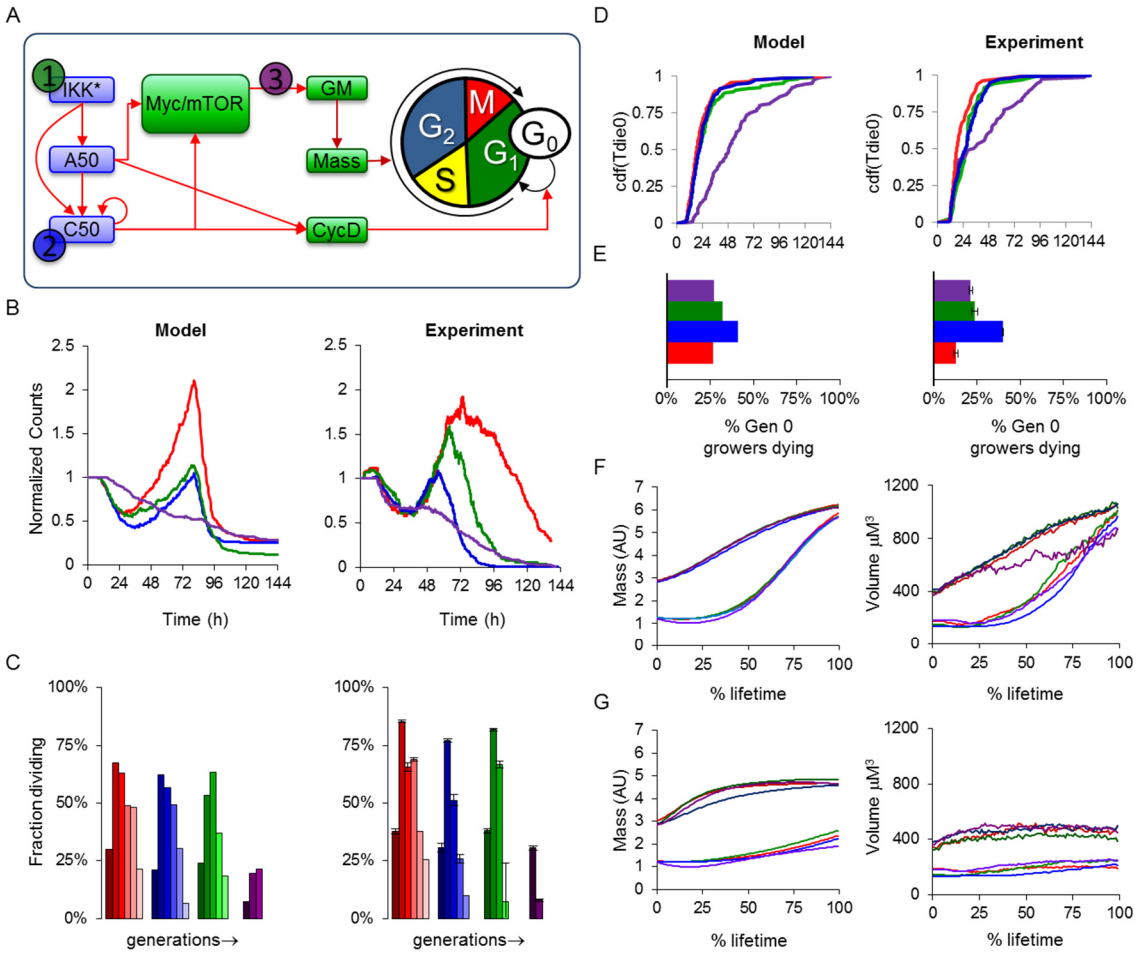

Figure. 5.5. The multi-scale model predicts the effects of low stimulus, cRel knockout, and rapamycin treatment. After parameterizing the multi-scale model using results from wildtype B cells stimulated with 250 nM CpG (red), we predicted the effects of decreasing IKK duration (green), lack of NFκB cRel (blue), and decreased protein synthesis (purple) *in silico*, and compared the results to those from analogous time-lapse microscopy experiments where we stimulated with only 10 nM CpG, used cRel deficient cells, or pretreated with 1 ng/mL rapamycin (**A**). **B-F**) Side-by-side comparison of modeling and experimental results: total cell counts (**B**), fraction of dividing cells in each generation (**C**), cumulative distribution of progenitor death times (**D**),fraction of growing progenitors that died (**E**), average growth trajectories for growing (**F**) and non-growing (**G**) generation 0 and 1 cells as a function of % lifetime. Error bars = 1/n.

5.2.3. Testing how extrinsic variability affects the population response

Given that our model incorporates parameters for various sources of extrinsic noise, NFκB induction strength, and total IKK protein levels, we concluded our study by simulating how protein variability, and the strength of NFκB signaling affects the population response (Figure 5.6). We found that protein variability plays a dramatic role in controlling both the fraction of responding cells in each generation as well as the duration of the cell-cycle and death pathways. Specifically, doubling the coefficient of variation associated with protein synthesis/degradation kinetics, or total protein amounts resulted in a dramatic increase in the total population of cells caused by a sustained cell-cycling, faster interdivision times, and longer survival times (Figure 5.6, red). The opposite is true if protein variability is halved (Figure 5.6, blue). Interestingly, increasing the variability of the total IKK between cells resulted in a nearly identical outcome, however increasing the induction strength of NFκB cRel, and p50 as well as the amount of IKK resulted in ~2.5 fold increase in the population response, while leaving division and death timing intact. This was caused by an increase in the fraction of dividing cells for all generations, however increase NFκB induction had a large effect on late activation (generations 4+), while increased IKK tended to upregulate early activation (generation 0).

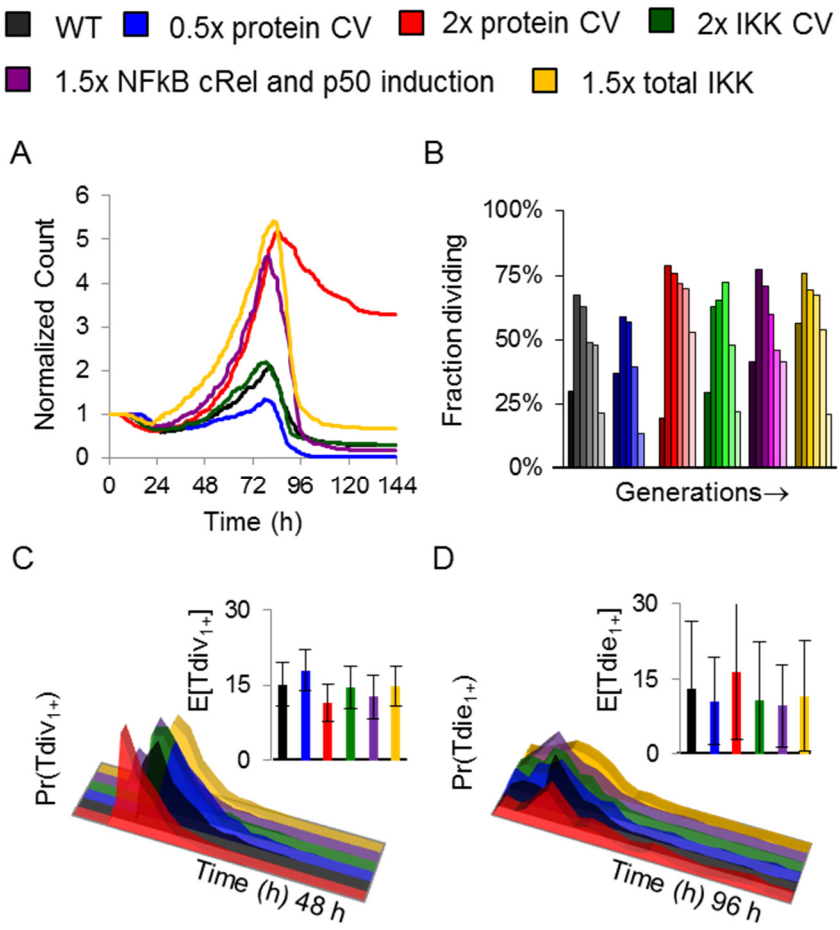

Figure 5.6. NFκB levels determine fate, while protein variability affects both timing variability and fate. Simulations were repeated with lower protein variability (blue), higher protein variability (red), higher IKK abundance variability (green), increased NFκB cRel and p50 induction (purple), and increased IKK abundance (yellow). Population count dynamics (**A**), fraction of dividing cells in each generation (**B**), and generation 1+ division (**C**), and death (**D**) times are shown. Insets summarize mean and standard deviation of the fate time distributions.

5.3. Discussion

Agent-based models (ABMs) explicitly model autonomous entities within a system and provide a natural computational framework for modeling immune processes (recently reviewed in [145,146]). As such, ABMs have been successfully utilized to provide insights into molecular dynamics of the NFκB signaling system [191], wound healing [190], the multi-scale effects of acute inflammation [194], as well as the implications of transgenerational epigenetic inheritance [165], and even the evolution of aging [166]. We constructed a multi-scale agent-based model to test if NFκB enforcement of the decision, coupled with extrinsic heterogeneity in the cellular state could describe the observed time-lapse cellular dynamics an population response. Since the number of parameters typically scales non-linearly with the size of the model, our strategy was to use previously established models, and manually parameterize just the connections between them based on the aforementioned experimental observations. Surprisingly, we were able to recapitulate all of the major features of the cellular and population responses (Figure 5.4) by imposing reasonable NFκB driven Bcl_{XL}, Myc, cyclinD transcription, and Myc-dependent general machinery production (general machinery synthesis was originally controlled by mass, which was in turn controlled by the general machinery forming a positive feedback loop [152]). To simulate the population response, we encapsulated the integrated B cell model into cellular agents which were initialized with differences in starting protein concentrations or synthesis/degradation rates analogously to previous studies [193,195]. It is important to note, that we did not explicitly bias cells toward one fate or the other in our simulations, instead allowing both processes to run simultaneously, however in practice fate was biased by the nuclear dynamics of NFκB, which promoted transcription of anti-apoptotic Bcl_{XL} as well as growth via the upregulation of Myc, and cell-cycle progression by

enhancing transcription of cyclinD. Furthermore, *in silico* knockout of NFκB cRel, which can promote its own transcription, essentially halves the population response as NFκB RelA, the only remaining NFκB family member that is able to trans-activate gene expression, drops to levels that are insufficient for promoting growth/cell-cycle progress and survival after only a few generations (Figure 5.5). Decreasing the duration of the IKK input faithfully captured the population and cellular behavior of cells stimulated with a decreased concentration of the CpG stimulus, suggesting that a graded response to the intensity of the stimulus may be achieved on the population level by modulating the duration that upstream kinases remain active. Simulations suggest that further gradation may be achieved by modulating the amount of upstream kinases (Figure 5.6, yellow), or the strength of NFκB induction (Figure 5.6, purple), affecting the fraction of cells that divide in early or late generations, respectively. Interestingly, simulations reveal that the amount of extrinsic protein variability controlled both the fraction of cells dividing in later generations, as well as the timing of division and apoptosis in cells. Higher protein variability alone led to out of control growth and prolonged survival of B cell populations, indicative of a tumor state. Treatment with rapamycin, which results in slowed growth and cell-cycle exit after just one division (Figure 5.6, purple), can be modeled by simply decreasing the protein translation rate by 30%, indicating that even a modest decrease in general cellular machinery or metabolism can dramatically decrease the population dynamics of rapidly dividing cell populations.

5.4. Methods

The multi-scale modeling Matlab 2012b files are included as MultiScale.zip in the supplementary files. Videos of tracked B cells stimulated with 10 nM CpG, missing NFκB cRel, or treated with rapamycin, are included in the supplemental files as WT10nM.mpg, CKO250nM.mpg, and Rap250nM.mpg.

5.4.1. Multi-scale agent-based modeling

Ordinary differential equation models of the cell-cycle [152], apoptosis [193] and NFκB signaling (Almaden, *in press*) were implemented in Matlab (Mathworks), using the ode15s solver for stiff problems. The modules were connected by imposing cooperative Hill activation of the CyclinD, Myc, and Bcl_{XL} promoters:

$$\frac{d[tX]_{X=CycD,Myc,BclXL}}{dt} = a_x\left[(1-b_x)\frac{\left(\frac{\left(k_{A50}[A50_n]+k_{C50}[C50_n]\right)}{k_x}\right)^2}{1+\left(\frac{\left(k_{A50}[A50_n]+k_{C50}[C50_n]\right)}{k_x}\right)^2}+b_x\right]-a_x^{-1}[tX],$$

where k_{A50} and k_{C50} are constants determining the relative activation strength of nuclear RelA:p50 heterodimer and cRel:p50 heterodimer, respectively. The constants a_x, a_x^{-1}, b_x and k_x determine the transcription rate, transcript degradation rate, the degree of basal activation and the concentration resulting in half-maximal activation of the promoter for gene x, respectively. Our molecular assays revealed that cRel deficient cells had approximately half the mTORc activity and approximately one third the Bcl_{XL} activity, therefore we set k_{A50} and k_{C50} to 0.5 for all promoters except for the Bcl_{XL} promoter for which we decreased k_{A50} to 0.333, while increasing k_{C50} to 0.666. For simplicity, we also assumed that the growth of general cellular machinery, the model species representing

catabolism and protein synthesis in the cell, was dependent on the current mass, and the concentration of Myc:

$$\frac{d[GM]}{dt} = a_{GM}\left[(1-b_{GM})\left(\frac{\left([Myc/TOR]/k_{GM}\right)^2}{1+\left([Myc/TOR]/k_{GM}\right)^2}\right)\left(c_{GM}[Mass]^2 e^{-d_{GM}[Mass]^2}\right)+b_{GM}\right]-a_{GM}^{-1}[GM]$$

,

where a_{GM}, a_{GM}^{-1}, b_{GM}, c_{GM}, d_{GM}, and k_{GM} are constants that normalize for synthesis rate, degradation rate, basal activity, early mass-dependent growth rate, and maximum cell size, respectively. The integrated model consisting of these three modules constituted one cellular agent, and was solved independently in a generation-by-generation fashion until the simulation time limit was reached, the cell divided ([cdh20] >0.2), or the cell died ([cPARP] ≥ 25,000 molecules/cell). Upon division, two new copies of the model were generated with half the mass and general machinery (we assumed that the concentration of all other species was unchanged). If daughter volume variability was modeled, the mass and general machinery were multiplied by a constant r_a or r_b such that $r_a \sim \mathrm{N}(1.0, CV_{partition})$ and $r_b = 1 - r_a$, where $CV_{partition}$ is a the coefficient of variability of daughters measured from wildtype microscopy. In addition, to mimic protein concentration remixing which leads to the loss of correlation with subsequent divisions, we generated independent log-normally distributed (if not modeling synthesis and degradation), or normally distributed protein synthesis and degradation reactions concentrations as well as log-normally distributed total IKK concentrations and set the daughter values to the average of the newly generated and the value inherited from the mother. This ensured that the daughter cells had correlated protein dynamics, but that the correlation decreased with each generation. At the time of division, nuclear proteins were redistributed evenly among the nucleus and cytoplasm to mimic nuclear envelope

breakdown. Models that ended in death were removed from the pool of running models. Multi-scale models, which consisted of many such cellular agents, were initialized at generation 0 to contain n independent integrated models. To model cell-to-cell protein abundances, we initialized each model with initial protein concentrations sampled from lognormal distributions if the total protein concentration was fixed, or with normally-distributed protein synthesis and degradation rates if the protein had explicit synthesis and degradation reactions defined. In addition, the total amount of IKK, the upstream signal responsible for NFκB activation, was also assumed to be log-normally distributed. Finally, we assumed that the initial mass and general machinery of cells was normally distributed as determined by microscopy. After an initial equilibration phase with only basal IKK signaling to NFκB, a quiescent steady state was achieved as defined by lack of cell-cycle progression and species stabilization. Then, all models were solved independently for each generation until the simulation time was elapsed. For a full description of model reactants, parameters, fluxes, and species, please see refer to the appendices.

5.5. Acknowledgements

Chapter 5, in part, is currently being prepared for submission for publication of the material and may appear as Maxim N. Shokhirev, Jonathan Almaden, Jeremy Davis-Turak, Harry Birnbaum, Theresa M. Russell, Jesse A.D. Vargas, Alexander Hoffmann. “A multi-scale approach reveals that NFκB enforces a decision to divide or die in B cells.” Jonathan Almaden helped with B-cell purification. The dissertation author was the primary investigator and author of this paper.

Chapter 6

Conclusion

In this chapter I would like to briefly and informally provide a historic context for each chapter, summarize major findings, discuss the possible implications of the results, and elaborate on how these studies can be extended in the future.

6.1. Chapter 2

Chapter 2 is the culmination of four-year effort to develop and publish a tool for interpreting CFSE flow cytometry time courses. This began as a rotation project in the summer of 2009, when my thesis advisor, Alex, showed me a then recently published paper detailing the cyton model [44], which introduced me to the complexity and heterogeneity of the B-cell immune response. I spent the next few days implementing the model and experimenting with the parameters. My rotation project culminated in a computational tool for fitting generation cell counts using various algorithms. I drafted the first outline for the paper in September of 2010 and began to write it up soon after. One of the goals of the study was to account for the inherent measurement noise by repeatedly fitting generational cell counts fitted using a third-party software called FlowJo (TreeStar). This seemed very *ad hoc* to me as the solutions depended on a very complex objective function and the quality of the FlowJo fitting, making quantitative validation of the tool challenging. Therefore, I decided to try to fit the CFSE data directly, thereby eliminating the middle man (FlowJo). Unfortunately, this turned out to be a major programming challenge as the interpretation of CFSE datasets requires user input in the form of manual gating, channel compensation, and peak calling. This resulted in the

development of FlowMax, a computational suite that incorporates all of the necessary function for flow cytometry analysis as well as peak calling, and cyton model fitting tools (see supplementary files for source code and succinct tutorial). In late 2009, the group that published the cyton model published the most influential paper of my Ph.D. career [21], in which they detailed a single-cell time-lapse microscopy study of stimulated primary B cells. The results indicated that B cells did not grow in their last division, suggesting that instead of a race, B cells may in fact be “deciding” their fate. This prompted us to reformulate the original cyton model, in which dividing cells can still die, to the fcyton model in which growing B cells can only divide, while non-responding cells can only die. With FlowMax as my sandbox, and the reformulated fcyton model in hand, I spent the next two years characterizing the FlowMax methodology (Figure 2.1), applying the tool to CFSE time courses of wildtype and NFκB deficient B cells, and periodically resubmitting the manuscript.

There were several key results that surfaced during the course of our investigations. First, it became apparent that some parameters were always accurately determined, while others could not be systematically determined even in the presence of perfect datasets. This suggests that some parameters have a large impact on the solution (e.g. the fraction of responding progenitors), while other parameters could be typically be kept random without significant loss of concordance (e.g. the average death time of responding cells). Furthermore, we found that solution accuracy was robust to poor CFSE staining (wide peaks), but sensitive to the quality of the initial purification process. In addition, the number of time points is not as crucial as long as the population dynamics can be sampled at early, intermediate, and late times. Therefore, it is generally better to sample at say 24 h, 72 h, and 120 h post stimulation than at 48 h, 60 h, 72 h, 84 h, 96 h post stimulation as the later time course is likely to miss both the initial

divisions and late-phase contraction of a typical B-cell response. Together, these results demonstrate that a single-set of “best-fit” solutions is meaningless without some measure of sensitivity and degeneracy, which is achieved during FlowMax fitting using sensitivity estimation, and subsequent agglomerative clustering of the sensitivity ranges until only disjoint solution spaces remain. Finally, when we turned FlowMax to phenotyping of NFκB deficient B-cells stimulated with LPS and anti-Igm, we confirmed that cRel is essential for BCR signaling and important for TLR4 signaling, affecting primarily the fraction of cells that respond, as well as survival in TLR4 stimulated cells. On the other hand, *NFκB1*, the gene encoding NFκB p105/p50 plays a repressive role during BCR signaling by turning down late cell-cycle reentry, while playing a role similar to cRel in the enforcement of B-cell activation and survival during TLR4 stimulation.

While the tool has already been used subsequent studies [150] and (Almaden, *in press*; and Chapter 3), it took several years of resubmissions (from PNAS, to Immunity, PLoS Comp. Biology, and finally to PLoS One), before it was finally accepted for publication. In hindsight, a better approach may have been to focus on characterizing other CFSE datasets, while devoting only several figures to the description and characterization of the tool, which resulted in a long and technical paper that generated considerable friction with reviewers. Instead, we could have focused on analyzing CFSE datasets from B cells treated with various NFκB, cell-cycle, and apoptosis inhibitors to characterize the effect that pharmalogical perturbation has on the distributions of cellular outcomes (e.g. how do specific inhibitors affect division timing, the fraction of responders, etc.). In addition, it would have been interesting to see how the proliferative patterns changed when various cell types were mixed, as populations could be distinguished with the help of fluorescently labeled antibodies specific for B cells, such as B220. By tracking two populations simultaneously and comparing the behavior to that

of purified subsets alone, it should be possible to determine the contributions that cohabitation has on specific cellular parameters (such as the fraction of responding cells). Importantly, since the population response is robust, FlowMax can be used as a fast user-friendly tool for the characterization of patient samples. For example, lymphomas may be characterized in the presence of chemotherapeutic drugs targeting specific components of the cell death, signaling, or cell-cycle pathways followed by FlowMax analysis to test if the target pathway was indeed affected (Figure 6.1). Tumor characterization is typically done using gene expression profiling, however, due to the extreme heterogeneity of tumor samples, a better approach may be to phenotype the collective population dynamics of the tumor, resulting in potentially more robust classification, personalized treatment, and improved survival [22,168,196] FlowMax is available free of charge as a supplemental file, and its source may be adapted as better population models become available, thereby serving as a general computational framework for analyzing ubiquitous CFSE flow cytometry datasets. At a minimum it can be used in lieu of costly commercial packages for routine flow cytometry analysis and quantification.

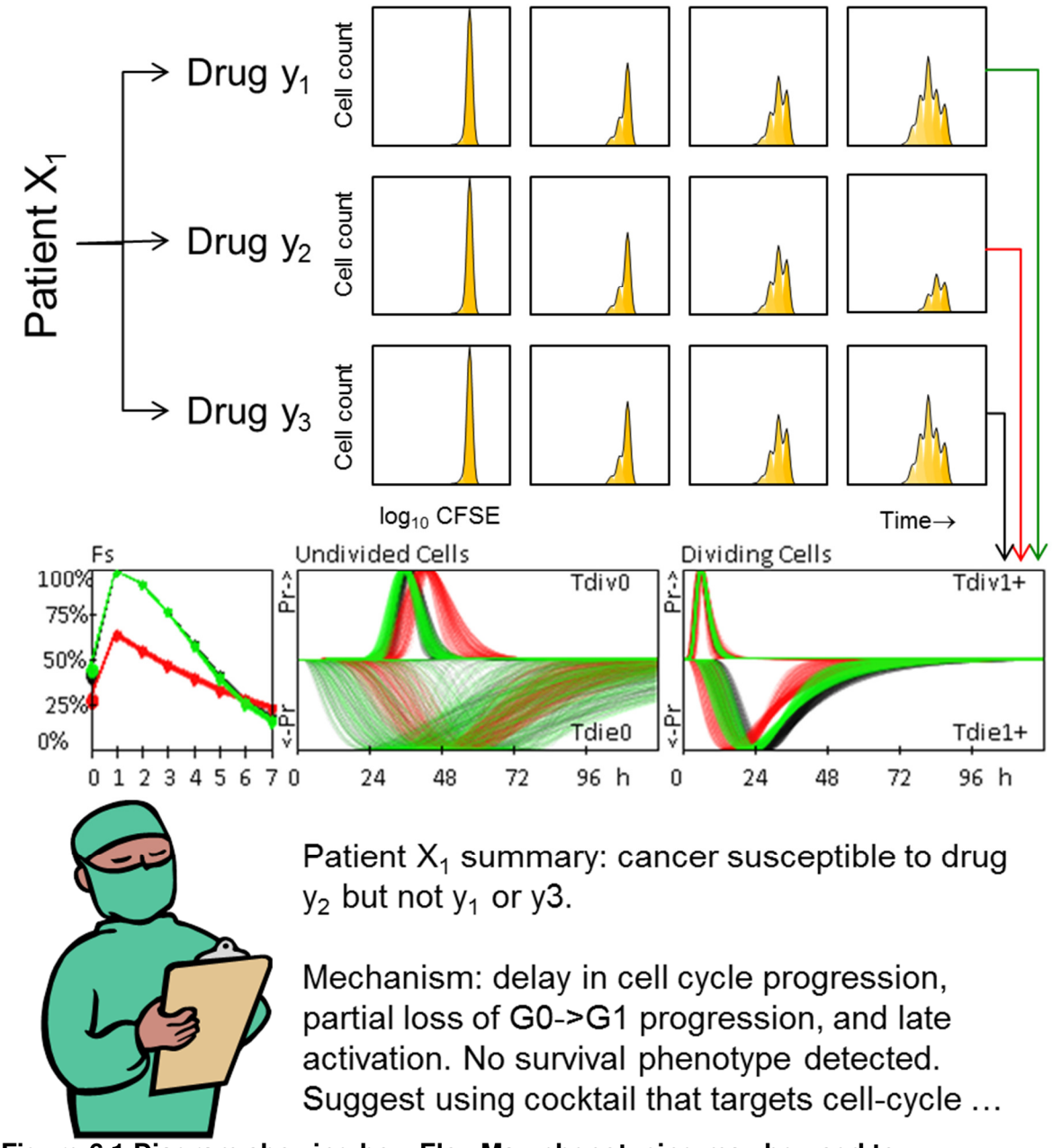

Patient X_1 summary: cancer susceptible to drug y_2 but not y_1 or y3.

Mechanism: delay in cell cycle progression, partial loss of G0->G1 progression, and late activation. No survival phenotype detected. Suggest using cocktail that targets cell-cycle …

Figure 6.1 Diagram showing how FlowMax phenotyping may be used to characterize the mechanics of B cell tumors from specific individuals.

6.2. Chapter 3

In this chapter, we developed a time-lapse microscopy and cell-tracking pipeline to characterize the growth pattern and genealogy of hundreds of individual B cells. I first proposed using time-lapse microscopy to characterize the behavior of B cells shortly

after reading the study by Hawkins and coworkers which showed that it is feasible and highly informative [21]. In addition, a recent paper by the Covert group showed that NFκB signaling is heterogeneous on the single-cell level [197], reinforcing the idea that microscopy can be used to tie together molecular and cellular scales. In fact, I suggested measuring single-cell NFκB dynamics in B-cells as part of my second year qualifying exam. This was a risky venture at the time, as I had no prior experience with microscopy and our lab had just started to look into purchasing a microscope. Nevertheless, I started to routinely take videos of B cells as soon as we purchased our first microscope. To say that this was a daunting challenge would be an understatement. In fact, it took over a year before I could find the optimal conditions under which B cells would not immediately die, get swept away by convection currents, or die from dried out well conditions. After trying everything from 3D printing of custom designed micro grids, application of various coatings to the bottom of the well, etc. I ended up finding that B-cells at a concentration of ~ 50,000 per/mL stimulated with 10-250 nM CpG, and seeded into 1536-well clear-bottom uncoated plastic micro plates resulted in minimal convection, typical cell proliferation of 7-8 division rounds, and typically at least 120 h of imaging time before the wells started to appreciable dry out.

After successfully taking 8,000 images of hundreds of cells, I quickly became overwhelmed with data, and had to find methods for reliably quantifying cellular behavior in the images. At the time, no freely available tools were available for accurately tracking B cells, which are highly mobile, deformable, growing, dividing, and dying. In the first year, I attempted to automate cell tracking with modest results obtained when B cell boundaries were easy to discern. Unfortunately, automated tracking of B cell dynamics turns out to be a computationally hard problem and my automated methods ultimately ended in disaster after tracking cells for just several hours due to runaway error

accumulation. In desperation, I turned to a semi-automated approach which relied on human input to tackle the challenging problem of resolving ambiguous tracks. I spent the next year building training and utilizing a software tool that used a modified Hough transform [198] to detect cells, followed by an active-contour approach [118,199] for predicting cell shape from one frame to the next by taking into account nearby edges, cell shape, size, and rough paths laid out by the curator. When parameterized, this approach allowed me to track arbitrarily difficult cell paths as fast as my own mind could solve the problem, reducing the time to track a single cell from many hours to several minutes on average. The tracking tool dubbed Force-based Algorithm Semi-automated Tracker (FAST), is provided as a supplemental file along with videos of tracked cells from wildtype, NFκB cRel deficient, and drug-treated cells.

Tracking wildtype B cells revealed that B cells can be described as either growing and dividing, or poorly growing and dying, suggesting that only one process is active in the cells at the same time. This was also shown using the observed time to decision (start of growth), time to death, and time to division distributions, which predict that most cells would start to grow and then die if division and death processes were occurring in simultaneously in cells. In fact, we observe the opposite as almost all growing cells are protected from death especially since death typically occurs earlier than division in generation 0 cells. This prompted us to explore the molecular drivers of this decision making process using molecular assays.

Having established the experimental and computational pipeline for tracking populations of dividing and dying B cells, and having applied it to four particular datasets of interest, it is clear that the stage is set to characterize the single-cell behavior of lymphocytes under other conditions. For example, cell-cycle and apoptosis inhibitors can be used to further phenotype the mechanistic roles of cyclins (primarily cyclin E which is

implicated in controlling cell cycle reentry in proliferating cells [25]), and cell cycle inhibitors $p21^{cip}$ and $p27^{kip}$. Furthermore, it would be great to test if B cells treated with apoptosis blockers were indeed quiescent, as it entirely possible that decision enforcement is not permanent, but acts transiently in the first several division rounds to ensure rapid expansion. Indeed, we observed that decision enforcement is typically lost after the first few rounds of division even when NFκB cRel is present to act as enforcer, reinforcing the general theme that NFκB cRel is important for keeping cells committed for at least several cell-cycles. Under this hypothesis, tracking IkBδ deficient cells should reveal a prolonged response caused by late-phase loss of NFκB inhibition and prolonged decision enforcement provided the upstream signaling mediators remain activated by receptor activity for sufficiently long periods. Finally, it would be informative to see if B cells that have decreased receptor turnover rates experience a prolonged response, as receptor signaling to IKK drives NFκB activation, and tapers off as receptors and mediators are recycled.

6.3. Chapter 4

Single cell molecular assays are the subject of Chapter 4 and are the culmination of several fruitful collaborative efforts between myself various members of the signaling systems lab and the Fluidigm Corp. which provided training, materials, and live expertise for performing the single-cell RNA sequencing experiments. Andrew Doedens, a post-doctoral scholar in Ananda Goldraths lab generously lent us a fluorescently labeled anti-NFκB cRel antibody to use in immunofluorescence studies, which was useful for determining the abundance of cRel in single cells. Jesse Vargas helped design the IF experiments and trained me to carry out the protocol. Jon Almaden ran a series of western blots testing for mTORc1 activation and an RT-PCR analysis of Bcl_{XL}

transcription. Finally, Jeremy Davis-Turak, and Harry Birnbaum collaborated together to align, map, and normalize the single-cell RNA sequencing dataset.

This project was first developed in the fall of 2013 as it became clear that we did not know how the B-cell decision was determined on the molecular level. Single-cell RNA sequencing and immunofluorescence studies were carried out simultaneously in an attempt to characterize the global transcriptome signature of large (i.e decided to respond) and small cells (i.e. failed to respond). As single-cell transcriptome sequencing was still brand new at the time and required considerable investment of time and money to optimize, we decided to take advantage of a live demonstration to facilitate discovery, while avoiding early mistakes that typically pop up when first starting to optimize a new experimental methodology. Luckily, we were able to capture several dozen B cells and proceeded to prepare oligonucleotide libraries for the five smallest and five largest cells as well as bulk positive, bulk 0 h, and negative controls. Analyzing the results, we found that there was high cell-to-cell variability in transcript levels even within groups of large and small cells. Nevertheless when we scored each gene using a metric that took into account significant counts for all cells within a group a familiar pattern arose. Big cells tended to upregulate gene regulation, metabolism, cell-cycle, and apoptosis genes, while down-regulating adhesion and autophagy/senescence pathways. Furthermore, the NFκB signaling pathway was significantly upregulated in large cells. This prompted us to probe for specific NFκB monomers and relevant downstream targets of NFκB by immunofluorescence and traditional biochemical studies confirming that NFκB cRel mediates growth and survival in B cells.

In the immediate future, it would be great to confirm the effect of NFκB cRel on the abundance of Myc, and Cyclin D2/3 in B cells by RT-PCR and western blot, The relative magnitude of the change would help to further constrain the multi-scale model

presented in chapter 5. In addition, looking at several time points prior to 24 h (at 2 h and 8 h post stimulation) could help trace the dynamics of essential molecular players providing temporal constraints for the multi-scale modeling effort. This work could be carried out in the span of a few weeks or months by the next generation of undergraduate and graduate students.

Future single-cell assays promise exciting revelations of single cell behaviors. Clearly, being able to directly link readouts for several proteins and cell size in individual cells is key to deciphering molecular relationships in the context of dramatic heterogeneity caused by variability in extrinsic cell states (e.g. tumors and organs). The challenge will be in proper sampling. Single-cell transcriptome sequencing is expensive and at best currently yields 96 cell samples per microfluidic chip, making studies of low-abundance cell subsets laborious and exceedingly expensive. Nevertheless, this is a powerful method for studying cellular processes that are driven by heterogeneous cellular states. As these data quantify the abundance of tens of thousands of transcripts within each cell, data analysis will continue to dominate experimental workflow. Given the chance and resources, it would be interesting to scale up the experiment we performed in this chapter tenfold to obtain transcriptome information on approximately 50 small and 50 large cells for both wildtype and aberrant B cells at 2 h, 8h, an 24 h post stimulation with CpG, BAFF, and CD40L, which signal through the canonical, non-canonical, and both NFκB pathways, respectively, providing a wealth of data on cell-to-cell variability, dynamics, disease mechanisms, and signaling crosstalk. The future of single-cell fluorescence in B-cells likely lies in live-cell microscopy of B cells from genetically engineered mice expressing fluorescently-labeled NFκB cRel, Myc, Bcl_{XL} and Cyclins D2/3 and E. As it is possible to reconstruct B-cell genealogical trees, concurrent measurements of key molecular players will provide essential clues to how dynamics

dictate decision making, as the history of signaling molecules provides more information content than individual snapshots. Furthermore, as the timing of division and death processes varies considerably between cells, dynamic observations of key molecular regulators can be directly compared to the timing of events in individual cells.

6.4. Chapter 5

The culmination of the dissertation lies with the construction and parameterization of a multi-scale agent-based model consisting of a population of integrated ODE models running in parallel, thereby simulating the population response as a function of the biochemical reactions governing NFκB signaling, apoptosis, and cell-cycling. The first step in model construction was the reimplementation of the established Conradie/Tyson model [152] of the mammalian cell cycle into a common language (Matlab). Matlab was selected for two main reasons. First, the NFκB signaling models developed in our lab are all implemented in Matlab, second Matlab offers convenient and efficient solvers for inherently stiff systems of ODEs (all three of these models are inherently stiff) as well as conventions for parallelizing computation across up to 12 cores, essentially speeding up the computation by another order of magnitude (essential considering the size the model and the fact that hundreds of copies of the model will need to be simulated in parallel to obtain a single multi-scale solution). In the early days, I even considered implementing a GPU-based solver, but luckily realized that this is not feasible for models of this size (not to mention the complexity of implementing an ODE solver). Model integration proceeded in three steps over the next year. First, the cell-cycle model was implemented in Matlab and tested for solution accuracy. Next, the cell-cycle model was combined with the xEARM model that was being developed by Paul Loriaux in the lab [156] and a basic population consisting of competing outcomes could

be modeled for the first time. At this time, the sensitivity of various parameters on the timing of division and death was performed (Figure 5.2). Finally, the NFκB model was incorporated and implicated in the production of Myc, CyclinD, and Bcl_{XL}. By encompassing each integrated model within autonomous agents, we could readily account for cell-to-cell extrinsic variability by distributing the starting protein concentrations (or synthesis an degradation rates which are themselves functions of proteasome and ribosome abundance variability), the initial size of cells, and the variability associated with uneven distribution of cell mass at the time of division. Furthermore, this enabled us to explicitly account for correlations in the timing of processes between sister and cousin cells by implementing remixing of protein abundances inherited from the mother cell.

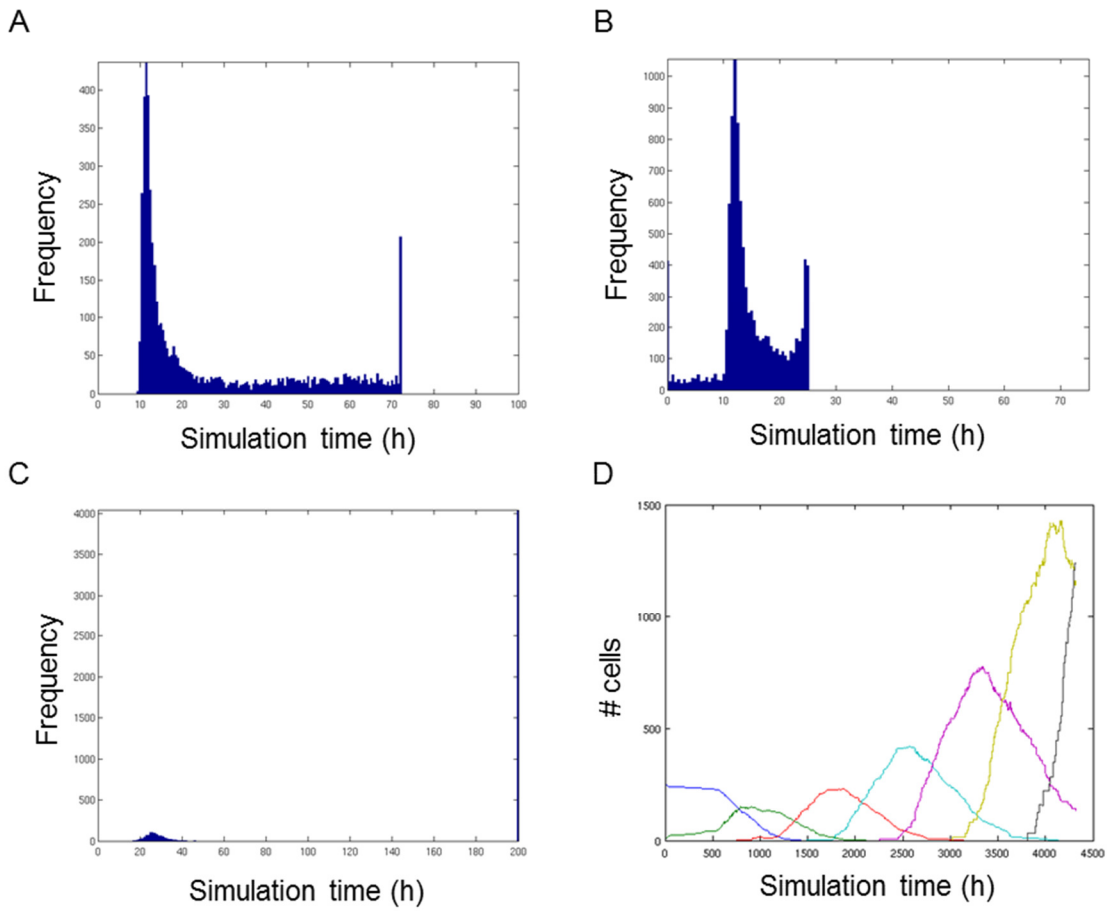

Figure 6.2. Early iteration of the integrated cell-cycle/apoptosis models. **A**) Variability in the timing of the first division. **B**) Variability in the timing of the subsequent division. **C**) Variability in the timing of cell death (notice that many cells survived indefinitely). **D**) Population counts of agents in each generation. Notice that cell populations increased indefinitely as there was no mechanism for controlling division/death rates as a function of generation or time.

Upon completing chapters 3 and 4, we were finally poised to parameterize the model, with NFκB-driven synthesis of pro-survival Bcl_{XL}, Myc, and CyclinD using the results from the molecular assays and time-lapse imaging studies to ensure that the model could accurately recapitulate the observed doubling in total cell count during peak response, an initial ~35% of progenitors dividing, monotonically decreasing fractions of cells that divide in subsequent divisions starting with a high fraction of cells dividing again after the first division, as well as the characteristic observed size trajectories of growing and non-growing cells, and observed Tdiv and Tdie distributions. The resulting model was then used to predict the effects decreased stimulation (faster decaying IKK activity), cRel deficiency, and rapamycin pretreatment (30% drop in protein synthesis). Subsequent time-lapse imaging experiments showed remarkably similar responses, suggesting that the model was generally applicable to many different situations. Finally, we used the model to demonstrate that protein variability is expected to affect both timing variability as well as the magnitude of the population response, while increased average IKK levels and NFκB cRel transcription resulted in increased population responses but unchanged variability in the timing of division or death.

While the multi-scale model will undoubtedly be continuously modified as new parameters and molecular players come to light, an exciting next step would be to explicitly model the activation of various TLRs and the BCR, enabling the prediction of pathogen specific immunity different pathogens will activate specific receptors with varied strengths. Furthermore, by explicitly modeling receptor dynamics, we can predict how receptor, and receptor-proximal components will affect the population response. Finally, since the B cell receptor is unique and undergoes class-switching and somatic hyper mutation, an agent-based model could be readily extended to study the population

dynamics of the GC reaction and adaptive immunity providing insights into both branches of the immune response (Figure 6.3).

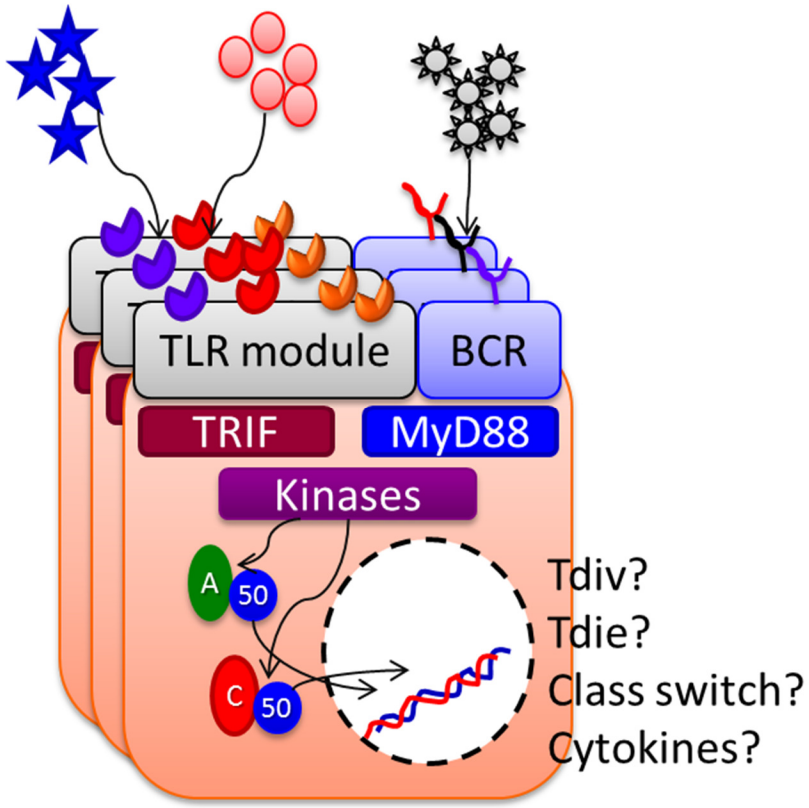

Figure 6.3. The multi-scale receptor-specific population model.
By incorporating modules for TLR and BCR mediated activation of Kinases via TRIF and/or MyD88, we can expand the multi-scale model to explore pathogen specificity, receptor editing, as well as paracrine/autocrine signaling across scales.

Appendices

These appendices tabulate the various reactants, reactions, parameters, fluxes, and extrinsic variability coefficients required for modeling the integrated B cell multi-scale model. Matlab model files are included as MultiScale.zip in the supplementary files.

A. Integrated B-cell model species. Prior to simulation, the model was equilibrated starting from initial concentrations, x_0, with basal IKK signaling and no death signal (L=0) for a period of 24 h. Due to relatively high initial cyclin levels, the equilibration was repeated until the cell divided ([Mass] and [GM] was halved as usual).

#	Species	x_0	#	Species	x_0	#	Species	x_0	#	Species	x_0
1	tIkBa	0	**37**	IkBbA50n	0	**73**	pC3	10000	**109**	CytoC	0
2	IkBa	0	**38**	IkBeA50	0	**74**	C8-pC3	0	**110**	Apaf	100000
3	IkBan	0	**39**	IkBeA50n	0	**75**	C3	0	**111**	Apaf-CytoC	0
4	tIkBb	0	**40**	IkBdA50	0	**76**	pC6	10000	**112**	act_Apaf	0
5	IkBb	0	**41**	IkBdA50n	0	**77**	C3-pC6	0	**113**	pC9	100000
6	IkBbn	0	**42**	5050	0	**78**	C6	0	**114**	Apop	0
7	tIkBe	0	**43**	5050n	0	**79**	C6-pC8	0	**115**	Apop-pC3	0
8	IkBe	0	**44**	IkBa5050	0	**80**	XIAP	100000	**116**	cSmac	0
9	IkBen	0	**45**	IkBa5050n	0	**81**	XIAP-C3	0	**117**	Apop-XIAP	0
10	tIkBd	0	**46**	IkBb5050	0	**82**	PARP	1000000	**118**	cSmac-XIAP	0
11	IkBd	0	**47**	IkBb5050n	0	**83**	C3-PARP	0	**119**	C3_Ub	0
12	IkBdn	0	**48**	IkBe5050	0	**84**	CPARP	0	**120**	CycA	0.014254
13	tRelA	0	**49**	IkBe5050n	0	**85**	Bid	60000	**121**	CycB	2.228995
14	RelA	0	**50**	IkBd5050	0	**86**	C8-Bid	0	**122**	CycD	0.411217
15	RelAn	0	**51**	IkBd5050n	0	**87**	tBid	0	**123**	CycE	0.170235
16	tP50	0	**52**	C50	0	**88**	Mcl1	20000	**124**	tCycD	0
17	P50	0	**53**	C50n	0	**89**	Mcl1-tBid	0	**125**	tBclXL	1000
18	P50n	0	**54**	IkBaC50	0	**90**	Bax	80000	**126**	Cdh1	1
19	tcRel	0	**55**	IkBaC50n	0	**91**	tBid-Bax	0	**127**	CA	0.001343
20	cRel	0	**56**	IkBbC50	0	**92**	act_Bax	0	**128**	CD	0.039049
21	cReln	0	**57**	IkBbC50n	0	**93**	Baxm	0	**129**	CDc20	0.610581
22	AA	0	**58**	IkBeC50	0	**94**	BclXL	30000	**130**	CDc20T	2.967532
23	AAn	0	**59**	IkBeC50n	0	**95**	Baxm-Bcl2	0	**131**	CE	0.016231
24	IkBaAA	0	**60**	IkBdC50	0	**96**	Bax2	0	**132**	GM	0.747611
25	IkBaAAn	0	**61**	IkBdC50n	0	**97**	Bax2-Bcl2	0	**133**	IEP	0.791894
26	IkBbAA	0	**62**	L	0	**98**	Bax4	0	**134**	Mass	0.930762
27	IkBaAAn	0	**63**	R	1000	**99**	Bax4-Bcl2	0	**135**	p27	0.024804
28	IkBeAA	0	**64**	L-R	0	**100**	M	500000	**136**	PPX	1
29	IkBeAAn	0	**65**	DISC	0	**101**	Bax4-M	0	**137**	pp-Rb	9.859403
30	IkBdAA	0	**66**	flip	2000	**102**	AMito	0	**138**	E2F	1.2212
31	IkBdAAn	0	**67**	flip-DISC	0	**103**	mCytoC	500000	**139**	p-E2F	3.639173
32	A50	0	**68**	pC8	10e4	**104**	AMito-mCytoC	0	**140**	Rb	0.000975
33	A50n	0	**69**	DISC-pC8	0	**105**	aCytoC	0	**141**	E2F-Rb	0.035082
34	IkBaA50	0	**70**	C8	0	**106**	mSmac	100000	**142**	p-E2F-Rb	0.104543
35	IkBaA50n	0	**71**	Bar	1000	**107**	AMito-mSmac	0	**143**	Myc	0
36	IkBbA50	0	**72**	Bar-C8	0	**108**	aSmac	0	**144**	tMyc	0

B. Integrated B-cell model parameters.

#	Parameter	Description	Value	Units	Justification
1	**ki(1,α)**	→tIkbα	0.0009	nM min^{-1}	Parameter value chosen to fit mRNA and protein Expression profiles as measure by RNase Protection (RPA) and Western blot assays, reformulated from [147]to fit a Hill function where Hill coefficient = 1.1
2	**ki(2,α)**	tIkbα→	0.0438	min^{-1}	[148]
3	**ki(3,α)**	tIkbα→Ikbα	12	Proteins/ mRNA min^{-1}	Derived from the elongation rate of the ribosome and corrected for th nucleotide spacing between adjacent ribosomes on the same transcript: 30 nt sec^{-1}/150 nt = 12 min^{-1}
4	**ki(4,α)**	Ikbα→	0.12	min^{-1}	As in #2
5	**ki(5,α)**	nIkbα→	0.12	min^{-1}	As in #2
6	**ki(6,α)**	Ikbα→ nIkbα	0.06	min^{-1}	As in #2
7	**ki(7,α)**	nIkbα→ Ikbα	0.012	min^{-1}	As in #2
8	**ki(8,α)**	transcription delay	0	min	As in #1
9	**ki(9,α)**	Hill c for inducible txn.	1.1		[150]
10	**ki(10,α)**	Hill Kd	150	nM	As in #1
11	**ki(11,α)**	Ikbα+IKK→IKK	0.00135	nM^{-1} min^{-1}	Based on measured IkB degradation time courses given numerical input
12	**ki(12,α)**	Ikbα:NFκB+IKK→IKK	0.00135	nM^{-1} min^{-1}	As in #11
13	**ki(13,α)**	Ikbα:NFκB→	0.00024	min^{-1}	Based on estimated 48 h half-life
14	**ki(14,α)**	nIkbα:NFκB→	0.00024	min^{-1}	As in #13
15	**ki(1,β)**	→tIkbβ	0.0006	nM min^{-1}	As in #1
16	**ki(2,β)**	tIkbβ→	0.00288	min^{-1}	As in #2
17	**ki(3,β)**	tIkbβ→Ikbβ	12	Proteins/ mRNA min^{-1}	As in #3
18	**ki(4,β)**	Ikbβ→	0.12	min^{-1}	As in #2
19	**ki(5,β)**	nIkbβ→	0.12	min^{-1}	As in #2
20	**ki(6,β)**	Ikbβ→ nIkbβ	0.009	min^{-1}	As in #2
21	**ki(7,β)**	nIkbβ→ Ikbβ	0.012	min^{-1}	As in #2
22	**ki(8,β)**	transcription delay	45	min	As in #1
23	**ki(9,β)**	Hill c for inducible txn.	1.1		As in #9
24	**ki(10,β)**	Hill Kd	150	nM	As in #1
25	**ki(11,β)**	Ikbβ+IKK→IKK	0.00045	nM^{-1} min^{-1}	As in #11
26	**ki(12,β)**	Ikbβ:NFκB+IKK→IKK	0.00045	nM^{-1} min^{-1}	As in #11
27	**ki(13,β)**	Ikbβ:NFκB→	0.00024	min^{-1}	As in #13
28	**ki(14,β)**	nIkbβ:NFκB→	0.00024	min^{-1}	As in #13
29	**ki(1,ε)**	→tIkbε	7.20E-05	nM min^{-1}	As in #1
30	**ki(2,ε)**	tIkbε→	0.00384	min^{-1}	As in #2
31	**ki(3,ε)**	tIkbε→Ikbε	12	Proteins/ mRNA min^{-1}	As in #3
32	**ki(4,ε)**	Ikbε→	0.01155	min^{-1}	Schuerenberg and Hoffmann, in preparation
33	**ki(5,ε)**	nIkbε→	0.01155	min^{-1}	As in #32
34	**ki(6,ε)**	Ikbε→ nIkbε	0.045	min^{-1}	As in #2
35	**ki(7,ε)**	nIkbε→ Ikbε	0.012	min^{-1}	As in #2
36	**ki(8,ε)**	transcription delay	45	min	As in #1
37	**ki(9,ε)**	Hill c for inducible txn.	1.1		As in #9
38	**ki(10,ε)**	Hill Kd	150	nM	As in #1
39	**ki(11,ε)**	Ikbε+IKK→IKK	0.0003375	nM^{-1} min^{-1}	As in #11
40	**ki(12,ε)**	Ikbε:NFκB+IKK→IKK	0.0003375	nM^{-1} min^{-1}	As in #11
41	**ki(13,ε)**	Ikbε:NFκB→	0.00024	min^{-1}	As in #13
42	**ki(14,ε)**	nIkbε:NFκB→	0.00024	min^{-1}	As in #13
43	**km(1,RelA)**	→tRelA	7.20E-05	nM min^{-1}	As in #1

#	Parameter	Description	Value	Units	Justification
44	**km(2,RelA)**	tRelA→	0.00288	min^{-1}	As in #2
45	**km(3,RelA)**	tRelA→RelA	12	Proteins/ mRNA min	As in #3
46	**km(4,RelA)**	RelA→	0.0231	min^{-1}	Based on estimated 30 min half-life of NFκB monomers
47	**km(5,RelA)**	nRelA→	0.0231	min^{-1}	As in #46
48	**km(6,RelA)**	transcription delay	60	min	Based on estimated 1 h delay from RPA experiments
49	**km(7,RelA)**	Hill c for inducible txn.	1		Assumed to be similar to #9
50	**km(8,RelA)**	Hill Kd	150	nM	As in #1
51	**km(1,p50)**	→tp50	4.68E-05	nM min^{-1}	Reduced to account for induced expression and a basal steady state of 4 nM RelA:p50 and 2 nM cRel:p50 in the nucleus.
52	**km(2,p50)**	tp50→	0.00288	min^{-1}	As in #2
53	**km(3,p50)**	tp50→p50	12	Proteins/ mRNA min	As in #3
54	**km(4,p50)**	p50→	0.0231	min^{-1}	As in #46
55	**km(5,p50)**	np50→	0.0231	min^{-1}	As in #46
56	**km(6,p50)**	transcription delay	60	min	As in #48
57	**km(7,p50)**	Hill c for inducible txn.	1		As in #49
58	**km(8,p50)**	Hill Kd	150	nM	As in #1
59	**km(1,cRel)**	→tcRel	4.68E-05	nM min^{-1}	As in #51
60	**km(2,cRel)**	tcRel→	0.00288	min^{-1}	As in #2
61	**km(3,cRel)**	tcRel→cRel	12	Proteins/ mRNA min	As in #3
62	**km(4,cRel)**	cRel→	0.0231	min^{-1}	As in #46
63	**km(5,cRel)**	ncRel→	0.0231	min^{-1}	As in #46
64	**km(6,cRel)**	transcription delay	60	min	As in #48
65	**km(7,cRel)**	Hill c for inducible txn.	1		As in #49
66	**km(8,cRel)**	Hill Kd	150	nM	As in #1
67	**kd(1,AA)**	RelA+RelA→AA	0.0006	nM^{-1} min^{-1}	Tsui et al. in press
68	**kd(2,AA)**	nRelA+nRelA→nAA	0.0006	nM^{-1} min^{-1}	As in #67
69	**kd(3,AA)**	AA→ RelA+RelA	0.48	min^{-1}	As in #67
70	**kd(4,AA)**	nAA→nRelA+nRelA	0.048	min^{-1}	As in #67
71	**kd(5,AA)**	AA→nAA	5.4	min^{-1}	As in #2
72	**kd(6,AA)**	nAA→AA	0.0048	min^{-1}	As in #2
73	**kd(7,AA)**	AA→	0.00024	min^{-1}	Based on estimated 48 hour half-life
74	**kd(8,AA)**	nAA→	0.00024	min^{-1}	As in #73
75	**kd(9,AA)**	IkB:AA→IkB	0.00024	min^{-1}	See #13
76	**kd(10,AA)**	nIkB:AA→nIkB	0.00024	min^{-1}	See #13
77	**kd(1,A50)**	RelA+p50→A50	0.001896	nM^{-1} min^{-1}	As in #67
78	**kd(2,A50)**	nRelA+np50→nA50	0.001896	nM^{-1} min^{-1}	As in #67
79	**kd(3,A50)**	A50→ RelA+p50	0.01896	min^{-1}	As in #67
80	**kd(4,A50)**	nA50→nRelA+np50	0.001896	min^{-1}	As in #67
81	**kd(5,A50)**	A50→nA50	5.4	min^{-1}	As in #2
82	**kd(6,A50)**	nA50→A50	0.0048	min^{-1}	As in #2
83	**kd(7,A50)**	A50→	0.00024	min^{-1}	As in #73
84	**kd(8,A50)**	nA50→	0.00024	min^{-1}	As in #73
85	**kd(9,A50)**	IkB:A50→IkB	0.00024	min^{-1}	See #13
86	**kd(10,A50)**	nIkB:A50→nIkB	0.00024	min^{-1}	See #13
87	**kd(1,5050)**	p50+p50→A50	0.0018	nM^{-1} min^{-1}	As in #67
88	**kd(2,5050)**	np50+np50→nA50	0.0018	nM^{-1} min^{-1}	As in #67
89	**kd(3,5050)**	5050→ p50+p50	0.054	min^{-1}	As in #67

#	Parameter	Description	Value	Units	Justification
90	**kd(4,5050)**	N5050→np50+np50	0.0054	min^{-1}	As in #67
91	**kd(5,5050)**	5050→n5050	5.4	min^{-1}	As in #2
92	**kd(6,5050)**	N5050→5050	0.0048	min^{-1}	As in #2
93	**kd(7,5050)**	5050→	0.00024	min^{-1}	As in #73
94	**kd(8,5050)**	N5050→	0.00024	min^{-1}	As in #73
95	**kd(9,5050)**	IkB:5050→IkB	0.00024	min^{-1}	See #13
96	**kd(10,5050)**	nIkB:5050→nIkB	0.00024	min^{-1}	See #13
97	**kd(1,C50)**	cRel+p50→A50	0.0018	nM^{-1} min^{-1}	As in #67
98	**kd(2,C50)**	ncRel +np50→nA50	0.0018	nM^{-1} min^{-1}	As in #67
99	**kd(3,C50)**	C50→ cRel +p50	0.054	min^{-1}	As in #67
100	**kd(4,C50)**	nC50→ncRel+np50	0.0054	min^{-1}	As in #67
101	**kd(5,C50)**	C50→nC50	5.4	min^{-1}	As in #2
102	**kd(6,C50)**	nC50→C50	0.0048	min^{-1}	As in #2
103	**kd(7,C50)**	C50→	0.00024	min^{-1}	As in #73
104	**kd(8,C50)**	nC50→	0.00024	min^{-1}	As in #73
105	**kd(9,C50)**	IkB:C50→IkB	0.00024	min^{-1}	See #13
106	**kd(10,C50)**	nIkB:C50→nIkB	0.00024	min^{-1}	See #13
107	**kdm(AA,A)**	Monomer induction	0		RelA is not induced by NFκB dimers.
108	**kdm(AA,50)**	Monomer induction	0		Set to 0 since RelA homodimer is 1000 fold less than RelA:p50 or cRel:p50 heterodimers in the nucleus.
109	**kdm(AA,C)**	Monomer induction.	0		As in #108
110	**kdm(A50,A)**	Monomer induction	0		As in #107
111	**kdm(A50,50)**	Monomer induction	10		Manually calibrated to ensure late-phase signaling of cRel:p50 heterodimer.
112	**kdm(A50,C)**	Monomer induction.	10		As in #111
113	**kdm(5050,A)**	Monomer induction	0		As in #107, also p50 homodimer does not induce gene expression.
114	**kdm(5050,50)**	Monomer induction	0		As in #113
115	**kdm(5050,C)**	Monomer induction.	0		As in #113
116	**kdm(C50,A)**	Monomer induction	0		As in #107
117	**kdm(C50,50)**	Monomer induction	10		As in #111
118	**kdm(C50,C)**	Monomer induction.	10		As in #111
119	**kp(1,AA,α)**	AA+IkBα→AA:IkBα	0.001344	nM^{-1} min^{-1}	As in #67
120	**kp(2,AA,α)**	AA:IkBα→ AA+IkBα	0.001344	min^{-1}	As in #67
121	**kp (3,AA,α)**	nAA+nIkBα→nAA:IkBα	2.68E-05	nM^{-1} min^{-1}	As in #67
122	**kp(4,AA,α)**	nAA:IkBα→ nAA+IkBα	2.68E-05	min^{-1}	As in #67
123	**kp(5,AA,α)**	AA:IkBα→ nAA:IkBα	0.276	min^{-1}	As in #2
124	**kp(6,AA,α)**	nAA:IkBα→ AA:IkBα	0.84	min^{-1}	As in #2
125	**kp(7,AA,α)**	Induction strength	25		As in #1
126	**kp(1,AA,β)**	AA+IkBβ→AA:IkBβ	0.3	nM^{-1} min^{-1}	As in #67
127	**kp(2,AA,β)**	AA:IkBβ→ AA+IkBβ	0.3	min^{-1}	As in #67
128	**kp (3,AA,β)**	nAA+nIkββ→nAA:IkBβ	0.0012	nM^{-1} min^{-1}	As in #67
129	**kp(4,AA,β)**	nAA:IkBβ→ nAA+IkBβ	0.0012	min^{-1}	As in #67
130	**kp(5,AA,β)**	AA:IkBβ→ nAA:IkBβ	0.0276	min^{-1}	As in #2
131	**kp(6,AA,β)**	nAA:IkBβ→ AA:IkBβ	0.42	min^{-1}	As in #2
132	**kp(7,AA,β)**	Induction strength	1		As in #1
133	**kp(1,AA,ε)**	AA+IkBε→AA:IkBε	0.000213	nM^{-1} min^{-1}	As in #67
134	**kp(2,AA,ε)**	AA:IkBε→ AA+IkBε	0.000213	min^{-1}	As in #67
135	**kp (3,AA,ε)**	nAA+nIkβε→nAA:IkBε	0.01692	nM^{-1} min^{-1}	As in #67
136	**kp(4,AA,ε)**	nAA:IkBε→ nAA+IkBε	0.01692	min^{-1}	As in #67
137	**kp(5,AA,ε)**	AA:IkBε→ nAA:IkBε	0.138	min^{-1}	As in #2
138	**kp(6,AA,ε)**	nAA:IkBε→ AA:IkBε	0.42	min^{-1}	As in #2

#	Parameter	Description	Value	Units	Justification
139	**kp(7,AA,ε)**	Induction strength	25		As in #1
140	**kp(1,A50,α)**	A50+IkBα→A50:IkBα	0.004806	nM^{-1} min^{-1}	As in #67
141	**kp(2,A50,α)**	A50:IkBα→ A50+IkBα	0.004806	min^{-1}	As in #67
142	**kp (3,A50,α)**	nA50+nIkBα→nA50:IkBα	0.0006	nM^{-1} min^{-1}	As in #67
143	**kp(4,A50,α)**	nA50:IkBα→ nA50+IkBα	0.0006	min^{-1}	As in #67
144	**kp(5,A50,α)**	A50:IkBα→ nA50:IkBα	0.276	min^{-1}	As in #2
145	**kp(6,A50,α)**	nA50:IkBα→ A50:IkBα	0.84	min^{-1}	As in #2
146	**kp(7,A50,α)**	Induction strength	200		As in #1
147	**kp(1,A50,β)**	A50+IkBβ→A50:IkBβ	0.000213	nM^{-1} min^{-1}	As in #67
148	**kp(2,A50,β)**	A50:IkBβ→ A50+IkBβ	0.000213	min^{-1}	As in #67
149	**kp (3,A50,β)**	nA50+nIkββ→nA50:IkBβ	0.01692	nM^{-1} min^{-1}	As in #67
150	**kp(4,A50,β)**	nA50:IkBβ→ nA50+IkBβ	0.01692	min^{-1}	As in #67
151	**kp(5,A50,β)**	A50:IkBβ→ nA50:IkBβ	0.0276	min^{-1}	As in #2
152	**kp(6,A50,β)**	nA50:IkBβ→ A50:IkBβ	0.42	min^{-1}	As in #2
153	**kp(7,A50,β)**	Induction strength	1		As in #1
154	**kp(1,A50,ε)**	A50+IkBε→A50:IkBε	0.001344	nM^{-1} min^{-1}	As in #67
155	**kp(2,A50,ε)**	A50:IkBε→ A50+IkBε	0.001344	min^{-1}	As in #67
156	**kp (3,A50,ε)**	nA50+nIkβε→nA50:IkBε	0.006	nM^{-1} min^{-1}	As in #67
157	**kp(4,A50,ε)**	nA50:IkBε→ nA50+IkBε	0.006	min^{-1}	As in #67
158	**kp(5,A50,ε)**	A50:IkBε→ nA50:IkBε	0.138	min^{-1}	As in #2
159	**kp(6,A50,ε)**	nA50:IkBε→ A50:IkBε	0.42	min^{-1}	As in #2
160	**kp(7,A50,ε)**	Induction strength	25		As in #1
161	**kp(1,5050,α)**	5050+IkBα→5050:IkBα	0	nM^{-1} min^{-1}	As in #67
162	**kp(2,5050,α)**	5050:IkBα→ 5050+IkBα	0	min^{-1}	As in #67
163	**kp (3,5050,α)**	n5050+nIkBα→n5050:IkBα	0	nM^{-1} min^{-1}	As in #67
164	**kp(4,5050,α)**	n5050:IkBα→ n5050+IkBα	0	min^{-1}	As in #67
165	**kp(5,5050,α)**	5050:IkBα→ n5050:IkBα	0	min^{-1}	As in #2
166	**kp(6,5050,α)**	n5050:IkBα→ 5050:IkBα	0	min^{-1}	As in #2
167	**kp(7,5050,α)**	Induction strength	0		As in #1
168	**kp(1,5050,β)**	5050+IkBβ→5050:IkBβ	0	nM^{-1} min^{-1}	As in #67
169	**kp(2,5050,β)**	5050:IkBβ→ 5050+IkBβ	0	min^{-1}	As in #67
170	**kp (3,5050,β)**	n5050+nIkββ→n5050:IkBβ	0	nM^{-1} min^{-1}	As in #67
171	**kp(4,5050,β)**	n5050:IkBβ→ 50A50+IkBβ	0	min^{-1}	As in #67
172	**kp(5,5050,β)**	5050:IkBβ→ 50A50:IkBβ	0	min^{-1}	As in #2
173	**kp(6,5050,β)**	n5050:IkBβ→ 5050:IkBβ	0	min^{-1}	As in #2
174	**kp(7,5050,β)**	Induction strength	0		As in #1
175	**kp(1,5050,ε)**	5050+IkBε→5050:IkBε	0	nM^{-1} min^{-1}	As in #67
176	**kp(2,5050,ε)**	5050:IkBε→ 5050+IkBε	0	min^{-1}	As in #67
177	**kp (3,5050,ε)**	n5050+nIkβε→n5050:IkBε	0	nM^{-1} min^{-1}	As in #67
178	**kp(4,5050,ε)**	n5050:IkBε→ n5050+IkBε	0	min^{-1}	As in #67
179	**kp(5,5050,ε)**	5050:IkBε→ n5050:IkBε	0	min^{-1}	As in #2
180	**kp(6,5050,ε)**	n5050:IkBε→ 5050:IkBε	0	min^{-1}	As in #2
181	**kp(7,5050,ε)**	Induction strength	0		As in #1
182	**kp(1,C50,α)**	C50+IkBα→A50:IkBα	0.003006	nM^{-1} min^{-1}	As in #67
183	**kp(2,C50,α)**	C50:IkBα→ A50+IkBα	0.003006	min^{-1}	As in #67
184	**kp (3,C50,α)**	nC50+nIkBα→nA50:IkBα	0.0048	nM^{-1} min^{-1}	As in #67
185	**kp(4,C50,α)**	nC50:IkBα→ nA50+IkBα	0.0048	min^{-1}	As in #67
186	**kp(5,C50,α)**	C50:IkBα→ nA50:IkBα	0.276	min^{-1}	As in #2
187	**kp(6,C50,α)**	nC50:IkBα→ A50:IkBα	0.84	min^{-1}	As in #2
188	**kp(7,C50,α)**	Induction strength	1		As in #1
189	**kp(1,C50,β)**	C50+IkBβ→C50:IkBβ	0.000213	nM^{-1} min^{-1}	As in #67
190	**kp(2,C50,β)**	C50:IkBβ→ C50+IkBβ	0.000213	min^{-1}	As in #67
191	**kp (3,C50,β)**	nC50+nIkββ→nC50:IkBβ	0.01692	nM^{-1} min^{-1}	As in #67
192	**kp(4,C50,β)**	nC50:IkBβ→ nC50+IkBβ	0.01692	min^{-1}	As in #67
193	**kp(5,C50,β)**	C50:IkBβ→ nC50:IkBβ	0.0276	min^{-1}	As in #2
194	**kp(6,C50,β)**	nC50:IkBβ→ C50:IkBβ	0.42	min^{-1}	As in #2
195	**kp(7,C50,β)**	Induction strength	1		As in #1
196	**kp(1,C50,ε)**	C50+IkBε→C50:IkBε	0.001344	nM^{-1} min^{-1}	As in #67
197	**kp(2,C50,ε)**	C50:IkBε→ C50+IkBε	0.001344	min^{-1}	As in #67

#	Parameter	Description	Value	Units	Justification
198	kp (3,C50,ε)	nC50+nIkβε→nC50:IkBε	2.68E-05	nM^{-1} min^{-1}	As in #67
199	kp(4,C50,ε)	nC50:IkBε→ nC50+IkBε	2.68E-05	min^{-1}	As in #67
200	kp(5,C50,ε)	C50:IkBε→ nC50:IkBε	0.138	min^{-1}	As in #2
201	kp(6,C50,ε)	nC50:IkBε→ C50:IkBε	0.42	min^{-1}	As in #2
202	kp(7,C50,ε)	Induction strength	250		As in #1
203	ka(1)	L+R→L:R	2.40E-05	mol^{-1} min^{-1}	Constants were derived using py-substitution to achieve similar steady state concentrations of species as described in an extant model of mammalian apoptosis [155], while also allowing cells to survive low doses of stimuluation. See [156].
204	ka(2)	L:R→L+R	6.00E-05	min^{-1}	As in #203
205	ka(3)	L:R→DISC (R*)	0.6	min^{-1}	As in #203
206	ka(4)	flip + DISC → flip:DISC	6.00E-05	mol^{-1} min^{-1}	As in #203
207	ka(5)	flip:DISC → flip + DISC	0.06	min^{-1}	As in #203
208	ka(6)	pC8 + DISC → DISC:pC8	6.00E-06	mol^{-1} min^{-1}	As in #203
209	ka(7)	DISC:pC8 → pC8 + DISC	0.06	min^{-1}	As in #203
210	ka(8)	DISC:pC8 → C8 + DISC	60	min^{-1}	As in #203
211	ka(9)	C8 + BAR → BAR:C8	6.00E-05	mol^{-1} min^{-1}	As in #203
212	ka(10)	BAR:C8 → C8 + BAR	0.06	min^{-1}	As in #203
213	ka(11)	pC3 + C8 → pC3:C8	6.00E-06	mol^{-1} min^{-1}	As in #203
214	ka(12)	pC3:C8 → pC3 + C8	0.06	min^{-1}	As in #203
215	ka(13)	pC3:C8 → C3 + C8	60	min^{-1}	As in #203
216	ka(14)	pC6 + C3 → pC6:C3	6.00E-06	mol^{-1} min^{-1}	As in #203
217	ka(15)	pC6:C3 → pC6 + C3	0.06	min^{-1}	As in #203
218	ka(16)	pC6:C3 → C6 + C3	60	min^{-1}	As in #203
219	ka(17)	pC8 + C6 →pC8:C6	6.00E-06	mol^{-1} min^{-1}	As in #203
220	ka(18)	pC8:C6 → pC8 + C6	0.06	min^{-1}	As in #203
221	ka(19)	pC8:C6 → C8 + C6	60	min^{-1}	As in #203
222	ka(20)	XIAP + C3 → XIAP:C3	0.00012	mol^{-1} min^{-1}	As in #203
223	ka(21)	XIAP:C3 →XIAP + C3	0.06	min^{-1}	As in #203
224	ka(22)	XIAP:C3 →XIAP + C3_U	6	min^{-1}	As in #203
225	ka(23)	PARP + C3 → PARP:C3	6.00E-05	mol^{-1} min^{-1}	As in #203
226	ka(24)	PARP:C3 → PARP + C3	0.06	min^{-1}	As in #203
227	ka(25)	PARP:C3 → CPARP + C3	1200	min^{-1}	As in #203
228	ka(26)	Bid + C8 → Bid:C8	6.00E-06	mol^{-1} min^{-1}	As in #203
229	ka(27)	Bid:C8 → Bid + C8	0.06	min^{-1}	As in #203
230	ka(28)	Bid:C8→ tBid + C8	60	min^{-1}	As in #203
231	ka(29)	tBid + Bcl2c → tBid:Bcl2c	6.00E-05	mol^{-1} min^{-1}	As in #203
232	ka(30)	tBid:Bcl2c → tBid + Bcl2c	0.06	min^{-1}	As in #203
233	ka(31)	Bax + tBid →Bax:tBid	6.00E-06	mol^{-1} min^{-1}	As in #203
234	ka(32)	Bax:tBid → Bax + tBid	0.06	min^{-1}	As in #203
235	ka(33)	Bax:tBid → aBax + tBid	60	min^{-1}	As in #203
236	ka(34)	aBax → MBax	0.6	min^{-1}	As in #203
237	ka(35)	MBax → aBax	60	min^{-1}	As in #203
238	ka(36)	MBax + BclXL → MBax:BclXL	6.00E-05	mol^{-1} min^{-1}	As in #203
239	ka(37)	MBax:BclXL → MBax + BclXL	0.06	min^{-1}	As in #203
240	ka(38)	MBax + MBax → Bax2	6.00E-05	min^{-1}	As in #203
241	ka(39)	Bax2 → MBax + MBax	0.06	min^{-1}	As in #203
242	ka(40)	Bax2 + Bcl2 → MBax2:Bcl2	6.00E-05	mol^{-1} min^{-1}	As in #203
243	ka(41)	MBax2:Bcl2 →Bax2 + Bcl2	0.06	min^{-1}	As in #203
244	ka(42)	Bax2 + Bax2→ Bax4	6.00E-05	mol^{-1} min^{-1}	As in #203
245	ka(43)	Bax4 → Bax2 + Bax2	0.06	min^{-1}	As in #203
246	ka(44)	Bax4 + Bcl2 → MBax4:Bcl2	6.00E-05	mol^{-1} min^{-1}	As in #203
247	ka(45)	MBax4:cl2→Bax4 + Bcl2	0.06	min^{-1}	As in #203
248	ka(46)	Bax4 + Mito → Bax4:Mito	6.00E-05	mol^{-1} min^{-1}	As in #203
249	ka(47)	Bax4:Mito →Bax4 + Mito	0.06	min^{-1}	As in #203
250	ka(48)	Bax4:Mito → AMito	60	min^{-1}	As in #203

#	Parameter	Description	Value	Units	Justification
251	**ka(49)**	AMito + mCytoC → AMito:mCytoC	0.00012	mol^{-1} min^{-1}	As in #203
252	**ka(50)**	AMito:mCytoC → AMito + mCytoC	0.06	min^{-1}	As in #203
253	**ka(51)**	AMito:mCytoC → AMito + ACytoC	600	min^{-1}	As in #203
254	**ka(52)**	AMito + mSMac → AMito:mSmac	0.00012	mol^{-1} min^{-1}	As in #203
255	**ka(53)**	AMito:mSMac →AMito + mSmac	0.06	min^{-1}	As in #203
256	**ka(54)**	AMito + mSMac→ AMito + ASmac	600	mol^{-1} min^{-1}	As in #203
257	**ka(55)**	ACytoC → cCytoC	60	min^{-1}	As in #203
258	**ka(56)**	cCytoC → ACytoC	0.6	min^{-1}	As in #203
259	**ka(57)**	Apaf + cCytoC → Apaf:cCytoC	3.00E-05	mol^{-1} min^{-1}	As in #203
260	**ka(58)**	Apaf:cCytoC → Apaf + cCytoC	0.06	min^{-1}	As in #203
261	**ka(59)**	Apaf:cCytoC → Apaf* + cCytoC	60	min^{-1}	As in #203
262	**ka(60)**	Apaf* + Procasp9→ Apoptosome	3.00E-06	mol^{-1} min^{-1}	As in #203
263	**ka(61)**	Apoptosome →Apaf* + Procasp9	0.06	min^{-1}	As in #203
264	**ka(62)**	Apop + pC3→Apop:pC3	3.00E-07	mol^{-1} min^{-1}	As in #203
265	**ka(63)**	Apop:pC3 → Apop + pC3	0.06	min^{-1}	As in #203
266	**ka(64)**	Apop:pC3→Apop + C3	60	min^{-1}	As in #203
267	**ka(65)**	ASmac →cSmac	60	min^{-1}	As in #203
268	**ka(66)**	cSmac →ASmac	0.6	min^{-1}	As in #203
269	**ka(67)**	Apop + XIAP→Apop:XIAP	0.00012	mol^{-1} min^{-1}	As in #203
270	**ka(68)**	Apop:XIAP → Apop + XIAP	0.06	min^{-1}	As in #203
271	**ka(69)**	cSmac + XIAP→ cSmac:XIAP	0.00042	mol^{-1} min^{-1}	As in #203
272	**ka(70)**	cSmac:XIAP→cSmac + XIAP	0.06	min^{-1}	As in #203
273	**ka(71)**	→R	2.312439	mol/min	As in #203
274	**ka(72)**	R →	0.01155245	min^{-1}	As in #203
275	**ka(73)**	→flip	1.15719366	mol/min	As in #203
276	**ka(74)**	flip→	0.01155245	min^{-1}	As in #203
277	**ka(75)**	flip:DISC→	0.01155245	min^{-1}	As in #203
278	**ka(76)**	→pC8	233.519067	mol/min	As in #203
279	**ka(77)**	pC8→	0.01155245	min^{-1}	As in #203
280	**ka(78)**	→ BAR	21.1716068	mol/min	As in #203
281	**ka(79)**	BAR→	0.03465736	min^{-1}	As in #203
282	**ka(80)**	BAR:C8→	0.11552453	min^{-1}	As in #203
283	**ka(81)**	→Bid	477.094542	mol/min	As in #203
284	**ka(82)**	Bid→	0.01155245	min^{-1}	As in #203
285	**ka(83)**	→Mcl1	246.045482	mol/min	As in #203
286	**ka(84)**	Mcl1→	0.01155245	min^{-1}	As in #203
287	**ka(85)**	tBid:Bcl2c →	0.01155245	min^{-1}	As in #203
288	**ka(86)**	→Bax	1201.64059	mol/min	As in #203
289	**ka(87)**	Bax →	0.01155245	min^{-1}	As in #203
290	**ka(88)**	BclXLt →BclXL	.307	min^{-1}	Value was derived such that the steady-state flux was identical to the original BclXL production flux, which did not explicitly model translation from transcript.
291	**ka(89)**	BclXL→	0.01155245	min^{-1}	As in #203
292	**ka(90)**	Baxm:BclXL →	0.01155245	min^{-1}	As in #203
293	**ka(91)**	Bax2:BclXL→	0.01155245	min^{-1}	As in #203
294	**ka(92)**	Bax4:BclXL→	0.01155245	min^{-1}	As in #203
295	**ka(93)**	AMito→Mito	0.11552453	min^{-1}	As in #203
296	**ka(94)**	Apaf*→Apaf	0.11552453	min^{-1}	As in #203
297	**ka(95)**	→XIAP	69320.9971	mol/min	As in #203
298	**ka(96)**	XIAP→	0.01155245	min^{-1}	As in #203
299	**ka(97)**	→mSmac	69315.2463	mol/min	As in #203

#	Parameter	Description	Value	Units	Justification
300	**ka(98)**	mSmac →	0.01155245	min^{-1}	As in #203
301	**ka(99)**	cSmac →	0.01155245	min^{-1}	As in #203
302	**ka(100)**	cSmac:XIAP→	0.01155245	min^{-1}	As in #203
303	**ka(101)**	→ pC3	7156.42702	mol/min	As in #203
304	**ka(102)**	pC3 →	0.01155245	min^{-1}	As in #203
305	**ka(103)**	C3_U →	0.01155245	min^{-1}	As in #203
306	**ka(104)**	→pC6	6942.8207	mol/min	As in #203
307	**ka(105)**	pC6→	0.01155245	min^{-1}	As in #203
308	**ka(106)**	C6 →	0.11552453	min^{-1}	As in #203
309	**ka(107)**	Apop:XIAP → Apop	0.01155245	min^{-1}	As in #203
310	**ka(108)**	→Parp	11571.1993	mol/min	As in #203
311	**ka(109)**	Parp→	0.01155245	min^{-1}	As in #203
312	**ka(110)**	cParp→	0.06931472	min^{-1}	As in #203
313	**ka(111)**	→L	0	mol/min	Set to zero to synchronize ligand abundance across cells (i.e. the ligand concentration is assumed to be constant)
314	**ka(112)**	L →	0	min^{-1}	As in #313
315	**ka(113)**	→mCytoC	5776.27053	mol/min	As in #203
316	**ka(114)**	mCytoC →	0.01155245	min^{-1}	As in #203
317	**ka(115)**	cCytoC→	0.11552453	min^{-1}	As in #203
399	**PP1A**	kcc(44)/(kcc(43)*(kcc(45)*([CycA]+[CycE])+kcc(46)*[CycB])+1)			As in #318
318	**kcc(1)**	Early and Delayed Response Genes (ERG/DERG) parameters in the original model that have been replaced with NFκB-mediated activation of CyclinD	0.004167	Units are arbitrary and non-biological. All rate constants are per min as with the NFκB and apoptosis models.	Refer to [152] for details.
319	**kcc(2)**		0.004167	As in #318	As in #318
320	**kcc(3)**		0.1	As in #318	As in #318
321	**kcc(4)**		0.005833	As in #318	As in #318
322	**kcc(5)**		0.000833	As in #318	As in #318
323	**kcc(6)**		0.3	As in #318	As in #318
324	**kcc(7)**		0.166667	As in #318	As in #318
325	**kcc(8)**	kcc(77)kcc(8)[tCycD]	0.833333	As in #318	As in #318
326	**kcc(9)**	kcc(9)[CD] kcc(9)[CycD]	0.083333	As in #318	As in #318
327	**kcc(10)**	kcc(10)[p27][CycD]	16.66667	As in #318	As in #318
328	**kcc(11)**	kcc(11)[CD]	0.166667	As in #318	As in #318
329	**kcc(12)**	kcc(77)(kcc(12)+kcc(13)[E2F])	0	As in #318	As in #318
330	**kcc(13)**		0.01	As in #318	As in #318
331	**kcc(14)**	V8	0.001667	As in #318	As in #318
332	**kcc(15)**	V8	0.033333	As in #318	As in #318
333	**kcc(16)**	kcc(16)[p27][CycE] kcc(16)[p27][CycA]	16.66667	As in #318	As in #318
334	**kcc(17)**	kcc(17)[CE] kcc(17)[CA]	0.166667	As in #318	As in #318
335	**kcc(18)**	V8	0.1	As in #318	As in #318
336	**kcc(19)**		1	As in #318	As in #318
337	**kcc(20)**		0.05	As in #318	As in #318
338	**kcc(21)**	kcc(77)kcc(21)[E2F]max(0,GMAct*(vcc(33)-vcc(55))*300)) if [Mass] > 0.5, 0 otherwise	0.008333	As in #318	As in #318
339	**kcc(22)**	kcc(22)[CDc20][CycA] kcc(22)[CDc20][CA]	0.333333	As in #318	As in #318

#	Parameter	Description	Value	Units	Justification
340	kcc(23)	kcc(77)(kcc(24)*(([CycB]/kcc(25))^2	0.001667	As in #318	As in #318
341	kcc(24)	/([CycB]/kcc(25))^2+1))+kcc(23)	0.01	As in #318	As in #318
342	kcc(25)		0.1	As in #318	As in #318
343	kcc(26)	V2	0.000833	As in #318	As in #318
344	kcc(27)		0.333333	As in #318	As in #318
345	kcc(28)		0.016667	As in #318	As in #318
346	kcc(29)	kcc(77)kcc(29)	0.333333	As in #318	As in #318
347	kcc(30)	V6	0.166667	As in #318	As in #318
348	kcc(31)		1.666667	As in #318	As in #318
349	kcc(32)		0.5	As in #318	As in #318
350	kcc(33)		1	As in #318	As in #318
351	kcc(34)		0.5	As in #318	As in #318
352	kcc(35)	RB total (not used)	1.666667	As in #318	As in #318
353	kcc(36)	[E2F-Rb](kcc(40)	3.3	As in #318	As in #318
354	kcc(37)	(([CycD]+[CD])kcc(36)+kcc(39)[Cyc	5	As in #318	As in #318
355	kcc(38)	A]+kcc(38)[CycB]+kcc(37)[CycD]))	5	As in #318	As in #318
356	kcc(39)	[p-E2F-Rb](kcc(40)	3	As in #318	As in #318
357	kcc(40)	(([CycD]+[CD])kcc(36)+kcc(39)[Cyc A]+kcc(38)[CycB]+kcc(37)[CycD]))	0.166667	As in #318	As in #318
358	kcc(41)	[pp-Rb](kcc(41)(kcc(44)-	0	As in #318	As in #318
359	kcc(42)	PP1A)+kcc(42)PP1A)	0.333333	As in #318	As in #318
360	kcc(43)	PP1A	1	As in #318	As in #318
361	kcc(44)	[pp-Rb](kcc(41)(kcc(44)- PP1A)+kcc(42)PP1A)	1	As in #318	As in #318
362	kcc(45)	PP1A	25	As in #318	As in #318
363	kcc(46)	PP1A	2	As in #318	As in #318
364	kcc(47)	((kcc(47)+kcc(48)[CDc20](1-	0.125	As in #318	As in #318
365	kcc(48)	[Cdh1]))/(kcc(49)-[Cdh1]+1) if	2.333333	As in #318	As in #318
366	kcc(49)	[Cdh1] <=1 else 0	0.01	As in #318	As in #318
367	kcc(50)	V4[Cdh1])/(kcc(50)+[Cdh1])	0.01	As in #318	As in #318
368	kcc(51)	V4	0.666667	As in #318	As in #318
369	kcc(52)		0	As in #318	As in #318
370	kcc(53)		1	As in #318	As in #318
371	kcc(54)		0.3	As in #318	As in #318
372	kcc(55)	kcc(77)kcc(55)	0.000833	As in #318	As in #318
373	kcc(56)	kcc(56)[PPX]	0.000833	As in #318	As in #318
374	kcc(57)	(kcc(57)[CycB](1-[IEP]))/(kcc(59)- [IEP]+1)	0.011667	As in #318	As in #318
375	kcc(58)	(kcc(58)[PPX][IEP])/(kcc(60)+[IEP])	0.03	As in #318	As in #318
376	kcc(59)	(kcc(57)[CycB](1-[IEP]))/(kcc(59)- [IEP]+1)	0.01	As in #318	As in #318
377	kcc(60)	(kcc(58)[PPX][IEP])/(kcc(60)+[IEP])	0.01	As in #318	As in #318
378	kcc(61)	kcc(77)(kcc(61)+kcc(62)[CycB])	0	As in #318	As in #318
379	kcc(62)		0.025	As in #318	As in #318
380	kcc(63)	kcc(63)[CDc20T] kcc(63)[CDc20]	0.025	As in #318	As in #318
381	kcc(64)	(kcc(64)[IEP]([CDc20T]- [CDc20]))/(kcc(66)- [CDc20]+[CDc20T])	0.083333	As in #318	As in #318
382	kcc(65)	kcc(65)[CDc20]/(kcc(67)+[CDC20])	0.041667	As in #318	As in #318
383	kcc(66)	(kcc(64)[IEP]([CDc20T]- [CDc20]))/(kcc(66)- [CDc20]+[CDc20T])	0.005	As in #318	As in #318
384	kcc(67)	kcc(65)[CDc20]/(kcc(67)+[CDC20])	0.005	As in #318	As in #318
385	kcc(68)	E2F Total (not used)	0.833333	As in #318	As in #318
386	kcc(69)	[p-E2F]kcc(69)	0.016667	As in #318	As in #318
387	kcc(70)	[E2F](kcc(70)+kcc(71)	8.33E-05	As in #318	As in #318
388	kcc(71)	*([CycA]+[CycB]))	0.016667	As in #318	As in #318
389	kcc(72)	[E2F][Rb]kcc(72) [Rb][p-E2F]kcc(72)	166.6667	As in #318	As in #318
390	kcc(73)	[p-E2F-Rb]kcc(73)	3.333333	As in #318	As in #318
391	kcc(74)	kcc(74)(0.01+0.99*GMAct*GMSize) if RbFrac < 0.8, kcc(74)*0.01 else	0.002	As in #318	As in #318

#	Parameter	Description	Value	Units	Justification
392	**kcc(75)**	kcc(75)[GM]	0.00015	As in #318	As in #318
393	**kcc(76)**	kcc(77)kcc(76)[GM]	0.0045	As in #318	As in #318
394	**kcc(77)**	Eps, the efficiency of protein translation reactions.	1 or 0.7 when simulating rapamycin	As in #318	As in #318 0.7 was manually derived.
395	**kcc(78)**	kcc(78)CycDAct	0.003	As in #318	Free parameters with values∈ [0.001-0.01]
396	**kcc(79)**	kcc(79)[tCycD]	0.002	As in #318	As in #395
397	**kcc(80)**	max(kcc(80)BclAct,0.01kcc(80)	8	As in #318	Free parameters with values∈ [1-10]
398	**kcc(81)**	kcc(81)[tBcl2]	0.005	As in #318	As in #395
399	**kcc(82)**	kcc(82)[tMycTor]	0.0035	As in #318	As in #395
400	**kcc(83)**	kcc(83)[MycTor]	0.0025	As in #318	As in #395
401	**kcc(84)**	kcc(84)[Mass]	0.0025	As in #318	As in #395
402	**kcc(85)**	kcc(85)MycAct	1	As in #318	As in #397
403	**kcc(86)**	kcc(86)[tMycTor]	0.0231	As in #318	Given 30 min half-life [200]
404	**V2**	kcc(28)*[CDc20]+kcc(26)*(1-[Cdh1])+kcc(27)*[Cdh1]			As in #318
405	**V4**	kcc(51)*(kcc(54)[CycA]+kcc(53)[CycB]+kcc(52)[CycE])			As in #318
406	**V6**	kcc(30)+kcc(31)*(kcc(34)[CycA]+kcc(33)[CycB]+kcc(32)[CycE]			As in #318
407	**V8**	((kcc(19)*([CycA]+[CycE])+kcc(20)[CycB]))*kcc(15))/([CycE]+[CE]_kcc(18))+kcc(14)			As in #318
408	**H**	Hill coefficient for Myc/Bcl/CycD/GM promoter activation		2	Manually fitted to ensure delayed dynamics in generation 0 cells as observed in this study.
409	**k(1,Myc/TOR)**	d[tMyc]/dt parameter		0.45	Derived from [178] and from pS6/IF measurements in this study
410	**k(2,Myc/TOR)**	d[tMyc]/dt parameter		0.45	As in #409
411	**k(3,Myc/TOR)**	d[tMyc]/dt parameter		0.1	NFκB independent activity assumed to be low As in #409
412	**k(4,Myc/TOR)**	d[tMyc]/dt parameter		1	Scaling factor
413	**k(5,Myc/TOR)**	d[tMyc]/dt parameter		0.01	Basal transcription
413	**k(1,Bcl)**	d[tBcl$_{XL}$]/dt parameter		0.3	Derived from IF and RT-PCR in this study
414	**k(2,Bcl)**	d[tBcl$_{XL}$]/dt parameter		0.6	As in #413
415	**k(3,Bcl)**	d[tBcl$_{XL}$]/dt parameter		0.1	NFκB independent activity assumed to be low
416	**k(4,Bcl)**	d[tBcl$_{XL}$]/dt parameter		1	As in #412
417	**k(5,Bcl)**	d[tBcl$_{XL}$]/dt parameter		0.01	As in #413
418	**k(1,CycD)**	d[tCycD]/dt parameter		0.45	We assumed equal NFκB RelA and cRel dependence for Cyclin D transcription as it is unclear how each monomer contributes to cyclin D2 or 3 mediated cell-cycle progression.[79]
419	**k(2,CycD)**	d[tCycD]/dt parameter		0.45	
420	**k(3,CycD)**	d[tCycD]/dt parameter		0.1	NFκB independent activity assumed to be low to ensure the observed dynamics.
421	**k(4,CycD)**	d[tCycD]/dt parameter		1	As in #412
422	**k(5,CycD)**	d[tCycD]/dt parameter		0.01	As in #413
423	**MycTor Kd**	NFκB scaling parameter that determines NFκB-mediated Myc/TOR activation		40 nM	Manually fitted to ensure wildtype B cell population dynamics.
424	**Bcl$_{XL}$Kd**	NFκB scaling parameter that determines NFκB-mediated Bcl$_{XL}$ activation		40 nM	As in #423
425	**CycDKd**	NFκB scaling parameter that determines NFκB-mediated CycD activation		40 nM	As in #423
426	**GMKd**	Myc/TOR scaling parameter that determines Myc/TOR-mediated GM growth		40 nM	As in #423

#	Parameter	Description	Units	Justification
427	**MycTORAct**	(((k(1,Myc)[nA50]+k(2,Myc)[nC50]+k(3,Myc)[IKK*])/MycTorKd)^H)/(k(4,Myc)+((k(1,Myc)[nA50]+k(2,Myc)[nC50]+k(3,Myc)[IKK*])/MycTorKd)^H)*(1-k(5,Myc))+k(5,Myc)	Unitless 0-1	Hill-based expression of Myc/TOR transcription activity. See #408-413
428	**BclAct**	(((k(1,Bcl)[nA50]+k(2, Bcl)[nC50]+k(3, Bcl)[IKK*])/ Bcl $_{XL}$Kd)^H)/(k(4, Bcl)+ ((k(1, Bcl)[nA50]+k(2, Bcl)[nC50]+k(3, Bcl)[IKK*])/ Bcl_{XL} Kd)^H)*(1-k(5,Bcl))+k(5,Bcl)	Unitless 0-1	Hill-based expression of Bcl_{XL} transcription activity. See #413-417
429	**CycDAct**	(((k(1,CycD)[nA50]+k(2,CycD)[nC50]+k(3,CycD)[IKK*])/CycDKd)^H)/(k(4,CycD)+((k(1,CycD)[nA50]+k(2,CycD)[nC50]+k(3,CycD)[IKK*])/CycDKd)^H)*(1-k(5,CycD))+k(5,CycD)	Unitless 0-1	Hill-based expression of CycD transcription activity. See #418-422
430	**GMAct**	([Myc/TOR]/GMKd)^H/(1+([Myc/TOR]/GMKd)^H)	Unitless 0-1	Assume basic Hill relationships between Myc/TOR and the accumulation of general machinery in the cell. See [49,58,66] and [61,62] reviewing myc and mTOR in the context of B-cell growth.
431	**RbFrac**	([Rb]+[E2F-Rb]+[p-E2F-Rb])/([Rb]+[E2F-Rb]+[p-E2F-Rb]+[pp-Rb])	Unitless 0-1	As in #318

C. Integrated B-cell model fluxes

#	Name	Flux equation	Justification
1-4	vd(1,d∈{AA,A50,5050,C50})	kd(1,d)[m∈{RelA,RelA,p50,cRel}][n∈{RelA,p50,p50,p50}]	See [150]
5-8	vd(2, d∈{AA,A50,5050,C50})	kd(2,d) [m∈{nRelA,nRelA,np50,ncRel}][n∈{nRelA,np50,np50,np50}]	As in #1
9-12	vd(3,d∈{AA,A50,5050,C50})	kd(3,d)[d]	As in #1
13-16	vd(4,d∈{AA,A50,5050,C50})	kd(4,d)[e∈{nAA,nA50,n5050,nC50}]	As in #1
17-20	vd(5,d∈{AA,A50,5050,C50})	kd(5,d)[d]	As in #1
21-24	vd(6,d∈{AA,A50,5050,C50})	kd(6,d)[e∈{nAA,nA50,n5050,nC50}]	As in #1
25-28	vd(7,d∈{AA,A50,5050,C50})	kd(7,d)[d]	As in #1
29-32	vd(8,d∈{AA,A50,5050,C50})	kd(8,d)[e∈{nAA,nA50,n5050,nC50}]	As in #1
33-44	vdi(1, d∈{AA,A50,5050,C50}, i∈{α,β,∈})	kp(1,d,i)[d][j∈{IkBα, IkBβ,IkB∈}]	As in #1
45-56	vdi(2, d∈{AA,A50,5050,C50}, i∈{α,β,∈})	kp(2,d,i)[e ∈{nAA,nA50,n5050,nC50}][j∈{nIkBα, nIkBβ,nIkB∈}]	As in #1
57-68	vdi(3, d∈{AA,A50,5050,C50}, i∈{α,β,∈})	kp(3,d,i)[d: j∈{IkBα, IkBβ,IkB∈}]	As in #1
69-80	vdi(4, d∈{AA,A50,5050,C50}, i∈{α,β,∈})	kp(4,d,i)[e ∈{nAA,nA50,n5050,nC50} : j∈{nIkBα, nIkBβ,nIkB∈}]	As in #1
81-92	vdi(5, d∈{AA,A50,5050,C50}, i∈{α,β,∈})	kp(5,d,i)[d: j∈{IkBα, IkBβ,IkB∈}]	As in #1
93-104	vdi(6, d∈{AA,A50,5050,C50}, i∈{α,β,∈})	kp(6,d,i)[e ∈{nAA,nA50,n5050,nC50} : j∈{nIkBα, nIkBβ,nIkB∈}]	As in #1
105-116	vdi(7, d∈{AA,A50,5050,C50}, i∈{α,β,∈})	ki(12, j∈{IkBα, IkBβ,IkB∈}) [d: j∈{IkBα, IkBβ,IkB∈}][IKK*]	As in #1
117-128	vdi(8, d∈{AA,A50,5050,C50}, i∈{α,β,∈})	ki(13, i)[d: j∈{IkBα, IkBβ,IkB∈}]	As in #1
129-140	vdi(9, d∈{AA,A50,5050,C50}, i∈{α,β,∈})	ki(14, i)[e ∈{nAA,nA50,n5050,nC50} : j∈{nIkBα, nIkBβ,nIkB∈}]	As in #1
141-152	vdi(10, d∈{AA,A50,5050,C50}, i∈{α,β,∈})	kd(9, d)[d: j∈{IkBα, IkBβ,IkB∈}]	As in #1
153-164	vdi(11, d∈{AA,A50,5050,C50}, i∈{α,β,∈})	ki(10, d)[e ∈{nAA,nA50,n5050,nC50} : j∈{nIkBα, nIkBβ,nIkB∈}]	As in #1

#	Name	Flux equation	Justification
165-167	vi(i∈{α,β,∈},t)	$ki(1,i)(1+\Sigma_{d\in(AA,A50,C50)}(kp(7,i)([e \in\{nAA,nA50,n5050,nC50\}]\|_{t-ki(8,i)} /ki(10,i))^{ki(9,i)})/ (1+\Sigma_{d\in(AA,A50,C50)}(([e \in\{nAA,nA50,n5050,nC50\}]\|_{t-ki(8,i)} /ki(10,i))^{ki(9,i)})/$	As in #1. The transcription rate is computed using a modified hill function which uses a sum of weighted contributions from each dimer and an explicit transcriptional delay to compute the transcription rate of each IkB transcript.
168-170	vm(m∈{A,50,C},t)	$km(1,m)(1+\Sigma_{d\in(AA,A50,C50)}(kdm(d,m)([e \in\{nAA,nA50,n5050,nC50\}]\|_{t-km(6,i)} /km(8,m))^{km(7,m)}) /(1+\Sigma_{d\in(AA,A50,C50)}(([e \in\{nAA,nA50,n5050,nC50\}]\|_{t-km(6,i)} /km(8,m))^{km(7,m)})$	As in #165-167. The transcription rate is computed using a modified hill function which uses a sum of weighted contributions from each dimer and an explicit transcriptional delay to compute the transcription rate of each NFκB monomer.
171	vtm(1,m∈{A,50,C})	km(2,m)[n∈{tRelA,tp50,tcRel}]	As in #1
172	vtm(2,m∈{A,50,C})	kcc(77)km(3,m)[n∈{tRelA,tp50,tcRel}]	As in #1
173	vtm(3,m∈{A,50,C})	km(4,m)[m]	As in #1
174	vtm(4,m∈{A,50,C})	km(5,m)[n∈{nRelA,np50,ncRel}]]	As in #1
175	vti(1, i∈{α,β,∈})	ki(2,i)[j∈{tIkBα, tIkBβ,tIkB∈}]	As in #1
176	vti(2, i∈{α,β,∈})	kcc(77)ki(3,i)[j∈{tIkBα, tIkBβ,tIkB∈}]	As in #1
177	vti(3, i∈{α,β,∈})	ki(11,i) [j∈{IkBα, IkBβ,IkB∈}][IKK*]	As in #1
178	vti(4, i∈{α,β,∈})	ki(4,i) [j∈{IkBα, IkBβ,IkB∈}]	As in #1
179	vti(5, i∈{α,β,∈})	ki(5,i) [j∈{nIkBα, nIkBβ,nIkB∈}]	As in #1
180	vti(6, i∈{α,β,∈})	ki(6,i) [j∈{IkBα, IkBβ,IkB∈}]	As in #1
181	vti(7, i∈{α,β,∈})	ki(7,i) [j∈{nIkBα, nIkBβ,nIkB∈}]	As in #1
182	va(1)	ka(1)[L][R]	See the original paper [156]
183	va(2)	ka(2)[L-R]	As in #182
184	va(3)	ka(3)[flip][DISC]	As in #182
185	va(4)	ka(4)[flip-DISC]	As in #182
186	va(5)	ka(5)[pC8][DISC]	As in #182
187	va(6)	ka(6)[DISC-pC8]	As in #182
188	va(7)	ka(7)[DISC-pC8]	As in #182
189	va(8)	ka(8)[C8][BAR]	As in #182
190	va(9)	ka(9)[BAR-C8]	As in #182
191	va(10)	ka(10)[pC3][C8]	As in #182
192	va(11)	ka(11)[pC3-C8]	As in #182
193	va(12)	ka(12)[pC3-C8]	As in #182
194	va(13)	ka(13)[pC6][C3]	As in #182
195	va(14)	ka(14)[pC6-C3]	As in #182
196	va(15)	ka(15)[pC6-C3]	As in #182
197	va(16)	ka(16)[pC8][C6]	As in #182
198	va(17)	ka(17)[pC8-C6]	As in #182
199	va(18)	ka(18)[pC8-C6]	As in #182
200	va(19)	ka(19)[XIAP][C3]	As in #182
201	va(20)	ka(20)[XIAP-C3]	As in #182
202	va(21)	ka(21)[XIAP-C3]	As in #182
203	va(22)	ka(22)[PARP][C3]	As in #182
204	va(23)	ka(23)[PARP-C3]	As in #182
205	va(24)	ka(24)[PARP-C3]	As in #182
206	va(25)	ka(25)[Bid][C8]	As in #182

#	Name	Flux equation	Justification
207	va(26)	ka(26)[Bid-C8]	As in #182
208	va(27)	ka(27)[Bid-C8]	As in #182
209	va(28)	ka(28)[tBid][Mcl1]	As in #182
210	va(29)	ka(29)[tBid-Mcl1]	As in #182
211	va(30)	ka(30)[Bax][tBid]	As in #182
212	va(31)	ka(31)[Bax-tBid]	As in #182
213	va(32)	ka(32)[Bax-tBid]	As in #182
214	va(33)	ka(33)[aBax]	As in #182
215	va(34)	ka(34)[mBax]	As in #182
216	va(35)	ka(35)[mBax][BclXL]	As in #182
217	va(36)	ka(36)[mBax-BclXL]	As in #182
218	va(37)	ka(37)[mBax]^2	As in #182
219	va(38)	ka(38)[Bax2]	As in #182
220	va(39)	ka(39)[Bax2][BclXL]	As in #182
221	va(40)	ka(40)[mBax2-BclXL]	As in #182
222	va(41)	ka(41)[Bax2]^2	As in #182
223	va(42)	ka(42)[Bax4]	As in #182
224	va(43)	ka(43)[Bax4][BclXL]	As in #182
225	va(44)	ka(44)[mBax4-BclXL]	As in #182
226	va(45)	ka(45)[Bax4][Mito]	As in #182
227	va(46)	ka(46)[Bax4-Mito]	As in #182
228	va(47)	ka(47)[Bax4-Mito]	As in #182
229	va(48)	ka(48)[AMito][mCytoC]	As in #182
230	va(49)	ka(49)[AMito-mCytoC]	As in #182
231	va(50)	ka(50)[AMito-mCytoC]	As in #182
232	va(51)	ka(51)[AMito][mSMac]	As in #182
233	va(52)	ka(52)[AMito-mSMac]	As in #182
234	va(53)	ka(53)[AMito][mSMac]	As in #182
235	va(54)	ka(54)[aCytoC]	As in #182
236	va(55)	ka(55)[cCytoC]	As in #182
237	va(56)	ka(56)[Apaf][cCytoC]	As in #182
238	va(57)	ka(57)[Apaf-cCytoC]	As in #182
239	va(58)	ka(58)[Apaf-cCytoC]	As in #182
240	va(59)	ka(59)[Apaf*][ProC9]	As in #182
241	va(60)	ka(60)[Apop]	As in #182
242	va(61)	ka(61)[Apop][pC3]	As in #182
243	va(62)	ka(62)[Apop-pC3]	As in #182
244	va(63)	ka(63)[Apop-pC3]	As in #182
245	va(64)	ka(64)[aSmac]	As in #182
246	va(65)	ka(65)[cSmac]	As in #182
247	va(66)	ka(66)[Apop][XIAP]	As in #182
248	va(67)	ka(67)[Apop-XIAP]	As in #182
249	va(68)	ka(68)[cSmac][XIAP]	As in #182
250	va(69)	ka(69)[cSmac-XIAP]	As in #182
251	va(70)	ka(70)	As in #182
252	va(71)	ka(71)[R}	As in #182
253	va(72)	ka(72)	As in #182
254	va(73)	ka(73)[flip]	As in #182
255	va(74)	ka(74)[flip-DISC]	As in #182
256	va(75)	ka(75)	As in #182
257	va(76)	ka(76)[pC8]	As in #182
258	va(77)	ka(77)	As in #182
259	va(78)	ka(78)[BAR}	As in #182
260	va(79)	ka(79)[BAR-C8]	As in #182
261	va(80)	ka(80)	As in #182
262	va(81)	ka(81)[Bid]	As in #182
263	va(82)	ka(82)	As in #182
264	va(83)	ka(83)[Mcl1]	As in #182
265	va(84)	ka(84)[tBid-Mcl1]	As in #182
266	va(85)	ka(85)	As in #182
267	va(86)	ka(86)[Bax]	As in #182
268	va(87)	ka(87)	As in #182
269	va(88)	ka(88)[BclXL]	As in #182

#	Name	Flux equation	Justification
270	va(89)	ka(89)[mBax-BclXL]	As in #182
271	va(90)	ka(90)[Bax2-BclXL]	As in #182
272	va(91)	ka(91)[Bax4-BclXL]	As in #182
273	va(92)	ka(92)[AMito]	As in #182
274	va(93)	ka(93)[Apaf*]	As in #182
275	va(94)	ka(94)	As in #182
276	va(95)	ka(95)[XIAP]	As in #182
277	va(96)	ka(96)	As in #182
278	va(97)	ka(97)[mSmac]	As in #182
279	va(98)	ka(98)[cSmac]	As in #182
280	va(99)	ka(99)[cSmac-XIAP]	As in #182
281	va(100)	ka(100)	As in #182
282	va(101)	ka(101)[pC3]	As in #182
283	va(102)	ka(102)[C3_U]	As in #182
284	va(103)	ka(103)	As in #182
285	va(104)	ka(104)[pC6]	As in #182
286	va(105)	ka(105)[C6]	As in #182
287	va(106)	ka(106)[Apop-XIAP]	As in #182
288	va(107)	ka(107)	As in #182
289	va(108)	ka(108)[Parp]	As in #182
290	va(109)	ka(109)[cParp]	As in #182
291	va(110)	ka(110)	As in #182
292	va(111)	ka(111)[L]	As in #182
293	va(112)	ka(112)	As in #182
294	va(113)	ka(113)[mCytoC]	As in #182
295	va(114)	ka(114)[cCytoC]	As in #182
296	vcc(1)	kcc(79)[tCycD]	See the original paper for justification [152].
297	vcc(2)	kcc(81)[tBcl2]	As in #296
298	vcc(3)	kcc(9)[CD]	As in #296
299	vcc(4)	kcc(9)[CycD]	As in #296
300	vcc(5)	kcc(16)[p27][CycE]	As in #296
301	vcc(6)	kcc(16)[p27][CycA]	As in #296
302	vcc(7)	kcc(10)[p27][CycD]	As in #296
303	vcc(8)	kcc(11)[CD]	As in #296
304	vcc(9)	kcc(22)[CDc20][CycA]	As in #296
305	vcc(10)	kcc(22)[CDc20][CA]	As in #296
306	vcc(11)	kcc(17)[CE]	As in #296
307	vcc(12)	kcc(17)[CA]	As in #296
308	vcc(13)	V8[CE]	As in #296
309	vcc(14)	V8[CycE]	As in #296
310	vcc(15)	V6[p27]	As in #296
311	vcc(16)	V6[CE]	As in #296
312	vcc(17)	V6[CD]	As in #296
313	vcc(18)	V6[CA]	As in #296
314	vcc(19)	V2[CycB]	As in #296
315	vcc(20)	((kcc(47)+kcc(48)[CDc20](1-[Cdh1]))/(kcc(49)-[Cdh1]+1) if [Cdh1] <=1 else 0	As in #296
316	vcc(21)	V4[Cdh1])/(kcc(50)+[Cdh1])	As in #296
317	vcc(22)	kcc(56)[PPX]	As in #296
318	vcc(23)	(kcc(57)[CycB](1-[IEP]))/(kcc(59)-[IEP]+1)	As in #296
319	vcc(24)	(kcc(58)[PPX][IEP])/(kcc(60)+[IEP])	As in #296
320	vcc(25)	kcc(63)[CDc20T]	As in #296
321	vcc(26)	(kcc(64)[IEP]([CDc20T]-[CDc20]))/(kcc(66)-[CDc20]+[CDc20T])	As in #296
322	vcc(27)	kcc(65)[CDc20]/(kcc(67)+[CDC20])	As in #296
323	vcc(28)	kcc(63)[CDc20]	As in #296
324	vcc(29)	[E2F-Rb](kcc(40)(([CycD]+[CD])kcc(36)+kcc(39)[CycA]+kcc(38)[CycB]+kcc(37)[CycD]))	As in #296
325	vcc(30)	[p-E2F- Rb](kcc(40)(([CycD]+[CD])kcc(36)+ kcc(39)[CycA]+kcc(38)[CycB]+kcc(37)[CycD]))	As in #296
326	vcc(31)	kcc(74)(0.01+0.99*GMAct*GMSize) if RbFrac < 0.8, kcc(74)*0.01 otherwise	As in #296

#	Name	Flux equation	Justification
327	vcc(32)	kcc(75)[GM]	As in #296
328	vcc(33)	kcc(77)kcc(76)[GM]	As in #296
329	vcc(34)	kcc(78)CycDAct	As in #296
330	vcc(35)	kcc(77)(kcc(61)+kcc(62)[CycB])	As in #296
331	vcc(36)	kcc(77)kcc(21)[E2F]max(0,GMAct*(vcc(33)-vcc(55))*300)) if [Mass] > 0.5, 0 otherwise	As in #296
332	vcc(37)	kcc(77)kcc(55)	As in #296
333	vcc(38)	kcc(77)(kcc(12)+kcc(13)[E2F])	As in #296
334	vcc(39)	kcc(77)kcc(8)[tCycD]	As in #296
335	vcc(40)	kcc(77)kcc(29)	As in #296
336	vcc(41)	max(kcc(80)BclAct,0.01kcc(80)	As in #296
337	vcc(42)	kcc(77)(kcc(24)*(([CycB]/kcc(25))^2/([CycB]/kcc(25))^2+1))+kcc(23)	As in #296
338	vcc(43)	[Rb](kcc(40)*([CycD]+[CD]kcc(36)+kcc(39)[CycA]+kcc(38)[CycB]+kcc(37)[CycE]))	As in #296
339	vcc(44)	[pp-Rb](kcc(41)(kcc(44)-PP1A)+kcc(42)PP1A)	As in #296
340	vcc(45)	[E2F-Rb]kcc(73)	As in #296
341	vcc(46)	[E2F](kcc(70)+kcc(71)([CycA]+[CycB]))	As in #296
342	vcc(47)	[p-E2F]kcc(69)	As in #296
343	vcc(48)	[E2F][Rb]kcc(72)	As in #296
344	vcc(49)	[p-E2F-Rb]kcc(73)	As in #296
345	vcc(50)	[Rb][p-E2F]kcc(72)	As in #296
346	vcc(51)	[p-E2F-Rb]kcc(69)	As in #296
347	vcc(52)	[E2F-Rb](kcc(70)+kcc(71)([CycA]+[CycB]))	As in #296
348	vcc(53)	kcc(82)[tMycTor]	As in #296
349	vcc(54)	kcc(83)[MycTor]	As in #296
350	vcc(55)	kcc(84)[Mass]	As in #296
351	vcc(56)	kcc(85)MycAct	As in #296
341	vcc(57)	kcc(86)[tMycTor]	As in #296

D. Integrated B-cell model reactions

#	Species	Reaction	Justification
1	d[tRelA]/dt	vm(RelA)-vtm(1,RelA)[tRelA]	See [150]
2	d[tp50]/dt	vm(p50)-vtm(1,p50)[tp50]	As in #1
3	d[tcRel]/dt	vm(cRel)-vtm(1,cRel)[tcRel]	As in #1
4	d[RelA]/dt	vd(3,AA)*2+vd(3,A50)-vd(1,AA)-vd(1,A50)+vtm(2,RelA)[tRelA]-vtm(3,RelA)[RelA]	As in #1
5	d[nRelA]/dt	vd(4,AA)*2+vd(4,A50)-vd(2,AA)-vd(2,A50)-vtm(4,RelA)[nRelA]	As in #1
6	d[p50]/dt	vd(3,5050)*2+vd(3,A50)-+vd(3,C50)-vd(1,A50)-vd(1,C50)-vd(1,5050))+vtm(2,p50)[tp50]-vtm(3,p50)[p50]	As in #1
7	d[np50]/dt	vd(4,5050)*2+vd(4,A50)-+vd(4,C50)-vd(2,A50)-vd(2,C50)-vd(2,5050) -vtm(4,p50)[np50]	As in #1
8	d[cRel]/dt	vd(3,C50)-vd(1,C50))+vtm(2,cRel)[tcRel]-vtm(3,cRel)[cRel]	As in #1
9	d[ncRel]/dt	vd(4,C50)-vd(2,C50) -vtm(4,cRel)[ncRel]	As in #1
10	d[AA]/dt	vd(1,AA)-vd(3,AA)-vd(5,AA)+vd(6,AA)-vd(7,AA)-vdi(1,AA,[α,β,ε])+vdi(2,AA,[α,β,ε])+vdi(7,AA, [α,β,ε])+vdi(8,AA,[α,β,ε])	As in #1
11	d[A50]/dt	vd(1,A50)-vd(3,A50)-vd(5,A50)+vd(6,A50)-vd(7,A50)-vdi(1,A50,[α,β,ε])+vdi(2,A50, [α,β,ε])+vdi(7,A50, [α,β,ε])+vdi(8,A50,[α,β,ε])	As in #1
12	d[5050]/dt	vd(1,5050)-vd(3,5050)-vd(5,5050)+vd(6,5050)-vd(7,5050)-vdi(1,5050,[α,β,ε])+vdi(2,5050, [α,β,ε])+vdi(7,5050, [α,β,ε])+vdi(8,5050,[α,β,ε])	As in #1
13	d[C50]/dt	vd(1,C50)-vd(3,C50)-vd(5,C50)+vd(6,C50)-vd(7,C50)-vdi(1,C50,[α,β,ε])+vdi(2,C50, [α,β,ε])+vdi(7,C50, [α,β,ε])+vdi(8,C50,[α,β,ε])	As in #1
14	d[nAA]/dt	vd(2,AA)-vd(4,AA)-vd(6,AA)+vd(5,AA)-vd(8,AA)-vdi(2,AA,[α,β,ε])+vdi(4,AA,[α,β,ε])+vdi(9,AA, [α,β,ε])	As in #1
15	d[nA50]/dt	vd(2,A50)-vd(4,A50)-vd(6,A50)+vd(5,A50)-vd(8,A50)-vdi(2,A50,[α,β,ε])+vdi(4,A50, [α,β,ε])+vdi(9,A50, [α,β,ε])	As in #1
16	d[n5050]/dt	vd(2,5050)-vd(4,5050)-vd(6,5050)+vd(5,5050)-vd(8,5050)-vdi(2,5050,[α,β,ε])+vdi(4,5050, [α,β,ε])+vdi(9,5050, [α,β,ε])	As in #1
17	d[nC50]/dt	vd(2,C50)-vd(4,C50)-vd(6,C50)+vd(5,C50)-vd(8,C50)-vdi(2,C50,[α,β,ε])+vdi(4,C50, [α,β,ε])+vdi(9,C50, [α,β,ε])	As in #1

#	Species	Reaction	Justification
18	d[AA:IkBα,AA:IkBβ, AA:IkBε]/dt	vdi(1,AA, [α,β,ε])-vdi(3,AA, [α,β,ε])-vdi(5,AA, [α,β,ε])+vdi(6,AA, [α,β,ε])-vdi(7,AA, [α,β,ε])-vdi(8,AA, [α,β,ε])-vdi(10,AA, [α,β,ε])	As in #1
19	d[A50:IkBα,A50:IkBβ, A50:IkBε]/dt	vdi(1,A50, [α,β,ε])-vdi(3,A50, [α,β,ε])-vdi(5,A50, [α,β,ε])+vdi(6,A50, [α,β,ε])-vdi(7,A50, [α,β,ε])-vdi(8,A50, [α,β,ε])-vdi(10,A50, [α,β,ε])	As in #1
20	d[5050:IkBα, 5050:IkBβ, 5050:IkBε]/dt	vdi(1,5050, [α,β,ε])-vdi(3,5050, [α,β,ε])-vdi(5,5050, [α,β,ε])+vdi(6,5050, [α,β,ε])-vdi(7,5050, [α,β,ε])-vdi(8,5050, [α,β,ε])-vdi(10,5050, [α,β,ε])	As in #1
21	d[C50:IkBα,C50:IkBβ , C50:IkBε]/dt	vdi(1,C50, [α,β,ε])-vdi(3,C50, [α,β,ε])-vdi(5,C50, [α,β,ε])+vdi(6,C50, [α,β,ε])-vdi(7,C50, [α,β,ε])-vdi(8,C50, [α,β,ε])-vdi(10,c50, [α,β,ε])	As in #1
22	d[nAA:nIkBα,nAA:nIkBβ, nAA:nIkBε]/dt	vdi(2,AA, [α,β,ε])-vdi(4,AA, [α,β,ε])-vdi(6,AA, [α,β,ε])+vdi(5,AA, [α,β,ε])-vdi(9,AA, [α,β,ε])-vdi(11,AA, [α,β,ε])	As in #1
23	d[nA50:nIkBα, nA50:nIkBβ, nA50:nIkBε]/dt	vdi(2,A50, [α,β,ε])-vdi(4,A50, [α,β,ε])-vdi(6,A50, [α,β,ε])+vdi(5,A50, [α,β,ε])-vdi(9,A50, [α,β,ε])-vdi(11,A50, [α,β,ε])	As in #1
24	d[n5050:nIkBα, n5050:nIkBβ, n5050:nIkBε]/dt	vdi(2,5050, [α,β,ε])-vdi(4,5050, [α,β,ε])-vdi(6,5050, [α,β,ε])+vdi(5,5050, [α,β,ε])-vdi(9,5050, [α,β,ε])-vdi(11,5050, [α,β,ε])	As in #1
25	d[nA50:nIkBα, nA50:nIkBβ, nA50:nIkBε]/dt	vdi(2,C50, [α,β,ε])-vdi(4,C50, [α,β,ε])-vdi(6,C50, [α,β,ε])+vdi(5,C50, [α,β,ε])-vdi(9,C50, [α,β,ε])-vdi(11,C50, [α,β,ε])	As in #1
26	d[tIkbα,tIkBβ,tIkBε]/dt	vi([α,β,∈])- vti(1, [α,β,ε])[tIkbα,tIkBβ,tIkBε]	As in #1
27	d[Ikbα,IkBβ,IkBε]/dt	$\sum_{d=[AA,A50,5050,C50]}\{$ vdi(3,d, [Ikbα,IkBβ,IkBε])+vdi(10,d, [Ikbα,IkBβ,IkBε])- vdi(1,d, [Ikbα,IkBβ,IkBε]) $\}$ +vti(2, [α,β,ε])[tIkbα,tIkBβ,tIkBε]- vti(3, [α,β,ε])[Ikbα,IkBβ,IkBε]- vti(4, [α,β,ε])[Ikbα,IkBβ,IkBε]- vti(6, [α,β,ε])[nIkbα,nIkBβ,nIkBε]+ vti(7, [α,β,ε])[Ikbα,IkBβ,IkBε]	As in #1
28	d[nIkbα,nIkBβ,nIkBε]/dt	$\sum_{d=[AA,A50,5050,C50]}\{$ vdi(4,d, [Ikbα,IkBβ,IkBε])+vdi(11,d, [Ikbα,IkBβ,IkBε])- vdi(2,d, [Ikbα,IkBβ,IkBε]) $\}$- vti(5, [α,β,ε])[nIkbα,nIkBβ,nIkBε]+ vti(6, [α,β,ε])[Ikbα,IkBβ,IkBε]- vti(7, [α,β,ε])[nIkbα,nIkBβ,nIkBε]	As in #1
29	d[L]/dt	0	See [156]
30	d[R]/dt	-va(1) + va(2) + va(71) - va(72)	As in #29
31	d[L-R]/dt	va(1) - va(2) - va(3)	As in #29
32	d[DISC]/dt	va(3) - va(4) + va(5) - va(6) + va(7) + va(8)	As in #29
33	d[flip]/dt	-va(4) + va(5) + va(73) - va(74)	As in #29
34	d[flip-DISC]/dt	va(4) - va(5) - va(75)	As in #29
35	d[pC8]/dt	-va(6) + va(7) - va(17) + va(18) + va(76) - va(77)	As in #29
36	d[DISC-pC8]/dt	va(6) - va(7) - va(8)	As in #29
37	d[C8]/dt	va(8) - va(9) + va(10) - va(11) + va(12) + va(13) + va(19) - va(26) + va(27) + va(28)	As in #29
38	d[Bar]/dt	-va(9) + va(10) + va(78) - va(79)	As in #29
39	d[Bar-C8]/dt	va(9) - va(10) - va(80)	As in #29
40	d[pC3]/dt	-va(11) + va(12) - va(62) + va(63) + va(101) - va(102)	As in #29
41	d[C8-pC3]/dt	va(11) - va(12) - va(13)	As in #29
42	d[C3]/dt	va(13) - va(14) + va(15) + va(16) - va(20) + va(21) - va(23) + va(24) + va(25) + va(64)	As in #29
43	d[pC6]/dt	-va(14) + va(15) + va(104) - va(105)	As in #29
44	d[C3-pC6]/dt	va(14) - va(15) - va(16)	As in #29
45	d[C6]/dt	va(16) - va(17) + va(18) + va(19) - va(106)	As in #29
46	d[C6-pC8]/dt	va(17) - va(18) - va(19)	As in #29
47	d[XIAP]/dt	-va(20) + va(21) + va(22) - va(67) + va(68) - va(69) + va(70) + va(95) - va(96)	As in #29
48	d[XIAP-C3]/dt	va(20) - va(21) - va(22)	As in #29
49	d[PARP]/dt	-va(23) + va(24) + va(108) - va(109)	As in #29
50	d[C3-PARP]/dt	va(23) - va(24) - va(25)	As in #29
51	d[CPARP]/dt	va(25) - va(110)	As in #29
52	d[Bid]/dt	-va(26) + va(27) + va(81) - va(82)	As in #29
53	d[C8-Bid]/dt	va(26) - va(27) - va(28)	As in #29

#	Species	Reaction	Justification
54	d[tBid]/dt	va(28) - va(29) + va(30) - va(31) + va(32) + va(33)	As in #29
55	d[Mcl1]/dt	-va(29) + va(30) + va(83) - va(84)	As in #29
56	d[Mcl1-tBid]/dt	+ va(29) - va(30) - va(85)	As in #29
57	d[Bax]/dt	-va(31) + va(32) + va(86) - va(87)	As in #29
58	d[tBid-Bax]/dt	va(31) - va(32) - va(33)	As in #29
59	d[act_Bax]/dt	va(33) - va(34) + va(35)	As in #29
60	d[Baxm]/dt	va(34) - va(35) -1/mvol*va(36) + va(37) -1/mvol*2*va(38) +2*va(39)	As in #29
61	d[Bcl2]/dt	-1/mvol*va(36) + va(37) -1/mvol*va(40) + va(41) -1/mvol*va(44) + va(45) + va(88) - va(89)	As in #29
62	d[Baxm-Bcl2]/dt	1/mvol*va(36) - va(37) - va(90)	As in #29
63	d[Bax2]/dt	1/mvol*va(38) - va(39) -1/mvol*va(40) + va(41) -2/mvol*va(42) +2*va(43)	As in #29
64	d[Bax2-Bcl2]/dt	1/mvol*va(40) - va(41) - va(91)	As in #29
65	d[Bax4]/dt	1/mvol*va(42) - va(43)-1/mvol*va(44) + va(45) -1/mvol*va(46) + va(47)	As in #29
66	d[Bax4-Bcl2]/dt	1/mvol*va(44) - va(45) - va(92)	As in #29
67	d[M]/dt	-1/mvol*va(46) + va(47) + va(93)	As in #29
68	d[Bax4-M]/dt	1/mvol*va(46) - va(47) - va(48)	As in #29
69	d[AMito]/dt	va(48) -1/mvol*va(49) + va(50) + va(51) -1/mvol*va(52) + va(53) + va(54) - va(93)	As in #29
70	d[mCytoC]/dt	-1/mvol*va(49) + va(50) + va(113) - va(114)	As in #29
71	d[AMito-mCytoC]/dt	1/mvol*va(49) - va(50) - va(51)	As in #29
72	d[ACytoC]/dt	va(51) - va(55) + va(56)	As in #29
73	d[mSmac]/dt	-1/mvol*va(52) + va(53) + va(97) - va(98)	As in #29
74	d[AMito-mSmac]/dt	1/mvol*va(52) - va(53) - va(54)	As in #29
75	d[ASmac]/dt	va(54) - va(65) + va(66)	As in #29
76	d[CytoC]/dt	va(55) - va(56) - va(58) + va(59) + va(57) - va(115)	As in #29
77	d[Apaf]/dt	-va(58) + va(59) + va(94)	As in #29
78	d[Apaf-CytoC]/dt	va(58) - va(59) - va(57)	As in #29
79	d[act_Apaf]/dt	va(57) - va(60) + va(61) - va(94)	As in #29
80	d[pC9]/dt	-va(60) + va(61)	As in #29
81	d[Apop]/dt	va(60) - va(61) - va(62) + va(63) + va(64) - va(67) + va(68) + va(107)	As in #29
82	d[Apop-pC3]/dt	va(62) - va(63) - va(64)	As in #29
83	d[cSmac]/dt	va(65) - va(66) - va(69) + va(70) - va(99)	As in #29
84	d[Apop-XIAP]/dt	va(67) - va(68) - va(107)	As in #29
85	d[cSmac-XIAP]/dt	va(69) - va(70) - va(100)	As in #29
86	d[C3_Ub]/dt	va(22) - va(103)	As in #29
87	d[CycA]/dt	vcc(36)+vcc(12)+vcc(18)-vcc(9)-vcc(6)	See [152]
88	d[CycB]/dt	vcc(42)-vcc(19)	As in #87
89	d[CycD]/dt	vcc(39)+vcc(17)+vcc(8)-vcc(7)-vcc(4)	As in #87
90	d[CycE]/dt	vcc(38)+vcc(11)+vcc(16)-vcc(14)-vcc(5)	As in #87
91	d[mCycD]/dt	vcc(34)-vcc(1)	As in #87
92	d[mBcl2]/dt	vcc(41)-vcc(2)	As in #87
93	d[Cdh1]/dt	vcc(20)-vcc(21)	As in #87
94	d[CA]/dt	vcc(6)-vcc(12)-vcc(18)-vcc(10)	As in #87
95	d[CD]/dt	vcc(7)-vcc(8)-vcc(17)-vcc(3)	As in #87
96	d[CDc20]/dt	vcc(26)-vcc(27)-vcc(28)	As in #87
97	d[CDc20T]/dt	vcc(35)-vcc(25)	As in #87
98	d[CE]/dt	vcc(5)-vcc(11)-vcc(13)-vcc(16)	As in #87
99	d[GM]/dt	vcc(31)-vcc(32)	As in #87
100	d[IEP]/dt	vcc(23)-vcc(24)	As in #87
101	d[Mass]/dt	vcc(33)-vcc(55)	As in #87
102	d[p27]/dt	vcc(40)+vcc(3)+vcc(8)-vcc(15)-vcc(5)-vcc(6)-vcc(7)+vcc(11)+vcc(12)+vcc(13)+vcc(10)	As in #87
103	d[PPX]/dt	vcc(37)-vcc(22)	As in #87
104	d[pp-Rb]/dt	vcc(29)+vcc(30)+vcc(43)-vcc(44)	As in #87
105	d[E2F]/dt	vcc(29)+vcc(45)+vcc(47)-vcc(46)-vcc(48)	As in #87
106	d[p-E2F]/dt	vcc(30)+vcc(49)+vcc(46)-vcc(47)-vcc(50)	As in #87
107	d[Rb]/dt	vcc(44)+vcc(45)+vcc(49)-vcc(48)-vcc(50)-vcc(43)	As in #87
108	d[E2F-Rb]/dt	vcc(51)+vcc(48)-vcc(52)-vcc(29)-vcc(45)	As in #87
109	d[p-E2F-Rb]/dt	vcc(52)+vcc(50)-vcc(51)-vcc(30)-vcc(49)	As in #87
110	d[MYC]/dt	vcc(53)-vcc(54)	As in #87
111	d[mMYC]/dt	vcc(56)-vcc(57)	As in #87

E. Other simulation parameters

#	Parameter	Value	Description	Justification
1	RCV	0.1	Protein syn/deg CV	For simplicity we assumed synthesis and degradation rates were normally distributed with a CV of 0.1 about the parameter value. Thi s is similar to the approach taken in [156] and results a steady state protein concentration variability with CV ~ 0.25 [24]
2	CCV	0.25	If no protein syn/deg then the total free protein concentration CV	We assumed log-normally distributed initial protein concetrations about the x_0 mean with a CV of 0.25 as in [24]
3	PCV	0.07	Partition volume CV	The observed variability in relative volumes was normal with mean 1 and standard deviation of 0.07 from microscopy studies in this work
4	VCV	0.05	Starting volume CV	The observed starting volume variability of viable cells from microscopy studies.
5	IKKCV	0.25	IKK CV	As in #2
6	N	250	Initial number of cellular agents used in multiscale model.	This number was large enough to ensure that repeated simulations produced very similar results.
7	Simulation Replicates	2	Average of 2 250 agent runs.	Two simulations with 250 agents were used to create each simulation. The averages of two replicate simulations are reported.
8	Tmax	144 h	Total simulation time.	Six days of simulations was sufficient for capturing both the expansion and contraction periods of the population response. This is also the typical duration of time-lapse experiments.
9	AbsTol	1e-5	Absolution simulation tolerance for Matlab function ode15s	This was sufficiently low to produce accurate results. Increasing this number further resulted in noticeable changes in solution accuracy.
10	RelTol	1e-3	Relative tolerationce of simulation s using Matlab function ode15s	As in #9

Bibliography

1. Murphy K, Travers P, Walport M (2007) Janeway's Immunobiology (Immunobiology: The Immune System (Janeway)): Garland Science.

2. Pearce EL, Pearce EJ (2013) Metabolic pathways in immune cell activation and quiescence. Immunity 38: 633-643.

3. LeBien TW, Tedder TF (2008) B lymphocytes: how they develop and function. Blood 112: 1570-1580.

4. Gerondakis S, Siebenlist U (2010) Roles of the NF-kappaB pathway in lymphocyte development and function. Cold Spring Harb Perspect Biol 2: a000182.

5. Wang YH, Zhang Z, Burrows PD, Kubagawa H, Bridges SL, Jr., Findley HW, Cooper MD (2003) V(D)J recombinatorial repertoire diversification during intraclonal pro-B to B-cell differentiation. Blood 101: 1030-1037.

6. Cooper MD (2002) Exploring lymphocyte differentiation pathways. Immunol Rev 185: 175-185.

7. Fulcher DA, Basten A (1994) Reduced life span of anergic self-reactive B cells in a double-transgenic model. J Exp Med 179: 125-134.

8. Treml LS, Quinn WJ, 3rd, Treml JF, Scholz JL, Cancro MP (2008) Manipulating B cell homeostasis: a key component in the advancement of targeted strategies. Arch Immunol Ther Exp (Warsz) 56: 153-164.

9. Nagai Y, Garrett KP, Ohta S, Bahrun U, Kouro T, Akira S, Takatsu K, Kincade PW (2006) Toll-like receptors on hematopoietic progenitor cells stimulate innate immune system replenishment. Immunity 24: 801-812.

10. Cahalan MD, Gutman GA (2006) The sense of place in the immune system. Nat Immunol 7: 329-332.

11. Cerutti A, Puga I, Cols M (2011) Innate control of B cell responses. Trends Immunol 32: 202-211.

12. Tonegawa S (1983) Somatic generation of antibody diversity. Nature 302: 575-581.

13. Malu S, Malshetty V, Francis D, Cortes P (2012) Role of non-homologous end joining in V(D)J recombination. Immunol Res 54: 233-246.

14. Peled JU, Kuang FL, Iglesias-Ussel MD, Roa S, Kalis SL, Goodman MF, Scharff MD (2008) The biochemistry of somatic hypermutation. Annu Rev Immunol 26: 481-511.

15. Cooper MD, Alder MN (2006) The evolution of adaptive immune systems. Cell 124: 815-822.

16. Kumar H, Kawai T, Akira S (2011) Pathogen recognition by the innate immune system. Int Rev Immunol 30: 16-34.

17. Browne EP (2012) Regulation of B-cell responses by Toll-like receptors. Immunology 136: 370-379.

18. Agrawal S, Gupta S (2011) TLR1/2, TLR7, and TLR9 signals directly activate human peripheral blood naive and memory B cell subsets to produce cytokines, chemokines, and hematopoietic growth factors. J Clin Immunol 31: 89-98.

19. Krieg AM, Yi AK, Matson S, Waldschmidt TJ, Bishop GA, Teasdale R, Koretzky GA, Klinman DM (1995) CpG motifs in bacterial DNA trigger direct B-cell activation. Nature 374: 546-549.

20. Hawkins ED, Turner ML, Wellard CJ, Zhou JH, Dowling MR, Hodgkin PD (2013) Quantal and graded stimulation of B lymphocytes as alternative strategies for regulating adaptive immune responses. Nat Commun 4: 2406.

21. Hawkins ED, Markham JF, McGuinness LP, Hodgkin PD (2009) A single-cell pedigree analysis of alternative stochastic lymphocyte fates. Proc Natl Acad Sci U S A 106: 13457-13462.

22. Flowers CR, Armitage JO (2010) A decade of progress in lymphoma: advances and continuing challenges. Clin Lymphoma Myeloma Leuk 10: 414-423.

23. Seifert M, Scholtysik R, Kuppers R (2013) Origin and pathogenesis of B cell lymphomas. Methods Mol Biol 971: 1-25.

24. Gaudet S, Spencer SL, Chen WW, Sorger PK (2012) Exploring the contextual sensitivity of factors that determine cell-to-cell variability in receptor-mediated apoptosis. PLoS Comput Biol 8: e1002482.

25. Flusberg DA, Roux J, Spencer SL, Sorger PK (2013) Cells surviving fractional killing by TRAIL exhibit transient but sustainable resistance and inflammatory phenotypes. Mol Biol Cell 24: 2186-2200.

26. Dimberg LY, Anderson CK, Camidge R, Behbakht K, Thorburn A, Ford HL (2013) On the TRAIL to successful cancer therapy? Predicting and counteracting resistance against TRAIL-based therapeutics. Oncogene 32: 1341-1350.

27. Yap TA, Gerlinger M, Futreal PA, Pusztai L, Swanton C (2012) Intratumor heterogeneity: seeing the wood for the trees. Sci Transl Med 4: 127ps110.

28. Schliemann M, Bullinger E, Borchers S, Allgower F, Findeisen R, Scheurich P (2011) Heterogeneity reduces sensitivity of cell death for TNF-stimuli. BMC Syst Biol 5: 204.

29. Fallahi-Sichani M, Honarnejad S, Heiser LM, Gray JW, Sorger PK (2013) Metrics other than potency reveal systematic variation in responses to cancer drugs. Nat Chem Biol 9: 708-714.

30. Frank SA, Rosner MR (2012) Nonheritable cellular variability accelerates the evolutionary processes of cancer. PLoS Biol 10: e1001296.

31. Meyer-Bahlburg A, Rawlings DJ (2008) B cell autonomous TLR signaling and autoimmunity. Autoimmun Rev 7: 313-316.

32. Pai S, Thomas R (2008) Immune deficiency or hyperactivity-Nf-kappab illuminates autoimmunity. J Autoimmun 31: 245-251.

33. Rickert RC, Jellusova J, Miletic AV (2011) Signaling by the tumor necrosis factor receptor superfamily in B-cell biology and disease. Immunol Rev 244: 115-133.

34. Goldin LR, Landgren O (2009) Autoimmunity and lymphomagenesis. Int J Cancer 124: 1497-1502.

35. Milner JD, Holland SM (2013) The cup runneth over: lessons from the ever-expanding pool of primary immunodeficiency diseases. Nat Rev Immunol 13: 635-648.

36. Xiao X, Miao Q, Chang C, Gershwin ME, Ma X (2014) Common variable immunodeficiency and autoimmunity - an inconvenient truth. Autoimmun Rev.

37. Kumar H, Kawai T, Akira S (2009) Toll-like receptors and innate immunity. Biochem Biophys Res Commun 388: 621-625.

38. Peng SL (2005) Signaling in B cells via Toll-like receptors. Curr Opin Immunol 17: 230-236.

39. Lopez-Yglesias AH, Zhao X, Quarles EK, Lai MA, VandenBos T, Strong RK, Smith KD (2014) Flagellin induces antibody responses through a TLR5- and inflammasome-independent pathway. J Immunol 192: 1587-1596.

40. Hidmark A, von Saint Paul A, Dalpke AH (2012) Cutting edge: TLR13 is a receptor for bacterial RNA. J Immunol 189: 2717-2721.

41. Raetz M, Kibardin A, Sturge CR, Pifer R, Li H, Burstein E, Ozato K, Larin S, Yarovinsky F (2013) Cooperation of TLR12 and TLR11 in the IRF8-dependent IL-12 response to Toxoplasma gondii profilin. J Immunol 191: 4818-4827.

42. Mulla MJ, Myrtolli K, Tadesse S, Stanwood NL, Gariepy A, Guller S, Norwitz ER, Abrahams VM (2013) Cutting-edge report: TLR10 plays a role in mediating bacterial peptidoglycan-induced trophoblast apoptosis. Am J Reprod Immunol 69: 449-453.

43. Jiang W, Lederman MM, Harding CV, Rodriguez B, Mohner RJ, Sieg SF (2007) TLR9 stimulation drives naive B cells to proliferate and to attain enhanced antigen presenting function. Eur J Immunol 37: 2205-2213.

44. Hawkins ED, Turner ML, Dowling MR, van Gend C, Hodgkin PD (2007) A model of immune regulation as a consequence of randomized lymphocyte division and death times. Proc Natl Acad Sci U S A 104: 5032-5037.

45. Hawkins ED, Hommel M, Turner ML, Battye FL, Markham JF, Hodgkin PD (2007) Measuring lymphocyte proliferation, survival and differentiation using CFSE time-series data. Nat Protoc 2: 2057-2067.

46. Duffy KR, Wellard CJ, Markham JF, Zhou JH, Holmberg R, Hawkins ED, Hasbold J, Dowling MR, Hodgkin PD (2012) Activation-induced B cell fates are selected by intracellular stochastic competition. Science 335: 338-341.

47. Shokhirev MN, Hoffmann A (2013) FlowMax: A Computational Tool for Maximum Likelihood Deconvolution of CFSE Time Courses. PLoS One 8: e67620.

48. Spencer SL, Cappell SD, Tsai FC, Overton KW, Wang CL, Meyer T (2013) The proliferation-quiescence decision is controlled by a bifurcation in CDK2 activity at mitotic exit. Cell 155: 369-383.

49. Link JM, Hurlin PJ (2014) The activities of MYC, MNT and the Max-Interactome in lymphocyte proliferation and oncogenesis. Biochim Biophys Acta.

50. Renault TT, Chipuk JE (2013) Getting away with murder: how does the BCL-2 family of proteins kill with immunity? Ann N Y Acad Sci 1285: 59-79.

51. O'Dea E, Hoffmann A (2010) The regulatory logic of the NF-kappaB signaling system. Cold Spring Harb Perspect Biol 2: a000216.

52. Lenert P, Stunz L, Yi AK, Krieg AM, Ashman RF (2001) CpG stimulation of primary mouse B cells is blocked by inhibitory oligodeoxyribonucleotides at a site proximal to NF-kappaB activation. Antisense Nucleic Acid Drug Dev 11: 247-256.

53. Hannink M, Temin HM (1990) Structure and autoregulation of the c-rel promoter. Oncogene 5: 1843-1850.

54. Ten RM, Paya CV, Israel N, Le Bail O, Mattei MG, Virelizier JL, Kourilsky P, Israel A (1992) The characterization of the promoter of the gene encoding the p50 subunit of NF-kappa B indicates that it participates in its own regulation. EMBO J 11: 195-203.

55. Haskill S, Beg AA, Tompkins SM, Morris JS, Yurochko AD, Sampson-Johannes A, Mondal K, Ralph P, Baldwin AS, Jr. (1991) Characterization of an immediate-early gene induced in adherent monocytes that encodes I kappa B-like activity. Cell 65: 1281-1289.

56. Tian B, Nowak DE, Jamaluddin M, Wang S, Brasier AR (2005) Identification of direct genomic targets downstream of the nuclear factor-kappaB transcription factor mediating tumor necrosis factor signaling. J Biol Chem 280: 17435-17448.

57. Shih VF, Tsui R, Caldwell A, Hoffmann A (2011) A single NFkappaB system for both canonical and non-canonical signaling. Cell Res 21: 86-102.

58. Nie Z, Hu G, Wei G, Cui K, Yamane A, Resch W, Wang R, Green DR, Tessarollo L, Casellas R, Zhao K, Levens D (2012) c-Myc is a universal amplifier of expressed genes in lymphocytes and embryonic stem cells. Cell 151: 68-79.

59. Duyao MP, Buckler AJ, Sonenshein GE (1990) Interaction of an NF-kappa B-like factor with a site upstream of the c-myc promoter. Proc Natl Acad Sci U S A 87: 4727-4731.

60. Pohl T, Gugasyan R, Grumont RJ, Strasser A, Metcalf D, Tarlinton D, Sha W, Baltimore D, Gerondakis S (2002) The combined absence of NF-kB1 and c-Rel reveals that overlapping roles of these transcription factors in the B cell lineage are restricted to the activation and function of mature cells. PNAS: 4514-4519.

61. Limon JJ, Fruman DA (2012) Akt and mTOR in B Cell Activation and Differentiation. Front Immunol 3: 228.

62. Zeng H, Chi H (2013) mTOR and lymphocyte metabolism. Curr Opin Immunol 25: 347-355.

63. Xu ZZ, Xia ZG, Wang AH, Wang WF, Liu ZY, Chen LY, Li JM (2013) Activation of the PI3K/AKT/mTOR pathway in diffuse large B cell lymphoma: clinical significance and inhibitory effect of rituximab. Ann Hematol 92: 1351-1358.

64. Hanahan D, Weinberg RA (2011) Hallmarks of cancer: the next generation. Cell 144: 646-674.

65. Porta C, Paglino C, Mosca A (2014) Targeting PI3K/Akt/mTOR Signaling in Cancer. Front Oncol 4: 64.

66. Wang R, Dillon CP, Shi LZ, Milasta S, Carter R, Finkelstein D, McCormick LL, Fitzgerald P, Chi H, Munger J, Green DR (2011) The transcription factor Myc controls metabolic reprogramming upon T lymphocyte activation. Immunity 35: 871-882.

67. Dan HC, Cooper MJ, Cogswell PC, Duncan JA, Ting JP, Baldwin AS (2008) Akt-dependent regulation of NF-{kappa}B is controlled by mTOR and Raptor in association with IKK. Genes Dev 22: 1490-1500.

68. Dhingra R, Gang H, Wang Y, Biala AK, Aviv Y, Margulets V, Tee A, Kirshenbaum LA (2013) Bidirectional regulation of nuclear factor-kappaB and mammalian target of rapamycin signaling functionally links Bnip3 gene repression and cell survival of ventricular myocytes. Circ Heart Fail 6: 335-343.

69. Radhakrishnan P, Bryant VC, Blowers EC, Rajule RN, Gautam N, Anwar MM, Mohr AM, Grandgenett PM, Bunt SK, Arnst JL, Lele SM, Alnouti Y, Hollingsworth MA, Natarajan A (2013) Targeting the NF-kappaB and mTOR pathways with a quinoxaline urea analog that inhibits IKKbeta for pancreas cancer therapy. Clin Cancer Res 19: 2025-2035.

70. Wang Z, Sicinski P, Weinberg RA, Zhang Y, Ravid K (1996) Characterization of the mouse cyclin D3 gene: exon/intron organization and promoter activity. Genomics 35: 156-163.

71. Guttridge DC, Albanese C, Reuther JY, Pestell RG, Baldwin AS, Jr. (1999) NF-kappaB controls cell growth and differentiation through transcriptional regulation of cyclin D1. Mol Cell Biol 19: 5785-5799.

72. Huang Y, Ohtani K, Iwanaga R, Matsumura Y, Nakamura M (2001) Direct trans-activation of the human cyclin D2 gene by the oncogene product Tax of human T-cell leukemia virus type I. Oncogene 20: 1094-1102.

73. Cheng S, Hsia CY, Leone G, Liou HC (2003) Cyclin E and Bcl-xL cooperatively induce cell cycle progression in c-Rel-/- B cells. Oncogene 22: 8472-8486.

74. Chen F, Demers LM, Vallyathan V, Lu Y, Castranova V, Shi X (1999) Involvement of 5'-flanking kappaB-like sites within bcl-x gene in silica-induced Bcl-x expression. J Biol Chem 274: 35591-35595.

75. Hinz M, Krappmann D, Eichten A, Heder A, Scheidereit C, Strauss M (1999) NF-kappaB function in growth control: regulation of cyclin D1 expression and G0/G1-to-S-phase transition. Mol Cell Biol 19: 2690-2698.

76. Cato MH, Chintalapati SK, Yau IW, Omori SA, Rickert RC (2011) Cyclin D3 is selectively required for proliferative expansion of germinal center B cells. Mol Cell Biol 31: 127-137.

77. Lam EW, Glassford J, Banerji L, Thomas NS, Sicinski P, Klaus GG (2000) Cyclin D3 compensates for loss of cyclin D2 in mouse B-lymphocytes activated via the antigen receptor and CD40. J Biol Chem 275: 3479-3484.

78. Tanguay DA, Colarusso TP, Pavlovic S, Irigoyen M, Howard RG, Bartek J, Chiles TC, Rothstein TL (1999) Early induction of cyclin D2 expression in phorbol ester-responsive B-1 lymphocytes. J Exp Med 189: 1685-1690.

79. Piatelli M, Tanguay D, Rothstein T, Chiles T (2003) Cell cycle control mechanisms in B-1 and B-2 lymphoid subsets. Immunol Res 27: 31-52.

80. Pham LV, Tamayo AT, Yoshimura LC, Lo P, Ford RJ (2003) Inhibition of constitutive NF-kappa B activation in mantle cell lymphoma B cells leads to induction of cell cycle arrest and apoptosis. J Immunol 171: 88-95.

81. Kong LJ, Chang JT, Bild AH, Nevins JR (2007) Compensation and specificity of function within the E2F family. Oncogene 26: 321-327.

82. Hatakeyama M, Weinberg RA (1995) The role of RB in cell cycle control. Prog Cell Cycle Res 1: 9-19.

83. Grumont RJ, Rourke IJ, Gerondakis S (1999) Rel-dependent induction of A1 transcription is required to protect B cells from antigen receptor ligation-induced apoptosis. Genes Dev 13: 400-411.

84. Waterfield M, Jin W, Reiley W, Zhang M, Sun S-C (2004) IκB Kinase Is an Essential Component of the Tpl2 Signaling Pathway. Molecular and Cellular Biology 24: 6040-6048.

85. Babu GR, Jin W, Norman L, Waterfield M, Chang M, Wu X, Zhang M, Sun SC (2006) Phosphorylation of NF-kappaB1/p105 by oncoprotein kinase Tpl2: implications for a novel mechanism of Tpl2 regulation. Biochim Biophys Acta 1763: 174-181.

86. Banerjee A, Gugasyan R, McMahon M, Gerondakis S (2006) Diverse Toll-like receptors utilize Tpl2 to activate extracellular signal-regulated kinase (ERK) in hemopoietic cells. Proc Natl Acad Sci U S A 103: 3274-3279.

87. Belich MP, Salmeron A, Johnston LH, Ley SC (1999) TPL-2 kinase regulates the proteolysis of the NF-kappaB-inhibitory protein NF-kappaB1 p105. Nature 397: 363-368.

88. Weston SA, Parish CR (1990) New fluorescent dyes for lymphocyte migration studies. Analysis by flow cytometry and fluorescence microscopy. J Immunol Methods 133: 87-97.

89. M R (2011) Interpretation of Cellular proliferation Data: Avoid the Panglossian. Cytometry: 95-101.

90. Zilman A, Ganusov VV, Perelson AS (2010) Stochastic models of lymphocyte proliferation and death. PLoS One 5.

91. Miao H, Jin X, Perelson A, Wu H (2012) Evaluation of Multitype Mathematical Models for CFSE-Labeling Experiment Data. Bull Math Biol 74: 300-326.

92. Smith JA, Martin L (1973) Do cells cycle? Proc Natl Acad Sci U S A 70: 1263-1267.

93. De Boer RJ, Oprea M, Antia R, Murali-Krishna K, Ahmed R, Perelson AS (2001) Recruitment times, proliferation, and apoptosis rates during the CD8(+) T-cell response to lymphocytic choriomeningitis virus. J Virol 75: 10663-10669.

94. Revy P, Sospedra M, Barbour B, Trautmann A (2001) Functional antigen-independent synapses formed between T cells and dendritic cells. Nat Immunol 2: 925-931.

95. De Boer RJ, Homann D, Perelson AS (2003) Different dynamics of CD4+ and CD8+ T cell responses during and after acute lymphocytic choriomeningitis virus infection. J Immunol 171: 3928-3935.

96. Pilyugin SS, Ganusov VV, Murali-Krishna K, Ahmed R, Antia R (2003) The rescaling method for quantifying the turnover of cell populations. J Theor Biol 225: 275-283.

97. Luzyanina T, Mrusek S, Edwards JT, Roose D, Ehl S, Bocharov G (2007) Computational analysis of CFSE proliferation assay. J Math Biol 54: 57-89.

98. Luzyanina T, Roose D, Schenkel T, Sester M, Ehl S, Meyerhans A, Bocharov G (2007) Numerical modelling of label-structured cell population growth using CFSE distribution data. Theor Biol Med Model 4: 26.

99. Banks HT, Sutton KL, Thompson WC, Bocharov G, Doumic M, Schenkel T, Argilaguet J, Giest S, Peligero C, Meyerhans A (2011) A new model for the estimation of cell proliferation dynamics using CFSE data. J Immunol Methods 373: 143-160.

100. Gett AV, Hodgkin PD (2000) A cellular calculus for signal integration by T cells. Nat Immunol 1: 239-244.

101. Leon K, Faro J, Carneiro J (2004) A general mathematical framework to model generation structure in a population of asynchronously dividing cells. J Theor Biol 229: 455-476.

102. De Boer RJ, Perelson AS (2005) Estimating division and death rates from CFSE data. Journal of Computational and Applied Mathematics 184: 140-164.

103. Ganusov VV, Pilyugin SS, de Boer RJ, Murali-Krishna K, Ahmed R, Antia R (2005) Quantifying cell turnover using CFSE data. J Immunol Methods 298: 183-200.

104. De Boer RJ, Ganusov VV, Milutinovic D, Hodgkin PD, Perelson AS (2006) Estimating lymphocyte division and death rates from CFSE data. Bull Math Biol 68: 1011-1031.

105. Lee HY, Perelson AS (2008) Modeling T cell proliferation and death in vitro based on labeling data: generalizations of the Smith-Martin cell cycle model. Bull Math Biol 70: 21-44.

106. Deenick EK, Gett AV, Hodgkin PD (2003) Stochastic model of T cell proliferation: a calculus revealing IL-2 regulation of precursor frequencies, cell cycle time, and survival. J Immunol 170: 4963-4972.

107. Hasenauer J, Schittler D, Allgöwer F (2012) Analysis and Simulation of Division- and Label-Structured Population Models. Bull Math Biol 74: 2692-2732.

108. Metzger P, Hasenauer J, Allgöwer F. Modeling and analysis of division-, age-, and label structured cell populations. In: Larjo AS, S.; Farhan, M.; Bossert, M.; Yli-Harja, O., editor. TICSP; 2012; Ulm, Germany. Tampere International Center for Signal Processing. pp. 60-63.

109. Schittler DH, J.;Allgöwer, F. A model for proliferating cell populations that accounts for cell types. In: Larjo AS, S.; Farhan, M.; Bossert, M.; Yli-Harja, O., editor. TICSP; 2012; Ulm, Germany. Tampere International Center for Signal Processing. pp. 84087.

110. J. Hasenauer DS, F. Allgower (2012) A computational model for proliferation dynamics of division- and label-structured populations. Technical Report arXiv 1202.4923v1.

111. Hyrien O, Chen R, Zand MS (2010) An age-dependent branching process model for the analysis of CFSE-labeling experiments. Biol Direct 5: 41.

112. Hyrien O, Zand MS (2008) A Mixture Model With Dependent Observations for the Analysis of CSFE–Labeling Experiments. Journal of the American Statistical Association 103: 222-239.

113. Shokhirev MN, Hoffmann A (2013) Quantitative deconvolution of CFSE cell population time courses with confidence. PLoS One.

114. Lecault V, Vaninsberghe M, Sekulovic S, Knapp DJ, Wohrer S, Bowden W, Viel F, McLaughlin T, Jarandehei A, Miller M, Falconnet D, White AK, Kent DG, Copley MR, Taghipour F, Eaves CJ, Humphries RK, Piret JM, Hansen CL (2011) High-throughput analysis of single hematopoietic stem cell proliferation in microfluidic cell culture arrays. Nat Methods 8: 581-586.

115. Polonsky M, Zaretsky I, Friedman N (2013) Dynamic single-cell measurements of gene expression in primary lymphocytes: challenges, tools and prospects. Brief Funct Genomics 12: 99-108.

116. Chakravorty R, Rawlinson D, Zhang A, Markham J, Dowling MR, Wellard C, Zhou JH, Hodgkin PD (2014) Labour-efficient in vitro lymphocyte population tracking and fate prediction using automation and manual review. PLoS One 9: e83251.

117. Meijering E, Dzyubachyk O, Smal I (2012) Methods for cell and particle tracking. Methods Enzymol 504: 183-200.

118. Li K, Miller ED, Chen M, Kanade T, Weiss LE, Campbell PG (2008) Cell population tracking and lineage construction with spatiotemporal context. Med Image Anal 12: 546-566.

119. Hadjidemetriou S, Gabrielli B, Pike T, Stevens F, Mele K, Vallotton P (2008) Detection and tracking of cell divisions in phase contrast video microscopy. Proc of the Third MICCAI Worshop on Microscopic Image Analysis with Applications in Biology.

120. Hand AJ, Sun T, Barber DC, Hose DR, MacNeil S (2009) Automated tracking of migrating cells in phase-contrast video microscopy sequences using image registration. J Microsc 234: 62-79.

121. Becker T, Rapoport D, Mamlouk A (2011) Adaptive Mitosis Detection in Large in vitro Stem Cell Populations using Timelapse Microscopy. In: Handels H, Ehrhardt J, Deserno TM, Meinzer H-P, Tolxdorff T, editors. Bildverarbeitung für die Medizin 2011: Springer Berlin Heidelberg. pp. 49-53.

122. Kachouie NN, Fieguth PW (2007) Extended-Hungarian-JPDA: exact single-frame stem cell tracking. IEEE Trans Biomed Eng 54: 2011-2019.

123. Musicki D, Evans R. Linear joint integrated probabilistic data association - LJIPDA; 2002 10-13 Dec. 2002. pp. 2415-2420 vol.2413.

124. Rapoport DH, Becker T, Madany Mamlouk A, Schicktanz S, Kruse C (2011) A novel validation algorithm allows for automated cell tracking and the extraction of biologically meaningful parameters. PLoS One 6: e27315.

125. Kiss A, Horvath P, Rothballer A, Kutay U, Csucs G (2014) Nuclear motility in glioma cells reveals a cell-line dependent role of various cytoskeletal components. PLoS One 9: e93431.

126. Sacan A, Ferhatosmanoglu H, Coskun H (2008) CellTrack: an open-source software for cell tracking and motility analysis. Bioinformatics 24: 1647-1649.

127. Lamprecht MR, Sabatini DM, Carpenter AE (2007) CellProfiler: free, versatile software for automated biological image analysis. Biotechniques 42: 71-75.

128. Eilken HM, Nishikawa S, Schroeder T (2009) Continuous single-cell imaging of blood generation from haemogenic endothelium. Nature 457: 896-900.

129. Sulston JE, Horvitz HR (1977) Post-embryonic cell lineages of the nematode, Caenorhabditis elegans. Dev Biol 56: 110-156.

130. Boyle TJ, Bao Z, Murray JI, Araya CL, Waterston RH (2006) AceTree: a tool for visual analysis of Caenorhabditis elegans embryogenesis. BMC Bioinformatics 7: 275.

131. Murray JI, Bao Z, Boyle TJ, Waterston RH (2006) The lineaging of fluorescently-labeled Caenorhabditis elegans embryos with StarryNite and AceTree. Nat Protoc 1: 1468-1476.

132. Stadler C, Rexhepaj E, Singan VR, Murphy RF, Pepperkok R, Uhlen M, Simpson JC, Lundberg E (2013) Immunofluorescence and fluorescent-protein tagging show high correlation for protein localization in mammalian cells. Nat Methods 10: 315-323.

133. Lindstrom S (2012) Flow cytometry and microscopy as means of studying single cells: a short introductional overview. Methods Mol Biol 853: 13-15.

134. Wu AR, Neff NF, Kalisky T, Dalerba P, Treutlein B, Rothenberg ME, Mburu FM, Mantalas GL, Sim S, Clarke MF, Quake SR (2014) Quantitative assessment of single-cell RNA-sequencing methods. Nat Methods 11: 41-46.

135. Treutlein B, Brownfield DG, Wu AR, Neff NF, Mantalas GL, Espinoza FH, Desai TJ, Krasnow MA, Quake SR (2014) Reconstructing lineage hierarchies of the distal lung epithelium using single-cell RNA-seq. Nature.

136. Jaitin DA, Kenigsberg E, Keren-Shaul H, Elefant N, Paul F, Zaretsky I, Mildner A, Cohen N, Jung S, Tanay A, Amit I (2014) Massively parallel single-cell RNA-seq for marker-free decomposition of tissues into cell types. Science 343: 776-779.

137. Deng Q, Ramskold D, Reinius B, Sandberg R (2014) Single-cell RNA-seq reveals dynamic, random monoallelic gene expression in mammalian cells. Science 343: 193-196.

138. Islam S, Zeisel A, Joost S, La Manno G, Zajac P, Kasper M, Lonnerberg P, Linnarsson S (2014) Quantitative single-cell RNA-seq with unique molecular identifiers. Nat Methods 11: 163-166.

139. Schmid I, Uittenbogaart CH, Giorgi JV (1991) A gentle fixation and permeabilization method for combined cell surface and intracellular staining with improved precision in DNA quantification. Cytometry 12: 279-285.

140. Ning L, Liu G, Li G, Hou Y, Tong Y, He J (2014) Current Challenges in the Bioinformatics of Single Cell Genomics. Front Oncol 4: 7.

141. Dobin A, Davis CA, Schlesinger F, Drenkow J, Zaleski C, Jha S, Batut P, Chaisson M, Gingeras TR (2013) STAR: ultrafast universal RNA-seq aligner. Bioinformatics 29: 15-21.

142. Heinz S, Benner C, Spann N, Bertolino E, Lin YC, Laslo P, Cheng JX, Murre C, Singh H, Glass CK (2010) Simple combinations of lineage-determining transcription factors prime cis-regulatory elements required for macrophage and B cell identities. Mol Cell 38: 576-589.

143. Wang J, Duncan D, Shi Z, Zhang B (2013) WEB-based GEne SeT AnaLysis Toolkit (WebGestalt): update 2013. Nucleic Acids Res 41: W77-83.

144. Oshlack A, Robinson MD, Young MD (2010) From RNA-seq reads to differential expression results. Genome Biol 11: 220.

145. Narang V, Decraene J, Wong SY, Aiswarya BS, Wasem AR, Leong SR, Gouaillard A (2012) Systems immunology: a survey of modeling formalisms, applications and simulation tools. Immunol Res 53: 251-265.

146. An G, Mi Q, Dutta-Moscato J, Vodovotz Y (2009) Agent-based models in translational systems biology. Wiley Interdiscip Rev Syst Biol Med 1: 159-171.

147. Werner SL, Kearns JD, Zadorozhnaya V, Lynch C, O'Dea E, Boldin MP, Ma A, Baltimore D, Hoffmann A (2008) Encoding NF-kappaB temporal control in response to TNF: distinct roles for the negative regulators IkappaBalpha and A20. Genes Dev 22: 2093-2101.

148. Shih VF-S, Kearns JD, Basak S, Savinova OV, Ghosh G, Hoffmann A (2009) Kinetic control of negative feedback regulators of NF-κB/RelA determines their pathogen- and cytokine-receptor signaling specificity. Proceedings of the National Academy of Sciences 106: 9619-9624.

149. Kearns JD, Hoffmann A (2009) Integrating computational and biochemical studies to explore mechanisms in NF-{kappa}B signaling. J Biol Chem 284: 5439-5443.

150. Alves BN, Tsui R, Almaden J, Shokhirev MN, Davis-Turak J, Fujimoto J, Birnbaum H, Ponomarenko J, Hoffmann A (2014) IkappaB{varepsilon} Is a Key Regulator of B Cell Expansion by Providing Negative Feedback on cRel and RelA in a Stimulus-Specific Manner. J Immunol 192: 3121-3132.

151. Powathil GG, Adamson DJ, Chaplain MA (2013) Towards predicting the response of a solid tumour to chemotherapy and radiotherapy treatments: clinical insights from a computational model. PLoS Comput Biol 9: e1003120.

152. Conradie R, Bruggeman FJ, Ciliberto A, Csikasz-Nagy A, Novak B, Westerhoff HV, Snoep JL (2010) Restriction point control of the mammalian cell cycle via the cyclin E/Cdk2:p27 complex. FEBS J 277: 357-367.

153. Singhania R, Sramkoski RM, Jacobberger JW, Tyson JJ (2011) A hybrid model of mammalian cell cycle regulation. PLoS Comput Biol 7: e1001077.

154. Gerard C, Goldbeter A (2012) From quiescence to proliferation: Cdk oscillations drive the mammalian cell cycle. Front Physiol 3: 413.

155. Albeck JG, Burke JM, Spencer SL, Lauffenburger DA, Sorger PK (2008) Modeling a snap-action, variable-delay switch controlling extrinsic cell death. PLoS Biol 6: 2831-2852.

156. Loriaux PM, Tesler G, Hoffmann A (2013) Characterizing the relationship between steady state and response using analytical expressions for the steady states of mass action models. PLoS Comput Biol 9: e1002901.

157. Aldridge BB, Burke JM, Lauffenburger DA, Sorger PK (2006) Physicochemical modelling of cell signalling pathways. Nat Cell Biol 8: 1195-1203.

158. Chylek LA, Harris LA, Tung CS, Faeder JR, Lopez CF, Hlavacek WS (2014) Rule-based modeling: a computational approach for studying biomolecular site dynamics in cell signaling systems. Wiley Interdiscip Rev Syst Biol Med 6: 13-36.

159. Gillespie DT, Hellander A, Petzold LR (2013) Perspective: Stochastic algorithms for chemical kinetics. J Chem Phys 138: 170901.

160. Bajikar SS, Janes KA (2012) Multiscale models of cell signaling. Ann Biomed Eng 40: 2319-2327.

161. Powathil GG, Gordon KE, Hill LA, Chaplain MA (2012) Modelling the effects of cell-cycle heterogeneity on the response of a solid tumour to chemotherapy: biological insights from a hybrid multiscale cellular automaton model. J Theor Biol 308: 1-19.

162. Rejniak KA, Anderson AR (2011) Hybrid models of tumor growth. Wiley Interdiscip Rev Syst Biol Med 3: 115-125.

163. Folcik VA, An GC, Orosz CG (2007) The Basic Immune Simulator: an agent-based model to study the interactions between innate and adaptive immunity. Theor Biol Med Model 4: 39.

164. Liu G, Qutub AA, Vempati P, Mac Gabhann F, Popel AS (2011) Module-based multiscale simulation of angiogenesis in skeletal muscle. Theor Biol Med Model 8: 6.

165. Jiao B, Ma H, Shokhirev MN, Drung A, Yang Q, Shin J, Lu S, Byron M, Kalantry S, Mercurio AM, Lawrence JB, Hoffmann A, Bach I (2012) Paternal RLIM/Rnf12 is a survival factor for milk-producing alveolar cells. Cell 149: 630-641.

166. Shokhirev MN, Johnson AA (2014) Effects of extrinsic mortality on the evolution of aging: a stochastic modeling approach. PLoS One 9: e86602.

167. Wolkenhauer O, Auffray C, Jaster R, Steinhoff G, Dammann O (2013) The road from systems biology to systems medicine. Pediatr Res 73: 502-507.

168. Wright DW, Wan S, Shublaq N, Zasada SJ, Coveney PV (2012) From base pair to bedside: molecular simulation and the translation of genomics to personalized medicine. Wiley Interdiscip Rev Syst Biol Med 4: 585-598.

169. Subramanian VG, Duffy KR, Turner ML, Hodgkin PD (2008) Determining the expected variability of immune responses using the cyton model. J Math Biol 56: 861-892.

170. Roeder M (2011) Interpretation of Cellular proliferation Data: Avoid the Panglossian. Cytometry: 95-101.

171. Banerjee A, Grumont R, Gugasyan R, White C, Strasser A, Gerondakis. S (2008) NF-kB1 and c-Rel cooperate to promote the survival of TLR4-activated B cells by neutralizing Bim via distinct mechanisms. Blood: 5063-5073.

172. Savinova OV, Hoffmann A, Ghosh G (2009) The Nfkb1 and Nfkb2 Proteins p105 and p100 Function as the Core of High-Molecular-Weight Heterogeneous Complexes. Molecular Cell 34: 591-602.

173. Hulspas R, O'Gorman MR, Wood BL, Gratama JW, Sutherland DR (2009) Considerations for the control of background fluorescence in clinical flow cytometry. Cytometry B Clin Cytom 76: 355-364.

174. Callard R, Hodgkin P (2007) Modeling T- and B-cell growth and differentiation. Immunological Reviews 216: 119-129.

175. Kirkpatrick S, Gelatt CD, Jr., Vecchi MP (1983) Optimization by simulated annealing. Science 220: 671-680.

176. S K, D GC, P VM (1983) Optimization by Simulated Annealing. Science New Series: 671-680.

177. Yusuf I, Fruman DA (2003) Regulation of quiescence in lymphocytes. Trends Immunol 24: 380-386.

178. Grumont RJ, Strasser A, Gerondakis S (2002) B cell growth is controlled by phosphatidylinosotol 3-kinase-dependent induction of Rel/NF-kappaB regulated c-myc transcription. Mol Cell 10: 1283-1294.

179. Church DM, Goodstadt L, Hillier LW, Zody MC, Goldstein S, She X, Bult CJ, Agarwala R, Cherry JL, DiCuccio M, Hlavina W, Kapustin Y, Meric P, Maglott D, Birtle Z, Marques AC, Graves T, Zhou S, Teague B, Potamousis K, Churas C, Place M, Herschleb J, Runnheim R, Forrest D, Amos-Landgraf J, Schwartz DC, Cheng Z, Lindblad-Toh K, Eichler EE, Ponting CP, Mouse Genome Sequencing C (2009) Lineage-specific biology revealed by a finished genome assembly of the mouse. PLoS Biol 7: e1000112.

180. Gilmore TD (2014) NF-kB Target Genes. http://www.bu.edu/nf-kb/gene-resources/target-genes/: Boston University.

181. Schneider HC, Klabunde T (2013) Understanding drugs and diseases by systems biology? Bioorg Med Chem Lett 23: 1168-1176.

182. Behar M, Barken D, Werner SL, Hoffmann A (2013) The dynamics of signaling as a pharmacological target. Cell 155: 448-461.

183. Basak S, Kim H, Kearns JD, Tergaonkar V, O'Dea E, Werner SL, Benedict CA, Ware CF, Ghosh G, Verma IM, Hoffmann A (2007) A fourth IkappaB protein within the NF-kappaB signaling module. Cell 128: 369-381.

184. Shih VF, Davis-Turak J, Macal M, Huang JQ, Ponomarenko J, Kearns JD, Yu T, Fagerlund R, Asagiri M, Zuniga EI, Hoffmann A (2012) Control of RelB during dendritic cell activation integrates canonical and noncanonical NF-kappaB pathways. Nat Immunol 13: 1162-1170.

185. Bertolusso R, Tian B, Zhao Y, Vergara L, Sabree A, Iwanaszko M, Lipniacki T, Brasier AR, Kimmel M (2014) Dynamic cross talk model of the epithelial innate immune response to double-stranded RNA stimulation: coordinated dynamics emerging from cell-level noise. PLoS One 9: e93396.

186. Gerard C, Gonze D, Lemaigre F, Novak B (2014) A model for the epigenetic switch linking inflammation to cell transformation: deterministic and stochastic approaches. PLoS Comput Biol 10: e1003455.

187. Mukherjee SP, Behar M, Birnbaum HA, Hoffmann A, Wright PE, Ghosh G (2013) Analysis of the RelA:CBP/p300 interaction reveals its involvement in NF-kappaB-driven transcription. PLoS Biol 11: e1001647.

188. Basak S, Behar M, Hoffmann A (2012) Lessons from mathematically modeling the NF-kappaB pathway. Immunol Rev 246: 221-238.

189. Csikasz-Nagy A (2009) Computational systems biology of the cell cycle. Brief Bioinform 10: 424-434.

190. Walker DC, Hill G, Wood SM, Smallwood RH, Southgate J (2004) Agent-based computational modeling of wounded epithelial cell monolayers. IEEE Trans Nanobioscience 3: 153-163.

191. Pogson M, Smallwood R, Qwarnstrom E, Holcombe M (2006) Formal agent-based modelling of intracellular chemical interactions. Biosystems 85: 37-45.

192. Kanehisa M (2013) Chemical and genomic evolution of enzyme-catalyzed reaction networks. FEBS Lett 587: 2731-2737.

193. Loriaux PM, Hoffmann A (2012) A framework for modeling the relationship between cellular steady-state and stimulus-responsiveness. Methods Cell Biol 110: 81-109.

194. An G (2008) Introduction of an agent-based multi-scale modular architecture for dynamic knowledge representation of acute inflammation. Theor Biol Med Model 5: 11.

195. Spencer SL, Sorger PK (2011) Measuring and modeling apoptosis in single cells. Cell 144: 926-939.

196. Hill BT, Sweetenham J (2012) Clinical implications of the molecular subtypes of diffuse large B-cell lymphoma. Leuk Lymphoma 53: 763-769.

197. Lee TK, Denny EM, Sanghvi JC, Gaston JE, Maynard ND, Hughey JJ, Covert MW (2009) A noisy paracrine signal determines the cellular NF-kappaB response to lipopolysaccharide. Sci Signal 2: ra65.

198. Ballard DH (1981) Generalizing the Hough transform to detect arbitrary shapes. Pattern Recognition 13: 111-122.

199. Shen H, Nelson G, Kennedy S, Nelson D, Johnson J, Spiller D, White MRH, Kell DB (2006) Automatic tracking of biological cells and compartments using particle filters and active contours. Chemometrics and Intelligent Laboratory Systems 82: 276-282.

200. Jones TR, Cole MD (1987) Rapid cytoplasmic turnover of c-myc mRNA: requirement of the 3' untranslated sequences. Mol Cell Biol 7: 4513-4521.